Body-wave seismic interferometry applied to earthquake- and storm-induced wavefields

Body-wave seismic interferometry applied to earthquake- and storm-induced wavefields

Proefschrift

ter verkrijging van de graad van doctor
aan de Technische Universiteit Delft,
op gezag van de Rector Magnificus prof. ir. K.C.A.M. Luyben,
voorzitter van het College voor Promoties,
in het openbaar te verdedigen op 7 september 2012 om 12:30 uur

door

Elmer RUIGROK

geofysisch ingenieur

geboren te Eindhoven

Dit proefschrift is goedgekeurd door de promotor:

Prof. dr. ir. C.P.A. Wapenaar

Samenstelling promotiecommissie:

Rector Magnificus	Technische Universiteit Delft	Voorzitter
Prof. dr. ir. C.P.A. Wapenaar	Technische Universiteit Delft	Promotor
Prof. dr. ir. E.C. Slob	Technische Universiteit Delft	
Prof. dr. G. Bertotti	Technische Universiteit Delft	
Prof. dr. S.A.P.L. Cloetingh	Utrecht Universiteit	
Prof. Dphil. Bsc. A. Curtis	The University of Edinburgh	
Dr. H. Paulssen	Utrecht Universiteit	
Drs. A. Verdel	TNO	

ISBN 978-90-8891-450-8

© 2012 E.N. Ruigrok, Section of Applied Geophysics and Petrophysics, Department of Geoscience & Engineering, Delft University of Technology, Delft, The Netherlands. Some rights reserved.
Chapter 2 is adapted from published work (© 2008 EAGE, doi: 10.1111/j.1365-2478.2008.00697.x) and reprinted here with permission from the European Association of Geoscientists and Engineers. Chapter 3 is adapted from published work (© 2010 RAS & DGG, doi: 10.1111/j.1365-246X.2010.04724.x) and reprinted here with permission from the Royal Astronomical Society and the Deutsche Geophysikalische Gesellschaft. Chapter 4 is adapted from published work (© 2012 AGU, doi:10.1029/2012GL051672) and reprinted here with permission from the American Geophysical Union. Chapter 5 is adapted from published work (© 2011 AdS, doi:10.1016/j.crte.2011.02.006) and reprinted here with permission from the Académie des Sciences / Elsevier Masson SAS. Chapter 6 is adapted from work that is published (© 2012 SSA, doi:10.1785/0120110242) and printed here with permission of the Seismological Society of America. Appendix C is adapted from published work (© 2012 AGU, doi:10.1029/2012GL051443) and reprinted here with permission from the American Geophysical Union.

SUPPORT
The research for this thesis has been financially supported by the Netherlands Organisation for Scientific Research (NWO) and by The Netherlands Research Centre for Integrated Solid Earth Sciences (ISES).

Typesetting system: LaTeX2e

Published by Uitgeverij BOXPress, Oisterwijk, The Netherlands
Printed by Proefschriftmaken.nl — Printyourthesis.com

Contents

1 Introduction **1**

1.1 Body-wave seismology 1

1.2 Receivers and natural sources 4

1.3 Seismic Interferometry 5

1.4 Objectives and Outline 7

I Earthquake applications **11**

2 Global-scale seismic interferometry **13**

2.1 Introduction 13

2.2 Derivation of global-scale seismic interferometric relations 16

2.2.1 Elastodynamic reciprocity theorem 16

2.2.2 Basic relation 19

2.2.3 Relation without near-offset responses 21

2.2.4 Acoustic relations 22

2.3 Global-scale acoustic wavefield modeling 23

2.4 Numerical illustration 27

2.5 Towards application 32

2.5.1 Stationary phase localization 32

2.5.2 PcP retrieval 33

2.5.3 Removing undesired events 37

2.6 Conclusions 38

2.A Derivation of generalized source-receiver reciprocity relations 40

2.B Artifacts . . . 44
2.B.1 Imperfections . . . 44
2.B.2 Noise . . . 44
2.B.3 Additional events . . . 45

3 Lithospheric-scale seismic interferometry: multi offset 49
3.1 Introduction . . . 49
3.2 Seismic Interferometry . . . 51
3.3 Laramie array . . . 55
3.4 Comparison of seismic interferometric approaches . . . 57
3.5 Imaging . . . 62
3.6 Conclusions . . . 67
3.A Sampling . . . 69
3.B Fresnel zone . . . 73
3.C Decomposition and estimation of the near-surface velocities . . . 75
3.D Correlation panels . . . 76
3.E Imaging stability . . . 80

4 Lithospheric-scale seismic interferometry: single offset 83
4.1 Introduction . . . 83
4.2 Global-phase seismic interferometry . . . 84
4.3 Data selection . . . 85
4.4 Processing . . . 87
4.5 Results . . . 89
4.6 Discussion . . . 91
4.A GloPSI auxiliary material . . . 92

II Microseism applications 95

5 Extraction of P-waves 97
5.1 Introduction . . . 97
5.2 Survey area and data inspection . . . 99
5.3 Origin of noise . . . 102

5.4 Noise seismic interferometry . . . 104
5.5 DF band . . . 107
5.6 MF band . . . 114
5.7 Discussion and conclusions . . . 116

6 Basin imaging 119
6.1 Introduction . . . 119
6.2 Noise analysis . . . 121
6.3 Body-wave seismic interferometry . . . 126
6.4 H/V-ratio . . . 130
6.4.1 Noise records . . . 130
6.4.2 Earthquake records . . . 132
6.4.3 Comparison . . . 133
6.5 Receiver function . . . 134
6.6 Discussion and conclusions . . . 136
6.7 Data and resources . . . 138

7 Conclusions and outlook 139
7.1 Conclusions . . . 139
7.2 Outlook . . . 142

A CMB imaging 145
A.1 Introduction . . . 145
A.2 SI by midpoint integration . . . 145
A.3 Numerical illustration . . . 147
A.4 Discussion . . . 148

B Q-estimation 151
B.1 Introduction . . . 151
B.2 Seismic interferometry by crosscorrelation (CC) . . . 151
B.3 Seismic interferometry by multidimensional deconvolution (MDD) . . . 154
B.4 Tracking internal events . . . 156
B.5 Q-estimation with internal events . . . 157
B.6 Conclusions . . . 160

C Anomaly scanning with P_{diff} **161**

C.1 Introduction 161

C.2 Crosscorrelation method 162

C.3 Inline scanning 163

C.4 Testing for source-side anomalies 165

C.5 Map scanning 166

C.6 Discussion 168

C.7 Conclusion 169

C.A P_{diff} auxiliary material 170

D Multidimensional deconvolution **173**

D.1 Introduction 173

D.2 Theory for one-sided illumination 174

D.3 Application to surface waves 177

D.4 Application to teleseismic body waves 181

Bibliography **183**

Summary **199**

Samenvatting **203**

The making of **207**

Curriculum Vitae **211**

Chapter 1

Introduction

1.1 Body-wave seismology

Not so long ago the Earth was believed to be flat, at least by part of the population. Since the crew of Ferdinand Magellan completed the voyage around the world in 1524, we are sure that we are living on a spherical structure, with a radius of $6.4 \cdot 10^3$ km. But what is inside it (Fig. 1.1a)? While the Earth's surface was further explored after Magellan's voyage, the Earth's internal domain remained a dark mystery for a long time. For an overview

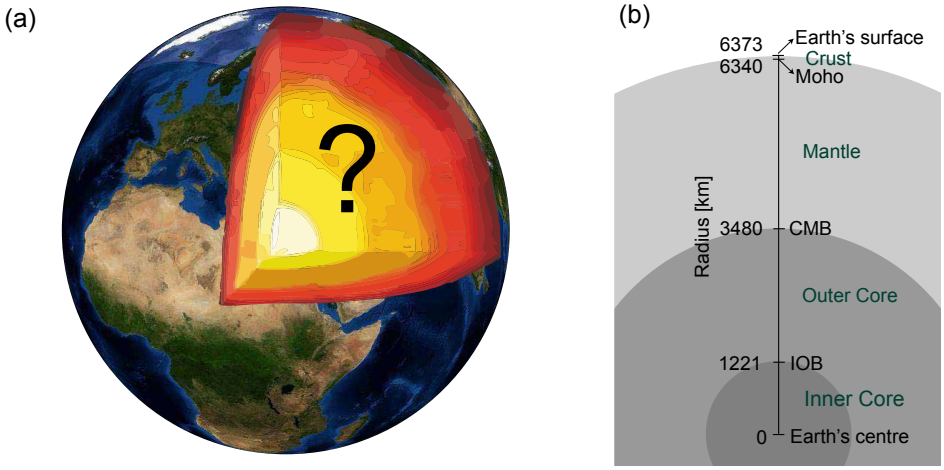


Figure 1.1 *With help of seismology our understanding of the Earth moved from (a) a solid mass with largely unknown composition to (b) a delineation in concentric shells with largely inferred composition. The main changes in rock properties occur at the inner-core outer-core boundary (IOB), the core-mantle boundary (CMB) and the mantle-crust boundary, better known as Mohorovičić (Moho).*

of our past imaginations and insights in the underworld, see Kroonenberg (2011). Not until the start of the 20th century, the upcoming science of seismology has contributed significantly to unveiling its interior. In the following we briefly introduce seismology and one of it's working horses, seismic imaging. Next, we sketch a brief historical development of seismology. In the end of this section, we outline one of the major challenges that is to be solved for future advance.

Seismologists study the trembling of the Earth. Much attention is paid to the main source of serious shaking: earthquakes. But also other seismic sources, like mining blasts, ocean storms and windmills are studied. An earthquake is a sudden displacement of a tiny fraction of the Earth's solid mass, over a fault. Besides to a lot of damage, this displacement leads to local expansions and contractions of rock. Because the Earth is to a certain extent elastic it has the tendency to bounce back to its original state. Because the expanded and contracted rock is connected to its vicinity, the expansions and contractions are passed on to the surrounding rock, which transmit the disturbances again further away from the source: propagating elastic disturbances or seismic waves are created. Both pressure waves and shear waves are initiated. In a pressure wave, the expansions and contractions are in the same direction as the wave propagates. The same type of wave exists in air and is called sound when it vibrates in the audible range. Unlike the air though, the solid Earth is rigid. Through this rigidity particles can also oscillate in the direction perpendicular to the direction of wave propagation. Such a wave is called a shear wave. Pressure and shear waves are called bulk or body waves, as they travel through the interior of the Earth. Besides body waves there are waves that only exist at and near the interface between the solid Earth and atmosphere (Rayleigh and Love waves), between water bodies and the atmosphere (surface gravity waves) and between the solid Earth and water bodies (Scholte waves). In the solid-Earth community, Rayleigh and Love waves are referred to as surface waves.

In this thesis we study the trembling of the Earth, with the aim of finding out what is inside it. This subclass of seismology is called seismic imaging. Seismic imaging finds its main use in the part of the Solid Earth that is within our reach. The deepest borehole (Kola, Russia) has only penetrated the upper 0.2 percent ($\approx$12 km) of Earth's radius. More conventionally though, only the upper 0.1 percent is affected by us. For this reachable range, seismic imaging can be used to find, e.g., water reservoirs, hydrocarbon accumulations, karst holes and solid sand layers. Imaging the deep (i.e., unreachable) Earth finds its main use in hazard assessment, besides satisfying our curiosity. Through imaging the deep Earth we can better understand earthquakes and volcanism. Imaging the deep Earth also improves our ability to assess the impacts of an earthquake. By characterizing the elastic parameters of the deep Earth, we can model elastic-wave propagation for a given earthquake, and therewith forecast the shaking that will be experienced at the Earth's surface.

In this thesis we focus on body waves. To investigate the Earth's interior, these are the most useful waves as they travel through the interior of the Earth, in contrast to surface waves. When these body waves reach the Earth's surface, it will start to move for a short duration. Consequently, we can locally record a wave by measuring the motion of the

Earth's surface. A device to record the Earth's vibration is called a seismograph, a (seismic) station, a seismometer, a geophone, a vibration sensor or simply a receiver. The recording of the Earth's local vibration as function of time is called a seismogram or a trace. If it was in the audible bandwidth, people would probably refer to it as the Earth's music. The analysis of these seismograms has led to major discoveries of the Earth's structure:

The discontinuity between the crust and mantle (Fig. 1.1b) was found by Andrya Mohorovičić (1909) by refraction seismology. He measured both a direct wave, traveling through the crust, as well as the so-called head wave, traveling through the upper part of the mantle. With the velocity difference he could delineate the thickness of the crust.

Richard Oldham (1906) discovered the existence of the Earth's core. Previously, the existence of a core had already been predicted by studies of the Earth's gravity. Oldham proved the existence by noticing a shadow zone for elastic waves. Beyond about $1.1 \cdot 10^4$ km from an earthquake (measured along the Earth's surface), the conventional direct waves did not arrive. The direct P-wave only was recorded again at much further distances. The direct S-wave was not recorded at all anymore. Consequently, the (outer) core could not be a rigid medium.

Inge Lehmann (1936) discovered the inner core by the observation of arrivals in the core's shadow zone. Birch (1940) suggested that the inner core should be solid. Not until 2000 (Deuss et al., 2000) there was direct evidence for the solid phase of the inner core, by the unequivocal observation of inner-core shear waves.

The main medium parameter that is extracted from seismic waves is its seismic velocity. This seismic velocity is a function of the elastic parameters of rocks, which are again affected by the pressure and temperature at depth. Using the seismic velocity in conjunction with other inferred rock parameters such as density, the rock's composition can be estimated. As outlined above, a rough (seismic velocity) structure of our planet was already known by the first half of the last century (Fig. 1.1b), which was succeeded by more precise models (e.g., Fig. 2.4). One large shortcoming of the models from that time was that they depicted velocity variation only in one dimension (1D). The Earth was regarded as a set of piecewise homogeneous concentric shells. Since then, there have been major advances in finding the laterally varying structure of the globe.

Inferring a (local) velocity model from wave-arrival times is formalized as travel-time tomography (TTT). With TTT, first a simple velocity model is assumed such that the sources can be located (and timed) with the help of first arrival times measured at a few different locations. Subsequently, one tries to find the velocity perturbation distribution (the actual velocity minus the assumed velocity distribution) of the media between the source and the receivers. The velocity perturbation is inverted from the measured travel times. Based upon the assumed velocity distribution, the ray paths of the arrivals at the different receivers are calculated. Next, it can be determined which velocity perturbations give the most accurate travel times for all the different arrivals.

Together with the analysis of surface waves, TTT has resulted in detailed velocity-

perturbation models (e.g., Aki et al., 1977; van der Hilst et al., 1997; Bijwaard & Spakman, 2000). However, from TTT only a smooth velocity model can be estimated. The Earth, though, is not overall a smoothly varying medium. Close to the surface, processes like sedimentation and intrusion have lead to sharp material contrasts. Also deep inside the Earth, there are sudden changes in composition and phase transitions. Sharp discontinuities lead to conversions and reflections of seismic waves. It is those reflections that are most suitable in imaging the discontinuities. The technique developed to do this, is called seismic reflection imaging (SRI). In fact, the reachable subsurface has intensively been studied throughout the world using SRI. In a SRI experiment, every point in the subsurface (within the area of investigation) is illuminated from different angles. To accomplish this, a dense source and receiver distribution is necessary. The recorded primary reflections are used to make an image of the reflectivity (i.e., contrasts in elastic medium parameters) of the subsurface. Through the availability of multi-angle reflection information, both a reflectivity image and a velocity model can be obtained. Though SRI is considered to be the most advanced technique for imaging the subsurface, the dense source (and receiver) distribution requirement limits the use for deep-Earth imaging. In this thesis we work on a methodology to alleviate the stringent requirement on the source distribution.

1.2 Receivers and natural sources

Nowadays receiver networks are not so much of a restriction. Seismometers are becoming more and more affordable and can be installed at almost any place on the Earth's surface or in shallow boreholes. Also offshore, the Earth can be sensed, using ocean-bottom seismometers. There are different global networks of isolated stations that measure continuously. The main networks are the American-run GSN and the French-run GEOSCOPE. Besides, there is a growing number of regional, more-or-less linear arrays of stations, which are only temporarily in the field (typically a few months to a few years). These arrays have regional imaging targets. Examples are the Laramie array (e.g., Hansen & Dueker, 2009), the Hi-CLIMB experiment (e.g., Nábělek et al., 2009) and the Batholiths experiment (e.g., van Wijk et al., 2011). Moreover, there is a development of worldwide installation of continuously measuring 2D arrays, e.g., USArray (e.g., Levander, 2003), KiK-net (e.g., Okada et al., 2004) and IberArray (e.g., Díaz et al., 2010), probably soon to be followed with similar arrays over the whole of Europe (EUROARRAY, e.g., Cloetingh et al. (2009)) and China (e.g., Dong et al., 2011).

Sources are still much of a restriction. In principle, massive controlled sources could be used to illuminate deep structure. These sources, like dynamite and atomic bombs, are not only costly, but may also lead to destruction in their immediate surroundings. Consequently, for imaging on a large scale, primarily natural (and thus uncontrolled) sources are used. From the imaging perspective, a disadvantage of natural sources is that their distribution is limited and irregular (Fig. 2.1). Also, their unpredictable occurrence time is highly unpractical. Moreover, natural sources may induce a very complicated vibration sequence (source time

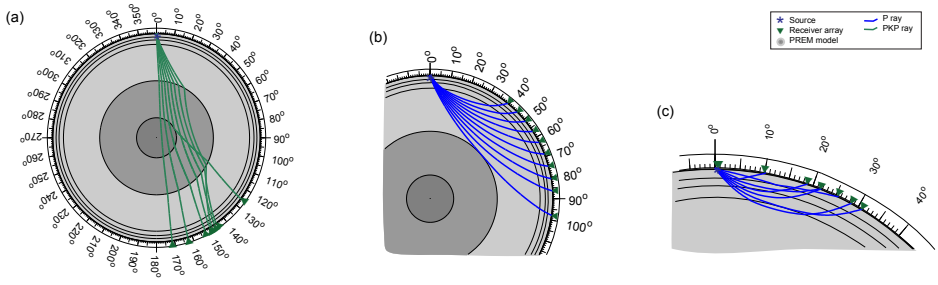


Figure 1.2 *Examples of (a) global, (b) teleseismic and (c) regional phases. Global phases are waves that traverse the core before reaching a receiver. In this thesis, teleseismic phases are defined as waves that travel through the lower mantle (> 660 km depth), but not through the core, before reaching a receiver. What remains are the regional (and local) phases, which are waves that never reach the lower mantle before reaching a receiver.*

function) that could last up till minutes for earthquakes and up till days for noise sources. All these characteristics make the use of natural sources for SRI inconvenient.

In this thesis we consider both earthquake responses and microseisms. An earthquake response is the Earth's vibration caused by an earthquake. A microseism is the Earth's vibration that is indirectly caused by swell waves in oceans. The measured body waves induced by earthquakes and microseism sources can be classified based upon the distance traversed between the source and receiver. We distinguish global, teleseismic and regional phases (Fig. 1.2). In this thesis we will leave out the complexities of regional phases and will only use teleseismic and global phases.

1.3 Seismic Interferometry

As discussed above, the uncontrolled nature of natural sources makes them less amenable for SRI. A record of naturally induced wavefields might initially make little sense, due to unknown source positions, long and complicated source-time functions, multiple sources being active at the same time, and an unknown and highly scattering medium. With seismic interferometry (SI) we aim to gain more control over the naturally induced wavefields. SI can be looked upon as a filtering operation. By the application of SI to the records of two stations, the waves that hit upon the first station, which then (multiply) reflect on subsurface interfaces before hitting the second station, are passed, while all other waves are suppressed. Consequently, a response can be obtained as if there were a source at the first station and a receiver at the other. In this case, we speak about a virtual source (at the position of the first station). When the retrieved response contains primary reflections, these can be isolated and used for SRI. When we apply SI to a regularly-spaced array of receivers, we could turn uncontrolled natural sources into a well-organized succession of virtual sources.

In the classical form, SI was derived as an autocorrelation of a (plane-wave) response detected at the free surface, due to a (deeply) buried source (Claerbout, 1968). Through this autocorrelation, the response could be retrieved as if there were a collocated source and receiver on the free surface. This idea was generalized to arbitrarily heterogeneous media for receivers at different locations (Rickett & Claerbout, 1999; Schuster, 2001; Wapenaar, 2003; Bakulin & Calvert, 2006). In the latter case, seismic observations at two different locations, A and B, are crosscorrelated and stacked over source positions. Given a sufficient distribution of sources, the complete response between A and B is retrieved. The initial derivations were for acoustic media. Later, the same principle was proven to work for elastic media (Wapenaar, 2004), for electromagnetic media (Slob et al., 2007) and interferometry was further generalized for different wave and diffusion phenomena (Wapenaar et al., 2006; Snieder et al., 2007; Weaver, 2008; Snieder et al., 2010).

The last few years, a few alternative SI implementations have been developed. Slob et al. (2007) introduced the application of SI by crossconvolution instead of crosscorrelation. In this case, one of the receivers needs to be located outside a volume surrounded by sources, and the other receiver inside this volume. The advantage of SI by crossconvolution is that losses are treated correctly. Also, losses are treated correctly when crosscorrelations of source responses are added that precisely compensate for the losses (Snieder, 2007). However, the necessary sources are unlikely present in an actual medium. As explained in Wapenaar et al. (2010b) a deconvolution of the wavefields detected at two different receivers (e.g., Trampert et al., 1993; Snieder & Safak, 2006; Vasconcelos & Snieder, 2008) may be casted in the framework of SI. The disadvantage of SI by deconvolution is the need for stabilization. The advantage is that losses are well accounted for. Besides losses, also an irregular source distribution may lead to suboptimal Green's function retrieval by crosscorrelation SI. Given a well sampled receiver array, besides losses and source wavelets, also imprints of an irregular source distribution can be deconvolved for. This is achieved by replacing the 1D deconvolution by a 2 or 3D deconvolution (Schuster & Zhou, 2006; Wapenaar et al., 2008b,c). This later implementation is called SI by multidimensional deconvolution (MDD). For a few applications to uncontrolled sources, see Appendix D.

Not only was the SI-principle extended to different media, also SI was extended beyond retrieving responses between two observation points. Curtis et al. (2009) retrieved the response between two source locations; thus creating a virtual receiver at a source location. If both many sources and many receivers are available, the virtual-source and virtual-receiver concept can be combined (Curtis & Halliday, 2010a). In this case, crosscorrelated or crossconvolved observations are integrated both over sources and receivers, to create the response at a virtual source due to a virtual receiver. Using this methodology, e.g., it would be possible to measure the response of an earthquake with a receiver that was installed only after the occurrence of that earthquake (Curtis et al., 2011). Poletto & Wapenaar (2009); Poletto & Farina (2010) introduced the virtual-reflector method. With this technique, the response can be created as if there were a reflector at a receiver position, by integrating crossconvolutions over receiver positions. Alternatively, a virtual reflector can be created at a source position

by integrating crossconvolutions over source positions.

SI inspired a number of other techniques, like the virtual refraction (Dong et al., 2006; Tatanova et al., 2008; Mikesell et al., 2009) and event location by crosscorrelation migration (Schuster et al., 2004; Xiao et al., 2009; Grandi & Oates, 2009). These methods share with SI that observations are crosscorrelated. However, unlike SI no (parts of the) Green's function are retrieved and therefore these methods cannot —senso stricto— be classified as SI. In Appendix C we present another method that was inspired by SI. Crosscorrelations of diffractions from the core-mantle boundary are used to swiftly scan anomalies in the crust and mantle.

The basic principles of SI are explained in Wapenaar et al. (2010a). For interferometric developments specified to global seismology, lithospheric imaging and noise recordings, we refer to Section 2.1, 3 and 5.1, respectively. For an overview of techniques used to improve the SI results, see Appendix D.

1.4 Objectives and Outline

The aim of this work is to improve the imaging of the interior of the Earth by the application of body-wave SI to naturally induced seismic data. By the application of SI we want to make naturally induced wavefields more amenable for the application of imaging algorithms. As we are interested in the deep Earth, we only focus on low-frequency waves (< 2 Hz). In Part I of this thesis, applications to earthquake recordings are considered. In Part II we evaluate the retrieval of reflections using microseisms.

In an earlier thesis from the same university, body-wave SI was applied to high-frequency recordings, with the aim to image shallow structures (Draganov, 2007). The follow up will be written by Carlos Almagro-Vidal. Also Ralf Feld will apply SI to uncontrolled sources. However, he will use electromagnetic rather than seismic waves, to image the very shallow subsurface (< 50 m). Two other theses focus on the application of body-wave SI to wavefields induced by controlled seismic (by Joost van der Neut, end 2012) and electromagnetic (Hunziker, 2012) sources. In both theses, the emphasis is on SI by MDD. Electromagnetic and seismic waves will be linked in the thesis of Niels Grobbe, which will be on electrokinetic SI.

We consider SRI as the imaging method of choice. As SRI needs (primary) reflections as input, our aim is to retrieve especially primary reflections with SI. In this thesis, we will do this for three different scales (Fig. 1.3). In Chapter 2 we look into the global-scale configuration. For this configuration, two seismic stations (or two arrays of stations) may be located anywhere on the globe and reflectors may be located anywhere in depth. In the drawn example (Fig. 1.3a) the imaging target is the elusive D'' layer, which is known to exist just above the core-mantle boundary, but has so far only been imaged in regions with abundant seismicity (Wang et al., 2006). We derive and numerically test relations to retrieve the complete response between two stations, using worldwide seismicity. The SI

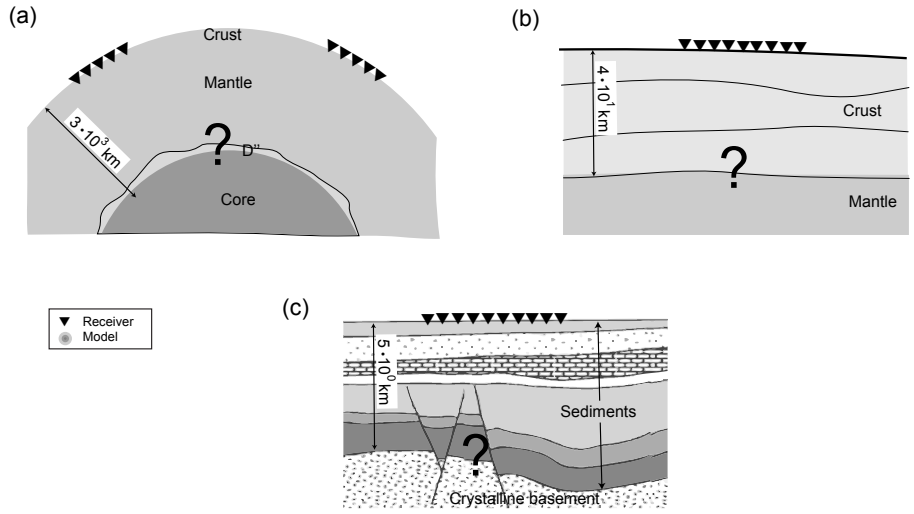


Figure 1.3 *The three different scales that are considered in this thesis: (a) global scale, (b) lithospheric scale and (c) basin scale. At the different scales, the common aim is to unveil the Earth's structure at the question marks (the imaging targets). For this purpose, we will apply seismic interferometry to natural source responses, to extract primary reflections between station positions (black triangles). The primary reflections are then used to make an image. (c) is adapted from Bosworth et al. (2008)*

relations are valid for a closed entity for seismic waves, like the Earth is by approximation. The relations do not account for inelastic losses, by which eventually all seismic energy is transformed to heat. Though normally of negligible influence, the SI relations also account for the rotation of the Earth. In practice, the distribution of the larger earthquakes is not wide enough to retrieve complete responses between any two points on the Earth. In the remainder of the chapter we therefore evaluate how SI can be of use for realistic distributions of seismicity. In Appendix A we make another step towards the application to field data. We acknowledge that a well-sampled array of stations is much easier to find than a wide surface distribution of high-magnitude seismicity. Therefore, we propose an SI relation that integrates over midpoints between receiver positions, instead of over sources. Using this relation, a reflection response can already be retrieved using only a single source.

In Chapter 3 we zoom in to the lithospheric-scale configuration (Fig. 1.3b). The lithosphere is the part of the solid Earth where most activity takes place. It makes up the crust and the upper part of the mantle. It is this part of the Earth that, broken into plates and fueled by convection in the mantle, undergoes birth (at midoceanic ridges), collisions (resulting in stunning topography) and death (subduction back into the mantle). Inspecting the Earth in depth unveils a part of the history of the lithosphere and tells us the processes still ongoing.

Information about the structure of the lithosphere is hidden in the coda of wavefields that arrive due to distant seismicity. We test a few different SI approaches to extract this information. We simultaneously test on synthesized earthquake responses and on actual responses, detected with the Laramie broadband array (2000-2001). We evaluate the requirements for obtaining multi-offset reflection responses that can also be used for obtaining a velocity model. We estimate this model for the subsurface below the Laramie array and we use it to locate the extracted reflectivity in subsurface space, thus creating a reflectivity image of the lithosphere.

In Chapter 4 we focus again on the lithospheric scale. This time, we assume that a velocity model is already available through other means. Consequently, only single-offset reflection responses are required to make an image. We use global phases (Fig. 1.2a) to obtain zero-offset reflection responses. We show the robustness of the method with data from the Hi-CLIMB experiment (2002-2005). The successive application of SRI unveils an image of the Indian-Eurasian Plate collision. In Appendix B we present a method that incorporates autocorrelations of similar planar wavefields to estimate loss factors of a layer near the Earth's surface.

The rediscovery of body waves in low-frequency noise ($<$1 Hz) opened up the research for the last two chapters. Using SI approaches similar to the ones used for earthquake recordings, we retrieve reflection responses from body-wave noise. The main difference between applications to noise and (large) earthquakes is that the origin of large earthquakes is known, whereas the origin of noise is generally not known. Therefore, the main challenge for noise applications is to unravel the noise illumination. For this purpose, in Chapter 5, we use a well-sampled areal array in Egypt to study the noise illumination in different frequency bands. We only select the noise records with a favorable body-wave content and process them into separate reflection responses, of both the lithosphere and the upper crust. In Chapter 6 we further evaluate what basin-scale information (Fig. 1.3c) can be extracted from the retrieved reflection responses. The wavelengths of the responses extracted from low-frequency noise are too large to image a sedimentary basin in detail. However, the sharp boundary between the sediments and the underlying crystalline rocks, can be delineated. For the same Egypt dataset, we compare the information that is extracted with SI with the information that is obtained when using two other passive seismic techniques, namely horizontal-to-vertical spectral ratio and receiver function.

At the end of each chapter conclusions are drawn, or the gained insights are discussed in a broader context. In Chapter 7 we give a summary of the conclusions and give an outlook of future developments.

Part I

Earthquake applications

Chapter 2

Global-scale seismic interferometry[1]

2.1 Introduction

Seismic reflection imaging (SRI) has proven to be the most successful technique for exploration of oil and gas. For the application of this technique, the subsurface needs to be illuminated from many different angles. With the acquired responses a high-resolution image of the subsurface can be made. On the exploration scale, the illumination from many directions can be achieved by using a dense grid of controlled sources at the surface (dynamite, vibrators, air guns). On a global scale, though, one is dependent on the natural-source distribution. Only the larger earthquakes generate enough energy to illuminate the deep interior of the Earth. These larger earthquakes are mainly situated along the active lithospheric plate boundaries (Fig. 2.1). Thus, there are many areas on the globe, beneath which the Earth's interior is not directly illuminated. It is especially this sparse source distribution that impedes the use of SRI on a global scale. Also, to get a better laterally varying velocity model using travel-time tomography or surface-wave dispersion studies, more source locations are required. The shortage of source locations on a global scale can be reduced with Seismic Interferometry (SI).

In recent years, there has been considerable progress in the development of SI techniques, see the July/August 2006 issue of Geophysics for an overview. SI is a method by which additional information can be extracted from wavefield responses. The responses measured at any combination of two receiver locations can be combined with SI to construct the response as if there were a source at one of the receiver locations and a receiver at the other. In this way, theoretically, a source can be created at any receiver position, provided there is enough illumination.

SI relations have been derived for two exploration-type configurations. The first configuration, for transient or noise sources in the subsurface, was introduced by Claerbout (1968) for

[1] This chapter has been published as a journal paper in *Geophysical Prospecting*, **56**, 395–417 (Ruigrok et al., 2008b). Note that minor changes have been introduced to make the text consistent with the other chapters of this thesis.

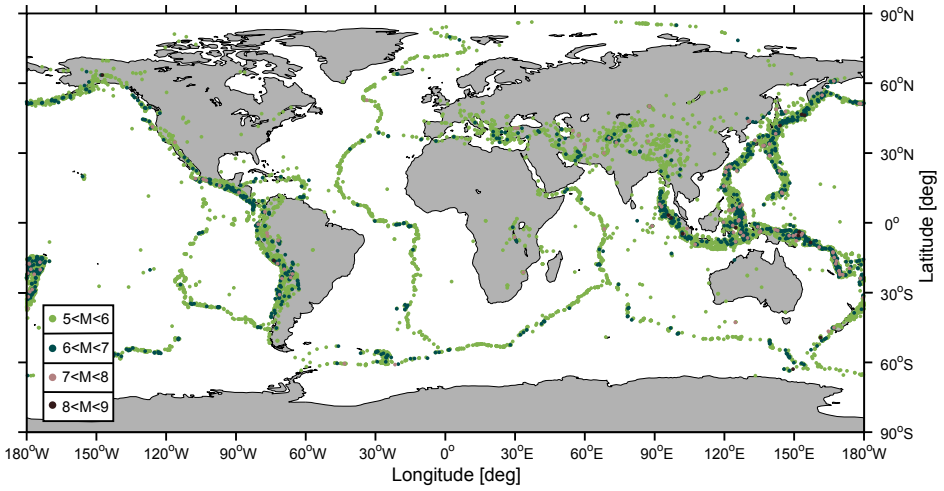


Figure 2.1 *Distribution of the larger earthquakes over the globe, from 1997 to 2007. Over 15,000 earthquakes with magnitude greater than 5.0 are plotted with clubs, of which the colors depict the magnitude. The map was made with data from the USGS National Earthquake Information Center.*

1D media and was proven to hold for a 3D arbitrary inhomogeneous medium by Wapenaar et al. (2002). These relations (for transient and for noise sources) were numerically validated by Draganov et al. (2004b) and successfully applied on real data by Draganov et al. (2007) for noise sources and by Shiraishi et al. (2006) for transient sources.

The other configuration, for controlled sources at the surface, was introduced by Schuster (2001). The technique, including an imaging step, was successfully applied on real data (Schuster et al., 2004). For the situation with receivers in a borehole, Bakulin & Calvert (2004) developed the 'virtual source method', by which the sources at the surface are redatumed through a complex overburden to the receiver positions in the borehole.

Independent of the developments in exploration geophysics, SI was also introduced in the solid Earth community. The work was inspired by ultrasonic experiments performed by Weaver & Lobkis (2001) and by time-reversed acoustics experiments (Derode et al., 2003b). Campillo & Paul (2003) used SI to construct surface-wave Green's functions between pairs of station positions. They used the diffusive part of the coda information from earthquake responses. Other researchers (Shapiro et al., 2005; Gerstoft et al., 2006; Yao et al., 2006) also applied SI to retrieve surface-wave Green's functions on a regional scale. They used different source types and correlation procedures. The retrieved Green's functions can directly be used to estimate velocity models of the crust and upper mantle with travel-time tomography and surface-wave dispersion studies.

Another application of SI in solid Earth research was introduced by Schuster et al. (2004).

They showed a synthetic example of applying SI and an imaging step on scattered teleseismic arrivals. They used the first reverberations of an incoming wavefront between the free surface and large crustal interfaces. This application has the same configuration as the exploration-scale case with transient or noise sources in the subsurface. The main difference is the scale. Also Fan et al. (2006), Kumar & Bostock (2006) and Abe et al. (2007) applied SI on regional-scale seismology using scattered teleseismic arrivals.

SI has not yet been applied in global-scale body-wave seismology. The application of SI on a global scale would reconstruct the responses from sources at locations where no earthquakes occur. Since the locations of the receivers are exactly known, so are the locations of the retrieved sources. This is not the case for real earthquakes, for which there is an uncertainty of the exact source locations. For example, SI could be applied on data from the USArray, of which the design is discussed in Levander (2003). Using SI, new source positions could be retrieved at any of the receiver positions. In this way, yet unknown responses become available for the application of travel-time tomography. The retrieval of a dense-enough sampling of source gathers would largely benefit the application of SRI, with which a much better image of the deep interior could be obtained.

As noted before, exact SI relations for transient sources were derived for exploration-type configurations (Wapenaar & Fokkema, 2006). Wave phenomena on the scale of the entire Earth cannot be described by these configurations. The main reason is the presence of a closed free surface, which traps the energy.

Weaver & Lobkis (2001) derived an interferometric relation for a diffuse wavefield in a closed system. They performed an experiment with random sources (acoustic thermal fluctuations in an ultrasonic experiment) placed throughout a volume. The Earth is not filled with random sources, at least not with sources exciting waves in the frequency bandwidth that is used in global seismology. Hence, the wavefield in the Earth is far from diffuse. Moreover, the noise sources near the surface (ocean-wave motion, etc.) do not excite enough energy to illuminate the very deep contrasts like the Core-Mantle Boundary (CMB).

In this chapter, we derive elastodynamic global-scale interferometric relations for transient sources (earthquakes) near the enclosing surface of the medium (the Earth's free surface). In this derivation, we take the rotation of the Earth into account. The acoustic versions of the relations are numerically validated with synthesized global-scale earthquake responses. Besides illustrating the derived relations numerically, we also use the synthesized responses to test one of the relations for more realistic situations, namely suboptimal source sampling and responses only from sources at a specific range of epicentral distances.

The terminology used in exploration-scale seismology is sometimes different from that used in solid Earth seismology (Table 2.1). In this chapter, no explicit choice has been made for one of the two. But to avoid confusion we consequently use the exploration terms 'source' and 'event' instead of solid-Earth terms 'seismic event' and 'phase', respectively.

Solid Earth	Exploration
source time function	source wavelet
epicentral distance	offset
seismogram	trace
station	receiver
seismic event	source
phase	event

Table 2.1 *Terminology, solid Earth versus exploration-scale seismology*

2.2 Derivation of global-scale seismic interferometric relations

In this section, we derive and clarify global-scale SI relations for transient sources near the surface. First the correlation-type reciprocity theorem is derived. Subsequently it is used to derive a global-scale SI relation that takes the rotation of the Earth and the Coriolis force into account. Afterwards we make a small adjustment to handle the absence of near-offset responses, as is common in the real Earth situation. With near-offset responses we mean the responses due to the sources which are in the direct neighborhood of the receiver location where we want to reconstruct a source. In the end of this section we present the acoustic versions of the derived relations.

2.2.1 Elastodynamic reciprocity theorem

We start with the derivation of the correlation-type elastodynamic reciprocity theorem in the frequency domain. A similar derivation (but without Coriolis force) can be found in Wapenaar & Fokkema (2006). The temporal Fourier transform of a space- and time-dependent quantity $p(\mathbf{x},t)$ is defined as

$$\hat{p}(\mathbf{x},\omega) = \int_{-\infty}^{\infty} p(\mathbf{x},t)e^{-j\omega t}dt, \tag{2.1}$$

where j is the imaginary unit and ω is the angular frequency. The hat above the quantities denotes that they are in the frequency domain. $\mathbf{x} = (x_1, x_2, x_3)$ denotes the position vector.

A reciprocity theorem relates two independent states in one and the same domain (de Hoop, 1988; Fokkema & van den Berg, 1993). Here we relate two elastodynamic states denoted with A and B. A state is characterized by the source state, the material state and the wavefield state. The source state defines the types, locations and timings of sources within the domain $\mathbb{D}$. The material state gives the relevant material properties within $\mathbb{D}$. In the elastodynamic case, these properties are mass density ρ and compliance s_{ijkl}. The wavefield state is an expression of the waves that exist within $\mathbb{D}$ due to sources within, on the boundary of, or outside the domain $\mathbb{D}$. The wavefield is characterized by the stress tensor $\tau_{ij}(\mathbf{x},t)$ and the particle velocity $v_i(\mathbf{x},t)$. The stress tensor and the particle velocity are coupled by the

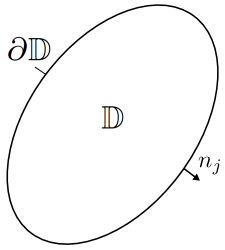


Figure 2.2 *Configuration for the application of Gauss' integral theorem and for relations derived from Gauss' integral theorem. It depicts the volume of integration, domain $\mathbb{D}$, enclosed by the surface of integration, $\partial\mathbb{D}$, and the outward pointing normal vector n_j.*

equation of motion, written in the space-frequency domain as (Dahlen & Tromp, 1998)

$$j\omega\hat{\rho}\hat{v}_i - \partial_j\hat{\tau}_{ij} + 2\hat{\rho}\epsilon_{ijk}\Omega_j\hat{v}_k = \hat{f}_i, \tag{2.2}$$

and the linearized stress-strain relation

$$-j\omega\hat{s}_{ijkl}\hat{\tau}_{kl} + (\partial_j\hat{v}_i + \partial_i\hat{v}_j)/2 = \hat{h}_{ij}, \tag{2.3}$$

where ∂_j denotes differentiation with respect to the spatial coordinates. ϵ_{ijk} is the Levi-Cevita operator, ϵ_{ijk} = 1 when ijk = 123; 231; 312, ϵ_{ijk} = -1 when ijk = 132; 213; 321, while ϵ_{ijk} = 0 otherwise. For repeated Latin subscripts Einstein's summation convention applies. In equation (2.2), the third term on the left-hand side is the apparent Coriolis force for a solid rotation with angular velocity Ω_j and $\hat{f}_i(\mathbf{x},\omega)$ is the external volume force density. In equation (2.3) $\hat{h}_{ij}(\mathbf{x},\omega)$ is the external deformation rate density. In equations (2.2) and (2.3) the medium parameters $\hat{\rho}$ and $\hat{s}_{ijkl}$ are for the moment frequency dependent and complex valued and thus account for inelastic losses in the medium.

We use the integral theorem of Gauss for any continuously differentiable vector function $\hat{p}_j$:

$$\oint_{\partial\mathbb{D}} \hat{p}_j n_j d^2\mathbf{x} = \int_{\mathbb{D}} \partial_j\hat{p}_j d^3\mathbf{x}, \tag{2.4}$$

where $\partial\mathbb{D}$ is the boundary of $\mathbb{D}$ and n_j is the outward-pointing unit vector normal to $\partial\mathbb{D}$ (Fig. 2.2), $d^3\mathbf{x}$ the elementary volume in 3-dimensional Euclidean space and $d^2\mathbf{x}$ the elementary area of $\partial\mathbb{D}$.

For $\hat{p}_j$ we choose an interaction function between the wavefield quantities of two elastodynamic states, denoted with A and B, respectively:

$$\hat{p}_j = -\hat{v}^*_{i,A}\hat{\tau}_{ij,B} - \hat{\tau}^*_{ij,A}\hat{v}_{i,B}, \tag{2.5}$$

in which * denotes complex conjugation and $\hat{\tau}_{ij,A}/\hat{\tau}_{ij,B}$ and $\hat{v}_{i,A}/\hat{v}_{i,B}$ denote the stress tensor and particle velocity of state A/B, respectively. Substituting equation (2.5) into Gauss'

integral theorem, applying the product rule for differentiation for the integrand of the volume integral, substituting equations (2.2) and (2.3) or their complex conjugated versions to replace $\partial_j \hat{\tau}^*_{ij,A}$, $\partial_j \hat{\tau}_{ij,B}$, $\partial_j \hat{v}^*_{i,A}$ and $\partial_j \hat{v}_{i,B}$, using the symmetry relations $s_{ijkl} = s_{klij}$ and $\tau_{ij} = \tau_{ji}$ and finally reordering the terms in integrals containing medium-parameter terms, source terms and Coriolis terms, yields

$$\begin{aligned}\oint_{\partial\mathbb{D}} \{-\hat{v}^*_{i,A}\hat{\tau}_{ij,B} - \hat{\tau}^*_{ij,A}\hat{v}_{i,B}\}n_j d^2\mathbf{x} = \\ - j\omega \int_{\mathbb{D}} \{\hat{\tau}^*_{ij,A}(\hat{s}_{ijkl,B} - \hat{s}^*_{ijkl,A})\tau_{kl,B} + \hat{v}^*_{i,A}(\hat{\rho}_{\mathcal{B}} - \hat{\rho}^*_{\mathcal{A}})\hat{v}_{i,B}\}d^3\mathbf{x} \\ + \int_{\mathbb{D}} \{-\hat{\tau}^*_{ij,A}\hat{h}_{ij,B} + \hat{v}^*_{i,A}\hat{f}_{i,B} - \hat{h}^*_{ij,A}\hat{\tau}_{ij,B} + \hat{f}^*_{i,A}\hat{v}_{i,B}\}d^3\mathbf{x} \\ - \int_{\mathbb{D}} \{2\hat{\rho}^*_{\mathcal{A}}\epsilon_{ijk}\hat{v}_{i,B}\Omega_{j,A}\hat{v}^*_{k,A} + 2\hat{\rho}_{\mathcal{B}}\epsilon_{ijk}\hat{v}^*_{i,A}\Omega_{j,B}\hat{v}_{k,B}\}d^3\mathbf{x}. \quad (2.6)\end{aligned}$$

Equation (2.6) is the Rayleigh-Betti reciprocity theorem of the correlation type accounting for Coriolis force.

From here onward we take the material states for state A and B equal and we consider lossless media. Hence $\hat{\rho}^*_{\mathcal{A}} = \hat{\rho}_{\mathcal{B}} = \rho$ and $\hat{s}^*_{ijkl,A} = \hat{s}_{ijkl,B} = s_{ijkl}$. As a result the integral with the medium-contrast interactions in (2.6) - the first integral on the right-hand side of the equation - vanishes.

For the application to global-scale wave phenomena we choose $\Omega_{j,A} = \Omega_{j,B} = \Omega_j$, which is the solid rotation of the Earth. The integral with the Coriolis terms in (2.6) - the third integral on the right-hand side of the equation - can now be rewritten as

$$- \int_{\mathbb{D}} \{2\rho(\epsilon_{ijk}\hat{v}_{i,B}\Omega_j\hat{v}^*_{k,A} + \epsilon_{ijk}\hat{v}^*_{i,A}\Omega_j\hat{v}_{k,B})\}d^3\mathbf{x}. \quad (2.7)$$

Using the property $\epsilon_{ijk} = -\epsilon_{kji}$ we may rewrite the last term under the integral as $-\epsilon_{ijk}\hat{v}^*_{k,A}\Omega_j\hat{v}_{i,B}$. Hence the third integral on the right-hand side of equation (2.6) vanishes as well.

Consequently, for a solid rotating lossless Earth the Rayleigh-Betti reciprocity theorem of the correlation type accounting for Coriolis force becomes

$$\begin{aligned}\oint_{\partial\mathbb{D}} \{-\hat{v}^*_{i,A}\hat{\tau}_{ij,B} - \hat{\tau}^*_{ij,A}\hat{v}_{i,B}\}n_j d^2\mathbf{x} = \\ \int_{\mathbb{D}} \{-\hat{\tau}^*_{ij,A}\hat{h}_{ij,B} + \hat{v}^*_{i,A}\hat{f}_{i,B} - \hat{h}^*_{ij,A}\hat{\tau}_{ij,B} + \hat{f}^*_{i,A}\hat{v}_{i,B}\}d^3\mathbf{x}, \quad (2.8)\end{aligned}$$

in which - surprisingly - no term is needed to account for the Coriolis force.

Fokkema & van den Berg (1993) related different acoustic states with the help of the acoustic version of equation (2.8), without considering rotation. Doing so, useful relations were

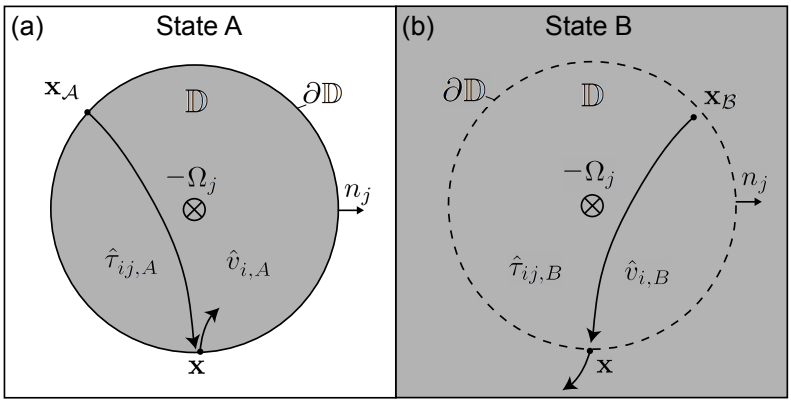


Figure 2.3 *Location of $\mathbf{x}_\mathcal{A}$, $\mathbf{x}_\mathcal{B}$ and $\mathbf{x}$ on a simplified Earth model, with rotation Ω_j opposite to the actual Earth's rotation. A domain $\mathbb{D}$ enclosed by a surface $\partial\mathbb{D}$ covers the entire inner space of the Earth, hence $\partial\mathbb{D}$ coincides with the free surface (denoted as FS). $\hat{\tau}_{ij}$ and $\hat{v}_i$ describe the wavefields within $\mathbb{D}$ and at $\partial\mathbb{D}$ due to a source at $\mathbf{x}_\mathcal{A}$ or $\mathbf{x}_\mathcal{B}$. (a) State A, Earth with FS (free surface); $\mathbf{x}_\mathcal{A}$ lays approximately at $\partial\mathbb{D}$. (b) State B, Earth without FS; $\mathbf{x}_\mathcal{B}$ lays just within $\mathbb{D}$.*

derived for seismic applications. Following a similar procedure, both acoustic and elastodynamic relations for SI were derived by Wapenaar & Fokkema (2006). Snieder (2007) used the acoustic version of equation (2.6), without considering rotation and without a complex density, but with a complex-valued compressibility ($\hat{\kappa}$, see equation (2.18)) to derive interferometric relations for attenuating acoustic media.

2.2.2 Basic relation

The representations for state A and state B are depicted in Fig. 2.3. States A and B are so-called Green's states: the sources are assumed to be impulses, such that the responses can be written as impulse responses or Green's functions. To link reality with a Green's state, a wavefield registration would need to be deconvolved for the source wavelet.

Fig. 2.3(a) depicts the representation for State A. Domain $\mathbb{D}$ covers the entire inner space of the Earth. The boundary surface $\partial\mathbb{D}$ of $\mathbb{D}$ coincides with the Earth's surface. A shallow-depth earthquake (source) has a hypocenter at $\mathbf{x}_\mathcal{A}$, which is approximately at the Earth's surface. The source in state A is represented as a boundary condition for the traction at the free surface (which is abbreviated as FS throughout the remainder of this text). The boundary condition for approaching the FS from its interior (Earth) is

$$\lim_{\mathbf{x}\uparrow\mathbf{x_{FS}}} \hat{\tau}_{ik}(\mathbf{x})n_k = \delta(\mathbf{x}-\mathbf{x}_\mathcal{A})\delta_{ip} \;\text{ for }\; \mathbf{x}\in\partial\mathbb{D}, \tag{2.9}$$

in which n_k denotes the outward pointing normal vector as depicted in Fig 2.2 and δ_{ip} is the Kronecker delta function, δ_{ip}=0 for $i\neq p$, δ_{ip}=1 for $i=p$. The Dirac delta function on the

		State A: free surface	State B: no free surface
$wavefield$ $\mathbf{x} \in \mathbb{D}$	$\hat{\tau}_{ij}$	$\hat{G}^{\tau,\tau}_{ij,p}(\mathbf{x}, \mathbf{x}_{\mathcal{A}}, \omega \mid -\mathbf{\Omega})$	$\hat{\tilde{G}}^{\tau,h}_{ij,qr}(\mathbf{x}, \mathbf{x}_{\mathcal{B}}, \omega \mid -\mathbf{\Omega})$
	$\hat{v}_i$	$\hat{G}^{v,\tau}_{i,p}(\mathbf{x}, \mathbf{x}_{\mathcal{A}}, \omega \mid -\mathbf{\Omega})$	$\hat{\tilde{G}}^{v,h}_{i,qr}(\mathbf{x}, \mathbf{x}_{\mathcal{B}}, \omega \mid -\mathbf{\Omega})$
$wavefield$ $\mathbf{x} \in \partial\mathbb{D}$	$\hat{\tau}_{ik}n_k$	$\delta(\mathbf{x} - \mathbf{x}_{\mathcal{A}})\delta_{ip}$	$\hat{\tilde{G}}^{\tau,h}_{i,qr}(\mathbf{x}, \mathbf{x}_{\mathcal{B}}, \omega \mid -\mathbf{\Omega})$
	$\hat{v}_i$	$\hat{G}^{v,\tau}_{i,p}(\mathbf{x}, \mathbf{x}_{\mathcal{A}}, \omega \mid -\mathbf{\Omega})$	$\hat{\tilde{G}}^{v,h}_{i,qr}(\mathbf{x}, \mathbf{x}_{\mathcal{B}}, \omega \mid -\mathbf{\Omega})$
$source$ $\mathbf{x} \in \mathbb{D}$	$\hat{h}_{ij}$	0	$\delta(\mathbf{x} - \mathbf{x}_{\mathcal{B}})\delta_{iq}\delta_{jr}$
	$\hat{f}_i$	0	0

Table 2.2 *States for the elastodynamic reciprocity theorem, in which the source state is a representation for relatively shallow earthquakes.*

right-hand side of equation (2.9) is a 2D delta function in the tangential directions.

Fig. 2.3(b) depicts the representation for State B. A shallow-depth earthquake has a hypocenter at $\mathbf{x}_{\mathcal{B}}$, which is just within $\mathbb{D}$. This earthquake is assumed to be a deformation-rate source. State B is a representation for an Earth without FS. The response of state B can be obtained from a real Earth response by using, e.g., surface-related multiple elimination (SRME) (Berkhout & Verschuur, 1997; Verschuur & Berkhout, 1997).

The choices made above for the type of earthquake sources are not unique. Other source mechanisms can be dealt with, but will not be considered in this chapter.

The choice to include one state with FS and one without FS is not arbitrary. If we chose both states to include a FS there would be no integral left to be evaluated in equation (2.8). If we removed the FS in both states, then there would be no reflections at the FS, which are necessary for the retrieval of a response with SI.

States A and state B are representations of an Earth that is rotating in the opposite direction as compared to the actual rotation of the Earth Ω_j (Fig. 2.3). This choice will become clear later.

The mathematical expressions for the two elastodynamic states are listed in Table 2.2. States A and B are defined for one and the same lossless inhomogeneous elastodynamic medium. The wavefield quantities, $\hat{\tau}_{ij}$ and $\hat{v}_i$, can be represented as Green's functions everywhere within $\mathbb{D}$ and for state B also everywhere at $\partial\mathbb{D}$. In state A, at the FS, we can only have a traction vector $\hat{\tau}_{ik}n_k$ unequal to zero at the location of the source. However, because the FS can move freely, $\hat{v}_i$ can be non-zero everywhere at $\partial\mathbb{D}$. The source in state B is represented in the source state. Here the Dirac delta function is a 3D delta function.

The first and second superscript of the Green's function $\hat{G}$ denote, respectively, the observed response type (τ - stress tensor; v - particle velocity) and the source type (τ - traction source; h - deformation-rate source). The subscripts denote the components of the observed response and the source, respectively. When only one subscript belongs to the traction or deformation-rate source, it is a traction or deformation-rate vector acting on a plane

tangential to the FS. The bar in state B denotes a response without FS multiples. When the bar is omitted (as in state A) we mean the complete Green's function, including all FS multiples. $\hat{G}(\mathbf{x}, \mathbf{x}_{\mathcal{A}}, \omega \mid -\mathbf{\Omega})$ is the response observed at $\mathbf{x}$ due to a source at $\mathbf{x}_{\mathcal{A}}$, given as a function of frequency ω, for a medium rotating with minus the angular velocity of the Earth, $-\mathbf{\Omega}$.

We substitute the expressions of Table 2.2 into equation (2.8). Making use of the sifting property of the delta function and the multiplication property of the Kronecker delta function, we obtain

$$-\oint_{\partial\mathbb{D}} \{\hat{G}^{v,\tau}_{i,p}(\mathbf{x}, \mathbf{x}_{\mathcal{A}}, \omega \mid -\mathbf{\Omega})\}^* \hat{\bar{G}}^{\tau,h}_{i,qr}(\mathbf{x}, \mathbf{x}_{\mathcal{B}}, \omega \mid -\mathbf{\Omega}) d^2\mathbf{x} = \\ -\{\hat{G}^{\tau,\tau}_{qr,p}(\mathbf{x}_{\mathcal{B}}, \mathbf{x}_{\mathcal{A}}, \omega \mid -\mathbf{\Omega})\}^* + \hat{\bar{G}}^{v,h}_{p,qr}(\mathbf{x}_{\mathcal{A}}, \mathbf{x}_{\mathcal{B}}, \omega \mid -\mathbf{\Omega}). \quad (2.10)$$

We change the integration over receiver positions to an integration over source positions by applying the generalized source-receiver reciprocity relations for the Green's functions. In a rotating medium the usual source-receiver reciprocity relation breaks down, hence

$$\hat{G}(\mathbf{x}_{\mathcal{B}}, \mathbf{x}_{\mathcal{A}}, \omega \mid \mathbf{\Omega}) \neq \hat{G}(\mathbf{x}_{\mathcal{A}}, \mathbf{x}_{\mathcal{B}}, \omega \mid \mathbf{\Omega}). \quad (2.11)$$

However, in Appendix 2.A it is shown that generalized source-receiver reciprocity relations, with opposite rotation, do hold:

$$\hat{G}(\mathbf{x}_{\mathcal{B}}, \mathbf{x}_{\mathcal{A}}, \omega \mid \mathbf{\Omega}) = \hat{G}(\mathbf{x}_{\mathcal{A}}, \mathbf{x}_{\mathcal{B}}, \omega \mid -\mathbf{\Omega}). \quad (2.12)$$

Thus using the generalized source-receiver reciprocity relations (2.A.6), (2.A.9), (2.A.4) and (2.A.8) and subsequently applying the inverse Fourier transform, we obtain the following expression in the time domain:

$$\oint_{\partial\mathbb{D}} G^{v,\tau}_{p,i}(\mathbf{x}_{\mathcal{A}}, \mathbf{x}, -t \mid \mathbf{\Omega}) * \bar{G}^{\tau,h}_{qr,i}(\mathbf{x}_{\mathcal{B}}, \mathbf{x}, t \mid \mathbf{\Omega}) d^2\mathbf{x} = \\ G^{v,h}_{p,qr}(\mathbf{x}_{\mathcal{A}}, \mathbf{x}_{\mathcal{B}}, -t \mid \mathbf{\Omega}) - \bar{G}^{\tau,f}_{qr,p}(\mathbf{x}_{\mathcal{B}}, \mathbf{x}_{\mathcal{A}}, t \mid \mathbf{\Omega}), \quad (2.13)$$

in which $*$ denotes convolution. Equation (2.13) is the basic global-scale SI relation for the actual rotating Earth. It states that we can reconstruct Green's functions between receiver position $\mathbf{x}_{\mathcal{A}}$ and $\mathbf{x}_{\mathcal{B}}$ in a rotating Earth when we cross-correlate responses at $\mathbf{x}_{\mathcal{A}}$ and $\mathbf{x}_{\mathcal{B}}$ resulting from sources at all $\mathbf{x}$ on $\partial\mathbb{D}$ and subsequently integrate along these sources.

We have shown here that the Green's function retrieval is in principle also valid for rotating media. Similar to flow, as discussed by Wapenaar (2006), rotation breaks time reversal and source-receiver reciprocity, but does not break Green's function retrieval by SI.

2.2.3 Relation without near-offset responses

In the previous section, we derived an SI relation that contains an integration over responses from sources all around the globe. In reality, one would like to simulate a source on a place

where no earthquakes occur. This would mean that at least the near-offset responses are missing.

To evaluate what happens if we cannot integrate over the near-offset part, we divide the integration surface $\partial\mathbb{D}$ in a near-offset part $\partial\mathbb{D}_0$ with respect to $\mathbf{x}_\mathcal{A}$ and the remaining surface $\partial\mathbb{D}_1$:

$$\partial\mathbb{D} = \partial\mathbb{D}_0 + \partial\mathbb{D}_1. \tag{2.14}$$

We substitute the expressions of Table 2.2 into equation (2.8), apply the sifting property for the Delta function and the multiplication property of the Kronecker Delta function in the volume integral and replace the complete surface integral by an integration over $\partial\mathbb{D}_1$, yielding

$$\begin{aligned}\int_{\partial\mathbb{D}_1} \delta(\mathbf{x}-\mathbf{x}_\mathcal{A})\delta_{ip}\hat{\bar{G}}^{v,h}_{i,qr}(\mathbf{x},\mathbf{x}_\mathcal{B},\omega \mid -\boldsymbol{\Omega})d^2\mathbf{x} \\ + \int_{\partial\mathbb{D}_1} \{\hat{G}^{v,\tau}_{i,p}(\mathbf{x},\mathbf{x}_\mathcal{A},\omega \mid -\boldsymbol{\Omega})\}^* \hat{\bar{G}}^{\tau,h}_{i,qr}(\mathbf{x},\mathbf{x}_\mathcal{B},\omega \mid -\boldsymbol{\Omega})d^2\mathbf{x} \approx \\ \{\hat{G}^{\tau,\tau}_{qr,p}(\mathbf{x}_\mathcal{B},\mathbf{x}_\mathcal{A},\omega \mid -\boldsymbol{\Omega})\}^*.\end{aligned} \tag{2.15}$$

By not including the integration over $\partial\mathbb{D}_0$, we do not perfectly satisfy the representation in Table 2.2. Thus equation (2.15) is not exact.

Since $\partial\mathbb{D}_1$ does not include $\mathbf{x}_\mathcal{A}$, $\delta(\mathbf{x}-\mathbf{x}_\mathcal{A})$ is zero for all $\mathbf{x}\,\epsilon\,\partial\mathbb{D}_1$ and the first term on the left-hand side of equation (2.15) vanishes. We apply generalized source-receiver reciprocity relations for Green's functions (2.A.6), (2.A.9) and (2.A.4). Subsequently applying the inverse Fourier transform, we obtain the following expression in the time domain:

$$\int_{\partial\mathbb{D}_1} G^{v,\tau}_{p,i}(\mathbf{x}_\mathcal{A},\mathbf{x},-t \mid \boldsymbol{\Omega}) * \bar{G}^{\tau,h}_{qr,i}(\mathbf{x}_\mathcal{B},\mathbf{x},t \mid \boldsymbol{\Omega})d^2\mathbf{x} \approx G^{v,h}_{p,qr}(\mathbf{x}_\mathcal{A},\mathbf{x}_\mathcal{B},-t \mid \boldsymbol{\Omega}). \tag{2.16}$$

Equation (2.16) states that, when no measurements of near sources are available, we can only reconstruct the Green's function $G^{v,h}_{p,qr}(\mathbf{x}_\mathcal{A},\mathbf{x}_\mathcal{B},-t \mid \boldsymbol{\Omega})$, which contains the FS multiples. The part of the response that is accurately reconstructed depends on the stationary points that are included in the integration and hence it depends on the size of $\partial\mathbb{D}_1$.

2.2.4 Acoustic relations

For acoustic media the wavefield is characterized by the pressure $p(\mathbf{x},t)$ and particle velocity $v_i(\mathbf{x},t)$. The pressure and the particle velocity are coupled by the linearized equation of motion, written in the space-frequency domain as,

$$j\omega\hat{\rho}\hat{v}_i + \partial_i\hat{p} + 2\hat{\rho}\epsilon_{ijk}\Omega_j\hat{v}_k = \hat{f}_i \tag{2.17}$$

and the linearized stress-strain relation

$$j\omega\hat{\kappa}\hat{p} + \partial_i\hat{v}_i = \hat{q}. \tag{2.18}$$

In equation (2.17), again the apparent Coriolis force is included, for a solid rotation with angular velocity Ω_j. In equation (2.18), $\hat{\kappa}$ is the compressibility which is frequency dependent and complex valued to account for inelastic losses in the medium and $\hat{q}$ is the volume source density of volume injection rate.

Following the same approach as in Section 2.2.1, but applying Gauss theorem on the interaction function between two acoustic states A and B,

$$\hat{p}^*_{\mathcal{A}}\hat{v}_{i,B} + \hat{v}^*_{i,A}\hat{p}_{\mathcal{B}}, \tag{2.19}$$

and substituting equations (2.17) and (2.18) in the resulting expression, the acoustic correlation-type reciprocity theorem can be derived. Substituting the acoustic counterparts of states A and B, as listed in Table 2.2, into the acoustic correlation-type reciprocity theorem and applying the generalized acoustic source-receiver reciprocity relations, (2.A.14) - (2.A.17), the acoustic global-scale SI relations can be derived. Alternatively, we can directly rewrite the elastic SI relations, (2.13) and (2.16), by replacing the superscripts h by q, τ by p and leaving out all the subscripts. Note that, comparing equations (2.17) and (2.18) with equations (2.2) and (2.3), the sign of the pressure is defined opposite to the that of the stress tensor. Thus, every time we replace τ by p we also need to introduce a minus sign. Doing so, the acoustic global-scale SI relation reads

$$\oint_{\partial\mathbb{D}} G^{v,p}(\mathbf{x}_{\mathcal{A}}, \mathbf{x}, -t \mid \mathbf{\Omega}) * \bar{G}^{p,q}(\mathbf{x}_{\mathcal{B}}, \mathbf{x}, t \mid \mathbf{\Omega}) d^2\mathbf{x} = \\ G^{v,q}(\mathbf{x}_{\mathcal{A}}, \mathbf{x}_{\mathcal{B}}, -t \mid \mathbf{\Omega}) + \bar{G}^{p,f}(\mathbf{x}_{\mathcal{B}}, \mathbf{x}_{\mathcal{A}}, t \mid \mathbf{\Omega}) \tag{2.20}$$

and the acoustic global-scale SI relation without near offset reads

$$\int_{\partial\mathbb{D}_1} G^{v,p}(\mathbf{x}_{\mathcal{A}}, \mathbf{x}, -t \mid \mathbf{\Omega}) * \bar{G}^{p,q}(\mathbf{x}_{\mathcal{B}}, \mathbf{x}, t \mid \mathbf{\Omega}) d^2\mathbf{x} \approx G^{v,q}(\mathbf{x}_{\mathcal{A}}, \mathbf{x}_{\mathcal{B}}, -t \mid \mathbf{\Omega}), \tag{2.21}$$

where v and f are in the direction perpendicular to the FS.

In the following we will take $\mathbf{\Omega} = \mathbf{0}$.

2.3 Global-scale acoustic wavefield modeling

In the previous section, we derived relations for obtaining new seismic responses from the correlation of existing global-scale responses. This section deals with the generation of global-scale synthetic earthquake responses (seismograms) with which we can illustrate the derived relations.

We synthesize the seismograms with a simplified 2D acoustic lossless Earth model based on the Preliminary Reference Earth Model (PREM, Dziewonski & Anderson (1981)). The medium parameters vary only in the radial direction (r). The rotation of the Earth is neglected. Locations on the 2D Earth model are given as function of radius and epicentral distance (Δ), ranging from -180 to $180°$.

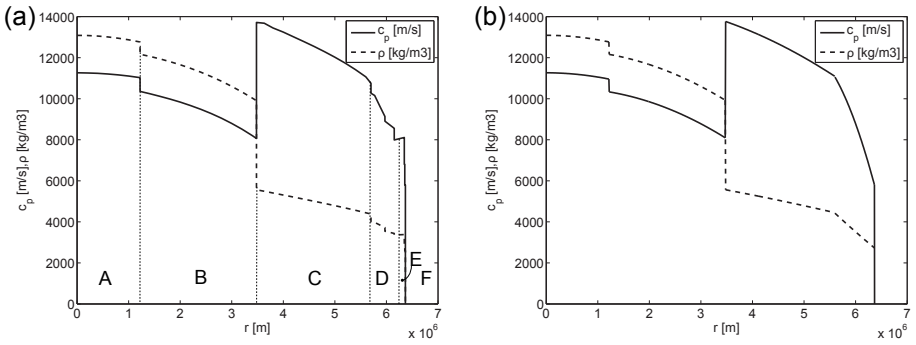


Figure 2.4 *(a) The compressional-wave velocity c_p and density ρ as functions of the radius r. Values were taken from the PREM model. With increasing r, subsequently the inner core (denoted with A), outer core (B), lower mantle (C), transition zone (D), asthenosphere and lithosphere (E) and atmosphere (F) are encountered. (b) To create this smoothed version of the PREM model the discontinuities in the transition zone, upper mantle and crust were taken out*

Fig. 2.4(a) shows a graph of the PREM model P-wave velocity c_P and density ρ as a function of the radius of the Earth. The radius is zero at the center of the Earth and increases to an average thickness of 6371 km at the Earth's surface. Fig. 2.4(b) shows our simplified version of the PREM model. As compared to the original PREM model the outermost 3 km were removed and the discontinuities in the crust and upper mantle were taken away. This simplification eases the discretization of the model and eases the interpretation of the forward modeled responses.

We model the wavefield with a staggered finite-difference scheme of the acoustic wave equation (Virieux, 1986). To enable the 2D FD modeling, the PREM model is transformed into a 2D rectangular gridded velocity and density model. We choose the grids small enough (2 by 2 km) to obviate grid dispersion and ensure stability by satisfying the criteria as derived in Lines et al. (1999).

FD is not the most accurate technique available for synthesizing global-scale seismograms. Still it is the method of choice for our illustration, since consequent inaccuracies are of no harm and the computational affordability and easy adjustability make it a practical scheme to implement.

We generate the responses for state B with the same model as for state A, but with the FS removed. Different sources and receivers are placed in the model, to generate all the responses that occur in the acoustic global scale SI relations, (2.20) and (2.21). As a source wavelet we use the first derivative of a Gaussian wavelet, with a peak frequency at 0.156 Hz.

A source is initiated at $\Delta = 0^\circ$ at zero time. Every 0.05 s new values for the wavefield are calculated at every grid point. Starting at 200 s, every 300 s a snapshot is taken from the

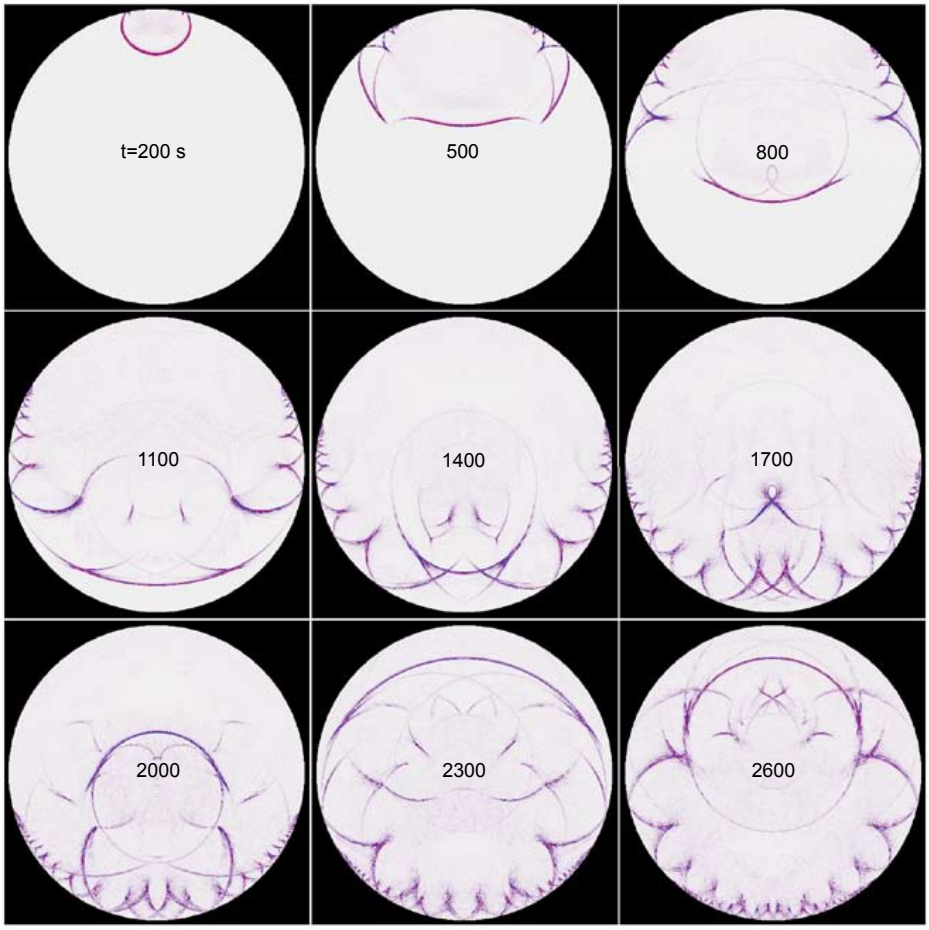


Figure 2.5 *Snapshots of the wavefield spreading through the smoothed PREM model (for state A). The wavefield was initiated by an effective dipole source at 4 km depth. The snapshots were taken at 200, 500, 800, 1100, 1400, 1700, 2000, 2300 and 2600 seconds, respectively.*

pressure at every grid point. Fig. 2.5 shows the evolving pressure distribution throughout the model for state A. The wavefield can be seen to propagate only within the Earth due to the presence of a FS. The wavefield after 200 s (upper left panel) is not perfectly circular due to the increasing velocity gradient in the crust and mantle. The wavefield is propagating much slower in the transverse direction than in the radial direction. Because of this, part of the wavefield starts to propagate along rays that bend towards the FS. After 500 s (the upper middle panel) a part of the wavefield has reflected a few times from the FS already. In the same panel, the reflection from the CMB almost hits the FS. Also in this panel, the transmitted wavefield traveling in the radial direction is on its way through the inner core. On the subsequent panels the interaction of the wavefield with the different boundaries results in more and more events. The most pronounced are the FS reflections of the direct wave.

From $\Delta = -180^\circ$ to 180° receivers are placed in the model. In total there are 2880 receivers which corresponds to one receiver per 0.125° or 14 km. Every 0.4 s the wavefield is registered at the grid points where the receivers are placed. Fig. 2.6(a) shows the v-registrations of the receivers for state A and (b) shows the v-registrations for state B. The first 3000 s of the registrations are plotted. Only the responses for receivers between $\Delta = 0^\circ$ and 180° are shown. The other 180° of responses are identical because an axi-symmetric model is used. The kinematics of the arrivals can clearly be seen. The amplitude is shown as a color variation from blue (negative) to zero (white) and positive (red). With the current plotting resolution, the true amplitude variation cannot be distinguished. High amplitudes were clipped, such that lower-amplitude arrivals can still be distinguished. The kinematics of the p-response of state A (measured just below the FS) and state B look identical with the v-response. For this reason the p-responses are not shown here.

We compare our FD numerical results with arrival times generated by ray tracing. The computed ray-tracing arrival-times (Knapmeyer, 2004) are plotted, with green crosses, in the same figure (Fig. 2.6). The events are assigned names according to the conventional (IASPEI) nomenclature (Storchak et al., 2003).

Generally, we see a good correspondence between the FD-modeled response and the ray-tracing arrival times. Since the FD modeling uses an adjusted version of the PREM model (Fig. 2.4(b)) whereas the ray tracing uses the original PREM model (Fig. 2.4(a)), the travel-time correspondence is of course not perfect.

The FD-modeled response for state A (Fig. 2.6(a)) contains very-high-order FS multiples. The infinite-order FS multiple is a surface wave. This linear event is denoted with 'L'. In the actual Earth the high-order FS multiples cannot be distinguished. This notable difference is because the model we use is 2D and lossless and without the discontinuities in the upper mantle and crust. Another difference is that refractions, e.g. Pc, are modeled with a faster amplitude decay than they have in the real Earth. This is an artifact of the usage of a rectangular grid. Because of this rectangular grid the interface is not just discontinuous in the radial direction but contains also little variations in the tangential direction by which a

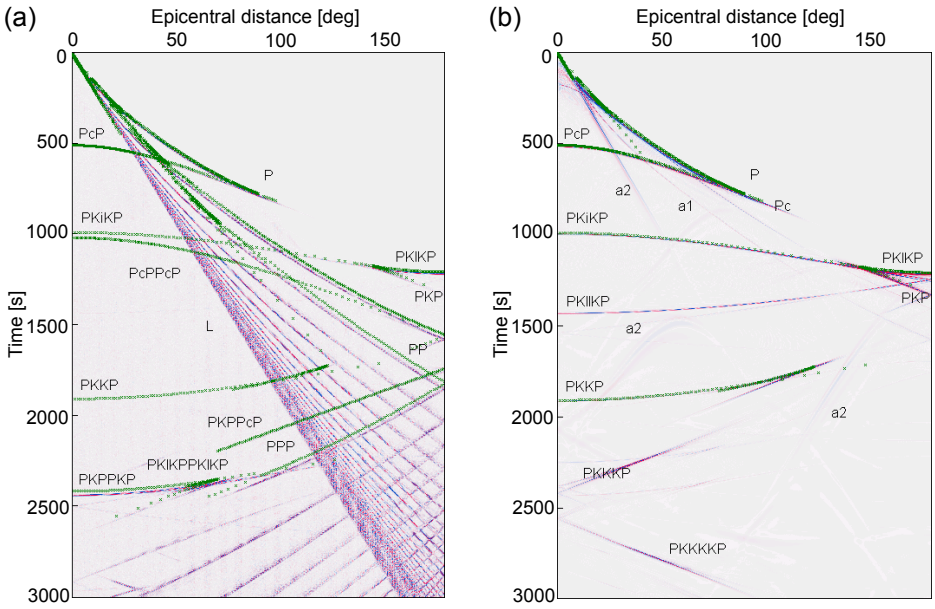


Figure 2.6 *Comparison between FD-modeled responses and ray-tracing arrival-time functions. The horizontal axis shows epicentral distance in degrees and the vertical axis shows time in seconds. The FD-modeled reflection responses of the Earth (a) with and (b) without FS multiples. Ray-tracing arrival times are plotted with green crosses in the same figures. Note that for the FD modeling an adjusted version of the PREM model is used (Fig. 2.4(b)) whereas for the ray tracing the original PREM model is used (Fig. 2.4(a)). Note also that positive time axis points downwards, as is conventional in exploration-scale seismology, but unconventional in solid Earth seismology.*

wave traveling along the interface is scattered.

In the FD-modeled response for state B (Fig. 2.6(b)), the reflection due to the change in velocity/density gradient at 570 km depth (Fig. 2.4) can be seen. It is labeled with 'a1'. Additionally, low-frequency reflections can be seen, which are labeled with 'a2'. These are artifacts of the absorbing taper at the edges of the model. They were largely filtered out by the application of a high-pass filter.

2.4 Numerical illustration

In Section 2.2, two relations for global-scale SI were derived. Central in both relations is the correlation integral:

$$\oint_{\partial\mathbb{D}} G^{v,p}(\mathbf{x}_{\mathcal{A}},\mathbf{x},-t) * \bar{G}^{p,q}(\mathbf{x}_{\mathcal{B}},\mathbf{x},t)d^2\mathbf{x}. \tag{2.22}$$

The predicted output differs, depending on whether the entire surface integral is evaluated (equation 2.20) or the near-offset part (with respect to the receiver position where a source is retrieved) is left out (equation 2.21). In this section, the correlation integral is numerically tested on the synthesized global responses. The results of the numerical illustration are shown and discussed.

The FD-modeled responses (Section 2.3) can be written as a Green's function convolved with a source wavelet. For compactness we leave out this convolution with the source wavelet. Using the Green's function notation, we modeled responses $G^{v,p}(\mathbf{x},\mathbf{x}_{\mathcal{A}},t)$, $\bar{G}^{p,q}(\mathbf{x},\mathbf{x}_{\mathcal{B}},t)$, $G^{p,p}(\mathbf{x},\mathbf{x}_{\mathcal{A}},t)$ and $\bar{G}^{v,q}(\mathbf{x},\mathbf{x}_{\mathcal{B}},t)$. By applying the acoustic source-receiver reciprocity relations, (2.A.14) - (2.A.17), but without rotation, we have implicitly also modeled the responses $G^{v,p}(\mathbf{x}_{\mathcal{A}},\mathbf{x},t)$, $\bar{G}^{p,q}(\mathbf{x}_{\mathcal{B}},\mathbf{x},t)$, $G^{v,q}(\mathbf{x}_{\mathcal{A}},\mathbf{x},t)$ and $-\bar{G}^{p,f}(\mathbf{x}_{\mathcal{B}},\mathbf{x},t)$. Thus we have all the responses needed to illustrate the basic SI relation, (2.20).

For testing equation (2.21), not the complete FD-modeled responses are used but the Green's functions without the contributions of sources nearby $\mathbf{x}_{\mathcal{A}}$ and $\mathbf{x}_{\mathcal{B}}$.

The SI relations only contain a correlation of Green's functions. Our synthesized data are Green's functions convolved with a source wavelet, $s(t)$. Including the source wavelets in the basic SI relation in the frequency domain, results in multiplying each term with

$$\hat{s}^{*}(\omega)\hat{s}(\omega) = |\hat{s}(\omega)|^{2}, \tag{2.23}$$

which is the power spectrum of the source wavelet. In the time domain each term is convolved with

$$s(-t) * s(t), \tag{2.24}$$

which is the autocorrelation of the source wavelet. Since the FD-modeled result is a Green's function convolved with the source wavelet, we correlate it further with the source wavelet to give it the same phase information as the reconstructed result. Whenever we speak about the FD-modeled Green's function in this section, we mean the FD-modeled Green's function correlated with the source wavelet.

The first step of evaluating equation (2.22) numerically is a cross-correlation between the v-response measured at $\mathbf{x}_{\mathcal{A}}$, with the p-response without FS multiples measured at $\mathbf{x}_{\mathcal{B}}$. The correlation of responses with $\mathbf{x}_{\mathcal{A}}$ at $0^{\circ}\Delta$ and $\mathbf{x}_{\mathcal{B}}$ at $-90^{\circ}\Delta$ is depicted on the left-hand side of Fig. 2.7. The horizontal axes represent the source positions, ranging from $\Delta = -180^{\circ}$ to $\Delta = 180^{\circ}$ The result on the right-hand side of Fig. 2.7, is a correlation panel. Each trace in the correlation panel corresponds to a correlation of responses due to the same source.

The second step is visualized in Fig. 2.8. It is an integration over all the source positions, which in the numerical case is a stack of all traces in the correlation panel. As explained by Schuster et al. (2004), Wapenaar et al. (2004) and Snieder (2004), events with stationary phases (events that contain a $\partial_x\phi = 0$, where ϕ is the phase of an event and ∂_x denotes the derivative with respect to the source position) in the correlation panel add up during the integration process. All the other amplitudes in the correlation panel cancel by destructive

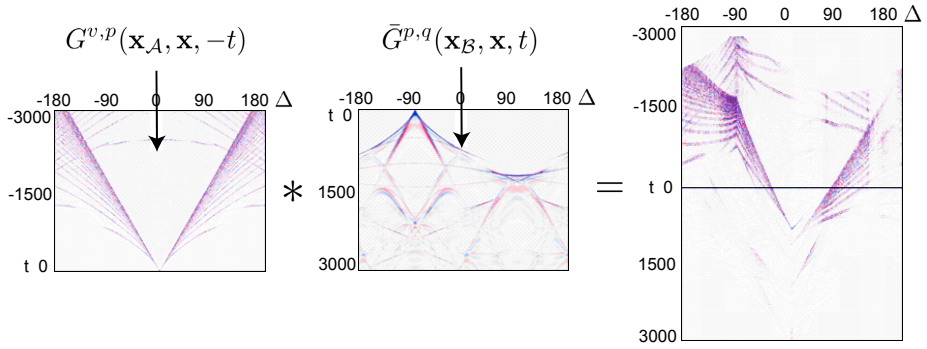


Figure 2.7 *Visualization of the integrand of equation (2.22). The left panel depicts the time-reversed response of state A recorded at $\Delta = 0°$, for sources in the range $-180° < \Delta < 180°$. It is convolved with the response of State B recorded at $-90°$ epicentral distance (middle panel). The right-hand panel shows the resulting correlation panel.*

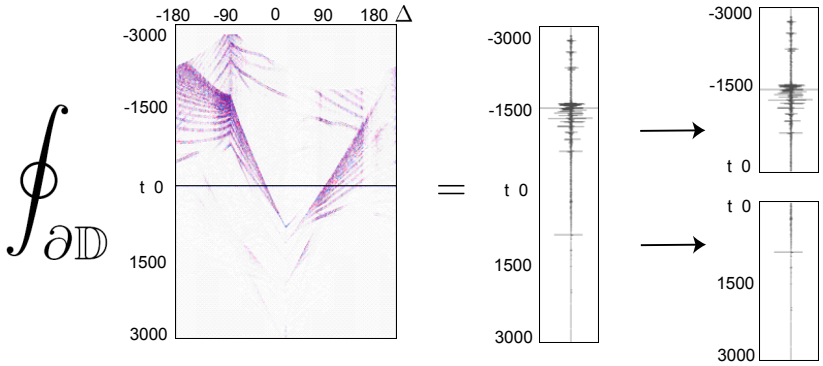


Figure 2.8 *Visualization of the integration process. The traces in the correlation panel (left) are summed to produce the trace in the middle panel. On the right, the causal and anti-causal part are depicted separately.*

interference. The resulting single trace (middle panel in Fig. 2.8) has a causal as well as an anti-causal part. According to equation (2.20) they should be $G^{v,q}(\mathbf{x}_\mathcal{A}, \mathbf{x}_\mathcal{B}, -t)$ and $\bar{G}^{p,f}(\mathbf{x}_\mathcal{B}, \mathbf{x}_\mathcal{A}, t)$, respectively.

Figs. 2.9(a) and 2.9(b) show the reconstructed time-reversed anticausal Green's function without using near-offset responses for time duration of 3000 and 6000 s, respectively, according to equation (2.21). The same amplitude scaling is used for both (a) and (b). Comparing (a) with (b) it can be seen that until 2000 s the same events are reconstructed and with the same amplitude. At later times, though, we can see in (b) events which cannot be seen in (a). To reconstruct a primary we need at least a first order multiple in the input

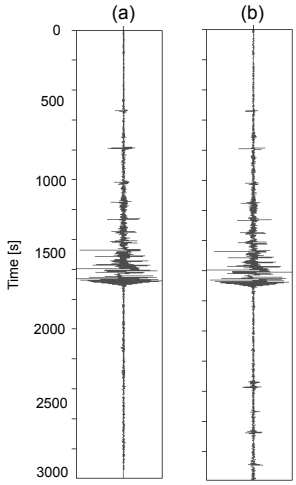


Figure 2.9 *Reconstructed time-reversed anticausal results without using near-offset responses. (a) and (b) are reconstructed traces for $\mathbf{x}_\mathcal{A}$ at $\Delta = 90^\circ$ from $\mathbf{x}_\mathcal{B}$, using an input response duration of respectively 3000 s and 6000 s.*

data (unless there is a delta pulse at time zero in the data). Because the response without FS multiples contains all the significant events before 2000 s (Fig. 2.6(b)), an input duration of 3000+2000 s must be sufficient to reconstruct correctly events occurring before 3000 s.

We have shown that by correlating G with $\bar{G}$ stable amplitudes can be retrieved, independent of the duration of the input responses. In the following, we will use an input duration of 6000 s to reconstruct all events before 3000 s with the correct (relative) amplitude.

Continuing our numerical illustration, the described steps of correlation and integration (Fig. 2.7 and 2.8) are repeated for all $\mathbf{x}_\mathcal{B}$'s around the model. That is, the same response $G^{v,p}(\mathbf{x}_\mathcal{A}, \mathbf{x}, t)$ is correlated with $\bar{G}^{p,q}(\mathbf{x}_\mathcal{B}, \mathbf{x}, t)$ and subsequently integrated, for varying $\mathbf{x}_\mathcal{B}$. Doing so we reconstruct responses measured at all epicentral distances, for a source at $\mathbf{x}_\mathcal{A}$.

Figs. 2.10(a) and (b) are the first 3000 s of the time-reversed anticausal reconstructed results for, respectively, the SI relation (2.20) and the SI relation without near offset (2.21). The reconstructed results are compared with the expected result, $G^{v,q}(\mathbf{x}_\mathcal{A}, \mathbf{x}_\mathcal{B}, t)$ as shown in Fig. 2.10(c). This result was obtained by direct modeling of a response at $\mathbf{x}_\mathcal{A}$ due to sources all around the Earth model.

There is a very good agreement between the different panels. All the FD-modeled events on Fig. 2.10(c) are reconstructed with SI in both (a) and (b). In (a) and (b) we see, additionally, some noise in the upper left corners and between 50 and $150^\circ\Delta$, at around 500 s, an event can be noticed, which is not modeled in (c).

Fig. 2.11(a) and (b) are the first 3000 s of the causal reconstructed results for, respectively,

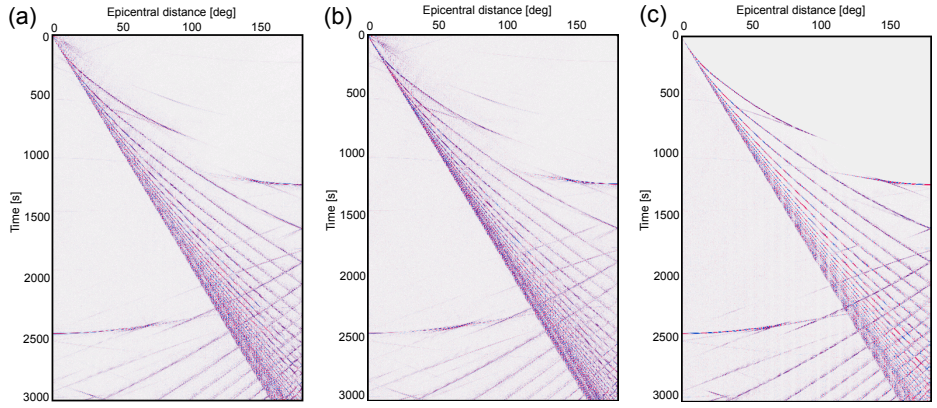


Figure 2.10 *Comparison of (a) the time-reversed anticausal reconstructed result and (b) the reconstruction without using near-offset responses with (c) the FD-modeled response, which is $G^{v,q}(\mathbf{x}_\mathcal{A}, \mathbf{x}, t)$. The horizontal axes show epicentral distance in degrees and the vertical axes shows time in seconds. As the responses are axi-symmetric, only the first 180° are shown. One degree Δ corresponds to 8 traces.*

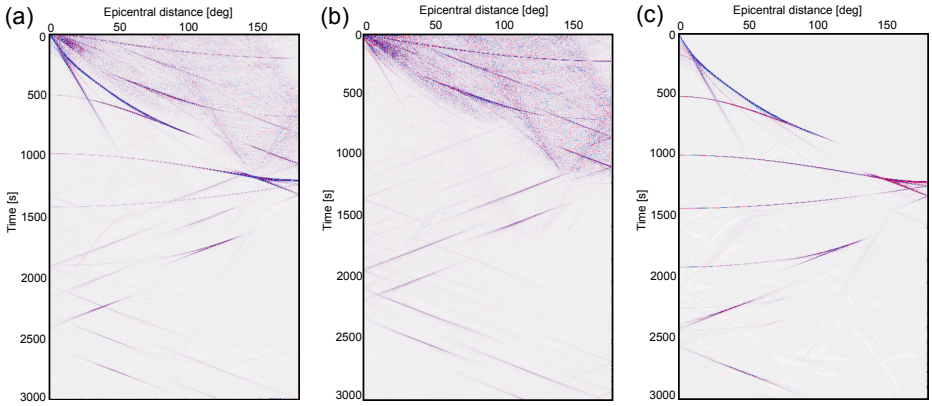


Figure 2.11 *(a) The causal reconstructed result, (b) the reconstructed result without using near-offset responses and (c) the FD-modeled response, which is $\bar{G}^{p,f}(\mathbf{x}, \mathbf{x}_\mathcal{A}, t)$. The horizontal axes show epicentral distance in degrees and the vertical axes shows time in seconds. For the responses are axi-symmetric, only the first 180° are shown. One degree Δ corresponds with 8 traces.*

the SI relation (2.20) and the SI relation without near offset (2.21). Fig. 2.11(c) shows the expected causal outcome for equation (2.20), which is $\bar{G}^{p,f}(\mathbf{x}_\mathcal{B}, \mathbf{x}_\mathcal{A}, t)$. The expected causal outcome for equation (2.21) is zero.

At first sight, there is quite a good agreement between the reconstructed responses - Fig.

2.11(a), and the FD-modeled response (c). Having a closer look at (a) it can be seen that still all events in (c) have been reconstructed. But there are strong artifacts as well. We see - especially at earlier times - noisy signal. And before the first 'real' arrival a few events were reconstructed that can not be seen in (c).

Fig. 2.11(b) contains the same artifacts as can be seen in (a). But for the artifacts, it is an empty response, as expected.

In Appendix 2.B, it is shown that the artifacts in Fig 2.10 and 2.11 are due to correlation noise and due to the reconstruction of internal events. It is shown that in our modeling these are present due to numerical errors. When applying SI to actual data, the artifacts could appear due to undersampling of source positions and an unequal illumination of the medium of interest from different angles, respectively.

We draw the conclusion that by applying equation (2.20), indeed we have reconstructed $G^{v,q}(\mathbf{x}_\mathcal{A}, \mathbf{x}_\mathcal{B}, t)$ and $\bar{G}^{p,f}(\mathbf{x}_\mathcal{B}, \mathbf{x}_\mathcal{A}, t)$. Also without using the near-offset contribution we were able to make a kinematically good estimation of $G^{v,q}(\mathbf{x}_\mathcal{A}, \mathbf{x}_\mathcal{B}, t)$, but not of $\bar{G}^{p,f}(\mathbf{x}_\mathcal{B}, \mathbf{x}_\mathcal{A}, t)$, as was expected by equation (2.21). The artifacts can be explained by numerical errors.

We evaluated the relations on a lossless Earth, since in our derivations no losses were assumed. Roux et al. (2005b) and Slob et al. (2006) showed that when SI is applied for media with moderate losses, still correct traveltimes but approximate amplitudes are retrieved. Internal events (Appendix 2.B.3) are amplified as soon as losses are introduced.

2.5 Towards application

Thus far, we considered ideal or semi-ideal situations with the availability of sources all around the globe or missing only near-offset sources. In reality, we will not have a dense (earthquake) source distribution in some mid- and far-offsets either. In this section, we show with a stationary phase analysis that also under suboptimal conditions we can still retrieve useful information from the application of the global-scale SI relations.

2.5.1 Stationary phase localization

The working principle of SI can be described as follows. First, observed responses measured at different epicentral distances, and due to the same sources, are correlated. Therewith, higher-order events become lower-order events. At times belonging to the kinematics of the Green's function that would be observed between the two locations between which the responses are measured, stationary phase events appear in the correlation panel. Then by stacking over the correlation panel, the signals at the stationary phases are selected and thus the desired Green's function is reconstructed. With a stationary phase event we mean a (part of an) event which contains a stationary phase. In this section, we analyze where these stationary phase events are located in the anticausal correlation panels.

In Fig. 2.12(a) we show the same anticausal part of the correlation panel as in Fig. 2.7, which was the result after correlating a response measured at $0°\Delta$ with the multiple-free response measured at $-90°\Delta$, both due to the same sources at all epicentral distances. To build up the correlation panel, 5760 sources around the model were used to satisfy the Nyquist spatial sampling criterion (Appendix 2.B.2). In Fig. 2.12(a) the different regions of this correlation panel are indicated with colors. The near-offset region, the region with correlations of responses due to sources which are close to the location $\mathbf{x}_\mathcal{B}$ where we want to retrieve a source, is indicated with green. The mid- (red) and far-offset (yellow) regions are the correlations of responses due to sources which are at an intermediate to far epicentral distance with respect to the location $\mathbf{x}_\mathcal{B}$ where we want to retrieve a source.

The locations of the stationary phase events can be recognized in the correlation panel (Fig. 2.12(a)) by noticing pieces of events where $\partial_x \phi = 0$. We subsequently stack over the different offset regions to identify the locations of stationary phase events which we might not directly identify visually on the correlation panel. The resulting traces are in Fig. 2.12(b)-(e). With the blue stars on the Earth models above the traces it is indicated from what epicentral distances the responses were used during the stacking.

When we stack over the complete correlation panel we get trace 2.12(b). When we only stack over the near-offset region, we get trace 2.12(c). It looks similar to (b). The near offset (in fact the zero offset) contains all the reconstructed events. When we stack over the mid-offset region we catch stationary phase events. The stacking result is trace (d). The far-offset region in the correlation panel contains stationary phase events for constructing events at later times and additional events, as can be seen in the resulting trace (e).

These observations match with the theory as expressed in equation (2.20) and (2.21). Practically, this means that to reconstruct certain events (kinematically correct), we only need to have the part of the (anticausal) correlation panel where the stationary phase arrivals occur. Thus to reconstruct a certain event, we only need responses from sources from a certain range of epicentral distances. In the next section, we clarify the possibilities of applying an SI relation (2.21) on global-scale seismological data with an example.

2.5.2 PcP retrieval

Assume we want to retrieve information about the CMB at the question mark location in Fig. 2.13. We have seismic stations at locations $\mathbf{x}_\mathcal{A}$ and $\mathbf{x}_\mathcal{B}$, at $\Delta = 0°$ and $45°$ on either side of the CMB part of interest. But since the Earth is not seismically active near $\mathbf{x}_\mathcal{A}$ and $\mathbf{x}_\mathcal{B}$, we cannot directly measure PcP between $\mathbf{x}_\mathcal{A}$ and $\mathbf{x}_\mathcal{B}$. There are 4 obvious possibilities in which we can still retrieve PcP using SI (sources in region 1,2,3 or 4 in Fig. 2.13). Assume the Earth is seismically active at around $\Delta = -45°$ (region 4) or at around $90°$ (region 1), then we can correlate $PcPPcP$ with PcP or vice versa to retrieve PcP. If the Earth is seismically active at around $-150°$ (region 3) or at around $-165°$ (region 2), then we can correlate PKP with $PKPPcP$ or vice versa to retrieve PcP. The epicentral distance values are not exact and only valid for our simplified Earth model (Fig. 2.4(b)). In

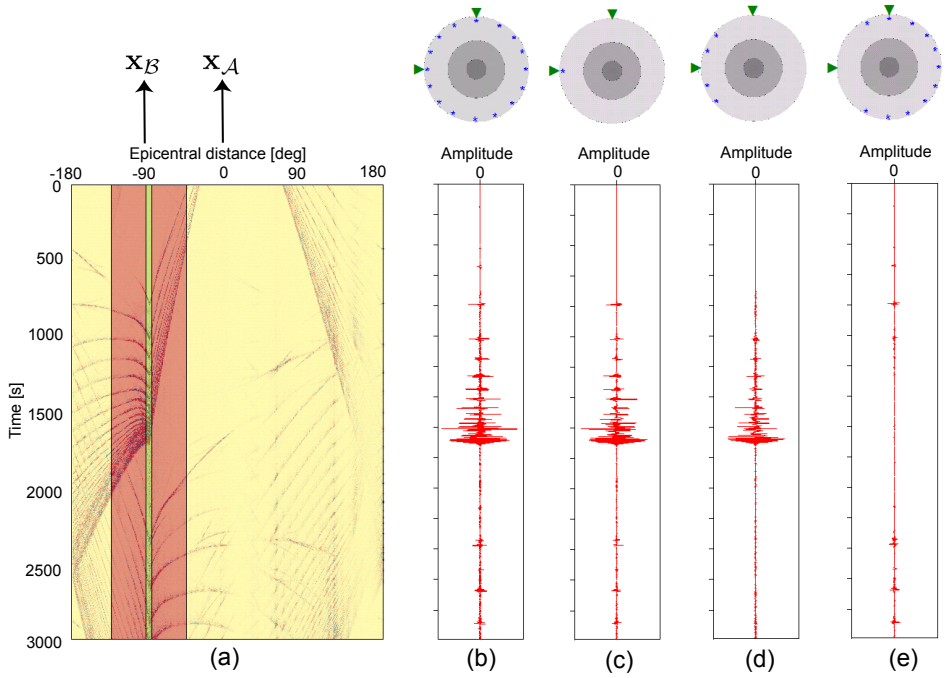


Figure 2.12 *The time-reversed anticausal correlation panel (a) after correlating a response measured at $\mathbf{x}_{\mathcal{A}}$ (at $\Delta = 0°$) with the response without FS multiples measured at $\mathbf{x}_{\mathcal{B}}$ ($\Delta = -90°$). The green, red and yellow colors on the correlation panel denote, respectively, the near-offset, the mid-offset and the far-offset region (with respect to the location $\mathbf{x}_{\mathcal{B}}$ where we want to retrieve a source). Stacking over the complete correlation panel, the near-offset, the mid-offset and the far-offset region, gives the traces (b), (c), (d) and (e), respectively. The traces are plotted with the same amplitude scale. The blue stars in the models above the traces indicate source regions from which the responses are observed and used for the reconstruction of the different traces. The green triangles indicate the positions where the responses are measured and between which a response is reconstructed.*

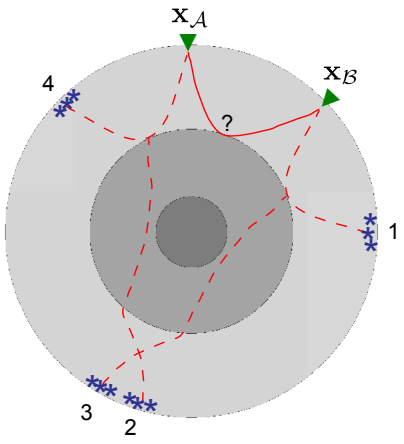


Figure 2.13 *Possible contributions for retrieving PcP between $\mathbf{x}_\mathcal{A}$ at $\Delta = 0°$ and $\mathbf{x}_\mathcal{B}$ at $45°$. 1,2,3 and 4 denote seismically active regions at around $\Delta = 90$, $-165°$, $-150°$ and $-45°$ from $\mathbf{x}_\mathcal{A}$, respectively.*

our modeling, $PKPPcP$ is a clearer arrival than $PcPPcP$ (Fig. 2.6). Thus here we use sources at around $-150°$ (region 3 in Fig. 2.13) to retrieve PcP.

Fig. 2.14(a) is a small portion of the correlation panel for $\mathbf{x}_\mathcal{A}$ and $\mathbf{x}_\mathcal{B}$ at $0°$ and $45°$ and sources between $-165°$ and $-135°$. The horizontal axis depicts the locations of the sources. The stationary phase for PcP due to a correlation of $PKPPcP$ (state A) with PKP (state B) can be distinguished between $-160°$ and $-140°$, around 610 s. Fig. 2.14(b) is just the contribution from the source right at the stationary phase ($\Delta = -148°$). Since with our modeling we know the exact location of the stationary phase, the contribution from just one source already suffices to retrieve PcP, though we would need to time-window the trace around the estimated PcP arrival time between $\mathbf{x}_\mathcal{A}$ and $\mathbf{x}_\mathcal{B}$, since at other times we have correlation noise. In reality, because of unknown deviations from a 1D reference model, we would need to stack over contributions from sources at an estimated range in which the stationary phase could be located. Fig. 2.14(c) is a stack of all the source contributions between $-160°$ and $-140°$, as were plotted in (a). Because of an ideal sampling (1 source per 7 km), just PcP is now retrieved and (almost) all correlation noise disappears. Fig. 2.14(d) is the directly FD-modeled response between $\mathbf{x}_\mathcal{A}$ and $\mathbf{x}_\mathcal{B}$. Comparing (c) with (d) we see that the kinematic retrieval of PcP is exact, but there are (numerical) errors in the phase characteristics.

In reality, we might not have available the responses due to a dense source distributions at around one of the four regions in Fig. 2.13. We can still retrieve reflection information of the question mark location on the CMB in Fig. 2.13, though, if we have an array of receivers at location $\mathbf{x}_\mathcal{A}$ and or $\mathbf{x}_\mathcal{B}$ and combine SI with migration. With an integration over receiver positions, as imbedded in the migration, the stationary phase contribution can be captured, that would otherwise just be missed by having only the response from one source in one of

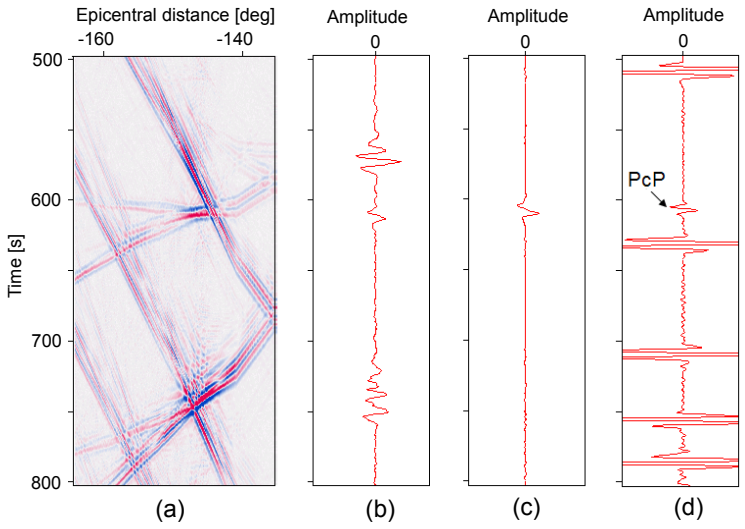


Figure 2.14 *PcP retrieval between $\mathbf{x}_{\mathcal{A}}$ and $\mathbf{x}_{\mathcal{B}}$ at $\Delta = 45°$. (a) portion of time-reversed anticausal correlation panel including the stationary phase for retrieval of PcP. (b) trace at $\Delta = -148°$ from the correlation panel. (c) summation of (a) over source positions. (d) FD-modeled response between $\mathbf{x}_{\mathcal{A}}$ and $\mathbf{x}_{\mathcal{B}}$.*

the 4 regions (Schuster et al., 2004; Wapenaar et al., 2004; Artman et al., 2004; Draganov et al., 2004a).

The source sampling around the globe is very good along specific lines, the lithospheric plate boundaries (Fig. 2.1), but not over large areas. Therefore it is most practical to use receivers that are inline with major earthquake belts and to apply SI in an approximate 2D sense, like in the above example. For a retrieved elastodynamic response, subsequently, another interferometric step can be used to isolate the surface waves (Halliday et al., 2007).

As input for our SI algorithms we need one response with and one without FS multiples. It is not easy to find a response with all the FS multiples removed, whereas all the other events are undistorted. E.g., a data driven method like surface related multiple removal (SRME) could be used. With the current sampling of sources and receivers on a global scale though, it is not yet feasible. As was shown in this section, SI can still be applied. In the above example the response without FS multiples is easily found by time windowing the response measured at $\mathbf{x}_{\mathcal{B}}$ around the time that PKP is expected. A similar approach is taken in Bakulin et al. (2007). Another possibility would be to use wavefield separation to approximate a response without FS multiples (Mehta et al., 2007). Or we could use the response including FS multiples, but due to sources at varying depths. With this approach Draganov et al. (2006) removed ghost events due to reflectors below the sources.

In Appendix A we propose an alternative method to retrieve PcP between two arrays by

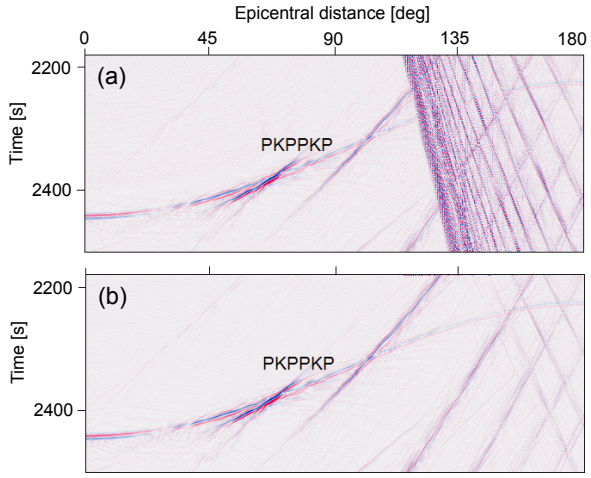


Figure 2.15 *Comparison of time-reversed anticausal reconstructions. For the upper panel, responses from sources all around the model (but the near offset) were used. For the lower panel, the responses from sources between* $\Delta = -24^\circ$ *and* 24° *were left out.*

integration over midpoint instead of source positions.

2.5.3 Removing undesired events

Because we know already roughly the velocity and density model of the Earth, we can model in what region of the correlation panels stationary phase events are expected. We can use this knowledge to select these events and to leave out stationary phase events leading to the reconstruction of undesired events. In this subsection, we illustrate this by trying not to reconstruct the very high-order FS multiples.

From an analysis as in Fig. 2.12 we know that the stationary phase events of the high-order FS multiples occur in the near-offset and a part of the mid-offset region of the correlation panels. Fig. 2.15(a) is a portion of Fig. 2.10, the time-reversed anticausal reconstruction result. Beyond $\Delta = 100^\circ$ a dense set of FS multiples obscures the $PKPPKP$ event. We repeat the same application of SI that was used to retrieve the response in Fig. 2.15(a), but now with leaving out the responses from sources between $\Delta = -24^\circ$ and 24°). Fig. 2.15(b) is a portion of the result. It indeed does not contain a large part of the higher-order FS multiples, whereas event $PKPPKP$ is preserved. Where $PKPPKP$ was masked by FS multiples in Fig. 2.15(a) it can clearly be seen in Fig. 2.15(b). We can achieve this result because stationary phase events leading to events that overlap in the reconstructed result do generally not overlap in the correlation panel. Hence the correlation panel can effectively be used as a domain to filter out (un)desired events.

2.6 Conclusions

We derived elastodynamic SI relations for transient sources near the closed surface of the Earth. This configuration intrinsically differs from configurations SI has been applied to thus far. The derived relations consist of a correlation integral, in which a response with FS multiples at one receiver is correlated with a response without FS multiples at another receiver. A response without FS multiples is necessary to prevent the occurrence of ghost events and to allow stable amplitude reconstructions in a closed system. Subsequently, the correlation result is integrated over the source locations, thus reconstructing a response between the two receiver locations.

The rotation of the Earth breaks source-receiver reciprocity, but SI relations are still valid. No extra term needs to be evaluated to take the Coriolis force into account.

Using synthesized global-scale earthquake responses we illustrated the acoustic versions of the derived SI relation for a non-rotating Earth. We also tested a slightly different SI relation for the situation when no near-offset responses are available. Both relations gave the expected reconstructed results. When responses due to sources all around the Earth are available both the full Green's function and the Green's function without FS multiples is reconstructed. When no responses are available from sources nearby the receiver position where we want to reconstruct a source only the Green's function including the FS multiples can be reconstructed.

The reconstructions were not without artifacts, viz. noise and additional events. We showed that these artifacts could be explained to be due to numerical errors.

For applications to global seismology, only the SI relation without near offset will be of use. Given the distribution of earthquakes around the globe, it will not be possible to reconstruct the complete response between any two receiver positions, since an overall dense source sampling is required. We showed that with a dense source sampling at a specific range of epicentral distances, we can still retrieve specific events between receiver positions. If the location of a stationary phase is known or if an array of receivers is used, one good quality earthquake response could already suffice to retrieve an event between receiver positions.

For the application of SI to actual earthquake data, preprocessing would be necessary. Responses due to different sources would need to be deconvolved for the different source wavelets, normalized for the differences in magnitude and filtered for the differences in source directivity. FS multiples would need to be separated. Also, because in the derivation of SI lossless media are assumed, factors need to be included that account for anelastic losses.

Since the rough velocity and density model of the Earth is already known, we can find out by modeling where in the correlation panel the stationary phases of specific events occur. Subsequently we can determine whether we properly sample certain stationary phase events with a (given) source-receiver configuration. Hence we have a tool to estimate what kind of events in the Green's function between two points on the surface can be reconstructed,

given responses from a certain range of epicentral distances with sources. We demonstrated that this knowledge of stationary phases locations in the correlation panel can also be used to filter out undesired events.

2.A Derivation of generalized source-receiver reciprocity relations

In this appendix the generalized source-receiver reciprocity relations for Green's functions are derived. Roux & Fink (1997) studied the violation of acoustic time-reversal for a rotating medium experimentally. In Dahlen & Tromp (1998) the general relation between a Green's function in the actual Earth and a Green's function in an Earth with a reversed sense of rotation (the anti-Earth) is given. Here we do the derivations to find the relevant relations for the source and receiver characteristics that are used in this chapter.

We start with the Rayleigh-Betti reciprocity theorem of the convolution type:

$$\oint_{\partial\mathbb{D}} \{\hat{v}_{i,A}\hat{\tau}_{ik,B} - \hat{\tau}_{ik,A}\hat{v}_{i,B}\}n_k d^2\mathbf{x} = \int_{\mathbb{D}} \{-\hat{\tau}_{ij,A}\hat{h}_{ij,B} - \hat{v}_{i,A}\hat{f}_{i,B} + \hat{h}_{ij,A}\hat{\tau}_{ij,B} + \hat{f}_{i,A}\hat{v}_{i,B}\}d^3\mathbf{x} - \int_{\mathbb{D}} \{2\rho\epsilon_{ijk}\hat{v}_{i,B}\Omega_{j,B}\hat{v}_{k,A} - 2\rho\epsilon_{ijk}\hat{v}_{i,A}\Omega_{j,A}\hat{v}_{k,B}\}d^3\mathbf{x}, \quad (2.A.1)$$

which is found by repeating the derivation for the Rayleigh-Betti reciprocity theorem of the correlation type (Section 2.2.1, equation (2.6)), but by using the interaction function $\{\hat{v}_{i,A}\hat{\tau}_{ij,B} - \hat{\tau}_{ij,A}\hat{v}_{i,B}\}$ instead of $\{-\hat{v}^*_{i,A}\hat{\tau}_{ij,B} - \hat{\tau}^*_{ij,A}\hat{v}_{i,B}\}$, and assuming equal medium parameters in both states.

Using the property $\epsilon_{ijk} = -\epsilon_{kji}$ we may rewrite the integral with the Coriolis terms, the second integral on the right-hand side of equation (2.A.1), as

$$-\int_{\mathbb{D}} \{2\rho\epsilon_{ijk}\hat{v}_{i,B}\Omega_{j,B}\hat{v}_{k,A} + 2\rho\epsilon_{ijk}\hat{v}_{i,B}\Omega_{j,A}\hat{v}_{k,A}\}d^3\mathbf{x}. \quad (2.A.2)$$

This integrand will vanish for $\Omega_{j,A} = -\Omega_{j,B}$, i.e., when the medium in state A is rotating opposite to the medium in state B. We choose $\Omega_{j,A} = \Omega_j$, which is a constant angular velocity, and $\Omega_{j,B} = -\Omega_j$. Thus the Rayleigh-Betti reciprocity theorem of the convolution type reduces to

$$\oint_{\partial\mathbb{D}} \{\hat{v}_{i,A}\hat{\tau}_{ik,B} - \hat{\tau}_{ik,A}\hat{v}_{i,B}\}n_k d^2\mathbf{x} = \int_{\mathbb{D}} \{-\hat{\tau}_{ij,A}\hat{h}_{ij,B} - \hat{v}_{i,A}\hat{f}_{i,B} + \hat{h}_{ij,A}\hat{\tau}_{ij,B} + \hat{f}_{i,A}\hat{v}_{i,B}\}d^3\mathbf{x}. \quad (2.A.3)$$

A domain $\mathbb{D}$ enclosed by a surface $\partial\mathbb{D}$ covers the entire inner space of the Earth, hence $\partial\mathbb{D}$ coincides with the FS (Fig. 2.A.1(a)). Only when sources are represented as boundary conditions at the FS, the traction vector $\hat{\tau}_{ik}n_k$ at $\partial\mathbb{D}$ will not be equal to zero. By making different choices for the sources in state A and B we end up with the desired relations for interchanging source and receiver positions.

One choice is to represent the source in state A as a boundary condition for the traction at the FS. In state B a deformation-rate source is chosen within the domain $\mathbb{D}$. The resulting expressions for the source and wavefield state at $\mathbb{D}$ and $\partial\mathbb{D}$ are given in Table 2.A.1.

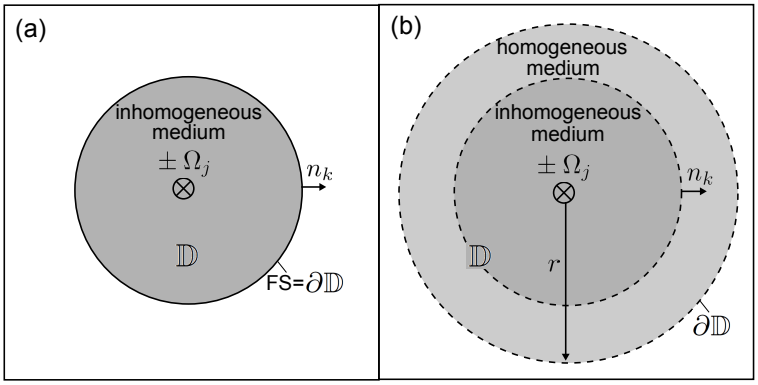


Figure 2.A.1 *Two configurations for the application of the elastodynamic reciprocity theorem, (a) one with a closed FS, and (b) one unbounded configuration.*

		State A: free surface	State B: free surface
$wavefield$ $\mathbf{x} \in \mathbb{D}$	$\hat{\tau}_{ij}$	$\hat{G}^{\tau,\tau}_{ij,p}(\mathbf{x}, \mathbf{x}_\mathcal{A}, \omega \mid \mathbf{\Omega})$	$\hat{G}^{\tau,h}_{ij,qr}(\mathbf{x}, \mathbf{x}_\mathcal{B}, \omega \mid -\mathbf{\Omega})$
	$\hat{v}_i$	$\hat{G}^{v,\tau}_{i,p}(\mathbf{x}, \mathbf{x}_\mathcal{A}, \omega \mid \mathbf{\Omega})$	$\hat{G}^{v,h}_{i,qr}(\mathbf{x}, \mathbf{x}_\mathcal{B}, \omega \mid -\mathbf{\Omega})$
$wavefield$ $\mathbf{x} \in \partial\mathbb{D}$	$\hat{\tau}_{ik}n_k$	$\delta(\mathbf{x} - \mathbf{x}_\mathcal{A})\delta_{ip}$	0
	$\hat{v}_i$	$\hat{G}^{v,\tau}_{i,p}(\mathbf{x}, \mathbf{x}_\mathcal{A}, \omega \mid \mathbf{\Omega})$	$\hat{G}^{v,h}_{i,qr}(\mathbf{x}, \mathbf{x}_\mathcal{B}, \omega \mid -\mathbf{\Omega})$
$source$ $\mathbf{x} \in \mathbb{D}$	$\hat{h}_{ij}$	0	$\delta(\mathbf{x} - \mathbf{x}_\mathcal{B})\delta_{iq}\delta_{jr}$
	$\hat{f}_i$	0	0

Table 2.A.1 *States for the elastodynamic reciprocity theorem with a traction source in state A and a deformation-rate source in state B.*

Substituting the states of Table 2.A.1 into equation (2.A.3), making use of the sifting property of the delta function and the multiplication property of the Kronecker delta function, yields

$$\hat{G}^{\tau,\tau}_{qr,p}(\mathbf{x}_\mathcal{B}, \mathbf{x}_\mathcal{A}, \omega \mid \mathbf{\Omega}) = \hat{G}^{v,h}_{p,qr}(\mathbf{x}_\mathcal{A}, \mathbf{x}_\mathcal{B}, \omega \mid -\mathbf{\Omega}), \tag{2.A.4}$$

in which $\mathbf{\Omega}$ denotes a solid rotation of the medium in $\mathbb{D}$.

Another choice is to represent both the source in state A and the source in state B as boundary condition for the traction at the FS. As there are no sources within $\mathbb{D}$ the first integral on the right-hand side of equation (2.A.3) will vanish. Thus the only term left over from equation (2.A.3) is the surface integral over the wavefield interactions

$$\oint_{\partial\mathbb{D}} \{\hat{v}_{i,A}\hat{\tau}_{ik,B} - \hat{\tau}_{ik,A}\hat{v}_{i,B}\}n_k d^2\mathbf{x} = 0. \tag{2.A.5}$$

The resulting expressions for the wavefield state at $\partial\mathbb{D}$ are given in Table 2.A.2. Substituting the states of Table 2.A.2 into equation (2.A.5), making use of the properties of the delta

		State A: free surface	State B: free surface
$wavefield$ $\mathbf{x}\partial\mathbb{D}$	$\hat{\tau}_{ik}n_k$	$\delta(\mathbf{x}-\mathbf{x}_{\mathcal{A}})\delta_{ip}$	$\delta(\mathbf{x}-\mathbf{x}_{\mathcal{B}})\delta_{iq}$
	$\hat{v}_i$	$\hat{G}^{v,\tau}_{i,p}(\mathbf{x},\mathbf{x}_{\mathcal{A}},\omega \mid \mathbf{\Omega})$	$\hat{G}^{v,\tau}_{i,q}(\mathbf{x},\mathbf{x}_{\mathcal{B}},\omega \mid -\mathbf{\Omega})$

Table 2.A.2 *States for the elastodynamic reciprocity theorem with traction sources in both states.*

		State A: no free surface	State B: no free surface
$wavefield$ $\mathbf{x}\in\mathbb{D}$	$\hat{\tau}_{ij}$	$\hat{\hat{G}}^{\tau,h}_{ij,pr}(\mathbf{x},\mathbf{x}_{\mathcal{A}},\omega \mid \mathbf{\Omega})$	$\hat{\hat{G}}^{\tau,f}_{ij,q}(\mathbf{x},\mathbf{x}_{\mathcal{B}},\omega \mid -\mathbf{\Omega})$
	$\hat{v}_i$	$\hat{\hat{G}}^{v,h}_{i,pr}(\mathbf{x},\mathbf{x}_{\mathcal{A}},\omega \mid \mathbf{\Omega})$	$\hat{\hat{G}}^{v,f}_{i,q}(\mathbf{x},\mathbf{x}_{\mathcal{B}},\omega \mid -\mathbf{\Omega})$
$source$ $\mathbf{x}\in\mathbb{D}$	$\hat{h}_{ij}$	$\delta(\mathbf{x}-\mathbf{x}_{\mathcal{A}})\delta_{ip}\delta_{jr}$	0
	$\hat{f}_i$	0	$\delta(\mathbf{x}-\mathbf{x}_{\mathcal{B}})\delta_{iq}$

Table 2.A.3 *States for the elastodynamic reciprocity theorem with a deformation-rate source in state A and a force source in state B.*

functions and bringing one of the resulting terms to the other side of the equal sign, we obtain

$$\hat{G}^{v,\tau}_{q,p}(\mathbf{x}_{\mathcal{B}},\mathbf{x}_{\mathcal{A}},\omega \mid \mathbf{\Omega}) = \hat{G}^{v,\tau}_{p,q}(\mathbf{x}_{\mathcal{A}},\mathbf{x}_{\mathcal{B}},\omega \mid -\mathbf{\Omega}). \tag{2.A.6}$$

Next, an Earth without FS is assumed. As in Fokkema & van den Berg (1993) domain $\mathbb{D}$ is chosen to be unbounded. It consists of two parts, as depicted in Fig. 2.A.1(b). The inner part is an inhomogeneous medium and contains the sources. The outer part consists of a source-free homogeneous medium and surrounds the first part.

The surface integral in equation (2.A.3) vanishes on account of the radiation conditions (Pao & Varatharajulu, 1976). Thus, the only term left over from equation (2.A.3) is the volume integral over the source-wavefield interactions

$$\int_{\mathbb{D}} \{-\hat{\tau}_{ij,A}\hat{h}_{ij,B} - \hat{v}_{i,A}\hat{f}_{i,B} + \hat{h}_{ij,A}\hat{\tau}_{ij,B} + \hat{f}_{i,A}\hat{v}_{i,B}\} d^3\mathbf{x} = 0. \tag{2.A.7}$$

By making various choices for the sources in state A and B we end up with the desired relations for interchanging source and receiver positions.

One choice is to represent the source in state A as a deformation-rate source, initiating a wavefield at $\mathbf{x}_{\mathcal{A}}$. For state B a force source is chosen, initiating a wave at $\mathbf{x}_{\mathcal{B}}$. The resulting expressions for the source state and wavefield state are given in Table 2.A.3.

Substituting the states of Table 2.A.3 into equation (2.A.7) and making use of the properties of the delta functions, yields

$$\hat{\hat{G}}^{v,h}_{q,pr}(\mathbf{x}_{\mathcal{B}},\mathbf{x}_{\mathcal{A}},\omega \mid \mathbf{\Omega}) = \hat{\hat{G}}^{\tau,f}_{pr,q}(\mathbf{x}_{\mathcal{A}},\mathbf{x}_{\mathcal{B}},\omega \mid -\mathbf{\Omega}). \tag{2.A.8}$$

		State A: no free surface	State B: no free surface
$wavefield$ $\mathbf{x} \in \mathbb{D}$	$\hat{\tau}_{ij}$ $\hat{v}_i$	$\hat{\bar{G}}^{\tau,h}_{ij,pr}(\mathbf{x}, \mathbf{x}_{\mathcal{A}}, \omega \mid \mathbf{\Omega})$ $\hat{\bar{G}}^{v,h}_{i,pr}(\mathbf{x}, \mathbf{x}_{\mathcal{A}}, \omega \mid \mathbf{\Omega})$	$\hat{\bar{G}}^{\tau,h}_{ij,qs}(\mathbf{x}, \mathbf{x}_{\mathcal{B}}, \omega \mid -\mathbf{\Omega})$ $\hat{\bar{G}}^{v,h}_{i,qs}(\mathbf{x}, \mathbf{x}_{\mathcal{B}}, \omega \mid -\mathbf{\Omega})$
$source$ $\mathbf{x} \in \mathbb{D}$	$\hat{h}_{ij}$ $\hat{f}_i$	$\delta(\mathbf{x} - \mathbf{x}_{\mathcal{A}})\delta_{ip}\delta_{jr}$ 0	$\delta(\mathbf{x} - \mathbf{x}_{\mathcal{B}})\delta_{iq}\delta_{js}$ 0

Table 2.A.4 *States for the elastodynamic reciprocity theorem with deformation-rate sources in both states.*

Another choice is to represent both the sources in state A and in state B as deformation-rate sources, initiating wavefields at $\mathbf{x}_{\mathcal{A}}$ and $\mathbf{x}_{\mathcal{B}}$, respectively. The resulting expressions for the source state and wavefield state are given in Table 2.A.4.

Substituting the states of Table 2.A.4 into equation (2.A.7), making use of the properties of the delta functions and omitting the subscript $_r$, yields

$$\hat{\bar{G}}^{\tau,h}_{qs,p}(\mathbf{x}_{\mathcal{B}}, \mathbf{x}_{\mathcal{A}}, \omega \mid \mathbf{\Omega}) = \hat{\bar{G}}^{\tau,h}_{p,qs}(\mathbf{x}_{\mathcal{A}}, \mathbf{x}_{\mathcal{B}}, \omega \mid -\mathbf{\Omega}). \tag{2.A.9}$$

In the time domain, equations (2.A.4), (2.A.6), (2.A.8) and (2.A.9), the generalized source-receiver reciprocity relations, read

$$G^{\tau,\tau}_{qr,p}(\mathbf{x}_B y, \mathbf{x}_{\mathcal{A}}, t \mid \mathbf{\Omega}) = G^{v,h}_{p,qr}(\mathbf{x}_{\mathcal{A}}, \mathbf{x}_{\mathcal{B}}, t \mid -\mathbf{\Omega}), \tag{2.A.10}$$

$$G^{v,\tau}_{q,p}(\mathbf{x}_{\mathcal{B}}, \mathbf{x}_{\mathcal{A}}, t \mid \mathbf{\Omega}) = G^{v,\tau}_{p,q}(\mathbf{x}_{\mathcal{A}}, \mathbf{x}_{\mathcal{B}}, t \mid -\mathbf{\Omega}), \tag{2.A.11}$$

$$\bar{G}^{v,h}_{q,pr}(\mathbf{x}_{\mathcal{B}}, \mathbf{x}_{\mathcal{A}}, t \mid \mathbf{\Omega}) = \bar{G}^{\tau,f}_{pr,q}(\mathbf{x}_{\mathcal{A}}, \mathbf{x}_{\mathcal{B}}, t \mid -\mathbf{\Omega}) \quad \text{and} \tag{2.A.12}$$

$$\bar{G}^{\tau,h}_{qs,p}(\mathbf{x}_{\mathcal{B}}, \mathbf{x}_{\mathcal{A}}, t \mid \mathbf{\Omega}) = \bar{G}^{\tau,h}_{p,qs}(\mathbf{x}_{\mathcal{A}}, \mathbf{x}_{\mathcal{B}}, t \mid -\mathbf{\Omega}). \tag{2.A.13}$$

We can directly find the generalized acoustic source-receiver reciprocity relations by replacing the superscripts h by q, τ by $-p$ and leaving out all the subscripts. Doing so, the acoustic versions of equations (2.A.10) - (2.A.13) become

$$G^{p,p}(\mathbf{x}_{\mathcal{B}}, \mathbf{x}_{\mathcal{A}}, t \mid \mathbf{\Omega}) = G^{v,q}(\mathbf{x}_{\mathcal{A}}, \mathbf{x}_{\mathcal{B}}, t \mid -\mathbf{\Omega}), \tag{2.A.14}$$

$$G^{v,p}(\mathbf{x}_{\mathcal{B}}, \mathbf{x}_{\mathcal{A}}, t \mid \mathbf{\Omega}) = G^{v,p}(\mathbf{x}_{\mathcal{A}}, \mathbf{x}_{\mathcal{B}}, t \mid -\mathbf{\Omega}), \tag{2.A.15}$$

$$\bar{G}^{v,q}(\mathbf{x}_{\mathcal{B}}, \mathbf{x}_{\mathcal{A}}, t \mid \mathbf{\Omega}) = -\bar{G}^{p,f}(\mathbf{x}_{\mathcal{A}}, \mathbf{x}_{\mathcal{B}}, t \mid -\mathbf{\Omega}) \quad \text{and} \tag{2.A.16}$$

$$\bar{G}^{p,q}(\mathbf{x}_{\mathcal{B}}, \mathbf{x}_{\mathcal{A}}, t \mid \mathbf{\Omega}) = \bar{G}^{p,q}(\mathbf{x}_{\mathcal{A}}, \mathbf{x}_{\mathcal{B}}, t \mid -\mathbf{\Omega}). \tag{2.A.17}$$

In a non-rotating medium source-receiver reciprocity holds. The source-receiver reciprocity relations are derived similarly to the derivation of the generalized source-receiver reciprocity relations (2.A.4), (2.A.6), (2.A.8) and (2.A.9), but with leaving out the argument indicating the sense of rotation. Thus the elastodynamic and acoustic source-receiver reciprocity relations are equations (2.A.10) - (2.A.13) and (2.A.14) - (2.A.17), respectively, without the argument indicating the sense of rotation.

2.B Artifacts

2.B.1 Imperfections

One large imperfection in our FD-modeled response of state B are the model boundary artifacts. These low-frequency events can be seen in Fig. 2.10.

With the FD modeling (Section 2.3), both the sources and the receivers were put at approximately 4 km depth. The resulting response of the model with FS is not optimal. The measured amplitude varies from receiver(set) to receiver(set). There turned out to be a large variation (2-10km) in the source/receiver distance to the FS, explaining the differences in amplitude in the measured responses.

The SI algorithm itself is insensitive to mis-positioning of the sources. Normally the mis-positioning gives, e.g., a small delay for the events arriving at $\mathbf{x}_A$ and a small delay for the events arriving at $\mathbf{x}_B$. After correlation this time-delay is removed. Because of two (numerical) reasons, the mis-positioning of the sources does lead to errors in our numerical implementation, though.

The first reason is that because sources are placed so close to the FS, a mis-positioning has an effect on the effective phase characteristic of the source wavelet. The phase characteristic of the source wavelet arriving at $\mathbf{x}_B$ does not change, though, as it is modeled independently in a model without FS.

The second reason is that we used one receiver gather to make receiver gathers at all other epicentral distances. This has as an effect that we correlate traces with each other which are not due to the same source, but are from sources with a different source (mis-)positioning.

2.B.2 Noise

According to the theory, by stacking over a correlation panel all amplitudes should interfere destructively, except for the physical events. We found that there was still some noise left, most obvious in Fig. 2.10(a) and (b).

To study the influence of the spatial sampling, we repeat the experiment as visualized in Figs. 2.7 and 2.8 for 5 different source samplings. Fig. 2.B.1 shows the reconstructed responses using the SI relation without near offset when using (a) 360, (b) 720, (c) 1440, (d) 2880 and (e) 5760 sources around the model. This corresponds to one source every (a) 111, (b) 56, (c) 28, (d) 14 and (e) 7 km, respectively.

When using 360 sources (a), the 'real' events can hardly be seen through the noise. Using more and more sources, thus increasing the spatial sampling, more and more noise can be seen to disappear. In (e), when using 5760 sources, only a fraction of the noise is left. This number of sources corresponds with the Nyquist spatial sampling criterion for the used frequencies and the minimum velocity in the model.

Here, we have shown that the noise is a function of the source sampling. Thus, this noise is

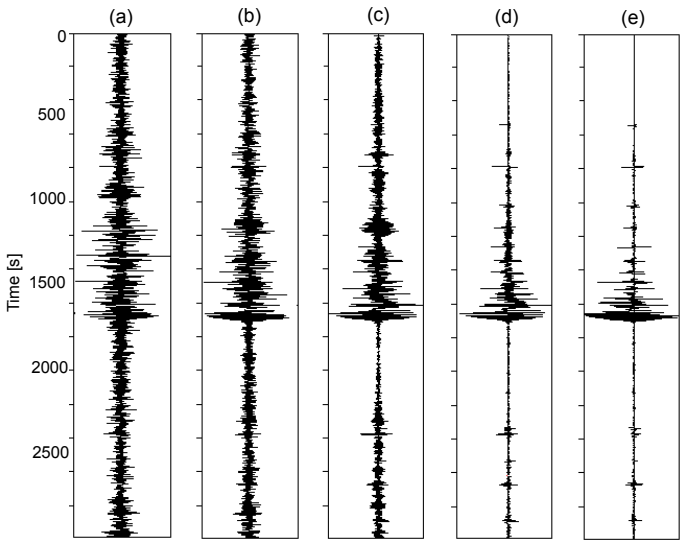


Figure 2.B.1 *The reconstructed result using the SI relation without near offset for $\mathbf{x}_\mathcal{A}$ at $90^\circ\,\Delta$ from $\mathbf{x}_\mathcal{B}$ with using respectively (a) 360, (b) 720, (c) 1440, (d) 2880 and (e) 5760 sources around the model.*

correlation noise, resulting from cross-correlations of all kinds of events that have not shared a common travelpath and thus does not lead to stationary phase events in the correlation panel. With a proper sampling the correlation noise almost completely disappears. The tiny amount left could be due to numerical errors as mentioned in the previous section.

2.B.3 Additional events

Here, we analyze the occurrence of additional events. These are reconstructed events which are not in the FD-modeled response. These are sometimes referred to as spurious multiples or non-physical events. They are most obvious in the causal result (Fig. 2.11(a) and (b)), but can also be seen in the anticausal result (Fig. 2.10(a) and (b)).

One possibility to reconstruct such additional event would be by a correlation of events as indicated on Fig. 2.B.2. We assume an Earth with two velocity contrast (CMB and inner core-outer core boundary), indicated with different levels of grey in the 2D Earth models. A reflection in the state A is correlated with a transmission in the computational state B resulting in an event with the kinematics as if there is a source a the CMB and a direct transmission was measured by a receiver, also at the CMB. On the right-hand side the phase characteristics of the reconstructed event is given, assuming a Gaussian source wavelet. We call such an event that is both initiated and measured at a boundary within the Earth, an internal event.

To test whether the additional events are actually internal events, we forward-model the

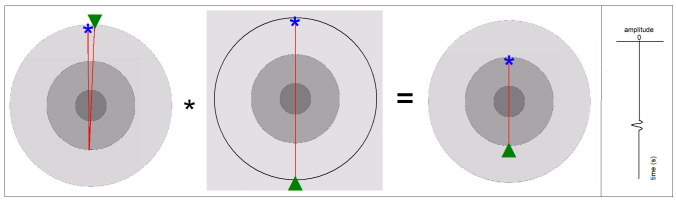


Figure 2.B.2 *Correlation example. The drawings are models of the Earth. The red lines are ray paths of specific events that are measured at a receiver (green triangle) and initiated by a source nearby the Earth's surface (blue star). The correlation of a specific reflection response (drawn in the left-hand model) with a transmission response (in middle model) results in an internal event (right-hand model). The trace on the right-hand side shows the phase-characteristic of the reconstructed event.*

response for one source at the CMB and register the response at receivers placed around the CMB. Also we place a source at the inner core-outer core boundary and measure the response at the same boundary. We plot the responses measured at the CMB upon the responses measured at the inner core-outer core boundary, resulting in Fig. 2.B.3(a). This combined response is compared with our previous reconstructed response (Figs. 2.10 and 2.11). Fig. 2.B.3(b), (c), (d) and (e) depict the first 1000 s of the causal reconstructed result, the causal result without near offset, the time-reversed anticausal correlation result and the anticausal result without near offset, respectively. It can clearly be seen that the additional events in the causal results indeed have the same kinematics as the events modeled in Fig. 2.B.3(a). The additional events in the anticausal result are less visible, but also follow the same kinematics.

From the above test it can be concluded that the additional events are (mainly) internal events that follow from a correlation of events as depicted in Fig. 2.B.2.

According to the derived relations for SI, though, no additional events are predicted. So, when the conditions assumed during the derivation of these relations are fulfilled, the additional events should not appear.

With a similar example as in Fig. 2.B.2, we can also explain how these additional events could disappear. In Fig. 2.B.4 a transmission in the state A is correlated with a reflection in state B resulting in an event with the kinematics as if there is a source a the CMB and a direct transmission was measured by receiver, also at the CMB. On the right-hand side the phase characteristics of the reconstructed event is given, assuming a Gaussian source wavelet. Now comparing Figs. 2.B.2 and 2.B.4 we see that the reconstructed events have precisely opposite phase characteristics. The summation of both correlation results should cancel these internal events.

Analyzing correlation panels (e.g., as depicted in Fig. 2.8) it can indeed be seen that these additional events have stationary phase events with opposite phase characteristic. So as the theory predicts and as can be intuitively understood by a simple analysis as above,

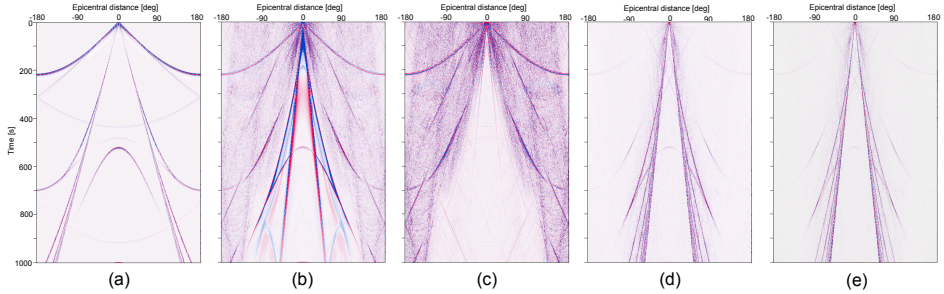


Figure 2.B.3 *Comparison of the reconstructed additional events with the FD-modeled responses of internal events; (a) the FD-modeled internal events measured and initiated at the CMB as well as measured and initiated at the inner core-outer core boundary; (b) is the causal reconstructed result and (c) is the causal result without near offset (as shown previously in Fig. 2.11(a) and (b)); (d) is the time-reversed anticausal correlation result and (e) is the result without near offset (as shown previously in Fig. 2.10(a) and (b)). The first 1000 s of the responses are shown, because in this time window the additional events were most obvious.*

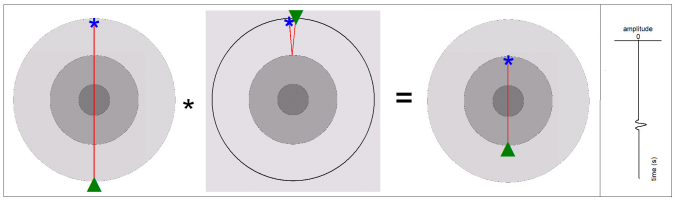


Figure 2.B.4 *Correlation example. The drawings are models of the Earth. The red lines are ray paths of specific events that are measured at the FS (green triangle) and initiated by a source nearby the Earth's surface (blue star). The correlation of a transmission response (drawn in left-hand model) with a specific reflection response (in middle model) gives an internal event (right-hand model). The traces on the right-hand side show the phase-characteristic of the event reconstructed.*

with a perfect source sampling (perfect illumination from all sides), with no losses within the model and with sufficiently long input responses, these additional events will cancel each other. In our case, it is especially the use of an input duration for which not yet all possible internal multiples have been recorded for state B that leads to unequal amplitudes of stationary phase events with opposite phase characteristics. Let us explain. Suppose we call the reconstructed internal event on the right-hand side in Fig. 2.B.4 $K+$. There is only one way to retrieve $K+$, that is by a correlation of PKP and PcP, as illustrated in Fig. 2.B.4. Suppose we call the reconstructed internal event on the right-hand side in Fig. 2.B.2 $K-$. Fig. 2.B.2 is an illustration of only one possibility to retrieve $K-$, that is by a correlation of $PKKP$ and PKP. But also a correlation of $P3KP$ and $PKKP$ gives $K-$ and a correlation of $P4KP$ and $P3KP$ gives $K-$, etc. The amplitude with which we retrieve $K-$ is thus a function of the recording length, or the order of $P*KP$ which we include. With our modeling we do not use higher orders than $P5KP$, while higher orders still have significant amplitude. Thus the sum of $K+$ and $K-$ is still a significant deviation from zero.

For real data, the sampling of opposite stationary phase events that should cancel each other, will never be identical. Also, the amplitudes will not be equal because of (different) losses and the duration of the input responses will always be limited. Hence, the (partial) reconstruction of these internal events will be an issue. If we know a-priori where the large contrast exits, we can model where the stationary phases of these internal events will occur in the correlation panels and filter them out.

Besides being a nuisance, these additional events could bring unprecedented possibilities. One of the stationary phase events can be selected and hence a response could be constructed as if induced and measured at, e.g., the CMB.

Chapter 3

Lithospheric-scale seismic interferometry: multi offset[1]

3.1 Introduction

A variety of seismic methods has been developed to image the lithosphere below an array of receivers using the body-wave responses from distant earthquakes. Particularly widely used are the receiver-function (RF) methods (Langston, 1977; Wilson & Aster, 2005), which image the P-S or S-P scattering potential. A higher resolution can be achieved when the complete forward-scattering potential is estimated (Bostock & Rondenay, 1999), given that the source time functions (STF) of each earthquake can be estimated and deconvolved reliably (Bostock, 2004). Free-surface-reflected phases (for example $Ppdp$ or $Ppds$) may be added to further enhance the resolution, but model information is required to do this.

An attractive alternative is to migrate reflection responses obtained with seismic interferometry (SI). SI refers to the principle of generating seismic responses by crosscorrelating seismic observations at different receiver locations (Wapenaar et al., 2008a; Schuster, 2009). This technique is frequently used for the retrieval of surface waves between seismic receivers since the pioneering work by Campillo & Paul (2003), but can in principle be used to retrieve a complete Green's function, including the reflection response (Wapenaar, 2004), dependent on the distribution of the actual sources. When a collection of reflection responses is obtained using SI, where a virtual source is retrieved at each station position, a reflectivity image can be constructed using standard seismic processing (Yilmaz & Doherty, 2000) as was shown by Draganov et al. (2009) for an exploration-scale passive dataset. A processing sequence that is similar to theirs could also be used for lithospheric imaging.

It was previously proposed by a number of researchers that SI may also be applied to transmission responses from distant earthquakes. Schuster et al. (2004) used only one synthetic

[1]This chapter has been published as a journal paper in *Geophysical Journal International*, **183**, 339–357 (Ruigrok et al., 2010a). Note that minor changes have been introduced to make the text consistent with the other chapters of this thesis.

phase response to obtain a reflectivity image of a crustal model. Their approach is based on the theory of Claerbout (1968), who showed that the reflection response of a horizontally layered medium may be retrieved from the autocorrelation of the plane-wave transmission response. For actual earthquake data the results would not be satisfactory, because the subsurface is far more complicated than horizontally layered. Moreover, the STF and any scattering that is experienced by a phase before entering the lithosphere, would need to be perfectly deconvolved for. Nowack et al. (2006) showed a more elaborate imaging, but still with only one synthetic phase response in the Born approximation. Similar numerical tests, but with complete transmission responses of subsurface sources appeared in Draganov et al. (2006). In both numerical studies, only a few sources sufficed to make an image, given that the velocity model of the subsurface was known because the retrieved reflections themselves were too distorted to be used for estimating a model. Fan et al. (2006) described a combined reflection-retrieval and multiple-elimination scheme. Also their scheme is valid for horizontally layered media. Kumar & Bostock (2006) applied SI successfully on field data recorded by a single station at Hyderabad, India. Using exceptionally high-quality data, they retrieved a multicomponent, rayparameter-limited, reflection response for this single station. Tonegawa et al. (2009) retrieved waves between tiltmeter stations in the Tokai region, Japan. They made the assumption that the lithosphere below the station contains strong point diffractors, like in the ultrasonic experiment by Derode et al. (2003b). They first removed the deterministic part of the phase responses and subsequently only crosscorrelated the lithospheric coda to achieve an isotropic illumination. With their processing they retrieved primarily direct waves. Abe et al. (2007) applied SI, combined with an imaging step, on field data recorded by a dense array of receivers in central Japan. They showed that the resulting image has a higher resolution than the image obtained from RF. They used phase responses from 10 earthquakes from varying azimuths. This might have sufficed to obtain a reliable image, though the work from Draganov et al. (2006) suggests that, for an approximately layered medium, this is insufficient for obtaining reliable reflection responses.

Despite a few imaging successes with the help of SI, the question remained whether, with SI, a true multidimensional lithospheric reflection response can be obtained under realistic conditions. The realistic conditions of concern are an irregular distribution of earthquakes, different phase-responses that overlap in time and a lithosphere that is unlikely to contain a large number of point scatterers. To address the applicability of SI under these conditions, we generate synthetic data with similar source-side reverberations (SSR) and illumination characteristics like a field dataset from the Laramie broadband array (2000-2001). We evaluate sampling requirements and introduce SI adaptations for irregular source distributions. Artifacts are to be expected, caused by both an irregular illumination and by SSR. Subsequently, we study with which SI adaptation these artifacts can be suppressed most successfully. After ascertaining the reliability of the retrieved reflections, we use them to estimate a 2D P-wave velocity model of the lithosphere. Finally, the imaging accuracy is shown by stacking and migrating the obtained reflection responses, for both the synthetic and field

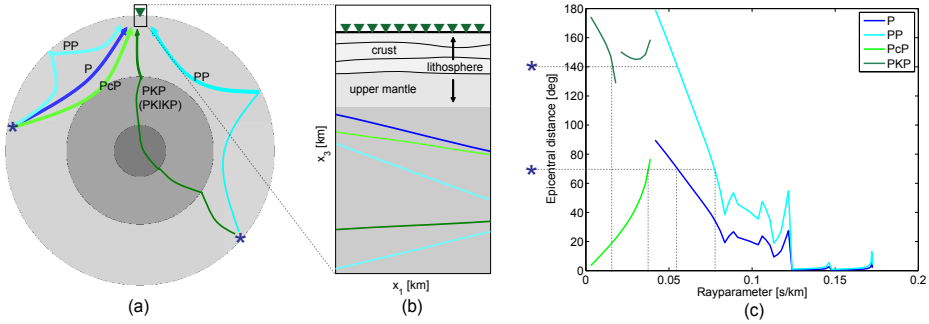


Figure 3.1 *(a) A depiction of the raypaths for different P-wave phases between two earthquake sources (stars) and a regional array of receivers (triangle). For the teleseismic source (left) P, PP and PcP are shown while for the global source (right) PKP (in fact its branch through the inner core, $PKIKP$) and PP are shown. (b) An enlargement of the subsurface below the array with the wavefronts of the different phases (colored dipping lines) traveling upwards, just before they hit the lithosphere from below. The lateral (x_1) and depth axis (x_3) have equal scaling. The wavefronts are depicted with only half the dip of what may be expected. In reality, the different phases arrive near the array with a considerable time lapse. (c) The different phases as a function of epicentral distance (Δ) and absolute rayparameter $|p|$ for which they exist (Knapmeyer, 2004). From this graph can be read, the $|p|$ of the phases caused by the teleseismic source ($\Delta = 70^\circ$) and the global source ($\Delta = 140^\circ$).*

data.

3.2 Seismic Interferometry

We apply SI to P-wave phases caused by distant earthquakes and their P-wave scattering near an array of receivers. Fig. 3.1(a) depicts the different P-wave phases that we consider. In particular, we use the direct transmissions P and PKP, since they are the first to arrive and are, consequently, not disturbed by coda from earlier phases. In Wapenaar & Fokkema (2006) an acoustic 3D SI relation is derived for a configuration with receivers on a free surface and illumination from below. This SI relation consists of correlations of receivers at the surface, followed by an integration of correlations over source positions in the subsurface. In Appendix 3.A we estimate what the minimum (in-plane) source sampling for this integral needs to be for a lithospheric application and show that the maximum allowed spacing between large earthquakes is about 1000 km. There are many places on Earth where this source density is not reached. Fortunately, the required source spacing can be reached when a 3D distribution of point sources may be represented by a 2D distribution of sources, in-plane with the receiver array. This will be shown in the following.

For distant earthquakes, the distance is much larger than the length of the array of receivers

and, consequently, an incoming wave caused by a distant earthquake is by approximation a plane wave when it reaches the lithosphere. In Fig. 3.1(b) the planar wavefronts of the different phases are depicted as they travel upwards through the mantle and just before they hit upon the heterogeneous lithosphere below the array. Thus, near the array, each global and teleseismic phase may be treated as a separate effective plane wave, characterized by a single horizontal rayparameter p. The SI relation from Wapenaar & Fokkema (2006) is written as an integration over point sources $\mathbf{x}$. In the following we will rewrite their relation to an integration over plane-wave sources expressed in p.

As a first step, we present a 2D approximation of the relation in Wapenaar & Fokkema (2006):

$$\int_{\partial\mathbb{S}_1} G(\mathbf{x}_\mathcal{A}, \mathbf{x}, -t) * G(\mathbf{x}_\mathcal{B}, \mathbf{x}, t) d\mathbf{x} \propto G(\mathbf{x}_\mathcal{B}, \mathbf{x}_\mathcal{A}, -t) + G(\mathbf{x}_\mathcal{B}, \mathbf{x}_\mathcal{A}, t), \tag{3.1}$$

where $G(\mathbf{x}_\mathcal{A}, \mathbf{x}, t)$ denotes the Green's function observed at location $\mathbf{x}_\mathcal{A}$ (one of the receivers) due to a source at $\mathbf{x}$ and where a proportionality sign is used since we have left out all the amplitude terms.

As a second step, we change the variables of integration from Cartesian (x_1, x_3) to polar coordinates (r, ϕ):

$$\int_{\partial\mathbb{S}_1} G(\mathbf{x}_\mathcal{A}, \mathbf{x}, -t) * G(\mathbf{x}_\mathcal{B}, \mathbf{x}, t) r d\phi \propto G(\mathbf{x}_\mathcal{B}, \mathbf{x}_\mathcal{A}, -t) + G(\mathbf{x}_\mathcal{B}, \mathbf{x}_\mathcal{A}, t), \tag{3.2}$$

where $\mathbf{x} = (r, \phi)$ on $\partial\mathbb{S}_1$, with r being the radius and ϕ the angle. $\partial\mathbb{S}_1$ is the surface (or actually a curved line in 2D) containing the sources. Together with the free surface it should ideally form a closed surface. The retrieved response $G(\mathbf{x}_\mathcal{B}, \mathbf{x}_\mathcal{A}, t)$ contains the reflection response between the two receiver positions (triangles in Fig. 3.1). To retrieve a response between one virtual source $\mathbf{x}_\mathcal{A}$ and several receivers, equation (3.2) would need to be repeated for varying $\mathbf{x}_\mathcal{B}$. Since a lossless medium is assumed for equation (3.2), the phase responses would need to be corrected for losses before crosscorrelation. In Appendix B and Draganov et al. (2010) a procedure is described to estimate an average quality factor Q with SI. This Q, in turn, may be used to estimate an amplitude correction term, to be applied to the data prior to crosscorrelation. We expect only small losses in the lithosphere. For small and moderate losses a correction may be left out (Slob et al., 2007; Ruigrok et al., 2009b).

As a third step, we change the coordinate of integration in equation (3.2) from ϕ to p (Appendix 3.A), yielding

$$\int G(\mathbf{x}_\mathcal{A}, p, -t) * G(\mathbf{x}_\mathcal{B}, p, t) \frac{r v_p}{\sqrt{1 - v_p^2 p^2}} dp \propto G(\mathbf{x}_\mathcal{B}, \mathbf{x}_\mathcal{A}, -t) + G(\mathbf{x}_\mathcal{B}, \mathbf{x}_\mathcal{A}, t), \tag{3.3}$$

where $G(\mathbf{x}_\mathcal{B}, p, t)$ is the phase response of a plane wave with rayparameter p measured at $\mathbf{x}_\mathcal{B}$. The term $\frac{r v_p}{\sqrt{1 - v_p^2 p^2}}$ weighs the contributions from different sources. Since v_p (velocity just below the lithosphere) is similar for different sources, the weighing term is only

smoothly varying in p and does therefore not alter the phase of the retrieved Green's function. On that account, we also neglect this amplitude term, reducing equation (3.3) to

$$\int G(\mathbf{x}_\mathcal{A}, p, -t) * G(\mathbf{x}_\mathcal{B}, p, t) dp \propto G(\mathbf{x}_\mathcal{B}, \mathbf{x}_\mathcal{A}, -t) + G(\mathbf{x}_\mathcal{B}, \mathbf{x}_\mathcal{A}, t). \tag{3.4}$$

Fig. 3.2(a) shows an ideal illumination from plane-wave sources (represented by stars) with which the complete response between $\mathbf{x}_\mathcal{A}$ and $\mathbf{x}_\mathcal{B}$ would be retrieved when equation (3.4) is implemented. The illumination is ideal when phase responses are available in a well-sampled range, $p = [0, \pm 1/v_p^{ns}]$ (Fig. 3.2(a)), where v_p^{ns} is the near-surface velocity. Fig. 3.2(b) depicts a more realistic illumination, with missing illumination at large rayparameters and an irregular illumination at small rayparameters. Large rayparameters correspond to body-wave phases from nearby sources of which the wavefields are not planar and for which different triplications cannot easily be separated and aligned. Omitting large rayparameters means that guided waves and body waves at large offsets would not be retrieved. Small rayparameters correspond to body-wave phases from distant sources with well-defined planar wavefields emerging on the lithosphere. By using illumination with small rayparameters, body waves at near and intermediate offsets can be retrieved, which are the most relevant ones for obtaining a reflectivity image. Using only P phases from teleseismic distances would not be sufficient, since their illumination is limited between rayparameters of $[-0.08, -0.04]$ and $[0.04, 0.08]$ s/km (Fig. 3.1(c)). PKP phases are used to fill the gap of the very small rayparameters, while PP and PcP are used to enhance the sampling. The irregular illumination stems from the irregular distribution of earthquakes and the heterogeneous nature of the Earth. The influence of this irregularity is studied in section 3.4.

With equation (3.4) both a causal and an acausal response are retrieved. This is explained in Fig. 3.2(c) for a single reflection. The reflection drawn between $\mathbf{x}_\mathcal{A}$ and $\mathbf{x}_\mathcal{B}$ can be retrieved at positive times by contributions from sources with positive p contributing to the Fresnel zone around the solid ray. The same reflection can be retrieved at negative times by contributions from sources with negative p contributing to the Fresnel zone around the dashed ray. The above reasoning holds for an approximately layered medium. For a complex medium, a phase with a negative rayparameter may still give contributions to $G(\mathbf{x}_\mathcal{B}, \mathbf{x}_\mathcal{A}, t)$, e.g., by scattering from point diffractors. The standard procedure would be to add the time-reversed acausal result of equation (3.4) to the causal result, to increase the effective sampling. Alternatively, the contributions from the negative rayparameters can be time-reversed prior to integration. If $[p^-_{min}, p^-_{max}]$ and $[p^+_{min}, p^+_{max}]$ are the rayparameter bands in which we have illumination, the discretized version of equation (3.4) can be split up in a sum over positive and negative rayparameters:

$$\sum_{p^-_{min}}^{p^-_{max}} I(\mathbf{x}_\mathcal{A}, \mathbf{x}_\mathcal{B}, p, t) \Delta p \propto G(\mathbf{x}_\mathcal{B}, \mathbf{x}_\mathcal{A}, -t) + N^-(t) \tag{3.5}$$

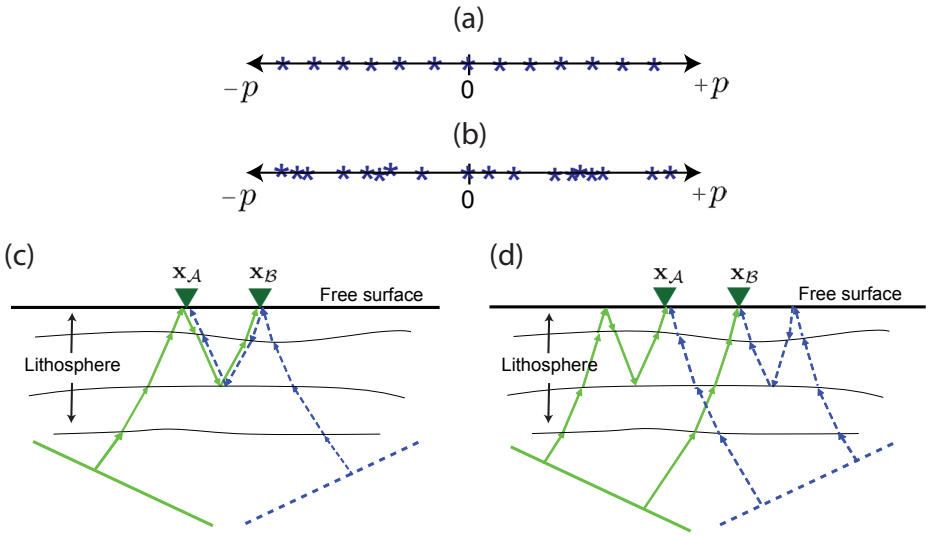


Figure 3.2 *In (a) an ideal illumination is shown for plane-wave sources, expressed in rayparameters. In (b) a more realistic distribution of plane-wave sources is shown. In (c) and (d) examples of ray paths are indicated that in (c) do contribute to the retrieval of a reflection after crosscorrelation, but in (d) do not.*

and

$$\sum_{p^+_{min}}^{p^+_{max}} I(\mathbf{x}_\mathcal{A}, \mathbf{x}_\mathcal{B}, p, t)\Delta p \propto G(\mathbf{x}_\mathcal{B}, \mathbf{x}_\mathcal{A}, t) + N^+(t), \tag{3.6}$$

where $I(\mathbf{x}_\mathcal{A}, \mathbf{x}_\mathcal{B}, p, t)$ stands for the integrand of equation (3.4). $N^-(t)$ and $N^+(t)$ contain correlations of non-specular rays, with negative and positive rayparameter, respectively. These are correlations of waves with non-overlapping raypaths (Fig. 3.2(d)). For an approximately 1D medium $N^\pm(t)$ would be zero if the sums (equations 3.5 and 3.6) cover the complete rayparameter band and satisfy the sampling condition for integral equation (3.4). For a strongly heterogeneous medium equations (3.5) and (3.6) would need to be summed to remove the noise terms. In practice, $N^\pm(t)$ contains remnants of the non-specular correlations, that have not canceled completely in the summation process. These remnants are called correlation noise. By adding the time reversed of equation (3.5) to equation (3.6),

$$\sum_{p^-_{min}}^{p^-_{max}} I(\mathbf{x}_\mathcal{A}, \mathbf{x}_\mathcal{B}, p, -t)\Delta p + \sum_{p^+_{min}}^{p^+_{max}} I(\mathbf{x}_\mathcal{A}, \mathbf{x}_\mathcal{B}, p, t)\Delta p \propto$$
$$2G(\mathbf{x}_\mathcal{B}, \mathbf{x}_\mathcal{A}, t) + N^-(-t) + N^+(t), \tag{3.7}$$

the effective sampling is increased while a part of the correlation noise is isolated at negative

times. Thus, by rejecting the negative times, the signal-to-noise ratio is increased. In the following we will call this the TRBI (time reversal before integration) approach. There is no need for applying TRBI when a well-sampled source distribution is available. For a strongly heterogenous subsurface it would even be disadvantageous to apply TRBI, because it would lead to additional noise that would otherwise (with equation 3.4) be canceled.

By using a limited rayparameter band, also the retrieved Green's function in equation (3.7) will be rayparameter limited. As a consequence, the slope of a primary reflection is incorrectly retrieved beyond a maximum half-offset $h_{max}(t)$. Assuming a well-sampled illumination band $[0, p_{max}]$, a 1D velocity model with an average velocity $\tilde{v}_p(t)$ and an infinite frequency, h_{max} may be expressed as

$$h_{max}(t) = \frac{p_{max} t \{\tilde{v}_p(t)\}^2}{2\sqrt{1 - \{\tilde{v}_p(t)\}^2 p_{max}^2}}, \tag{3.8}$$

where t is the minimum two-way traveltime.

To retrieve a reflection correctly for a finite frequency, a Fresnel zone around the stationary point needs to be sampled (Schuster et al., 2004; Snieder, 2004). Therefore, in practice, $h_{max}(t)$ will be smaller than estimated in equation (3.8).

The moment tensor of an earthquake is of little relevance for this application of SI. Since the size of a typical array of receivers ($< 10^2$ km) is at least one order of magnitude smaller than the distances to the sources ($> 10^3$ km), it may be assumed that the entire array lies within one focal plane. In this case, the observed responses at $\mathbf{x}_\mathcal{A}$ and $\mathbf{x}_\mathcal{B}$ in equation (3.4) may be written as a convolution of only the STF with the Green's functions $G(\mathbf{x}_\mathcal{A}, p, t)$ and $G(\mathbf{x}_\mathcal{B}, p, t)$. In principle, it would be better to remove the STFs prior to integration. Regrettably, it is notoriously hard to estimate the STFs reliably and to deconvolve them in a stable manner (Kumar & Bostock, 2006). This is especially so for the relative low-magnitude earthquakes recorded by a portable array, as in our case. In our experience, suppressing the sidelobes of the autocorrelated STFs in the integration process gives better results than removing the STFs prior to integration. By assigning an STF to the observed Green's functions in equation (3.4), the retrieved response will be a convolution of the Green's function between $\mathbf{x}_\mathcal{A}$ and $\mathbf{x}_\mathcal{B}$ with a stack of autocorrelations of all individual STFs. Through the autocorrelation, the STFs become all zero-phase, which facilitates a successful integration, even when the earthquake responses have very different —and very complicated— STFs.

3.3 Laramie array

We apply the above theory to earthquake responses recorded by the Laramie array. The array was installed near the town of Laramie, in Wyoming, USA and hence the name. It was deployed between October 2000 and May 2001 to study the Archean-Proterozoic Cheyenne Belt suture (Dueker & Zurek, 2001). The array consists of 31 three-component broadband receivers, as depicted in Fig. 3.3(a), with an average spacing of 2.6 km. The orientation of the array is favorable, approximately in-plane with a large part of the Ring of Fire (Fig.

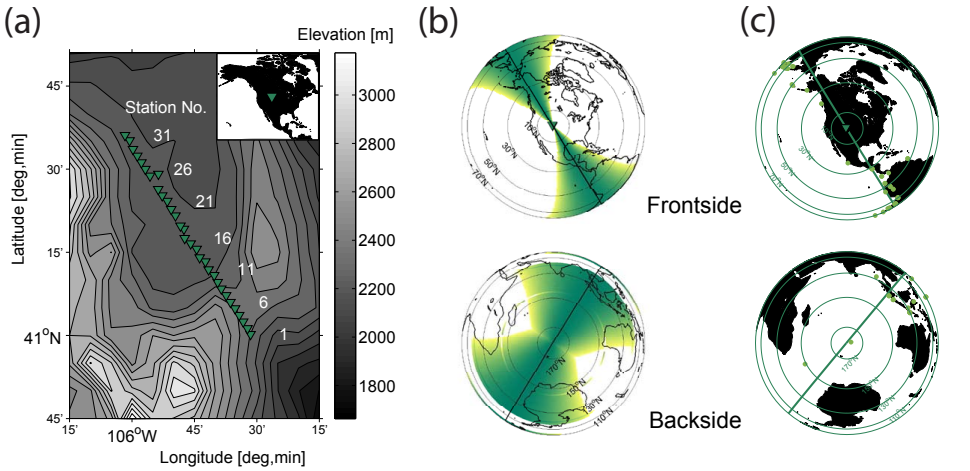


Figure 3.3 *(a) The Laramie array of seismic receivers (triangles) and the local topography (shading). (b) Approximation of the first Fresnel zone for the P and PKP phase, for epicentral distances $\Delta = [0, 90^\circ]$ (up) and $\Delta = [90, 180^\circ]$ (down), for an offset equal to or smaller than 40 km. (c) The distribution of earthquakes of which the responses are processed for $\Delta = [0, 90^\circ]$ (up) and $\Delta = [90, 180^\circ]$ (down). In (b) and (c) the concentric circles depict the epicentral distance with respect to the Laramie array. The straight line is the extended great circle through the array, which has an average orientation of 328°.*

3.3(c)). The data was previously processed to obtain RF images (Hansen & Dueker, 2009).

In equation (3.4), the integration is over plane waves radiated by sources in the vertical plane. For finite frequency, the source locations may be located outside this plane, as long as their contributions to the integral are in phase with the contribution from sources in the plane. Fig. 3.3(b) depicts the size of the region of source locations that would contribute in phase. This region is computed in Appendix 3.B. From all the recorded earthquake responses, only those are selected that are from sources within the colored zone in Fig. 3.3(b) and with a magnitude larger than 5. All the selected three-component responses are bandpass filtered between 0.3 and 1.5 Hz, rotated and decomposed to P-, SV- and SH components as further explained in Appendix 3.C. Using only the P-component, time-windows of 100 s are chosen to isolate P, PP, PcP and PKP arrivals and their reverberations, where possible. Subsequently, timing errors between the different receivers and statics are removed by aligning on the direct arrival with an iterative crosscorrelation scheme. Each trace in a phase response is normalized with the maximum amplitude of the direct arrival, to correct for differences in near-surface amplifications. An implicit assumption in relation (3.4) is that the plane waves have equal energy. Since this assumption is not fulfilled for natural sources, as a last step, we normalize the energy in each phase response. From 39 earthquake responses 69 separate phase responses are extracted.

Despite the fact that only events in the first Fresnel zone are selected, the average illumina-

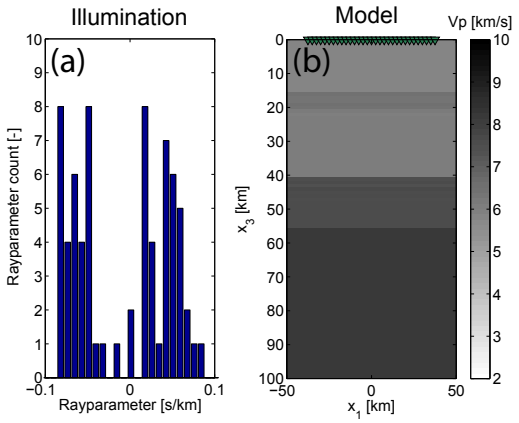


Figure 3.4 *(a) A histogram distribution of the rayparameters of the selected phase responses. A bin size $dp = 0.0083$ s/km is taken, which corresponds to the required sampling of equation (3.4). (b) A simplified P-wave velocity model (v_p) for the crust and upper mantle, with 31 receivers (triangles) on the free surface.*

tion is still not in-plane with the array (Fig. 3.3(c)). The azimuthal illumination bias, which leads to small kinematic errors in the retrieved response, is suppressed through the following azimuthal correction. We define p^{src} as the horizontal rayparameter connecting the source and the receiver through a homogeneous background model and $p^{1,src}$ as its projection on the array vector. Thus $p^{1,src} = p^{src}\cos(\theta)$, where the source-to-array azimuth θ is defined as the angle between the array orientation (a best fitting great circle through the stations) and a great circle through the source and the middle station. After aligning a response on the direct wave, the move-out is restored with traveltime differences computed with p^{src} instead of $p^{1,src}$. Hence, the direct wave obtains a move-out as if the source location was in-plane with the array. This azimuthal correction is justified if the array is small with respect to the distance to a source and if the medium may be approximated to be laterally invariant within the colored zone in Fig. 3.3(b).

3.4 Comparison of seismic interferometric approaches

The $p-$distribution of the 69 effective sources is depicted in Fig. 3.4(a). Clearly, the integral in equation (3.4) is sampled strongly irregularly. Rayparameters from P phases at teleseismic distances are overrepresented, whereas small rayparameters are underrepresented. To find a good approach to deal with the irregularity, we model a 2D synthetic dataset with the same irregular rayparameter distribution and receiver geometry as the actual dataset. We use a simplified lithospheric model (Fig. 3.4(b)) based on the findings of Chulick & Mooney (2002) from a nearby refraction survey. The main feature is the Moho at 40 km

depth, separating a crystalline crust (v_p=6.0 km/s, ρ=2730 kg/m^3) from the upper mantle (v_p=7.6 km/s, ρ=3310 kg/m^3). Subsequently, we apply SI to the 69 transmission responses, to retrieve the response as if there was a source at station 16 and receivers at all other station positions. To suppress edge effects, the edges of the integrand (in equation (3.4) and (3.7)) are tapered. In Fig. 3.5(a) one of the 69 synthetic transmission responses is shown. In Fig. 3.5(b)-(d) different approaches are tested to deal with the irregular source sampling. The retrieved responses are compared with a reference response (Fig. 3.5(e)) which is obtained by directly modeling the reflection response of a source at receiver position 16. In Fig. 3.5(e), primary reflections from all 4 interfaces can be distinguished, as well as first-order multiples from the upper three interfaces. Data at early times, bounded by $\pm h_{max}(t)/2$ (see equation (3.8)) has been muted.

Fig. 3.5(b) and (c) show responses retrieved with equation (3.4) after adding the time-reversed acausal result to the causal part and muting data at early times. In Fig. 3.5(b), nothing is done to take the source irregularity into account and, as a result, large artifacts can be seen. Overillumination leads here to artifacts at times before an actual reflection and with a slope opposite to the actual reflection. Underillumination (at small rayparameters) leads here to small spurious additions to the retrieval in the near-offset. Note the onset of the Moho reflection (the blue line at t$\approx$13 s) being more pronounced between station number 13 and 19. This is because of incomplete addition and cancelation in the stationary-phase region. When writing integral equation (3.4) as a sum, the infinitesimally small line element, dp, is replaced by a finite one, Δp. Hence, we would need to weigh the contribution of each effective source p_i by $\Delta p_i = |p_{i+1} - p_{i-1}|/2$, where p_{i+1} and p_{i-1} are the two neighboring effective sources. By implementing Δp weights (Fig. 3.5(c)), illumination artifacts are suppressed. When the TRBI approach is used (Fig. 3.5(d)), without Δp weights, also the irregularity artifacts are suppressed, but, additionally, amplitudes in the near-offset range are weakened. This is because the stationary-phase regions for events in the near-offset range are only partly sampled. The results can better be understood by studying visualizations of the integrands, see Appendix 3.D.

With the above application of SI, a lithospheric reflection response is obtained from receiver-side reverberations (RSR). However, the lithosphere near the source will be just as heterogeneous and lead to SSR. E.g., a direct P phase is followed, for intermediate to deep earthquakes, by two SSR from the free surface: the pP and sP phases. Only for very deep earthquakes, pP and sP arrive late enough such that their RSR can be untangled from the P-phase response. Only for very shallow earthquakes, the SSR can be treated as part of the STF. Hence, for most earthquakes, we would need to replace $G(\mathbf{x}_\mathcal{A}, p, -t)$ in equation (3.4) by a sum of effective phase responses, $G_P(\mathbf{x}_\mathcal{A}, p, -t) + G_{pP}(\mathbf{x}_\mathcal{A}, p, -t) + G_{sP}(\mathbf{x}_\mathcal{A}, p, -t)$, where the subscript denotes the phase, and $G(\mathbf{x}_\mathcal{B}, p, t)$ by similar terms. The resulting inte-

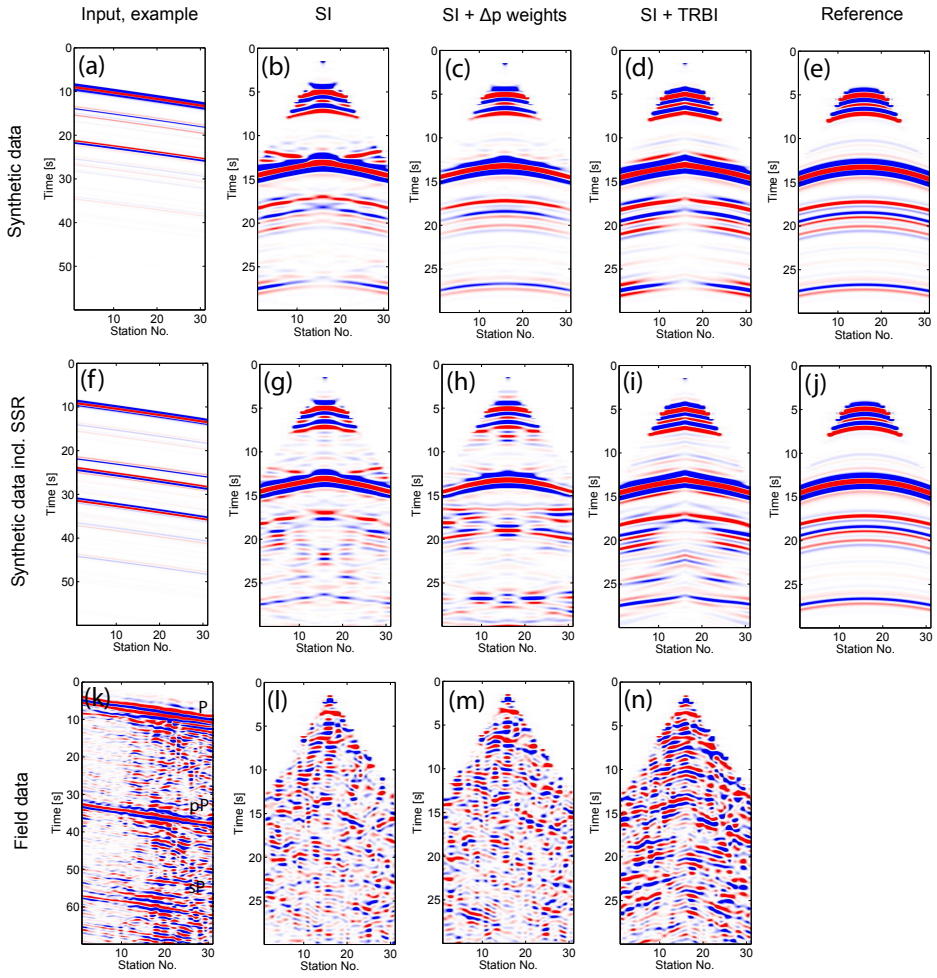


Figure 3.5 *(a) An example of the input for seismic interferometry (SI), an isolated phase response. (b)-(d) Estimations of the reflection response, with the three different SI approaches (see the main text for explanation). (e) The partially-muted directly modeled response for a source at receiver position 16. (g)-(i) Again a comparison of the three different SI approaches, but now source-side reverberations are included in the input, of which (f) is an example. (j) A repetition of the reference response (e). (l)-(n) A comparison of the same three SI approaches, but now with the composite phase responses from the Laramie field dataset as an input, of which (k) is one example.*

gral can be split up in a part that gives physical contributions to the retrieved result

$$\int [G_P(\mathbf{x}_\mathcal{A}, p, -t) * G_P(\mathbf{x}_\mathcal{B}, p, t) + G_{pP}(\mathbf{x}_\mathcal{A}, p, -t) * G_{pP}(\mathbf{x}_\mathcal{B}, p, t) + G_{sP}(\mathbf{x}_\mathcal{A}, p, -t) * G_{sP}(\mathbf{x}_\mathcal{B}, p, t)] dp, \quad (3.9)$$

and a part that contains only spurious cross terms

$$\int [G_P(\mathbf{x}_\mathcal{A}, p, -t) * G_{pP}(\mathbf{x}_\mathcal{B}, p, t) + G_P(\mathbf{x}_\mathcal{A}, p, -t) * G_{sP}(\mathbf{x}_\mathcal{B}, p, t) + G_{pP}(\mathbf{x}_\mathcal{A}, p, -t) * G_P(\mathbf{x}_\mathcal{B}, p, t) + G_{pP}(\mathbf{x}_\mathcal{A}, p, -t) * G_{sP}(\mathbf{x}_\mathcal{B}, p, t) + G_{sP}(\mathbf{x}_\mathcal{A}, p, -t) * G_P(\mathbf{x}_\mathcal{B}, p, t) + G_{sP}(\mathbf{x}_\mathcal{A}, p, -t) * G_{pP}(\mathbf{x}_\mathcal{B}, p, t)] dp. \quad (3.10)$$

The application of SI needs to be such, that spurious cross terms are adequately suppressed. To show the limitations imposed by these cross terms we create a new synthetic dataset which does not only contain an irregular distribution of effective sources, but which also contains SSR. The SSR are modeled for earthquake depths varying randomly between 10 and 150 km. One of the 69 composite transmission responses is shown in Fig. 3.5(f).

In Fig. 3.5(g)-(i) again the same approaches are tested as in Fig. 3.5(b)-(d), but now the composite transmission responses are used. For all approaches, a degradation of the quality of the retrieved responses can be noted, due to additional cross terms (equation (3.10)). Still, the actual reflection response prevails. This is because, for each earthquake, the SSR are different due to the varying depth of hypocenters and the varying source-side lithology. (In the modeling, the source-side lithology is not varied, though). The cross terms are therefore quite successfully suppressed when 69 phase responses are used (Fig. 3.5(g)), but they remain more prominent when contributions from different sources are weighted differently (Fig. 3.5(h)). The remnants of the cross terms can be noted here as cross-shaped artifacts. Note, e.g., the feature overlaying an actual arrival between 25 and 29 s. The TRBI approach (Fig. 3.5(i)) gives the best results. Since no weights are applied and cross terms at negative times are rejected, the spurious events are strongly suppressed. Only at near-offsets, where the actual events are retrieved with a weakened amplitude, spurious events can be noted. The results can be understood better by studying visualizations of the integrands, see Appendix 3.D.

Fig. 3.5(k) depicts the first 70 seconds of one actual transmission response from the Laramie dataset. This response is a mixture of the P, pP and sP phases and their RSR. For this earthquake, the STF is surprisingly transient. At receiver numbers larger than 11 strong near-surface reverberations are recorded, due to the presence of a sedimentary basin.

In Fig. 3.5(l)-(n) again the same approaches are tested as in Fig. 3.5(g)-(i), but now the actual transmission responses are used. After applying SI, the retrieved responses are deconvolved with an effective STF estimated from the response retrieved at station 16 (the

virtual source). At the sedimentary basin, near-surface reverberations are suppressed by using a larger deconvolution window. Although the actual subsurface below the Laramie array is far more complicated than the model used for the synthetics (Fig. 3.4(b)), the retrieved results (Fig. 3.5(l)-(n)) are consistent with the modeling results with composite transmission responses (Fig. 3.5(g)-(i)). In Fig. 3.5(l), spurious events can be noted. That is, normally one may expect reflections to have an increasing time with offset, but in Fig. 3.5(l) events can be seen that have an opposite move-out. When Δp weights are used (Fig. 3.5(m)), the spurious events are amplified. When TRBI is applied (Fig. 3.5(n)), most events with an erroneous move-out disappear and clear reflection-like events become visible. Similarly as with the modeling results, the near-offset data exhibit a weaker amplitude. From the move-out of the reflections as in Fig. 3.5(n), a velocity model can be derived, which is later used to migrate the reflections to the correct depth. From Fig. 3.5(l) and (m) or from RF data it would be much harder or even impossible, to derive a velocity model.

In Fig. 3.5, blue and red denote positive and negative amplitudes, respectively. For the modeling we used a first derivative of a Gaussian wavelet as an STF ($s(t)$). This can be seen in Fig. 3.5(a) and (f) where each arrival is convolved with a blue-red alteration (plus a small sidelobe). The STF of a reconstructed primary reflection (Fig. 3.5(b)-(d) and (g)-(i)) can be written as

$$s(-t) * \{\pm s(t)\}, \tag{3.11}$$

which is a Ricker wavelet (i.e., minus the second derivative of a Gaussian wavelet) if both STFs in equation (3.11) have the same sign. The reflection is constructed by a crosscorrelation of an arrival with another arrival that has bounced once more at the free surface. When the reflection is from an interface with an increase in impedance with depth, the second STF in equation (3.11) will have the opposite sign from the first one, because of the extra free-surface bounce. Hence, the effective STF will be blue-red-blue (see, e.g., the Moho reflection at $t = 14$ s in Fig. 3.5(b)). When the reflection is from an interface with a decrease in impedance with depth, the second STF in equation (3.11) will have the same sign as the first one, since it encounters a negative reflection coefficient two times more. Hence, the effective STF will be red-blue-red (see, e.g., the second reflection in Fig. 3.5(b), at $t = 7$ s). Also the effective wavelet for the field data resembles a Ricker wavelet, after applying SI and STF deconvolution. In theory, the deconvolution would lead to a Gaussian wavelet. In practice, extra ringing is introduced and the wavelet looks more like a Ricker wavelet. As for the synthetic data, a positive Ricker wavelet denotes an impedance decrease with depth.

In Fig. 3.6, five responses are shown, which are retrieved from the Laramie transmission data with the application of TRBI. On the top panels, the near-surface phases are especially pronounced. The first clear arrival in the panels, which looks like a direct wave, is in fact correlation noise (equation (3.7)), which result from remnants of crosscorrelations of direct waves at the edges of the illumination distribution (Ruigrok et al., 2008a). Apart from illumination considerations, the phase can also be judged to be spurious by its, for a direct wave, unphysical apparent velocity of $v_{p1} \approx 20$ km/s. On all top panels, a hyperbolic event can be seen at $t \approx 2.5$ s. This is a reflection from a large contrast in the upper crust, at $x_3 \approx$

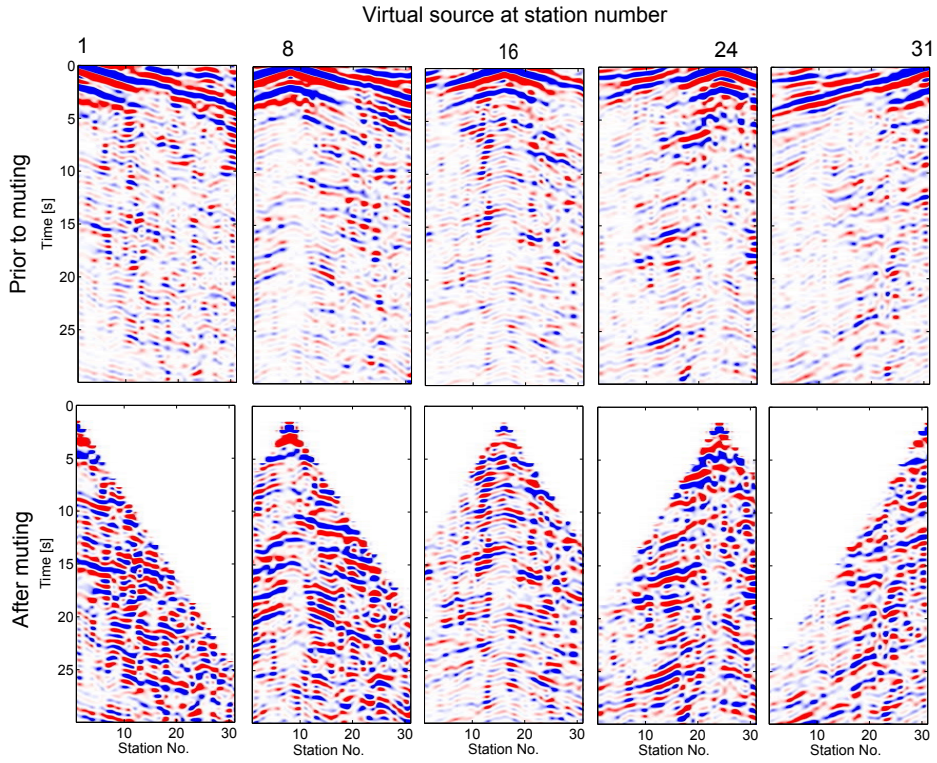


Figure 3.6 *Retrieved responses for a virtual source at, from left to right, receiver number 1, 8, 16, 24 and 31. On the top and bottom, respectively, the raw and muted retrieved responses are shown.*

5 km. Only in the near-offset, the move-out of this reflection is retrieved correctly. On the lower panels, the retrieved responses are shown after muting data at early times, bounded by $\pm h_{max}(t)/2$ (see equation 3.8). Hence, strong unphysical events are removed. In the response after muting, we may expect to see reflections and multiples, retrieved with the actual kinematics, as for the synthetic data (Fig. 3.5(i)). Nevertheless, also here an imprint of correlation noise still remains, partly caused by ringing from near-surface interfaces. In the next section, panels as in Fig. 3.6 will be used for further processing.

3.5 Imaging

In this section, we further process the retrieved reflection responses into images, using standard exploration-geophysics processing (Yilmaz & Doherty, 2000). We repeat SI with TRBI (Fig. 3.5(n)) to retrieve responses for a source at each of the 31 receiver locations. We resort the retrieved shot gathers to common-midpoint (CMP) gathers. Next, we estimate a 2D P-wave velocity model for the deeper subsurface. Velocities are estimated from the move-out

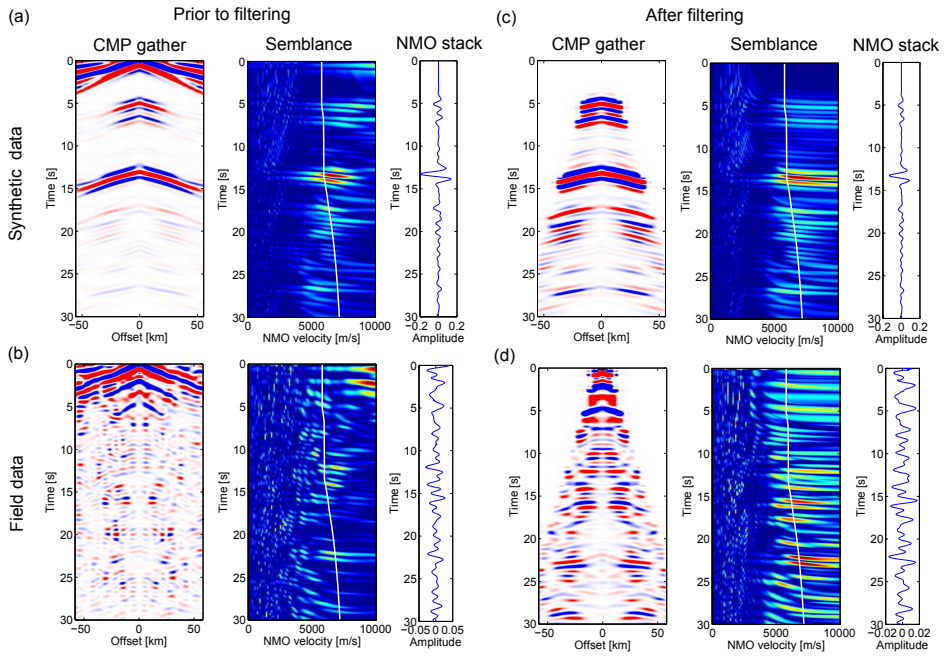


Figure 3.7 *A common-midpoint gather, retrieved with seismic interferometry, for the midpoint position coinciding with station 12 (left), its semblance (middle) and normal-move-out stack (right), using the model velocity function $v_p(t)$ as depicted by the white line in the semblance plot (middle). The same 3 panels are shown for the synthetic data (a), the field data (b) and the synthetic and field data after filtering, (c) and (d), respectively*

of primary reflections in the CMP gathers, through a semblance velocity analysis.

We start with processing the synthetic data. Fig. 3.7(a) depicts a CMP gather (left) for the midpoint position coinciding with station 12 (see Fig. 3.3(a)), its semblance (middle) and the stack over half-offset after normal-move-out (NMO) correction (right). If we denote a CMP panel in the time domain as $f^{CMP}(t,h)$, where h is the half-offset, we can write the NMO-corrected function for different velocities v_p as $f^{NMO}(t,h,v_p)$. We define the semblance f^S (as a variation of the one defined in Neidell & Taner (1971)) as the following weighted stack of $f^{NMO}(t,h,v_p)$ over half-offset:

$$f^S(t,v_p) = \frac{(\sum_h f^{NMO}(t,h,v_p))^2}{\sum_h (f^{NMO}(t,h,v_p))^{1.5}}, \tag{3.12}$$

which weighted stack is implemented with sliding time-windows with a duration of the dominant period in the signal. In equation (3.12), there is a power of 1.5 in the denominator instead of a more common power of 2. By using a reduced power, events with a higher amplitude in $f^{CMP}(t,h)$ are also emphasized in the semblance. Because of a limited sampling in half-offset, the semblance is aliased for small velocities.

In the semblance plot, a velocity function (white line) is drawn that corresponds to the actual velocities of the model that were used for computing the synthetics (Fig. 3.4(b)). During the first 10 seconds the velocity is overestimated by picking the highest amplitudes in the semblance. This is because near-surface reflections are retrieved with an erroneous move-out at larger offsets. At times later than 10 s the velocities can be estimated reasonably well from the semblance, until the time ($\approx 20s$) when multiples start arriving.

The NMO stack can be written as $\sum_h f^{NMO}(t, h, v_p(t))$. For the velocity function $v_p(t)$ the actual velocities are used (the white line in the semblance figure). If the correct velocities are used, the move-out of the reflections in $f^{CMP}(t, h)$ are perfectly removed and the NMO stack is an estimate of the response as if there were a coinciding receiver and source at the free surface (in this case at station location 12). In the stacking process noise and multiples are suppressed to a large extend.

Fig. 3.7(b) depicts the same type of panels as in Fig. 3.7(a) but now for the field data. For these data, the CMP gather (left) looks a lot more complicated and noisier. Besides primary reflections, the CMP gather also contains multiples and correlation noise (equation 3.7), which are both noise for an imaging scheme for primary reflections. In the semblance panel (middle) it is now hard to pick velocities. Therefore the data are filtered prior to velocity analysis. A filtering approach as described by Ryu (1982) is taken to suppress the noise. Each CMP gather is NMO corrected with a velocity function that is between the velocities of the primaries and multiples. Subsequently, after a temporal and spatial Fourier transform, the data at positive wavenumbers are removed and the remaining data are inverse Fourier transformed and inverse NMO corrected. Consequently, events with low apparent velocities are removed. This approach is successful in removing parts of the correlation noise, but the move-out discrimination between primaries and multiples is often not large enough to remove the multiples. To remove more correlation noise, another wavenumber filter is applied. It is assumed that at positive offsets, the move-out of arrivals is also positive. Therefore the data at negative wavenumbers are removed for the positive offsets, and similarly the data at positive wavenumbers are removed for the negative offsets. In the last filtering step, just like for Fig. 3.6(bottom), data at early times is removed.

Fig. 3.7(c) depicts the same type of panels as in Fig. 3.7(a) but now after filtering. Comparing Fig. 3.7(c) with 3.7(a) reveals that artifacts with erroneous move-out have been suppressed. In the semblance panel, some resolution in v_p has been lost through the filtering, but the maxima better follow the actual velocity trend (the white line). For the NMO stack in Fig. 3.7(c) it can be seen that the wavelet has improved. The Moho reflection in Fig. 3.7(c) ($t = 14$ s) better resembles a minus Ricker wavelet than in Fig. 3.7(a).

Fig. 3.7(d) depicts the same type of panels as in Fig. 3.7(b) but now after filtering. Comparing Fig. 3.7(d) with 3.7(b) reveals that artifacts with erroneous move-out have been suppressed. In Fig. 3.7(d) reflections are now visible that were largely hidden by correlation noise in Fig. 3.7(b). The semblance in Fig. 3.7(d) is now much better suited for picking a velocity trend than in Fig. 3.7(b). Despite the large differences between the CMP gathers

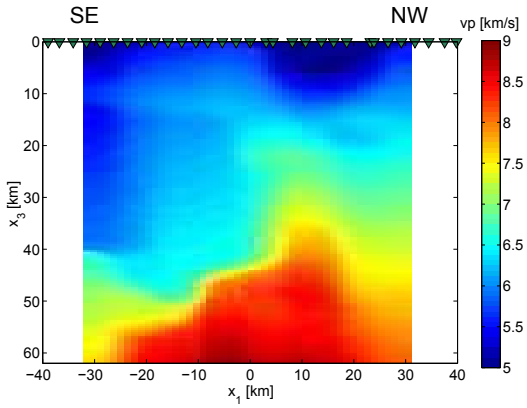


Figure 3.8 *Estimated velocity model of the lithosphere below the Laramie array*

and the semblances in Fig. 3.7(b) and 3.7(d), the NMO stacks are still quite similar, since in Fig. 3.7(d) especially noise has been removed that does not show up in the stack.

We repeat the semblance velocity analysis as in Fig. 3.7 for all CMP gathers with sufficient fold. Next, we compute the interval velocities from the estimated root-mean-square velocities (Dix, 1955). The resulting 1D velocity profiles are concatenated and smoothed with a median filter. Since reflections from shallow reflectors could only be retrieved at a limited offset, the CMP gathers cannot be used to reliably estimate the velocities in the upper crust ($x_3 = [0, 10]$ km). Fig. 3.C.1 depicts the near-surface velocity functions, as were estimated in the decomposition process (Appendix 3.C). The velocities are an average of the local velocities right under the receivers and are used as an estimate for the velocities in the upper 10 km. The combined velocity model, derived from the decomposition ($x_3 <= 10$km) and the semblance analysis ($x_3 > 10$ km) is depicted in Fig 3.8.

The CMP gathers close to the first and the last receiver are discarded due to limited fold. All other CMP gathers are NMO corrected and stacked to obtain pseudo zero-offset data. These are the responses as if there were coinciding receivers and sources at the free surface. In Fig. 3.9 the pseudo zero-offset data are depicted for the synthetic data (a) and the field data (b). The pseudo zero-offset data are consecutively post-stack Kirchhoff time migrated (Bleistein, 1999) and time-to-depth converted to obtain reflectivity images as a function of depth (Fig. 3.9(c) and (d)). For the latter two steps, the data-derived velocity model (Fig. 3.8) is used for the field data. For the synthetic data, the velocity model as depicted in Fig. 3.4(b) is used.

Comparing the final image obtained from the synthetic data in Fig. 3.9(c) with the model in Fig. 3.4(b), it can be seen that all interfaces are imaged at the correct depth, despite the limited and irregular illumination and despite the SSR. Additionally, below 55 km depth, multiples have caused spurious interfaces. The image obtained from the field data (Fig.

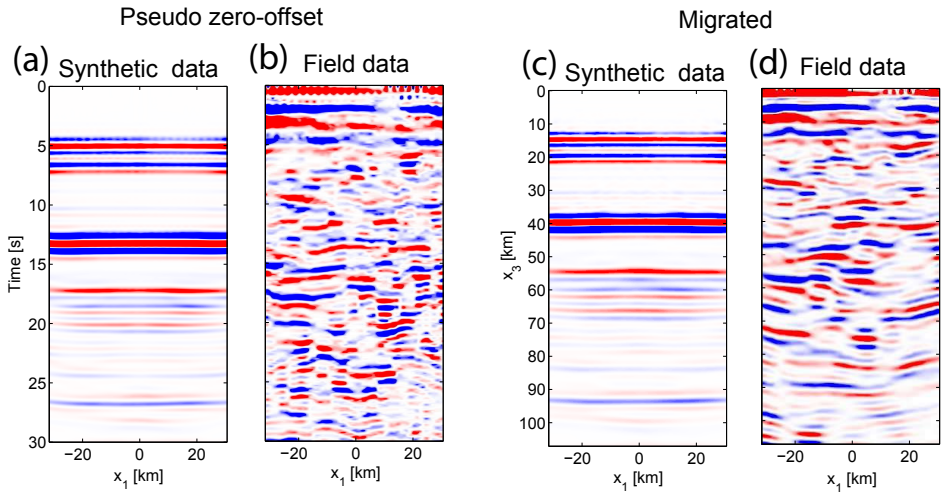


Figure 3.9 *Pseudo zero-offset data for (a) the synthetic data and (b) the field data. Post-stack migrated and time-to-depth converted images for (c) the synthetic data and (d) the field data. The horizontal axis is labeled with the inline position with respect to the middle receiver, which position is negative for receivers at the SE side and positive for receivers at the NW side. In (a) and (b) the vertical coordinate denotes two-way travel time.*

3.9(d)) might similarly be affected by multiples at larger depths. Moreover, the migration leads to finite aperture artifacts at depths larger than the length of the array. To limit both possible reasons for misinterpretation, the image is restricted to 64 km depth. Fig. 3.10 displays this restricted image with the same scaling on both axes and a cropping of the stronger amplitudes (in the near surface). In Appendix 3.E it is shown that the shallow reflectors in this image are consistently found for varying amounts of phase responses. The deeper reflectors, though, only become visible when a large number of phase responses is used. Only for a large amount of phase responses, the spurious events caused by SSR are sufficiently suppressed.

Fig. 3.10 shows a layered upper crust on top of a highly fragmented lower crust. A striking feature in the upper crust is a reduced reflectivity, near $x_1 \approx 10$ km. This zone of lower reflectivity likely continues through abrupt discontinuities in the lower crust and upper mantle, as highlighted by the gray shading. The position where this zone hits the surface is very close to where the Cheyenne Belt is expected from observations in the field (Hansen & Dueker, 2009). Thus, the gray shading in Fig. 3.10 is interpreted as the suture zone between Archean and Proterozoic terranes, on the NW and SE side, respectively. Consistent with an interpretation from Karlstrom & Humphreys (1998), the Proterozoic terrane is the upper plate. Because reflections from this zone have $|p| > 0.08$ s/km, this fault zone is not directly imaged with our limited illumination (Fig. 3.4(a)). As the Moho depth in the area is expected at $\approx 40km$ depth (Chulick & Mooney, 2002), we interpret the undulating

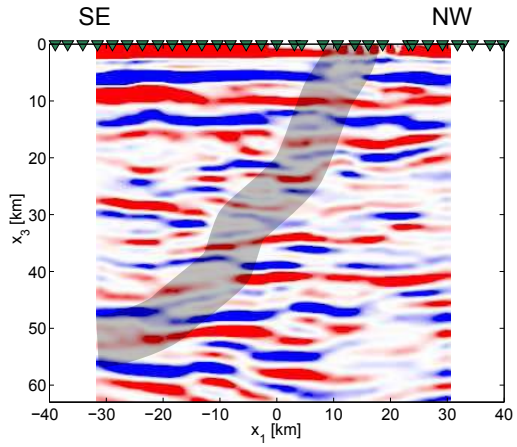


Figure 3.10 *The reflectivity image of the subsurface below the Laramie array, obtained by seismic interferometry. A blue-red-blue alternation may be interpreted as an interface with an increase in velocity with depth. An interpretation of the Cheyenne Belt is denoted by the dipping gray zone.*

feature at 42 km depth as the Moho. This Moho starts abruptly NW of the suture zone and is therefore interpreted to be Archean. Below 42 km still a chaotic distribution of apparent interfaces can be seen. A part of these might be caused by free-surface multiples from strong reflectors in the upper crust. A part of the features below 42 km might also be explained by underthrusting Proterozoic lower crust, as in Hansen & Dueker (2009).

Comparing Fig. 3.10 with the RF images from Hansen & Dueker (2009), similar large features are noticeable, but clearly SI leads to a higher-resolution image. Especially within the crust, much more detail can be seen in the SI image. E.g., the interface at 28 km depth between $x_1 \approx [-32, -12]$ km cannot be seen in the RF images. Moreover, with SI, the interfaces might have been migrated to a more accurate position, since a data-derived velocity model was used.

The final SI image may still be improved by pre-stack depth migration rather than post-stack time migration and by using a more advanced multiple-elimination scheme (Verschuur, 2006), although multiple removal on land is a notoriously difficult problem that requires dense sampling.

3.6 Conclusions

We studied the retrieval of reflections between the receivers of a regional array of broadband stations using seismic interferometry. Seismic interferometry consists of correlations of observations at different receiver locations, followed by an integration of the correlation

results. It is necessary to record enough effective sources from actual earthquakes to adequately sample this integral. For this reason, we used P phases complemented by PP, PcP and PKP, where the latter three phases are used to fill up the gaps in the illumination of the P phases. We showed first that a few months of data suffice to select an adequate distribution of phase responses, at least when the array is approximately in-plane with an earthquake belt. The irregularity of the phase distribution introduces over- and under-illumination artifacts to the retrieved responses. We showed that these artifacts can be suppressed by weighing the contributions to the integrand with the distances between the effective sources. When, in addition, the influence of source-side reverberations is taken into account, the weighing strategy turns out to degrade the retrieved response. We showed that, for this case, a better reflection response can be obtained when contributions from effective sources with either positive or negative rayparameters are time-reversed prior to integration. Using velocity analysis and seismic migration we further turned the retrieved body-wave responses into a reflectivity image. A high-resolution image was obtained from the lithosphere below the Laramie array with similar features as interpreted by other researchers from receiver-function images. Especially at larger depths, ghost interfaces caused by multiples were still present in the image. On the reflectivity image, we could track the Cheyenne Belt, a suture zone between Archean and Proterozoic terranes.

3.A Sampling

In this appendix we derive a sampling criterion for the 2D integral representations (3.1), (3.2) and (3.3). First, we argue that a sufficient source sampling is important. Then, we compute the Jacobians for the change in integration variables. Thereafter, we derive a sampling criterion in dp and use the Jacobians to find sampling criteria expressed in $d\phi$ and dx. Finally, we consider the required earthquake distribution for retrieving lithospheric reflections below the Laramie array.

For this analysis, we exploit the fact that the reference velocity model for the Earth is known. For this reason, we do not need to consider the complete Earth as an unknown heterogeneous medium (Fig. 3.1(a)), but we can directly focus on our medium of interest, the lithosphere below an array of receivers. By raytracing through the reference model, different phases induced by teleseismic and global earthquakes can be represented as individual sources on a large semisphere surrounding the lithosphere on the receiver side ($\partial\mathbb{S}_1$ in Fig. 3.A.1 and in equations (3.1) and (3.2)). It would be ideal for the application of seismic interferometry (SI) if the lithosphere consisted of a distribution of point scatterers as in the experiment by Derode et al. (2003b) or was bounded at the lower side by a highly scattering slab, as in the experiments by Derode et al. (2003a). In either case, illumination with a few sources from different directions would suffice to retrieve a Green's function between two station positions placed in or upon the lithosphere. This is because the illumination of a single phase with a very narrow rayparameter band is, by multiple scattering, increased to a broad and well-sampled rayparameter band, that represents the line integral in equation (3.1) or (3.2). Though there might be multiple scattering from point scatterers, especially in the crust, a more conventional depiction of the convergence zone and lithosphere is that of an approximately spherically layered medium. For a 1D layered medium, there are no scatterers (Huygens sources) adding rayparameters to the transmission responses. Therefore, the source surface $\partial\mathbb{S}_1$ (Fig. 3.A.1) needs to be sufficiently covered with effective sources. $\partial\mathbb{S}_1$ may have an arbitrary shape as long as it represents a sufficient illumination aperture.

The distance between a source $\mathbf{x}_i$ and its neighboring source $\mathbf{x}_{i+1}$ on $\partial\mathbb{S}_1$ is $dx = |\mathbf{x}_i - \mathbf{x}_{i+1}|$. The same separation can be expressed in source angle as $d\phi = |\phi_i - \phi_{i+1}|$ or in rayparameter as $dp = |p_i - p_{i+1}|$. For finding the relation between dx, $d\phi$ and dp, we compute the Jacobians for a change of integration from (x_1, x_3) to (r, ϕ):

$$J_1 = \left|\frac{\partial(x_1, x_3)}{\partial(r, \phi)}\right| = r, \tag{3.A.1}$$

and using that $p = sin\phi/v_p$, for a change of integration from (r, ϕ) to (r, p):

$$J_2 = \left|\frac{\partial(r, \phi)}{\partial(r, p)}\right| = \partial_p\phi = \frac{v_p}{\sqrt{1 - v_p^2 p^2}}. \tag{3.A.2}$$

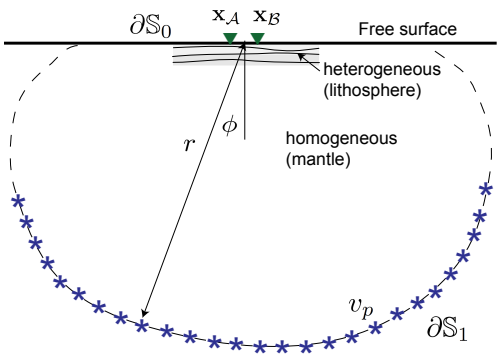


Figure 3.A.1 *An effective configuration for lithospheric-scale SI. A medium with receivers (triangles) on the free surface is illuminated from below with a distribution of sources, of which the location is given in polar coordinates* (r, ϕ).

Hence, for sources on the line $\partial\mathbb{S}_1$ we find:

$$dx = rd\phi = \frac{rv_p}{\sqrt{1 - v_p^2 p^2}} dp. \tag{3.A.3}$$

The retrieval of arrivals between two receiver positions is achieved by the crosscorrelation and stacking of arrivals in the transmission responses with similar raypaths. When raypaths coincide, the derivative of the phase with respect to the source coordinate is stationary. In the stationary-phase region (the Fresnel zone around the stationary phase) we only need limited sampling. Outside this region, though, the derivative with respect to the source coordinate increases (see Appendix 3.D). The sampling of the sources needs to be such that the non-stationary contributions interfere destructively. This destructive interference will happen when, after crosscorrelation, the time difference between a contribution from two neighboring sources is smaller than half the minimum period:

$$dt < \frac{1}{2f_{max}}. \tag{3.A.4}$$

A transmission response contains many different arrivals, of which the direct wave (^{dw}) and ghost reflections (^{gh}) are the most relevant for body-wave SI. Two direct waves between source $\mathbf{x}_i$ and receivers $\mathbf{x}_\mathcal{A}$ and $\mathbf{x}_\mathcal{B}$ can be described with their rayparameters, $p^{dw}_{\mathcal{A},i}$ and $p^{dw}_{\mathcal{B},i}$ (Fig. 3.A.2(left)). Similarly, two ghost reflections between source $\mathbf{x}_i$ and receivers $\mathbf{x}_\mathcal{A}$ and $\mathbf{x}_\mathcal{B}$ can be described as $p^{gh}_{\mathcal{A},i}$ and $p^{gh}_{\mathcal{B},i}$ (Fig. 3.A.2(right)). If we choose the distance to the source r (Fig. 3.A.1 and 3.A.2) much larger than the length of the array, the wavefield near the array will be planar. Hence, $p^{dw}_{\mathcal{A},i} = p^{dw}_{\mathcal{B},i}$. If we consider a layered subsurface and large r, also $p^{gh}_{\mathcal{A},i} = p^{gh}_{\mathcal{B},i}$. Moreover, if we only consider horizontal interfaces near the array, all

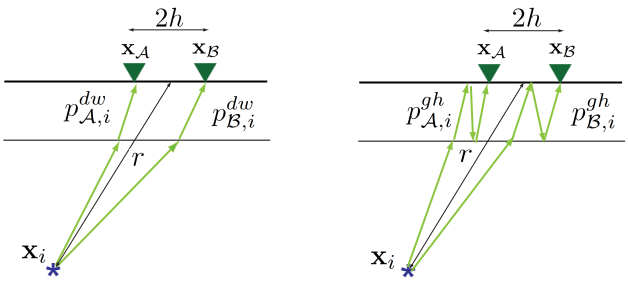


Figure 3.A.2 *The raypaths for two direct waves (left) and two ghost reflections (right)*

arrivals will have the same rayparameter:

$$p_i = p^{dw}_{\mathcal{A},i} = p^{dw}_{\mathcal{B},i} = p^{gh}_{\mathcal{A},i} = p^{gh}_{\mathcal{B},i}. \tag{3.A.5}$$

Hence, when equation 3.A.5 holds, the time difference of the wavefield caused by source $\mathbf{x}_i$, hitting upon receiver $\mathbf{x}_\mathcal{A}$ and $\mathbf{x}_\mathcal{B}$ can be expressed as

$$dt_i = \frac{2hsin(\phi_i)}{v_p} = 2hp_i, \tag{3.A.6}$$

where h is the half offset ($h = |\mathbf{x}_\mathcal{A} - \mathbf{x}_\mathcal{B}|/2$), ϕ_i is the angle of the ray with the normal, at the source, and v_p is the velocity of the medium, at the source position. After crosscorrelation, the time difference for two neighboring sources, $\mathbf{x}_i$ and $\mathbf{x}_{i+1}$, is:

$$dt = |dt_i - dt_{i+1}|. \tag{3.A.7}$$

When we combine relations (3.A.4), (3.A.6) and (3.A.7) we find the sampling criterion expressed in rayparameter:

$$dp < \frac{1}{4f_{max}h_{max}}, \tag{3.A.8}$$

where h_{max} is the maximum half offset of interest.

Combining relation (3.A.8) with (3.A.3) and taking $p_{min} = 0$ s/km, we find a sampling criterion expression in $d\phi$

$$d\phi < \frac{v_p}{4f_{max}h_{max}} \tag{3.A.9}$$

and a sampling criterion expressed in dx:

$$dx < \frac{r_{min}v_p}{4f_{max}h_{max}}. \tag{3.A.10}$$

In both expressions (3.A.9) and (3.A.10), the sampling is now also a function of the velocity of the medium in which the sources are, and the rayparameter. The higher the v_p, the larger the sampling in $d\phi$ and dx may be. Furthermore, expression (3.A.10) is also a function of

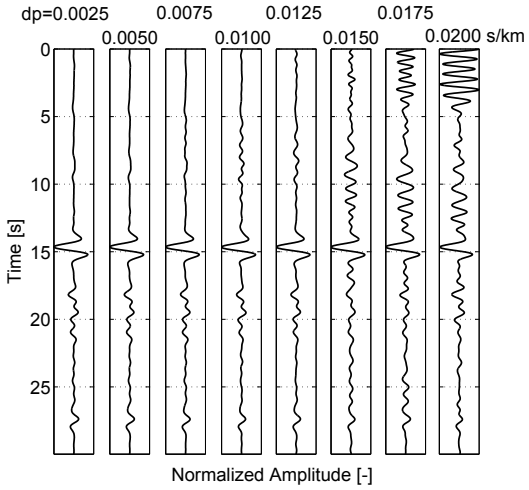


Figure 3.A.3 *The result after applying SI to synthetic transmission responses, for obtaining a virtual source and a receiver at a distance of 40 km. From left to right, the rayparameter spacing of the transmission responses is increased from $dp = 0.0025$ to $dp = 0.0200$ s/km.*

the minimum radius, which radius would be constant if $\partial\mathbb{S}_1$ was a semicircle. The larger the minimum radius, the larger the sampling in dx may be.

For an application of SI for lithospheric-scale imaging, using teleseismic and global phases, the approximations for deriving condition (3.A.8) are largely satisfied. When we take $h_{max} = 20$ km (the half offset between a virtual source at the middle receiver of the Laramie array and a receiver a the edge of the array) and take $f_{max} = 1.5$ Hz, we find $dp = 0.0083$ s/km.

We test the derived sampling condition on synthetic data. As in section 3.4, we use the simplified lithospheric model (Fig. 3.4(b)) to synthesize transmission responses with varying dp. Fig. 3.A.3 shows the results after applying SI for obtaining a virtual source at the middle receiver and a receiver at the edge of the array ($h_{max} = 20$ km). For $dp = 0.0025$, $dp = 0.0050$ and $dp = 0.0075$ s/km the retrieved results are almost identical. From $dp = 0.0100$ s/km onwards undersampling artefacts start to occur, which become more pronounced for larger spacings in dp.

By raytracing through the PREM model (Knapmeyer, 2004) we map the source sampling of $dp = 0.0083$ s/km to actual earthquake positions (Fig. 3.A.4). Only illumination from one side is shown, since this would be sufficient for imaging an approximately layered lithosphere. In reality, illumination from both sides would be combined to reach a better sampling and to increase the signal-to-noise ratio. If high quality data could be recorded and the source-time functions were very transient, data from less than 11 earthquakes would

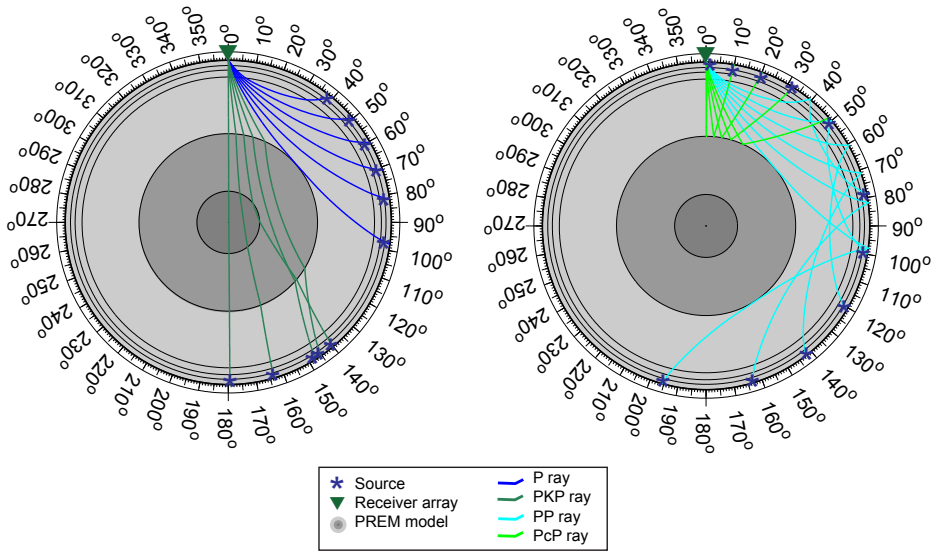


Figure 3.A.4 *The source sampling required for lithospheric-scale SI, raytraced to a distribution of earthquakes at regional, teleseismic and global distances. The minimum distribution for P and PKP phases (left) and for PP and PcP phases (right).*

be sufficient to retrieve a multidimensional reflection response. The required sampling and a sufficient illumination can be reached with P and PKP (Fig. 3.A.4(left)) or with PP and PcP (Fig. 3.A.4(right)), or with a combination of all these phases. For P and PcP phases, the maximum source spacing maps to a maximum allowed earthquake spacing of about 1000 km or Δ=10°. For PP phases, the maximum earthquake spacing is about 20°. For PKP phases, the required source spacing for the actual earthquakes can be seen to be highly variable as function of epicentral distance.

3.B Fresnel zone

For a linear array and a subsurface with small lateral variations, a 3D seismic-interferometry relation may be reduced to a 2D version (equation 3.4). For this 2D version, the integration is over sources that lay in a vertical plane through the receiver positions (Fig. 3.3(a)). In practice, the source locations may be located outside this plane, as long as their contributions to the integral are in phase with the contribution from sources in the plane. To find the region of acceptable source locations, we compute a proxy for the first Fresnel zone (Spetzler & Snieder, 2004), considering a response retrieval between station $\mathbf{x}_{\mathcal{A}}$ and $\mathbf{x}_{\mathcal{B}}$:

$$dt(\Delta,\theta) = dt_{\mathcal{AB}}(\Delta,\theta=0) - dt_{\mathcal{AB}}(\Delta,\theta) < \frac{1}{2f_{max}}, \tag{3.B.1}$$

where θ is the azimuth between the source and the array and f_{max} is the maximum frequency in the data. Here we assume a laterally invariant medium. Hence, all stationary phases must be located in the plane described by $(\Delta, \theta = 0)$. $dt_{\mathcal{AB}} = t^{gh}_{\mathcal{B}} - t^{dw}_{\mathcal{A}}$ is the travel-time difference of a ghost reflection traveling from the source to receiver $\mathbf{x}_{\mathcal{B}}$ and a direct wave traveling from the source to receiver $\mathbf{x}_{\mathcal{A}}$. When ghost reflections are considered from reflectors which are much closer to the receiver array than to the sources, the following approximation may be used:

$$t^{gh}_{\mathcal{B}}(\Delta, \theta = 0) - t^{gh}_{\mathcal{B}}(\Delta, \theta) \approx t^{dw}_{\mathcal{B}}(\Delta, \theta = 0) - t^{dw}_{\mathcal{B}}(\Delta, \theta). \tag{3.B.2}$$

Using approximation (3.B.2), condition 3.B.1 is simplified to

$$dt(\Delta, \theta) = t^{dw}_{\mathcal{B}}(\Delta, \theta = 0) - t^{dw}_{\mathcal{A}}(\Delta, \theta = 0) - (t^{dw}_{\mathcal{B}}(\Delta, \theta) - t^{dw}_{\mathcal{A}}(\Delta, \theta)) < \frac{1}{2f_{max}}. \tag{3.B.3}$$

Since we only consider responses due to distant sources we may use equation 3.A.6, with an additional $\cos(\theta)$ term to express the azimuthal dependence:

$$t^{dw}_{\mathcal{B}}(\Delta, \theta) - t^{dw}_{\mathcal{A}}(\Delta, \theta) = 2hpcos(\theta). \tag{3.B.4}$$

Combining equations 3.B.4 and 3.B.3, we find

$$(1 - cos(\theta))2hp < \frac{1}{2f_{max}}. \tag{3.B.5}$$

Thus, we can express the width of the Fresnel zone in azimuth as:

$$\theta_{FZ} < 2 \arccos(1 - \frac{1}{4h_{max}pf_{max}}). \tag{3.B.6}$$

Fig. 3.B.1 depicts the azimuthal extent of the Fresnel zone as a function of epicentral distance, for the four different phases considered in this chapter. These graphs are found by first computing the relationship between p and Δ through raytracing (Fig. 3.1(c)) and subsequently using relation 3.B.5, with for h_{max}=20 km and f_{max}=1.5 Hz. It is clear that the extent of the Fresnel Zone is highly dependent on the phase of consideration. E.g., the Fresnel zone for the PcP is very large, due to the small rayparameters involved, whereas for the P phase we may only include phases in a restricted azimuthal band.

In Fig. 3.3(b) the extent of the Fresnel zone for $h_{max} = 20$ km is plotted, on a global projection. Here only the direct-wave phases, P and PKP, are considered. The traveltime differences are computed using relation 3.B.3 and the resulting Fresnel zone is plotted in green. Dark green are locations for which the time difference is close to zero. Light green are locations for which the time difference is close to the threshold value (i.e., the right-hand side of relation 3.B.3). The function is evaluated for all source-array azimuths ($\theta = [0, 360°]$) and $\Delta = [0, 98°]$ for the P phase and $\Delta = [117, 180°]$ for the PKP phase. The travel-time differences are computed by raytracing through the PREM model. When P or PKP is triplicated, the fastest arrival time is taken.

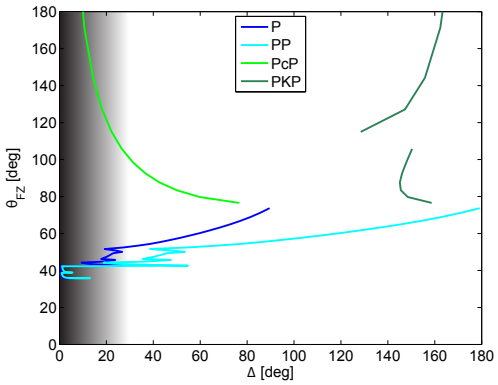


Figure 3.B.1 *Extent of the Fresnel zone expressed in source-to-array azimuth (θ_{FZ}) as a function of epicentral distance (Δ) for four different P-wave phases. The gray shading depicts the distance range in which the approximations made for computing θ_{FZ} are increasingly invalid.*

3.C Decomposition and estimation of the near-surface velocities

In order to apply acoustic SI relations (equation 3.4 and 3.7), we need to find the compressional-wave component u_p from the recorded data. The data is recorded as $\mathbf{u}_m = (u_Z, u_N, u_E)$ (particle velocity in the vertical, North and East directions). After rotation, the responses are composed as $\mathbf{u}_s = (u_Z, u_R, u_T)$ (vertical, radial and transverse directions). In this appendix, the last step is described, i.e., the decomposition into $\mathbf{u}_w = (u_P, u_{SV}, u_{SH})$ (compressional, shear inline and shear crossline).

The decomposition is performed by applying the inverse free-surface transfer matrix (Kennett, 1991), with which $\mathbf{u}_w$ is expressed as function of $\mathbf{u}_s$, p, v_p^{ns} and v_s^{ns}. The last two variables, the near-surface compressional- and shear-wave velocity are initially unknown, but can be computed from the same decomposition relations, with two additional conditions and when assuming a 1D and isotropic crust:

1. The decomposition should give maximum amplitude on u_P and minimum amplitude on the other components for a P-wave arrival.
2. The decomposition should give maximum amplitude on u_{SV} and minimum on the other components for an SV-wave arrival.

Hence, as derived in Bostock & Rondenay (1999), the near-surface velocities can be expressed as functions of the p, the amplitude ratio u_R/u_Z for an incoming P-wave and the amplitude ratio u_R/u_Z for an incoming SV-wave. For estimating v_s^{ns}, clean teleseismic P-wave arrivals are required. For estimating v_p^{ns}, additionally clean teleseismic S-wave arrivals are required.

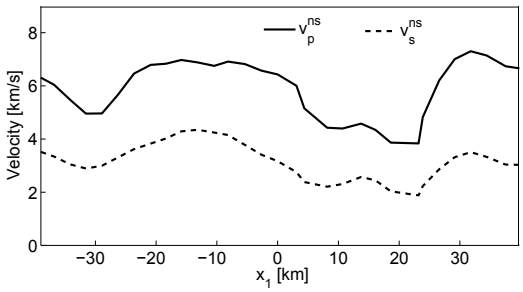


Figure 3.C.1 *Estimated velocity model of the near surface.*

For five earthquakes, we estimated the v_s^{ns} values per station and subsequently averaged and smoothed the found values. For estimating v_p^{ns}, additionally two S-wave arrivals were used. Fig. 3.C.1 depicts the resulting near-surface velocity functions. The presence of a sedimentary basin ($x_1 = [3, 25]$ km) can easily be distinguished from hard-rock sites.

In Fig. 3.C.2, the u_Z and u_R components (dashed black) are shown at two receiver positions, for a time-window around a P-phase arrival. Also, the results after decomposition, u_P and u_S, are shown in red. All used phase responses have relatively small incidence angles. Thus, generally, u_P is almost identical to u_Z, apart from the free surface amplification factor. The amplitudes on u_R and u_{SV} (conversions) are small with respect to the amplitudes on u_Z and u_P. The SV-wave component can be extracted quite well for a receiver at a hard-rock (Fig. 3.C.2(left)), but u_{SV} remains polluted with near-surface scattering at a station on the sedimentary basin (Fig. 3.C.2(right)). This is already a clear indication that the subsurface is not horizontally layered below these stations, which is a condition for the used decomposition relations. Because of the large contamination on u_{SV}, applying a RF analysis would be a big challenge for a significant part of this dataset. For P-wave interferometry, on the other hand, just using the Z-component might already give good results.

3.D Correlation panels

In this appendix, the integrands (correlation panels) of equation (3.4) and (3.7) are studied. This helps in understanding the modeling results as shown in Section 3.4. For the model as depicted in Fig. 3.4(b), transmission responses are modeled with the same rayparameter distribution as the Laramie phase distribution (Fig. 3.4(a)). The transmission responses are recorded by 31 receivers on the free surface. Subsequently, these transmission responses are used to estimate a retrieved response between receivers 16 and 8. Fig. 3.D.1 shows nine estimations of this response, for three different SI approaches (from left to right) and for 3 different datasets (from top to bottom). For each estimation, the different steps involved, are shown:

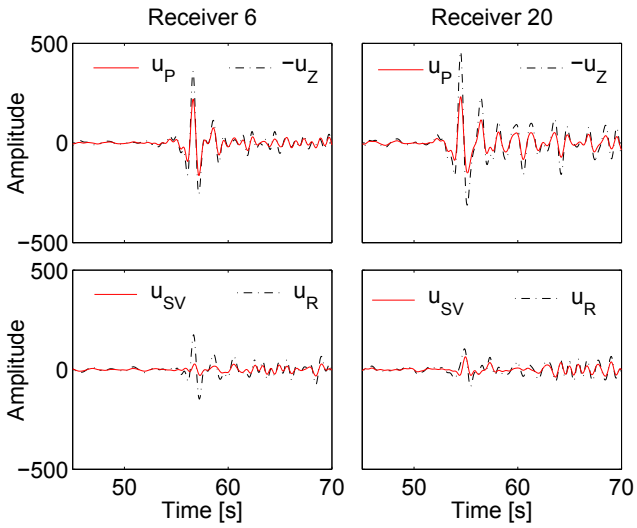


Figure 3.C.2 *Particle velocity registration before (u_Z, u_R) and after (u_P, u_{SV}) decomposition for receiver 6 (left) and 20 (right). A time-window is shown which contains a P-phase arrival with $p = 0.057$ s/km.*

1. A crosscorrelation of the transmission responses recorded at receivers 16 and 8. The crosscorrelation result is shown as a function of rayparameter (source position). With this visualization, the irregularity of the source distribution can easily be seen.

2. The result from integration over source positions. This boils down to stacking of the traces displayed in step 1, over rayparameter. For equation (3.7) (right panels) all the physical contributions are expected at positive times, thus the stacking result at negative times is muted.

3. For equation (3.4) (left and middle panels) also a third step is shown, which is an addition of the time-reversed acausal stack to the causal stack. For a perfect source distribution, this step may be left out, since the time-reversed acausal stack would be identical to the causal stack. For a biased irregular source distribution, the causal stack might be much more similar to the reflection response than the acausal stack, or vice versa. In this case, a better estimate is obtained when only one of the two is selected. For a more general irregular source distribution, as we have, the signal-to-noise ratio is improved by the addition of the time-reversed acausal stack to the causal stack.

Equation (3.4) is applied without (left panels) and with trace weighing (middle panels), based on Δp. In Fig. 3.D.1(right) no trace weighing is applied and contributions from negative p's are time-reversed prior to stacking. Due to limited illumination, the complete

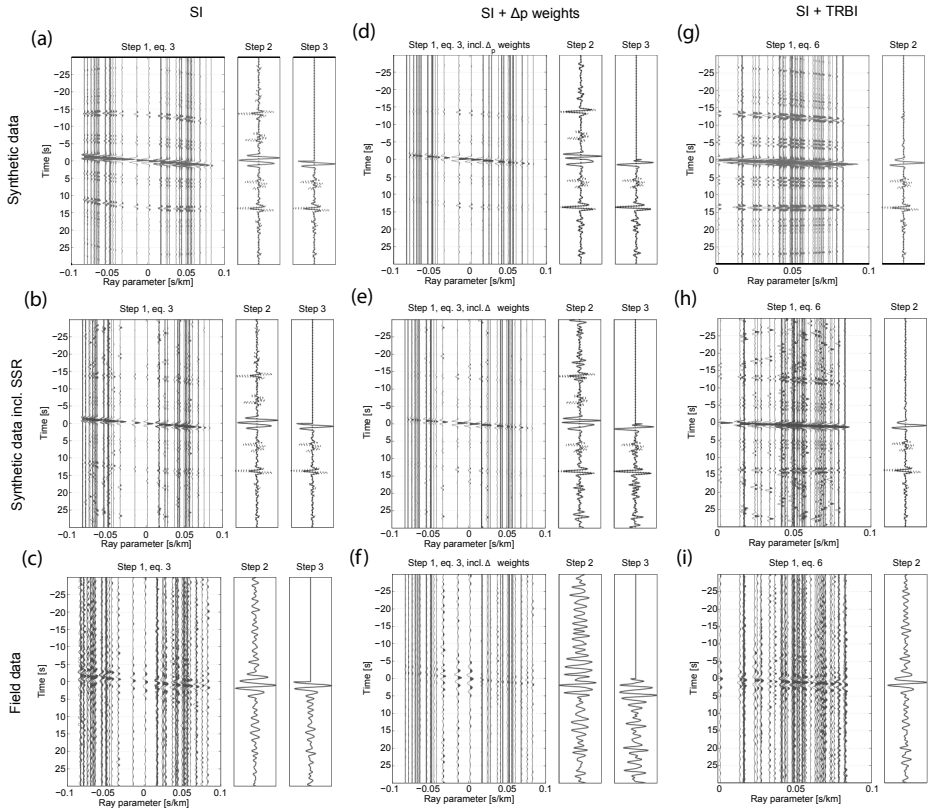


Figure 3.D.1 *Visualization of the integrand (correlation panel) and integral (stack) of the seismic interferometric relations for $\mathbf{x}_A$ and $\mathbf{x}_B$ at station 16 and 8, respectively, for synthetic data (upper and middle panels) and the field data (lower panels). In the integrand displays, the traces are ordered as function of rayparameter. For the synthetic data, in step 2 and 3, a reference response is shown as a black dotted line. In (a)-(c) no adjustment is made for the irregular source distribution, in (d)-(f) every trace is weighted by its distance to the neighboring traces and for (g)-(i) the traces caused by effective sources with negative rayparameters are time-reversed and displayed at positive rayparameter. (a), (d) and (g) are for isolated P-phase responses, whereas (b), (e) and (h) are for direct wave responses 'polluted' with two source-side reverberations (e.g. pP and sP) and (c), (f) and (i) are for the Laramie data from the field.*

integral in equation (3.4) cannot be evaluated. In step 2 and 3 the retrieved response (solid red) is, where possible, compared with a reference reflection response (dotted black). In step 1 the largest feature is the event around $t = 0$ s, which is due to a crosscorrelation of direct waves. The crosscorrelation of direct waves would lead to the retrieval of a direct wave if we had sufficient illumination. Since we lack illumination by high rayparameters the event around $t = 0$ s does not include a stationary-phase region (Fresnel zone around $\partial_p \phi = 0$, where ϕ is the phase of an event and ∂_p denotes the derivative with respect to the rayparameter) and the only thing we are left with after stacking (step 2) are the spurious edge effects. The first two reflections (step 2 and 3) are retrieved with lower amplitude because only part of their stationary-phase region is covered and it is only sparsely sampled (check the events with corresponding times in step 1). The third reflection (Moho reflection) is generally retrieved well, but with a too low amplitude. To perfectly retrieve this Moho reflection at this offset (21 km), the illumination range would need to be extended to $p \approx 0.010$ s/km. Reflections and multiples at times later than the primary Moho reflection are almost perfectly retrieved. Their stationary-phase region is located in the teleseismic rayparameter-range and is therefore well sampled.

First, we consider the application of SI to synthetic single-phase responses (Fig. 3.D.1 top panels). For all the different SI approaches, the kinematic retrieval is comparable, but with trace weighing (Fig. 3.D.1(d)) the dynamic retrieval is clearly the best, at least for the events for which a large part of the stationary-phase region was captured (events at times later than 10 s).

Second, we consider the application of SI to single-phase responses, polluted with two source-side reverberations (middle panels). In all correlation panels, the addition of spurious cross terms (equation 3.10) can clearly be seen. In Fig. 3.D.1(b) and (h), these cross-terms are suppressed quite successfully. In Fig. 3.D.1(e), these cross terms are not suppressed well; large deviations from the reference response can be noticed on the stack, e.g. at $t = 26$ s. This happens because some cross terms are boosted due to the weighs applied.

Third, we consider the application of SI to phase responses detected at the Laramie array (lower panels). For the field data, it is much harder to distinguish events in the correlation panels (step 1). The actual subsurface is much more complicated than the model used for the synthetic data (Fig. 3.4(b)). Only the event caused by the crosscorrelation of direct waves can clearly be seen in Fig. 3.D.1(c), (f) and (i). If this is not a clear linear event, errors were introduced during the preprocessing (e.g., a phase was misinterpreted). Of course it is not possible to compare the retrieved results (step 2 and step 3) with a reference response. Still it is clear that trace weighing (Fig. 3.D.1(f)) similarly as in Fig. 3.D.1(e), deteriorates the retrieval. Even more so for the field data, because trace weighing prejudices contributions from PKP phases here. PKP contains lower frequencies and more source-side reverberations than P, because it has seen more interfaces before it emerges on the lithosphere from below.

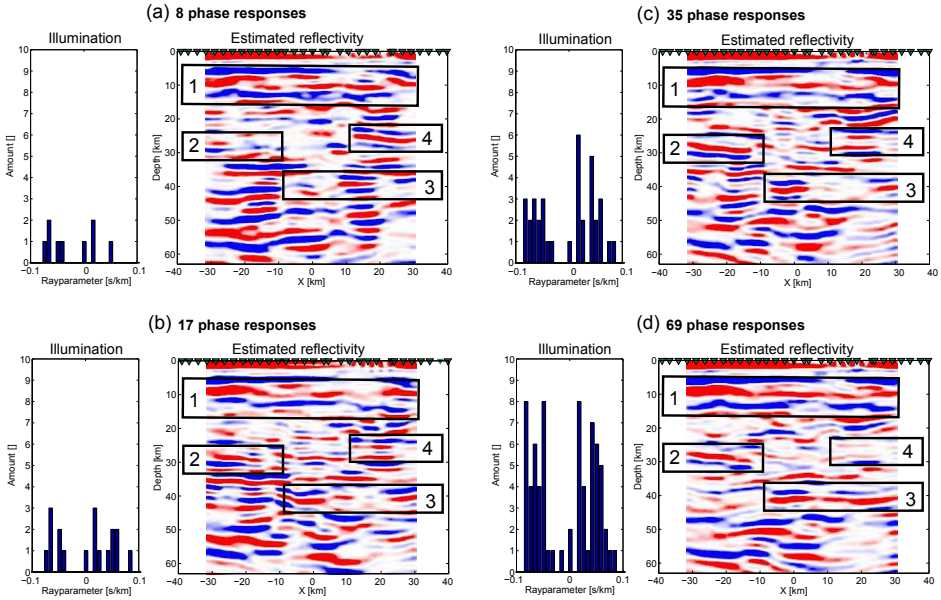


Figure 3.E.1 *In each subfigure (left) the rayparameter distrubution of a subset of phase responses and (right) the resulting image using only this subset of phase responses. The images are obtained using (a) 8, (b) 17, (c) 35 and (d) 69 phase responses.*

3.E Imaging stability

In this appendix, we test how consistently different reflectors are imaged when varying subsets of phase responses are used. For the illumination range we consider in this chapter (p=[-0.08,0.08] s/km) and the required sampling of $dp = 0.0083$ s/km (Appendix 3.A), a regular sampling of 21 clean phase responses would suffice to retrieve good-quality reflection responses. However, for an irregular illumination with phase responses polluted with source-side reverberations (SSR), many more phase responses are required. In section 3.4 it was shown that with 69 phase responses, the spurious contributions from SSR are significantly suppressed.

In the left-hand side of Fig. 3.E.1 subsets of the available phase responses are shown as rayparameter distributions. The subsets contain, from top to bottom, one-eighth, one-fourth, one-half and all of the available phase responses, respectively. The resulting images, for the different subsets, are shown on the right-hand side.

The shallow reflectors (see box 1 in Fig. 3.E.1) are consistently imaged for a varying amount of phase responses. Hence, the upper image (Fig. 3.E.1(a)) is already a good estimation of the shallow reflectivity, despite the fact that less phase responses are used than what the sampling condition prescribes. This is consistent with results from Draganov et al. (2006) and can be explained by the non-hyperbolic shape of undersampling artifacts. Due to this shape,

the sampling artifacts are largely suppressed by the migration process. The reflectivity at larger depths, though, is heavily distorted by spurious reflectors which result from SSR. Spurious events due to SSR exhibit hyperbolic move-out in the shotgather and common-midpoint domain and are thus not suppressed by the migration. Since the contributions that result from SSR do not decay with depth, whereas actual reflections do, the distortions become more pronounced for larger depths. This explains why the shallow reflectors (see box 1 in Fig. 3.E.1) are consistent with a varying amount of phase responses, whereas deeper reflectors (box 2 and 3 in Fig 3.E.1) only reveal themselves when larger numbers of phase responses are used, such that cross terms due to SSR (equation 3.10) are increasingly suppressed. An example of the spurious contributions are highlighted in box 4. The apparent reflector in (a) changes phase in (b) and (c) and almost completely disappears in (d). Considering that still quite some spurious amplitudes disappear when we use 69 (Fig 3.E.1(d)) instead of 35 (Fig 3.E.1(c)) phase responses, even more than 69 would be required to remove all spurious amplitudes.

Chapter 4

Lithospheric-scale seismic interferometry: single offset[1]

4.1 Introduction

A number of seismic methods exist to image the lithosphere below a collection of receivers, using distant earthquakes. Although both global and teleseismic phases could be used, in the current practice, especially teleseismic phases are utilized. In this manuscript we present a method that takes advantage of the availability of global phases.

Claerbout (1968) showed that the reflection response of a horizontally layered acoustic medium can be retrieved from the autocorrelation of a plane-wave transmission response. Later, his theory was generalized to arbitrarily heterogeneous media (Wapenaar, 2003; Derode et al., 2003a; Schuster et al., 2004) and to different wave and diffusion phenomena (Wapenaar et al., 2006; Snieder et al., 2007). Hence, nowadays we know how to retrieve P- and S-wave reflection responses between any two receivers at the Earth's surface. However, a wide distribution of earthquakes is required to achieve this (Abe et al. (2007); Tonegawa et al. (2009) & Section 2.4 & 3.A). This distribution does not always exist or it might take ages to detect. In this manuscript we propose a simple, but effective, alternative. We turn back to the original setting from Claerbout's paper and translate it to global-scale seismology. This new adaption we call Global-Phase Seismic Interferometry, which is abbreviated as GloPSI.

GloPSI can be applied on a single seismic station installed on a lithosphere of investigation. The P-wave reflection response is extracted by autocorrelating phase-responses. Considering the lithosphere is —grosso modo— horizontally layered, only incoming waves which impinge on the lithosphere near vertical incidence are needed. Thus, global phases, like $PKIKP$, are used. These global phases may be induced over a large area at the other

[1]This appendix has been published as a journal paper in *Geophysical Research Letters*, **39**, L11303, doi:10.1029/2012GL051672 (Ruigrok & Wapenaar, 2012). Note that minor changes have been introduced to make the text consistent with the other chapters of this thesis.

side of the globe. Due to the small angles of incidence, the source Fresnel zones for global phases are large. Consequently, the large area for which global phases exist only needs to be sparsely populated with seismicity. Another advantage of global phases is that the vertical-component record is already a good approximation of the P-wave transmission response. Consequently, the lower signal-to-noise of the horizontal components can be left out of the equation. For an array of receivers, the extracted reflection responses can be used to image the P-wave reflectivity of the lithosphere.

In the following we further explain GloPSI and apply it to data from the Hi-CLIMB experiment (2002-2005). This was a large and well-sampled seismic array, passing the Himalayas and a significant part of the Tibetan Plateau. For this array, images have been published, which were obtained by applying a wide suite of different geophysical techniques (Chen et al., 2010; Griffin et al., 2011; Hung et al., 2011; Nábělek et al., 2009; Nowack et al., 2010; Tseng et al., 2009; Xu et al., 2011). This enables benchmarking of the GloPSI results.

4.2 Global-phase seismic interferometry

Body waves from earthquakes at global distances travel through the mantle and core before they reach an array of seismic stations. Different stationary raypaths exist. Most prominent are PKP, $PKiKP$ and $PKIKP$, see Figure 4.1(a). When these waves reach the upper mantle below the array (Figure 4.1b) they are nearly planar. Direct waves are followed by reverberations in the lithosphere. The reverberations that hit one station, then (multiply) reflect on subsurface interfaces before reaching a receiver again, can be isolated with a technique called seismic interferometry. In the current application we only isolate reflections received by one and the same station $\mathbf{x}_{\mathcal{A}}$, see Figure 4.1(c). For a perfectly horizontally layered subsurface, illuminated with a plane wave, we could use the following relation (Claerbout, 1968; Wapenaar, 2003):

$$T(\mathbf{x}_{\mathcal{A}},\mathbf{p},-t) * T(\mathbf{x}_{\mathcal{A}},\mathbf{p},t) = -R(\mathbf{x}_{\mathcal{A}},\mathbf{p},-t) + \delta(t) - R(\mathbf{x}_{\mathcal{A}},\mathbf{p},t), \qquad (4.1)$$

where $T(\mathbf{x}_{\mathcal{A}},\mathbf{p},t)$ is the transmission response with $\mathbf{p}$=(p,θ), p is the absolute horizontal rayparameter, θ is the backazimuth, $R(\mathbf{x}_{\mathcal{A}},\mathbf{p},t)$ is the plane-wave reflection response, $\delta(t)$ is a delta pulse and $*$ denotes convolution. Thus the reflection response is obtained by autocorrelating the transmission response, selecting minus the causal result and muting the delta pulse.

In reality the lithosphere is not perfectly horizontally layered. Moreover, transmission responses are colored with source time functions $s_i(t)$, where $_i$ is a source index. Therefore

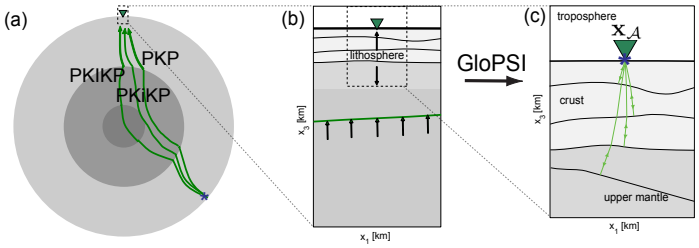


Figure 4.1 *(a) Raypaths (green lines) between a source (blue star) and a receiver (green triangle) for the most prominent global phases. Note that in reality not all 3 depicted phases exist for a given source-receiver distance (Fig. 2.10). (b) Enlargement of the medium below the receiver, with a global phase wavefront (green line) just before it impinges on the lithosphere. The application of Global-Phase seismic interferometry (GloPSI) results in (c), the zero-offset reflection response.*

we extend equation 4.1 to

$$\sum_{\theta_{min}}^{\theta_{max}} \sum_{p_{min}}^{p_{max}} T(\mathbf{x}_\mathcal{A}, \mathbf{p}, -t) * s_i(-t) * T(\mathbf{x}_\mathcal{A}, \mathbf{p}, t) * s_i(t) \propto$$
$$\{-R(\mathbf{x}_\mathcal{A}, \mathbf{x}_\mathcal{A}, -t) + \delta(t) - R(\mathbf{x}_\mathcal{A}, \mathbf{x}_\mathcal{A}, t)\} * S_n(t), \quad (4.2)$$

where $S_n(t)$ is the average of autocorrelations of the different source time functions. Thus, we repeat the autocorrelation for plane waves with varying illumination and stack the results. Through the autocorrelation both physical and spurious events are created. By stacking the correlations over an adequate illumination range the stationary events are enhanced (Snieder, 2004) while the spurious events, amongst others cross terms due to heterogeneities near the earthquake sources (expression 3.10), are suppressed. For global phases the raypa-rameter varies from p_{min}=0 to p_{max}=0.04 s/km. The backazimuth may range from θ_{min}=0 to θ_{max}=360°. This illumination range suffices to retrieve the zero-offset[2] reflection response $R(\mathbf{x}_\mathcal{A}, \mathbf{x}_\mathcal{A}, t)$ from horizontal and gently dipping interfaces. Nowack et al. (2006) applied autocorrelation, prior to migration, to only a single teleseismic phase and showed that still an acceptable image could be obtained in a setting with steeply dipping structure.

4.3 Data selection

We exemplify GloPSI with data from the Hi-CLIMB (Himalayan-Tibetan Continental Lithosphere During Mountain Building) experiment (2002-2005) (e.g., Nábělek et al., 2009; Nowack et al., 2010). A large array of stations was laid out to image a transect of the Indian-

[2]The zero-offset response is the response that would be measured if there were a coinciding source and receiver at the free surface

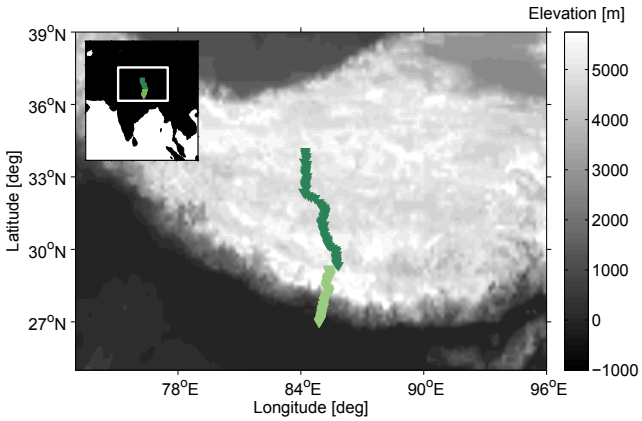


Figure 4.2 *Layout of the 2 selected subarrays from Hi-CLIMB, the Himalaya array (light-green triangles) and the Tibet array (dark-green triangles) plotted on top of an elevation map of the Tibetan Plateau.*

Eurasian Plate collision. Over the years, the array had a station distribution moving up from Northern India to Nepal and China. We select two approximately linear subarrays. Fig. 4.2 depicts the setting of the Tibet subarray (58 stations, denoted with dark-green triangles) and Himalaya subarray (61 stations, denoted with light-green triangles). The two subarrays were not simultaneously in the field. Consequently, we have two separate datasets. Below we describe the data selection for the Tibet array.

Figure 4.3(a) shows the area (light-gray shading) from which direct waves to the Hi-CLIMB subarray would travel through the core. We select 25 earthquakes with M>6 which are located within, or just outside, this area. For each earthquake we select a time-window that includes the first arrival and subsequent reverberations in the lithosphere. The first arrival is either $PKiKP$ or $PKIKP$ (see, e.g., Stein & Wysession (2003)). The upper bound of the time-window is limited by PP, which is not included due to its high rayparameter. This restriction leaves time-windows lasting between 150 and 350 s, depending on the great-circle distance.

Global phase responses may be rather complex due to triplications. E.g., one selected time-window may contain both a $PKIKP$ and PKP phase response. Autocorrelating such a time-window would lead to cross terms between $PKIKP$ and PKP, which do not contain subsurface information below the array. To limit the occurrence of such cross terms we only use the time-windows with a single dominant phase response. We use beamforming (e.g., Rost & Thomas, 2002) (see Figure 4.3b) to study the effective illumination. Hence, we reject time-windows which are not dominated by a single rayparameter. Also, we reject time-windows which are dominated by an incoming wave with a significant angle of incidence (a rayparameter exceeding 0.04 s/km). Consequently, 17 phase responses remain for

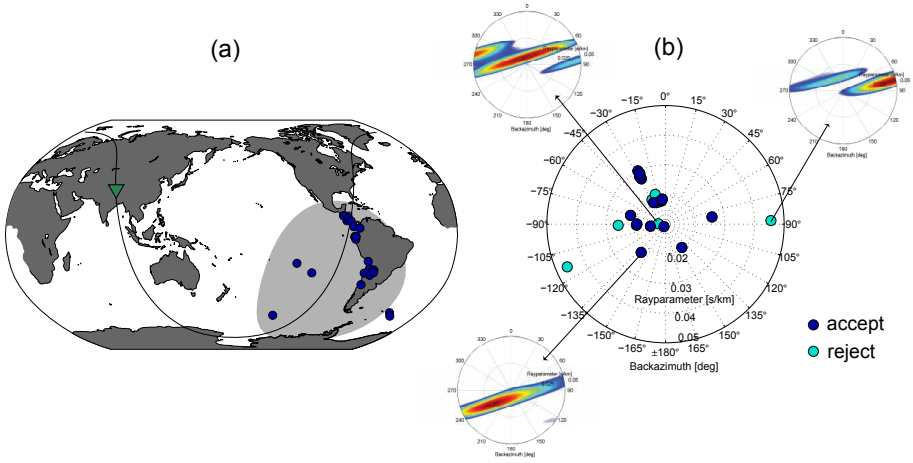


Figure 4.3 *(a) depicts the location of the Hi-CLIMB experiment (green triangle). The 25 selected earthquakes (blue dots) are all from within or near the area for which $PKIKP$ exists (light-gray shading). In (b), the middle figure shows the dominant (plane-wave) illumination for the 25 global-phase responses, of which 17 pass the beamforming test (accept, see main text) and 8 do not pass (reject). The dominant illumination is determined by selecting the coordinate with the largest beampower after beamforming. For the beamforming, all available Hi-CLIMB stations are used. Three examples of beampower plots are shown in the margins of (b).*

further processing.

For the Himalaya array there are less global phases available induced by M>6 earthquakes. Therefore, we lower the threshold to M>5.5 and find 52 global phases. Using the same procedure as described above, 34 phases remain for further processing.

4.4 Processing

We use the Z-component records as approximations of the P-wave transmission responses. To all selected phase responses we apply instrument-response deconvolution and bandpass filtering ([0.01 2.0] Hz). Subsequently, we apply equation 4.2. Thus, e.g., for the southernmost station in the Tibet (or Himalaya) array, the phase response of the first earthquake is autocorrelated. To this autocorrelation, the autocorrelation of the other 16 (or 33 for the Himalaya array) phase responses are added (i.e., the stack over **p**, equation 4.2) and the causal times are selected. This gives the first trace in Figure 4.4(a) (or 4.A.1a). The same process is repeated for all the other stations, yielding the other traces of the panel in Figure 4.4(a) (or 4.A.1a). This image is already a crude estimation of the zero-offset reflection response. However, the low frequency band dominates for global-phases and hence the low resolution.

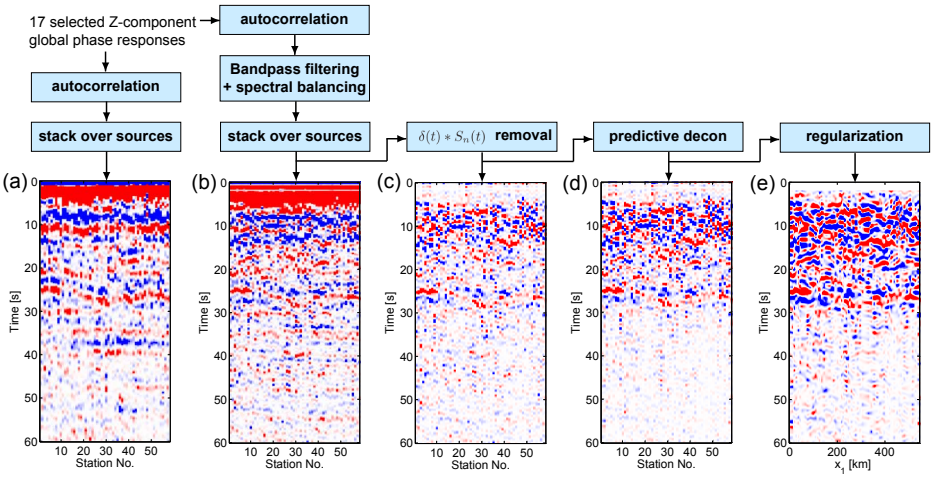


Figure 4.4 *5 stages of the estimated zero-offset reflection response below the Hi-CLIMB subarray (Fig. 4.2). From left to right (a–e), the estimation of the primary reflection response is improved by a succession of pre- and postprocessing algorithms (see text). The used algorithms are indicated on top of the zero-offset panels, in the form of a flowchart.*

Moreover, the spectral balance differs widely for the different phase responses, which impedes an optimal stacking. Therefore, we select a frequency band for which there is signal in all phase responses ([0.04 0.8] Hz) and we apply a spectral balancing (e.g., Bensen et al., 2007) before stacking, giving Figure 4.4(b) (or 4.A.1b). Through this processing both the resolution is improved and spurious events are more successfully stacked out. Still a large artifact remains around t=0, which is a pulse at t=0 convolved with the average autocorrelation of the 17 (or 34) earthquake source time functions ($\delta(t) * S_n(t)$, see equation 4.2). Here we can take advantage of the length of the array crossing highly heterogeneous terrain. Thus, the actual reflectivity is little coherent over the 58 (or 61) stations while the $t = 0$ artifact is coherent. Consequently, we largely suppress this artifact, while only marginally affecting the reflectivity, by subtracting the scaled average trace from each individual trace, giving Figure 4.4(c) (or 4.A.1c).

The last two processing steps are a preparation for reflectivity imaging through poststack Kirchhoff time migration (e.g., Yilmaz & Doherty, 2000; Buske et al., 2002). Through the application of GloPSI the complete reflection response is retrieved, containing both primary and multiple reflections. The primary reflections can easily be migrated into a reflectivity image. Hence, from this complete response (Figure 4.4c or 4.A.1c) we estimate the primary reflections only, using predictive deconvolution (Verschuur, 2006). We assume that multiple reflections are predominantly from crustal interfaces. For each trace it is evaluated whether the events at times larger than 20 seconds can be explained as a free-surface reverberation from events arriving prior to 20 seconds. Events that can be explained as such

are subtracted. For predictive deconvolution no velocity model needs to be known. This gives Figure 4.4(d) (or 4.A.1d). It can be seen that some later events have been removed. Due to the large topography below the Himalaya array, from sealevel to 5 km height (Figure 4.A.3a), an elevation correction is applied. Using an upper crustal velocity of 5.5 km/s we apply time shifts to the data, to move all data to a virtual recording level of 5 km above sealevel. The migration algorithm we use assumes a linear array of regularly spaced datapoints. Therefore, we project the snaking succession of datapoints (Figure 4.1d) to two straight lines. Subsequently, we bilinearly interpolate the data to a regular station spacing of 4 km. After interpolation we obtain Figure 4.4(e) (or 4.A.1e), which is the input for migration. The reflection response is now shown as function of x_1 (or x_1'), which is the (great-circle) distance with respect to the southernmost station in the array.

For imaging the P-wave reflectivity at the correct points in space we use a background velocity model based on a regional-scale tomography (Griffin et al., 2011). From the average station elevation (5 km) to the maximum Moho depth (75 km) we use a linear velocity gradient from 5.5 to 6.5 km/s. For the remaining depths we use the global 1D reference model ak135 (Kennett et al., 1995) which has an upper-mantle velocity of 8.04 km/s. The same hybrid 1D velocity model is used both for the time migration and time-to-depth conversion. The result, Figure 4.5, is discussed in the next section.

4.5 Results

Figure 4.5 shows the obtained P-wave reflectivity images, positioned below a perspective view of the Central and Western Tibetan Plateau. The emphasis is on the Tibet-array results. In Figure 4.A.3, the Himalaya-array results can be studied, as well as a larger depth range for both arrays. In these reflectivity images, a blue-red-blue alternation should be interpreted as an interface with a positive (i.e., increasing with depth) impedance contrast. Below we discuss a few features imaged below the Tibet array.

The first striking thing is a strong reflectivity until about 80 km depth and a reduced reflectivity at greater depths. At most locations, the zone of high reflectivity (the crust) is separated from the zone of less reflectivity (the upper mantle) by a strong reflector, the Moho. The Moho is imaged as a red feature at about 75 km depth. The remaining side lobes of the wavelet give rise to blue features at either side of the Moho. The same transition has been imaged with P-S (Nábělek et al., 2009; Nowack et al., 2010) and S-P (Xu et al., 2011) converted phases and with a single free-surface reflected S-phase (Tseng et al., 2009). The P-wave reflectivity image shows the crustal and upper mantle structure in more detail than previous results.

In the auxiliary material (Figure 4.A.2 and 4.A.3) we compare the P-wave reflectivity images with P-wave velocity perturbation images, as obtained by Hung et al. (2011). The main feature at the southside of the Tibet array is a low-velocity zone that straddles around the Indus Yarlung Suture. This zone corresponds with the Gyirong Graben, which is one of the

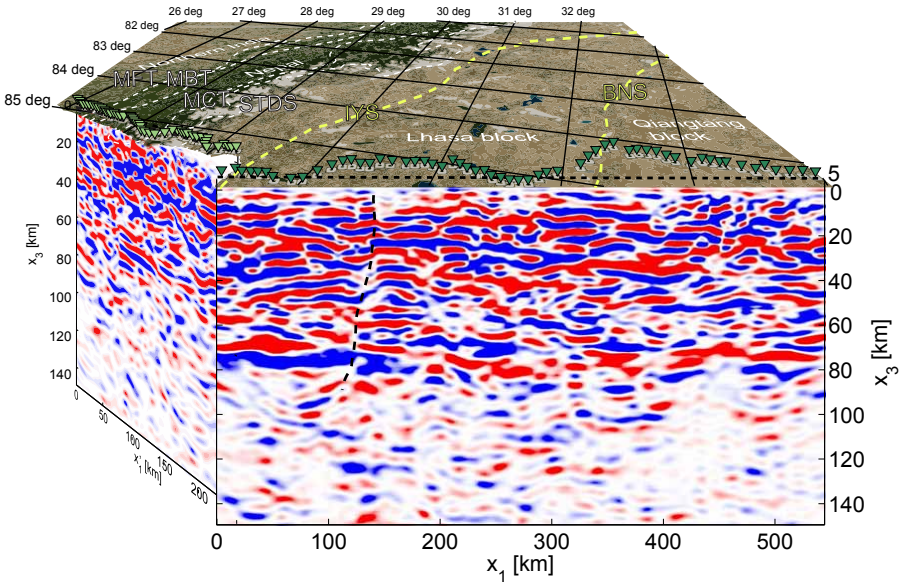


Figure 4.5 *the P-wave reflectivity images for (left) the Himalaya array and (right) the Tibet array, positioned below a satellite image of the Central and Western Tibetan Plateau. (For a non-perspective view of the Himalaya-array results, see Figure 4.A.3.) On the left-hand side, the snow-covered (i.e., white) Himalayas can be seen rising from the lush (i.e., green) Indo-Gangetic Plains to the plateau. The main tectonic blocks are indicted as well as the zones separating them. Left are the major shear zones related to the formation of the Himalayas (dashed white lines): MFT (Main Frontal Thrust), MBT (Main Boundary Thrust), MCT (Main Central Thrust) and STDS (South Tibetan Detachment System). Right are the suture zones related to the formation of the Tibetan Plateau (dashed yellow lines): IYS (Indus Yarlung Suture) and BNS (Banggong Nujiang Suture) (e.g., Yin & Harrison, 2000). On the Tibet reflectivity image, the northern limiting fault of the Gyirong Graben (black dashed line) is indicated. On the satellite image are indicated the actual station locations (green triangles) and the lines on which the data points have been projected (dashed black lines). The depth dimension (x_3) has been exaggerated by a factor of 2 with respect to the other dimensions.*

active rifting zones over which west-east extension of the Tibetan Plateau takes place (e.g., Randey et al., 1999). The edge of this low-velocity zone (denoted with a dashed black line in Figure 4.5 is sharply imaged with a discontinuity in reflectivity.

4.6 Discussion

It is needless to say that the migrated sections (Figure 4.5) could still be improved. Especially, the projection of a snaking succession of datapoints to a straight line, introduces errors, which map into the migrated image. These errors could be reduced by splitting up the array in, e.g., four piecewise linear subarrays, instead of two. Furthermore, the image could be improved by replacing the 1D velocity model by a 2D model, for the migration and time-to-depth conversion. Both changes would lead to an improved positioning of the reflectivity.

In the preceding we illustrated GloPSI with two arrays of stations. Note however that GloPSI is a single-station method. Timing errors between stations are of no concern. Only for more advanced postprocessing, arrays are required. If we had only one station, the artifact around t=0 could not be removed using the same array-method as we used for obtaining Figure 4.4(c). Still one would obtain a fair estimate of the zero-offset reflection response of the lithosphere, as in Figure 4.4(b), if no phase responses were used with triplication time differences of the duration of two-way traveltimes through the lithosphere.

GloPSI can also be applied for global S-phases like SKS, $SKKS$ and PKS to obtain an S-wave reflection response, which again could be further processed into an S-wave reflectivity image. A disadvantage of S-phases is that they are not the first to arrive and may thus be contaminated by coda from earlier phase arrivals. However, the fact that earthquakes radiate more S-wave than P-wave energy, might make up for this.

In this study we only used global phase responses. In principle, if there is large seismicity near the array, also PcP, ScS or PcS could be used. Core-reflected and core-transmitted phases have typically a different bandwidth. Hence, the resolution of the eventual image could be increased by merging responses retrieved with both types of phases.

GloPSI is complimentary to the receiver function method (RF) (Langston, 1979). Both methods can be applied to any (isolated) station, given that it has been long enough in the field to have a rich recording of high-magnitude global seismicity. For RF, all 3-component data are required, whereas for GloPSI only the Z-component suffices. With RF, receiver-side conversions are mapped to depth. These conversions are pronounced for incoming waves with a considerable angle of incidence. For this reason, especially teleseismic waves are used. GloPSI, on the other hand, uses only global-phase responses and maps reflectivity vertically below the station(s). Hence, the data input for both methods is independent. Still, the obtained images should be consistent. Thus by applying both methods, the reliability of our subsurface image will be improved.

4.A GloPSI auxiliary material

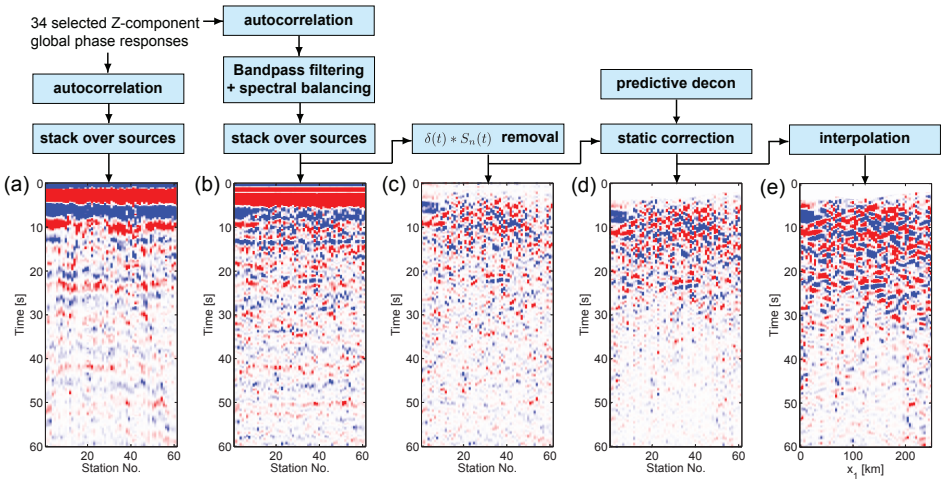


Figure 4.A.1 *5 stages of the estimated zero-offset reflection response below the Himalaya array (light-green line in Fig. 4.A.2). From left to right (a–e), the estimation of the primary reflection response is improved by a succession of pre- and postprocessing algorithms (see text in main document). The used algorithms are indicated on top of the zero-offset panels, in the form of a flowchart.*

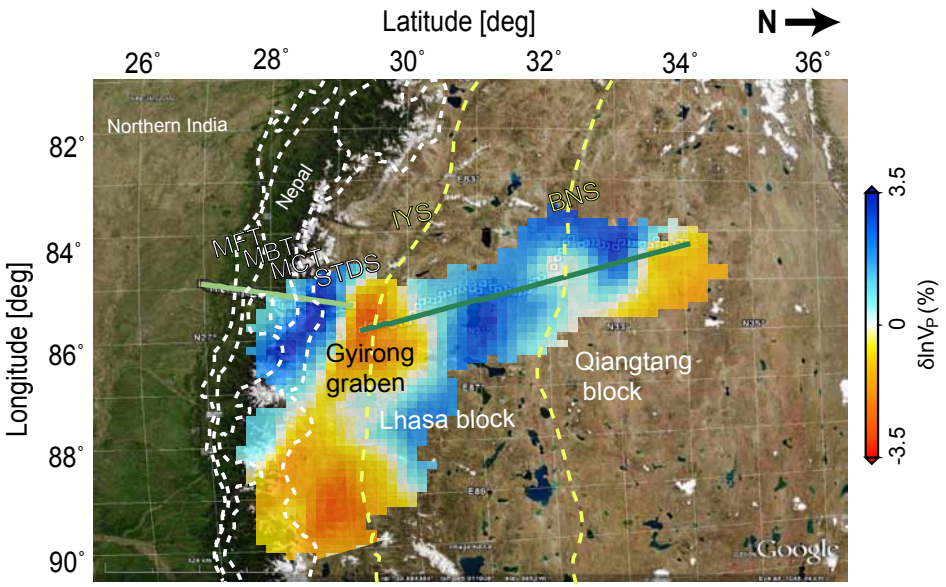


Figure 4.A.2 *A satellite image of the Central Himalayas and Central Tibetan Plateau, showing seismic stations (white squares with black dots) from the Hi-CLIMB experiment [e.g, Nábělek et al.(2009);Nowack et al.(2010)]. The station distribution is split into two subarrays, the Himalaya and the Tibet array. The linearized Himalaya and Tibet arrays are indicated with a light-green and dark-green line, respectively. The dashed white lines denote the major shear zones related to the formation of the Himalayas: MFT (Main Frontal Thrust), MBT (Main Boundary Thrust), MCT (Main Central Thrust) and STDS (South Tibetan Detachment System). The dashed yellow lines denote the suture zones related to the formation of the Tibetan Plateau: IYS (Indus Yarlung Suture) and BNS (Banggong Nujiang Suture) [e.g, Yin and Harrison, 2000]. The satellite image is overlain by a slice, taken at 56 km depth, from the P-wave velocity-anomaly model, as obtained by multiscale finite-frequency traveltime tomography [Hung et al., 2011]. The model shows the Gyirong Graben as a low-velocity anomaly straddling around the IYS, just north of the Himalayas. Around the other old suture zone, the BNS, a much weaker velocity anomaly can be identified.*

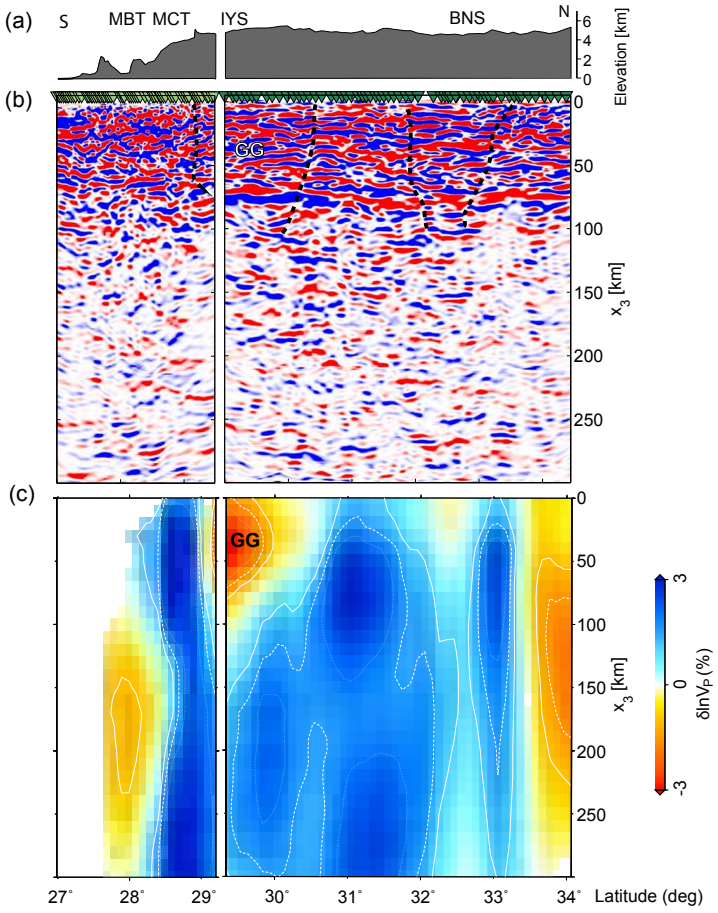


Figure 4.A.3 *(a) The topography below (left) the Himalaya array and (right) the Tibet array. For a map view of these seismic arrays, see Figure 4.A.2. (b) The obtained P-wave reflectivity images for the two arrays. The reflectivity images were obtained by the application of global-phase seismic interferometry and migration (see main text). The reflectivity images are compared with (c) two P-wave velocity-anomaly sections from the same locations. The latter sections were sliced from a 3D tomographic model [Hung et al., 2011]. Both on the reflectivity image and the tomographic image, the development of graben structures can be noted. On the reflectivity images, the limiting faults of the Gyirong Graben (GG), and the rifting zone around the Banggong Nujiang Suture (BNS), are identified by discontinuities in reflectivity in the crust (indicated with the dashed black lines). On the tomographic images, the weak zones along which east-west extension takes place are imaged as low-velocity anomalies in the crust. For the meaning of the undefined abbreviations in the figure (MBT, MCT and IYS), see Figure 4.A.2.*

Part II

Microseism applications

Chapter 5

Extraction of P-waves [1]

5.1 Introduction

There is a long history of studying noise within solid Earth seismology (Bonnefoy-Claudet et al., 2006). However, initially, the noise was not studied for its own merits. It was seen as a nuisance for studying the Earth through earthquake responses (e.g., Wilson et al. (2002)) or for testing compliance with the comprehensive nuclear-test-ban treaty (e.g., Mykkeltveit et al. (1990)). Hence, the noise studies were primarily concerned with understanding and suppressing the most disturbing type of noise, the microseisms. These microseims are ambient seismic vibrations related to swell waves in oceans.

Eventually, researchers realized that the noise itself can be used to study the Earth. In the second half of the last century, methods became popular to deduce Earth structure from noise, notably the spatial autocorrelation technique (Aki, 1965; Okada, 2003), the extraction of phase velocities from array measurements (Lacoss et al., 1969) and the horizontal-to-vertical spectral ratio technique (Nakamura, 2000). More recently, a technique was developed to turn noise from distant sources into a transient signal between two seismometers. This technique has been coined Green's function retrieval or seismic interferometry (SI) (Larose et al., 2006; Snieder et al., 2009; Schuster, 2009; Wapenaar et al., 2010a). Shapiro et al. (2005) used surface-wave microseismic noise from the Pacific to create a transient surface-wave record between stations in the Western USA, for example. Subsequently, using surface-wave inversion, they obtained a velocity model of the crust.

Because of the developments of the above methods, noise is more and more considered a merit rather than a nuisance. Consequently, the recent noise studies focus on a wider frequency range than just that of the microseisms. Moreover, the body-wave portion within the noise is gaining more attention.

Already in the seventies, Toksöz & Lacoss (1968) found that body waves dominated the

[1] This chapter has been published as a journal paper in *Comptes Rendus Geoscience*, **343**, 512–525 (Ruigrok et al., 2011). Note that minor changes have been introduced to make the text consistent with the other chapters of this thesis.

noise between 0.4 and 0.8 Hz, for an array measurement in Montana, USA. Soon after, Vinnik (1973) studied microseisms recorded in Kazakhstan. For this array in the middle of the continent he found that, from distant oceanic sources, no Rayleigh waves were recorded, but just P-phases. Recent studies have shown that body waves are in fact omnipresent in ocean-generated noise. Roux et al. (2005a) identified direct P-waves after crosscorrelating low-frequency noise. Gerstoft et al. (2006) found body waves in the double-frequency microseism band and could associate these to P-phases induced by hurricane Katrina. They made this noise recordings with an array in Southern California. In a later study, using the same array, they also found PP- and PKP phases in noise recordings (Gerstoft et al., 2008). They concluded that the body waves are induced year round and at many locations in the oceans. Landes et al. (2010) reached the same conclusions, using arrays in Turkey, Yellowstone and Kyrgyzstan. Zhang et al. (2009) found also a large proportion of body waves in noise between 0.6 and 2.0 Hz. Koper et al. (2010) used a worldwide distribution of arrays to study one year of noise. Per array, a small frequency band was chosen to beamform (Rost & Thomas, 2002) noise records. The frequency band depended on the spatial sampling of the arrays and varied between 0.5 to 4.0 Hz. For many of the arrays, besides the usual surface waves, a small portion of body waves was found. For some arrays, e.g. the ILAR array in Alaska, body-waves prevailed throughout the year.

The confirmation of the presence of body waves in low-frequency noise has made the noise more attractive for lithospheric imaging and even for exploration. Roux et al. (2005a) considered the use of regional P-wave noise for tomography, after the application of SI. Zhang et al. (2010) demonstrated the use of teleseismic P-wave noise for obtaining a lithospheric velocity model through tomography. Zhan et al. (2010) obtained S-wave Moho reflections through interferometrically processing noise records. Draganov et al. (2007, 2009) used higher-frequency ($>$1 Hz) noise to compose an exploration-scale reflection response. The retrieved responses were subsequently migrated to obtain a reflectivity image of the subsurface. If non-volcanic tremor may be counted as noise, then also Chaput & Bostock (2007) used noise to retrieve scattered body waves between stations. With the retrieved responses they could confirm structure at about 10 km depth.

From the point of view of hydrocarbon exploration, high-resolution seismic reflection data is the most important exploration tool. However, increasingly, companies integrate various types of data to paint a more complete picture of the potential reservoir. In most cases, regional geological information also plays a role in the evaluation of the hydrocarbon potential of a basin.

It is with these observations in mind that we study noise in the frequency range [0.03 1.0] Hz, recorded with an array in Egypt. We split up the noise in different frequency bands, encompassing the primary and secondary microseism and higher-frequency natural noise. This division is based on the potentially different origins of the noise for different frequencies. Our aim is to determine whether we can use the noise recorded in one or more of these frequency bands for SI.

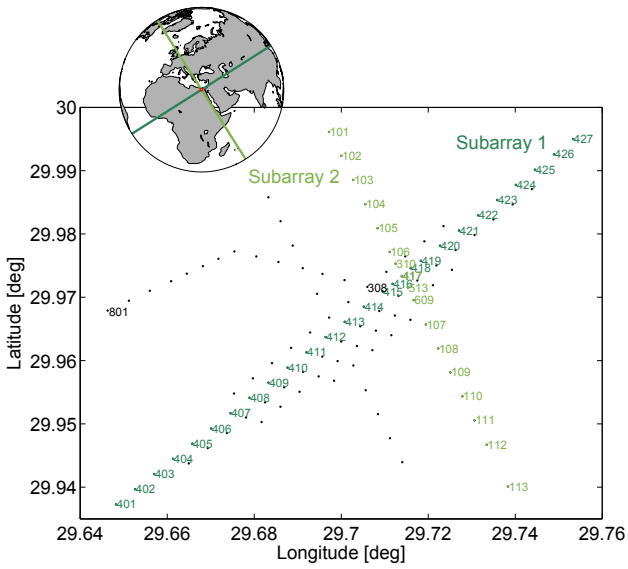


Figure 5.1 *The Egypt-array configuration. The 110 three-component stations are denoted with black dots. The stations for various subarrays are coloured and numbered. In the inset, the bearings of the different subarrays are shown as rhumb lines on a worldmap.*

From the theory behind SI we know that a favorable source distribution is required to extract meaningful responses from the noise (Wapenaar & Fokkema, 2006). Our primary goal is therefore to characterize the noise and identify – where possible – its source areas, so as to evaluate the illumination of the array. To this end, we split up the noise records in small time windows and apply beamforming to determine the slowness and azimuthal distribution of the noise. A rough estimate suffices, since the exact source locations are not relevant for SI (Wapenaar & Snieder, 2007). To further distinguish between surface-waves and body-waves, we perform the beamforming for all three components and additionally compute the power-spectrum density variations for all three components. The noise records with a favorable body-wave content are processed into reflection responses.

5.2 Survey area and data inspection

An array of three-component stations was installed in an area over the Northeast Abu Gharadig Basin in the Western Desert in Egypt. This location is about 230 km west of Cairo. While the area is unpopulated, there is some activity related to oil-and-gas production. Although several tracks in the area were being used by traffic from local producers, the nighttime was very quiet.

Fig. 5.1 depicts the receiver layout. 110 broadband seismometers (Trillium T40) were

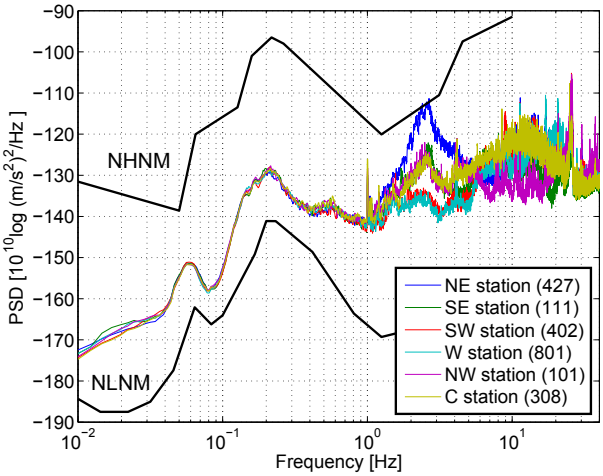


Figure 5.2 *Spatial variation of the power spectral density (PSD) for the Egypt array. The PSDs are compared with the new low noise model (NLNM) and new high noise model (NHNM) from Peterson (1993) (solid black lines). The PSDs are expressed in ground acceleration, which was computed from velocity recordings.*

placed in five parallel lines and three cross lines at varying angles. Inline interstation spacing was 500 m, with a more densely sampled (350 m) area in the middle of the array. In total, more than 40 hours of noise were simultaneously recorded on all 110 stations. The total survey area was about 60 km^2.

Most of the stations are installed on a gravel plane. However, between stations 420 and 423 there is one significant sand dune crossing subarray 1. In general, the topography is slightly undulating, but not to the extent that station corrections are required to account for it.

We start our data analysis by comparing our array measurements with worldwide measurements of ambient noise (Peterson, 1993). We compute power spectral densities (PSDs) with the recipe given in the above reference. A selected spatial distribution of the resulting PSDs is shown in Fig. 5.2. The PSDs are compared with the NLNM (New Low Noise Model) and the NHNM (New High Noise Model) from Peterson (1993), which values are obtained from Bormann (1998).

We observe a large similarity of the PSDs for the different stations between 0.01 and 1 Hz as opposed to large differences above 1 Hz. For many parts of the world 1 Hz separates the domain of domination by natural sources from a domain of domination by anthropogenic or cultural sources (Asten & Henstridge, 1984; Gutenberg, 1958). The distant natural noise sources ($f < 1$ Hz) are recorded similarly by all the stations, whereas the more nearby cultural noise sources ($f > 1$ Hz) are recorded with strongly varying amplitudes. E.g., the noise at around 2.5 Hz is stronger in the NE than on the SW side of the array, pointing to a

relatively nearby source at the NE side. Most likely it concerns car traffic.

For a further analysis we will leave out the frequency band [1.0 - 40.0] Hz, due to its complicated nature and an interstation separation that is not particularly suited for further multichannel processing at these higher frequencies.

The noise records below 1 Hz follow the global trend, indicated by the NLNM and NHNM. The single-frequency (SF) and double-frequency (DF) microseismic peaks can well be distinguished, at 0.058 and 0.21 Hz, respectively. Both peaks are related to storms crossing the oceans (e.g., Tanimoto & Atru-Lambin (2007)). The SF peak is thought to be induced primarily when a storm traverses continental margins (Cessaro, 1994). Due to the relatively small water column, storm-induced ocean waves (swell) can couple directly with the ocean floor and hence induce seismic waves, which can be recorded thousands of kilometers away from the source. The DF microseism is thought to be induced at many places in the oceans, also at locations with large water columns (Vinnik, 1973). Single storm-induced ocean waves do not lead to pressure variations at large depths. However, when ocean waves collide, a pressure variation does build up at the ocean floor, with double or triple the frequency of the individual waves (Longuet-Higgins, 1950). This pressure variation couples to the solid Earth with seismic waves that are significantly stronger than the waves induced at SF (see Fig. 5.2). Despite the fact that the DF-microseism noise could be induced anywhere in the ocean, it tends to be stronger near coasts. Specific coasts are good reflectors for ocean waves and hence provide the necessary opposing waves (Bromirski, 2001).

For the Egypt array, the SF and DF observation are closer to the NLNM than to the NHNM. This is not surprising, considering the distance to oceans with large storms. The nearby Mediterranean and Red Sea are relatively quiet, even in October.

For our analysis we only use the times for which all the stations were active and good quality data were recorded. The starting time of this period is 12 October 2009 14:00, which we set as time zero.

For obtaining a helicopter view of the noise record, we compute the PSD for one station (no. 402) as function of time. The 40 hours of continuous data are split up in windows of 10 minutes. For each of these windows the PSD is computed, using eight 75% overlying segments of 2^{14} samples. The resulting functions are plotted as function of time, yielding the noise spectrogram as displayed in Fig. 5.3.

Within the 40 hours window we identify all the large earthquake responses. The origin of all peaks below 1 Hz could be found by raytracing arrival times from earthquakes in a global catalogue (IRIS earthquake browser). All the identified source locations are plotted in the lower-right map in Fig. 5.3.

As in Fig. 5.2 we can easily identify the SF and DF microseism in Fig. 5.3. The DF microseism pops out as a stable ridge, marking its stability over time. The SF is significantly smaller and more hilly, marking a larger time variation.

The different types of noise are restricted to limited frequency bands. Hence, for the further

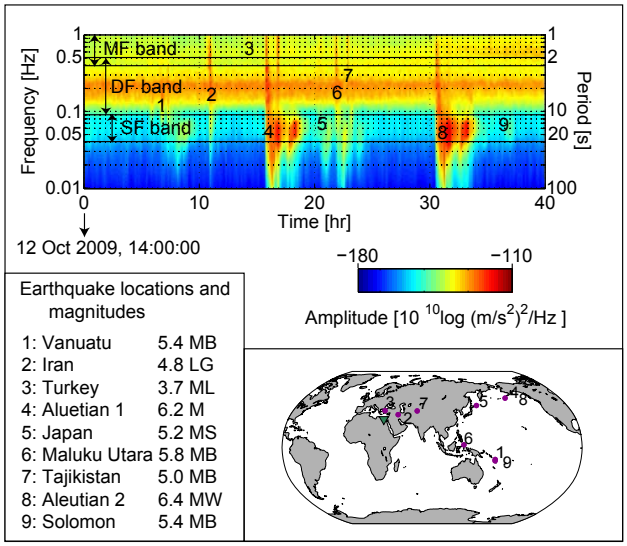


Figure 5.3 *The noise spectrogram (upper figure box), made up by a concatenation of power-spectrum densities (Fig. 5.2) based on 10 minute Z-component records detected at station 402. The transient events are caused by earthquakes. The identified earthquakes and their magnitudes (given in various scales) are listed in the lower-left box and are indicated on the spectrogram. Their locations are plotted on a world map (lower-right box). The data between 0.03 and 1.0 Hz are divided into three frequency bands (MF, DF and SF) marking different characteristics of the noise in the various bands.*

analysis and processing, we split up the data in a few distinct frequency bands, as depicted in Fig. 5.3. The first band is chosen around and named after the SF microseismic peak (SF band, [0.03 - 0.09] Hz). The second band encompasses the DF microseismic peak (DF band, [0.09 - 0.5] Hz). In Fig. 5.2 it can be seen that, below 1 Hz, there is a small third hill, peaking at 0.55 Hz. We choose the third band (MF band, [0.4 - 1.0] Hz) such that it encompasses this hill. Note that in previous literature not such MF band is defined. This MF noise gains in strength from about 30 hr onwards (Fig. 5.3).

5.3 Origin of noise

Within the 40 hours window (see Fig. 5.3) we now identify the origins of the noise. We do this by splitting up the 40 hours in non-overlapping time windows. We choose 10-minute windows for the SF and DF band and 5-minute windows for the higher-frequency MF band. Subsequently each time window is beamformed.

The beamforming is derived and explained in a large number of references, e.g., Lacoss et al. (1969); Rost & Thomas (2002). Here we only state the two basic steps. As a pre-

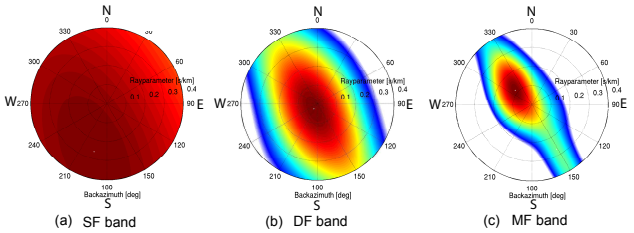


Figure 5.4 *A beampower output for (a) the SF band (using the first 600 seconds in hour 26), (b) the DF band (using the same time window) and (c) the MF band (using the first 300 seconds in hour 26). Taking the maximum beampower value, for the SF band we find: θ_{dom}=185^o, p_{dom}=0.251 s/km, for the DF band: θ_{dom}=216^o, p_{dom}=0.031 s/km and for the MF band: θ_{dom}=311^o, p_{dom}=0.117 s/km*

processing step, a time window and frequency band is selected from an array measurement. As a first step, all traces for this selection are mutually crosscorrelated. Hence, a crosscorrelation matrix is obtained which contains all the time differences between different waves arriving at the different stations. As a second step, these time differences are fit with a forward model. As a forward model, bandlimited plane waves with varying backazimuth θ and rayparameter p are considered. The degree to which the model fits the data is expressed in beam power. Thus, after beamforming the beampower is obtained as a function of backazimuth and rayparameter. The p and θ with the maximum beampower is chosen as the dominant rayparameter p_{dom} and the dominant backazimuth θ_{dom}, respectively.

The beamforming is implemented in the frequency domain (Lacoss et al., 1969). Instead of computing the beampower for each frequency sample individually, the frequency band is split up in bins and the beampower is only computed for a stack of the frequency samples within each bin. This procedure stabilizes the estimate. We choose 5 frequency bins per frequency band. For obtaining the final beampower, the beampowers for the different bins are stacked.

Fig. 5.4 shows an example of beampowers for the three different frequency bands we consider. The beampowers were computed using the first time window of hour 26 (see Fig. 5.3). In Fig. 5.4(a)-(c) the array signature can well be noted. The beampower has more resolution on the SW-NE than on the NW-SE transect due to a better coverage of stations on the former transect. Also, the difference in resolution is obvious for the different frequency bands. Nevertheless, a clear p_{dom} and θ_{dom} can be picked for each frequency band.

Note that, within the chosen time window, waves of similar strength, but from different sources or with different raypaths, might arrive. If this is the case in the SF band, beampowers from the different waves will inevitably interfere, due to the low resolution (Fig. 5.4a). For smaller distances in the p-θ plane, beampower interference will also occur in the DF- and MF-band (Fig. 5.4b,c). The longer time-records are included in the beamforming, the more different waves will arrive and the more severe the interference will be.

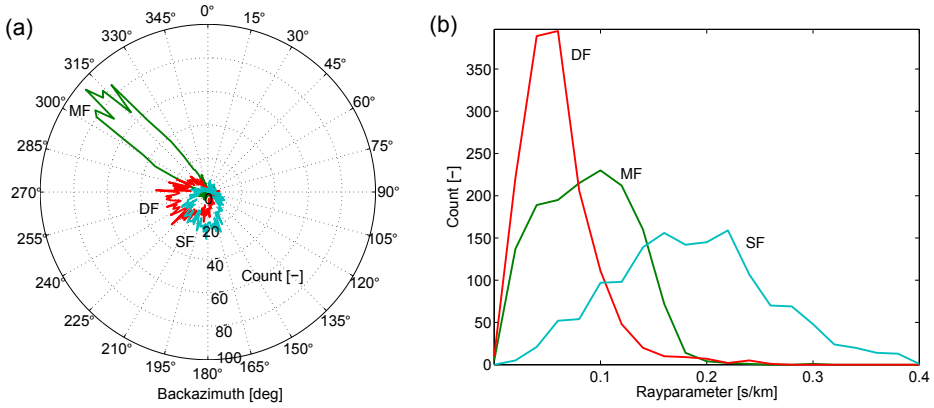


Figure 5.5 *(a) A rose diagram of the dominant noise directions and (b) a distribution plot of the dominant rayparameters, for the three different frequency bands of interest (see Fig. 5.3). The directions and rayparameters were estimated by beamforming 40 hours of data.*

Hence, we choose relatively small time windows to increase the chance to yield parameters of individual noise sources rather than averages over multiple sources.

After beamforming and automatic picking we obtain p_{dom} and θ_{dom} for all time windows and frequency bands. Figs. 5.5(a) and (b) show the resulting backazimuth and rayparameter distributions, respectively. We interpolated the distributions for the SF- and DF- to achieve the same number of total counts as in the MF band.

In all frequency bands prevailing noise directions exist. Noise from the direction of the Mediterranean dominates the MF band (and hence its name, Mediterranean Frequencies), whereas the SF- and DF-band seem to be susceptible to noise from especially the Southern Atlantic.

The rayparameter distribution (Fig. 5.5b) is rather broad for all bands considered. For body-wave seismic interferometry, the DF- and MF-band show the most favorable distribution, as we will see in the next section. The SF band contains primarily surface waves and is therefore considered to be unsuitable for body-wave SI.

In the following, we will first introduce noise SI and better analyze the wavemode content in the noise, before moving onwards to the actual SI processing. The analysis of the DF band (Section 5.5) is used to introduce our noise-analysis method.

5.4 Noise seismic interferometry

In our configuration we have receivers on the free surface, above the medium of interest (Fig. 5.1). Also the noise sources are at or near the free surface. However, because of the distance of the sources and the velocity gradient in the crust and mantle, effectively the medium of

interest is illuminated from below. For this configuration, Wapenaar & Fokkema (2006) derived interferometric relations. They found that the noise can be used to retrieve the Green's function between 2 receivers when 1) the noise sources are mutually uncorrelated and 2) a long time window of noise contains a good spatial distribution of noise sources. For details about the required distribution of sources we refer to Section 3.A. In practice, the second condition is unlikely to be fulfilled. Even if there was a perfect source distribution then the estimated Green's function would still be biased by differences in strength of the sources. To compensate for this, we split up the noise record in small time windows (panels) and root-mean-square normalize each panel. We make the assumption that each such panel is dominated only by a single noise source. This assumption is checked with beamforming (Section 5.3).

For SI we threat different phases from the same source as different effective sources illuminating the medium of interest with different angles of incidence. The wavefields due to the noise sources are assumed to be planar near the array. Hence, an effective source is parameterized with the beamforming output $\mathbf{p} = (p_{dom}, \theta_{dom})$, where p_{dom} and θ_{dom} are the dominant rayparameter and backazimuth of the noise. If a certain panel contains multiple strong beams of similar energy, this panel is rejected. For the accepted panels we can write the noise registration at stations $\mathbf{x}_\mathcal{A}$ and $\mathbf{x}_\mathcal{B}$ as

$$v(\mathbf{x}_\mathcal{A}, \mathbf{p}, t) = G(\mathbf{x}_\mathcal{A}, \mathbf{p}, t) * N_{dom}(t), \tag{5.1}$$

$$v(\mathbf{x}_\mathcal{B}, \mathbf{p}, t) = G(\mathbf{x}_\mathcal{B}, \mathbf{p}, t) * N_{dom}(t), \tag{5.2}$$

where v is the particle velocity registration, G is the Green's function describing the propagation of the dominant noise and N_{dom} is the source-time function of the dominant noise source. The only difference between this noise registration and a transient registration is the much longer source-time function. Hence, we can use a similar seismic interferometric relation as derived for transients (Section 3.2):

$$\sum_{\theta_{min}}^{\theta_{max}} \sum_{p_{min}}^{p_{max}} v(\mathbf{x}_\mathcal{A}, \mathbf{p}, -t) * v(\mathbf{x}_\mathcal{B}, \mathbf{p}, t) \Delta p \Delta\theta \propto$$
$$G(\mathbf{x}_\mathcal{B}, \mathbf{x}_\mathcal{A}, -t) * S_n(t) + G(\mathbf{x}_\mathcal{B}, \mathbf{x}_\mathcal{A}, t) * S_n(t), \tag{5.3}$$

where $S_n(t)$ is an average of autocorrelations of the noise. The relation in Section 3.2 was derived for source locations restricted to a vertical plane through the receivers. Here we do not make this restriction and hence the additional summation over backazimuth.

In the following, we will binarize the azimuthal dependence in relation 5.3. At the positions halfway between $\mathbf{x}_\mathcal{A}$ and $\mathbf{x}_\mathcal{B}$ the globe is divided into two hemispheres. For illumination from the hemisphere on which $\mathbf{x}_\mathcal{A}$ is situated, the rayparameter gets the addition of a superscript $^+$, whereas for illumination from the other hemisphere the rayparameter gets the addition of a superscript $^-$. In the following, the subscript $_{dom}$ is left out to simplify the

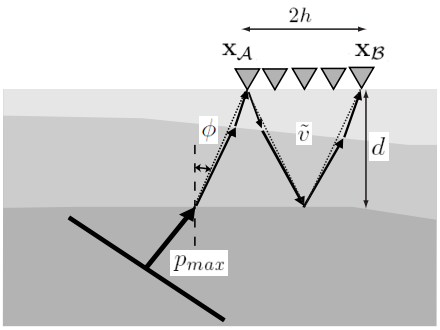


Figure 5.6 *Configuration for the computation of the required rayparameter (equation 5.6). The tilted line in the lower left denotes a plane-wave, illumination a two-layers-over-a-half-space model. Only the rays (denoted with arrows) are drawn that connect the outer two receivers of the array via a bounce from the second interface. The rays are the actual raypaths while the dotted lines would be the raypaths if the upper two layers were replaced by a layer with their average properties.*

notation. When we assume that the medium is approximately layered, equation 5.3 can now be split up into two equations

$$\sum_{p^-_{min}}^{p^-_{max}} v(\mathbf{x}_\mathcal{A}, p^-, t) * v(\mathbf{x}_\mathcal{B}, p^-, -t)\Delta p \propto G(\mathbf{x}_\mathcal{B}, \mathbf{x}_\mathcal{A}, t) * S_n(t), \tag{5.4}$$

$$\sum_{p^+_{min}}^{p^+_{max}} v(\mathbf{x}_\mathcal{A}, p^+, -t) * v(\mathbf{x}_\mathcal{B}, p^+, t)\Delta p \propto G(\mathbf{x}_\mathcal{B}, \mathbf{x}_\mathcal{A}, t) * S_n(t), \tag{5.5}$$

where the first summation was time-reversed such that the Green's function is retrieved at positive times. In our case, the bulk of the energy tends to be from one hemisphere only. Depending on the hemisphere with the dominating sources either equation 5.4 or 5.5 is used, for all time windows, to retrieve the Green's function. For noise sources from both hemispheres, the Green's function is obtained from a combination of equation 5.4 and 5.5, depending on the dominating direction in each time window. This approach was successfully tested for earthquake responses and was called TRBI (time-reversal before integration) in Section 3.2.

Our goal is to retrieve reflections from a wide source-receiver offset range. Most of the lithosphere is approximately horizontally layered. In this case, a zero-offset reflection response corresponds to $p \approx 0$. Consequently, to obtain this response, we also need illumination with $p_{min} \approx 0$. The required p_{max} is dictated by the largest source-receiver offset $2h$ and the shallowest interface d of interest, see Fig. 5.6. The largest offset would ideally be the offset between the two outer receivers in the array. The shallowest interface that could be observed

is restricted by the band limitation of the noise and interfering effects from correlations of direct waves. Consequently, reflections from the shallowest interfaces can normally not be retrieved. Fig. 5.6 shows the stationary illumination (Snieder, 2004) with a plane-wave source for the retrieval of a primary reflection from the second interface. We can express the rayparameter of this reflection as $p = \sin(\phi)/\tilde{v}$, where $\tilde{v}$ is the average velocity of the first two layers. Combining this last expression with $\sin(\phi) = h/(\sqrt{h^2 + d^2})$ yields

$$p_{max} \geq \frac{h}{\tilde{v}\sqrt{h^2 + d^2}}. \tag{5.6}$$

As long as the illumination range $[p_{min}, p_{max}]$ is well sampled p_{max} may be much larger than dictated by expression 5.6. However, since we are interested in reflections only, we always choose $p_{max} < 0.20$ s/km, which would be the rayparameter for a direct P-wave with a velocity of 5 km/s. Hence, we do not retrieve surface waves, which we otherwise would need to filter out again before migrating the retrieved responses.

5.5 DF band

We start the analysis of the data in the DF band ([0.09 - 0.5] Hz) by computing the PSD time-variation function, as in Fig. 5.3, but now only for the DF band and for all 3 components. The PSD time-variation function for the Z-component at station 402 is plotted in Fig. 5.7(a). With this plot we can study the amount of energy that is recorded for certain time intervals. Especially, we can study to what extent this energy is distributed over the entire frequency band.

Fig. 5.7(b) shows averages over frequency of the PSD time-variation functions. Thus, for each time interval, the sum of the PSD within the DF band is shown for the Z-component (blue line), the N-component (green line) and the E-component (red line). Hence, on this plot we can study the differences in recorded energy for the different components.

Figs. 5.7(c) and (d) show the time-variation graphs for the estimated θ_{dom} and p_{dom}, respectively. To make these graphs, the beamforming on the Z-component (as introduced in Section 5.3) has been repeated for the N- and E-components. The graphs have been smoothed using sliding average of three-sample windows. Similar p_{dom} for the different components would indicate the measurement of the same (mix of) wavemodes on all components. A similar θ_{dom} for the different components would hint at a susceptibility to a similar source (or mix of sources).

One important element for noise characterization in general is estimating the contribution of surface and body waves (Bonnefoy-Claudet et al., 2006). Using the four plots of Fig. 5.7 together, we can untangle the noise for a large part. Making the assumption that the noise sources are near the Earth's surface and far away we can already largely classify the arrivals based on their rayparameter, see Fig. 5.8. Rayparameters below 0.173 s/km can only be explained with body waves, whereas rayparameters above 0.312 s/km can only be explained with surface waves. Rayparameters between 0.224 and 0.312 s/km are harder to

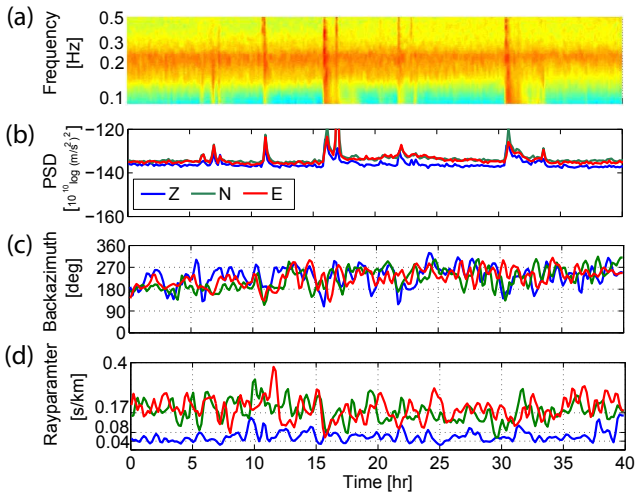


Figure 5.7 *DF-band noise-variation plots for 40 hours of data, starting 12 October 2009 at 14:00. (a) Power spectrum density (PSD) variation on the Z-component and, for all components, (b) the averaged (over frequency) PSD variation, (c) the backazimuth and (d) the rayparameter variation.*

classify, since they could be explained by both surface waves and local S-phases. For this p-band, Fig. 5.7(b) helps out.

Body waves from distant sources would arrive at the array with relatively small angles of incidence. Hence, P-wave arrivals would give a high PSD on the Z-component and little PSD on the other components. S-wave arrivals would give a high PSD on the horizontal components and a smaller PSD on the Z-component. When we observe similar PSDs on all components, this could be due to the arrival of P- and S-waves simultaneously or by the arrival of Rayleigh waves. In the first case, the rayparameter estimation for (one of the) horizontal components would be almost double the rayparameter estimation for the Z-component. In the second case, all (or at least one of the horizontal components and the Z-component) detect the same Rayleigh wave and hence would show similar rayparameter estimations.

Finally, Love waves are easily detected by their polarization in the horizontal plane. Hence, they are identified by much more energy on the horizontal components than on the vertical component.

Using the tools as described above, we characterize the noise in the DF band. Only a limited portion of the recorded energy is due to earthquake responses (Fig. 5.3). In Fig. 5.7(a) and (b), these can be recognized as high-energy transient events. In the DF band, the earthquake responses contain primarily body waves, judging from the short duration of the events in the PSD variation plot in comparison with the much longer duration for the same events in

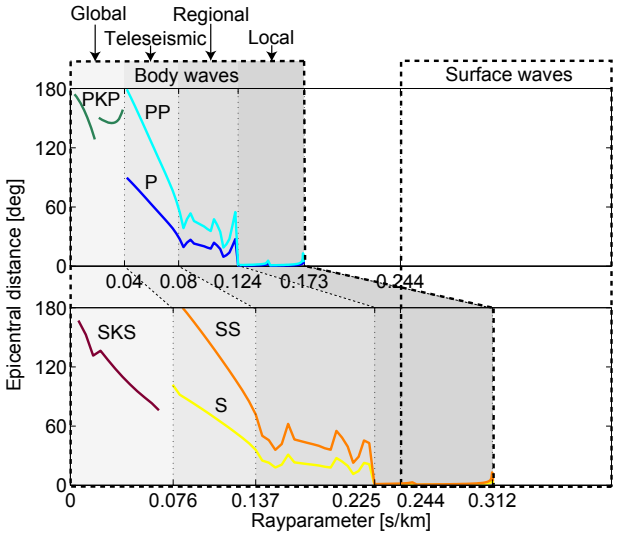


Figure 5.8 *Classification of phases based on rayparameter. For body waves, the four considered classes (indicated with grey shading) are based on the depth penetration of the waves. The four classes are global, teleseismic, regional and local, for waves reaching until within the core, the lower mantle, the lower crust and the upper crust, respectively. In the upper figure, the rayparameter versus distance graphs are shown for the most energetic P-phases, whereas in the lower figure the same functions for the most energetic S-phases are shown. The functions were computed with TTBox (Knapmeyer, 2004) using a 1D Earth model (PREM, (Dziewonski & Anderson, 1981). Using the same model, the lower rayparameter bound for surface waves (0.244 s/km or 4.10 km/s) was computed for a fundamental-mode Rayleigh wave with a peak frequency of 0.01 Hz.*

the SF band (Fig. 5.3). In the background of these transient peaks, we can notice a strong DF microseism with a dominant frequency around 0.22 Hz.

Fig. 5.7(c) shows the dominant backazimuth variation. The backazimuth estimations for the different components are not identical, but they do vary within the same range. Hence, it is likely that the different components are susceptible to the same source regions and that the differences are due to interfering waves and a limited beam resolution. The dominant source region moves gradually from South of the array (at hour=0) to West of the array (at hour=40).

Fig. 5.7(d) shows the dominant-rayparameter variation. A clear difference can be seen between the vertical component (blue line) and the horizontal components (green and red lines). Almost all rayparameters estimated for the Z-component can be explained with teleseismic and regional P-phases (see Fig. 5.8). The rayparameters on the horizontal components are significantly larger. These could be explained by teleseismic, regional and local

S-phases, but also sometimes with surface waves (see Fig. 5.8). The p-variation on the N-component sometimes follows the trend on the Z-component, e.g., between 20 and 28 hours. Hence, it is likely that also on this horizontal component body waves are recorded. However, the rayparameters on the horizontal components are relatively high with respect to the rayparameters on the vertical component. Therefore, only for a limited number of time windows the observations can be explained by a dominant P- or PP-phase on the Z-component, and a S- or SS-phase, due to the same source, on the N- and E- components. For all the other time windows, a contemporaneous surface wave would be required on the horizontal components.

The rayparameter distribution estimated for the Z-component is favorable for interferometric processing. The rayparameter band (see Fig. 5.5b) stretches from 0 until about 0.2 s/km. This is wide enough to retrieve wide-offset reflections below the array from the middle crust and deeper, as was worked out in Equation 3.8.

From Figs 5.1 and 5.5(a) we can infer that the azimuthal distribution of the sources is best suited for the retrieval of reflections below subarray 1. SW of the Egypt array there is a good distribution of sources, both with respect to rayparameter and azimuth. The source locations on the NE side of the array are very sparse and are hence rejected. Consequently we have only one-sided illumination and we can use equations 5.4 or 5.5.

Since subarray 1 is relatively small, we do not need the larger rayparameters, not even for the largest offset in the subarray. Using equation 5.6 with $\tilde{v} = 6$ km/s, $h = 6$ km and $t_0 = 5$ s, we find $p_{max} = 0.062$ s/km. Consequently, we may safely restrict the rayparameter band to the teleseismic and global range (see Fig. 5.8) for P-phases. This has as an advantage that we may leave out a decomposition into P- and S-waves, since for the global and teleseismic range we may assume that primarily P-waves are recorded on the Z-component.

We consider the 40 hours of noise presented on Fig. 5.3 for all stations in subarray 1 and split up the noise records in time windows of 10 minute duration. We do not discriminate between panels dominated by noise or dominated by earthquake responses. We do root-mean-square normalize each panel. Panels with $p^+ < .012$ s/km and $p^+ > 0.08$ s/km found through beamforming (Section 5.3), are rejected. Also, panels with a significant surface-wave pollution are rejected. We find these pollutions especially between 15 and 32 hours (see Fig. 5.7b), where the energy on the horizontal components is larger than on the vertical component. Consequently, from the 240 panels available per station combination, only 87 are used. For each selected time window, all traces are mutually crosscorrelated. For each combination of stations, the resulting crosscorrelations are ordered as a function of rayparameter. Fig. 5.9(left) shows the resulting correlation panel, i.e. $v(\mathbf{x}_\mathcal{A}, p^+, t) * v(\mathbf{x}_\mathcal{B}, p^+, -t)$, for one such combination of stations.

The largest features in Fig. 5.9(left), around t=0, are the average autocorrelations of source-time functions of the noise ($S_n(t)$, see equation 5.3) convolved with spikes at the time differences of the direct waves. The effective source-time functions of the noise are fairly consistent for the different rayparameters. They show a large drop in energy from t=0

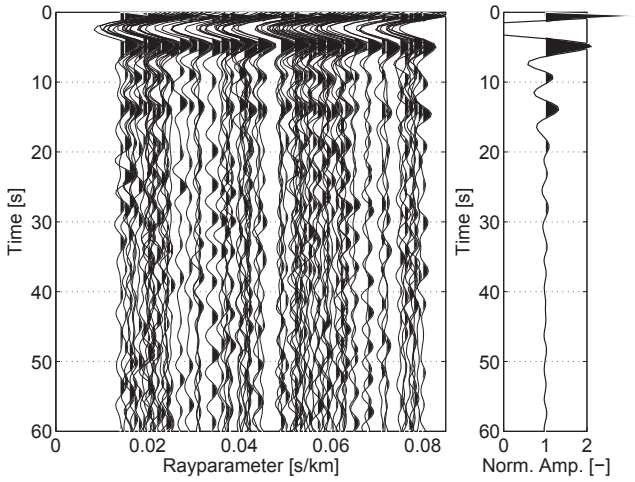


Figure 5.9 *Visualization of the integrand (correlation panel, left) and sum (stack, right) of the seismic interferometric relation (equation 5.5) for $\mathbf{x}_\mathcal{A}$ and $\mathbf{x}_\mathcal{B}$ both at station 413. The integrand is obtained by correlating noise records from the double frequency microseism.*

onwards until $t \approx 7.5$ seconds. At larger times the effective source-time functions are weaker and strongly varying, depending on the noise source, or mix of noise sources, that were active within a certain time window.

One other consistent feature can be observed in the correlation panel, with a negative phase at $t \approx 11$ s. This feature is mainly due to the correlation of the direct noise field with the free-surface reflected noise field as drawn in Fig. 5.6, and hence its negative phase.

The stack (the graph on the right-hand side in fig. 5.9) may be interpreted as the reflection response as if there were a source and a receiver at station 413 (which station is located in the middle of subarray 1, see Fig. 5.1). However, this stack is still imprinted by the limited illumination used and $S_n(t)$. At later times, the stack shows a few other events, which were not readily interpretable in the correlation panel, but are likely to be subsurface reflections.

Similar stacks are obtained for all other station-combinations in subarray 1. The resolution is slightly increased by deconvolution with the stack of autocorrelations of the direct noise field. As a deconvolution trace, a time window between -7.5 and 7.5 seconds is selected from the zero-offset retrieval.

Fig. 5.10(a) shows the resulting stacks of crosscorrelations of station 413 with all other stations in subarray 1. Hence, it is the estimation of the reflection response as if there were a source at station 413 and receivers at all other stations (such a panel is called a shotgather). The event with the largest amplitude could be interpreted as the direct field between the stations, if there was illumination from large rayparameters. Since we restricted the raypa-

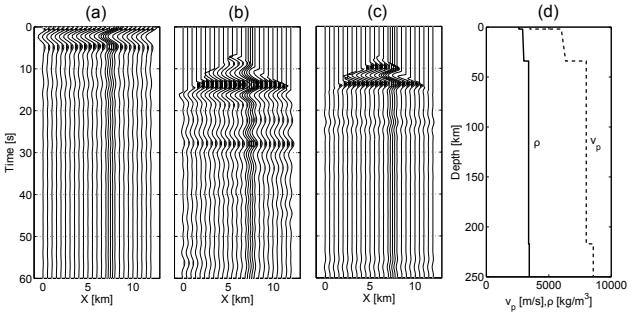


Figure 5.10 *A retrieved shotgather for a virtual source at station 413 and receivers at all station locations of subarray 1 (Fig. 5.1), (a) before and (b) after muting the spurious event near t=0, in comparison with (c) a synthetic shotgather for (d) a 1D Earth model for Northeast Africa.*

rameter band, this event between 0 and 7.5 seconds is an artifact. Fig. 5.10(b) shows the result after removing this artifact. It is compared with a synthetic reflection response (Fig. 5.10c). This synthetic response was obtained by forward modeling the wavefield due to a point source in the Cornell model for the crust in Northeast Africa (Seber et al., 1997), supplemented by the PREM model of the transition zone (Fig. 5.10d). The two main interfaces in this merged model are the Moho and Lehmann dicontinuity, at 34 and 217 km depth, respectively. The synthetic response (Fig. 5.10c) was convolved with a flipped Ricker wavelet to be consistent with the SI result (Fig. 5.10b).

In the reference response (Fig. 5.10c) three reflections can be seen: at 11 s the Moho reflection, at 22 s the Moho multiple and at 57 s the Lehmann reflection. In the retrieved response (Fig. 5.10b) the same three reflections can be identified at similar times. Additionally, a few reflections were retrieved that were not forward modeled. The reflections at 17 and 34 s could be the primary and multiple, respectively, of the Hales discontinuity (Kind & Li, 2007). The reflection at 28 s has the right phase and timing to be the lithosphere-asthenophere-boundary (LAB) reflection. The amplitude is surprisingly large, though. Consequently, the reflection around 56 s could be explained by either a primary reflection from the Lehmann discontinuity or as a multiple from the LAB.

In Fig. 5.11 we show the retrieved shotgathers for a few other virtual source locations on subarray 1. Note the consistency for the different features for the different shotgathers.

As a further processing, at all 110 stations (see Fig. 5.1) we retrieved the zero-offset reflection response and picked the two-way traveltime of the Moho reflection. Fig. 5.12 depicts an interpolated image of these traveltimes. With the assumption that the Moho itself is flat, the traveltime anomalies in Fig. 5.12 can be interpreted as structure in the crust.

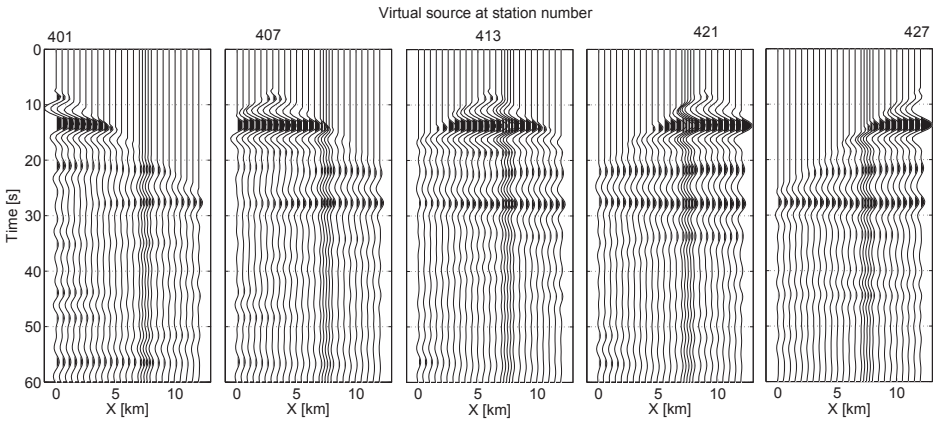


Figure 5.11 *Retrieved shotgathers for, from left to right, a virtual source at station number 401, 407, 413, 421 and 427, respectively, and receivers on all other station locations of subarray 1 (Fig. 5.1).*

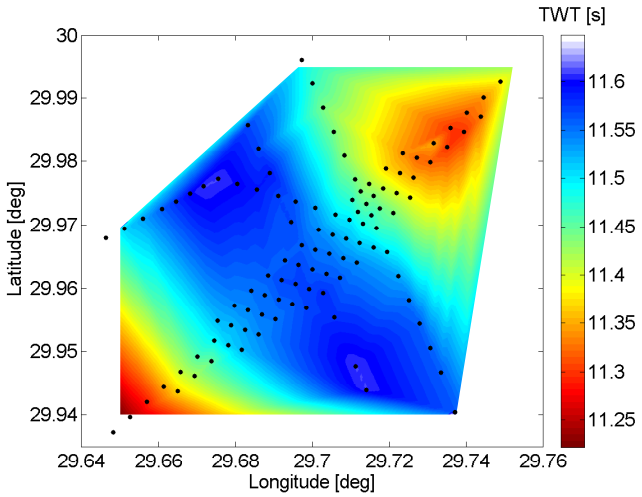


Figure 5.12 *A 2D interpolation of the two-way traveltimes (TWT) of the retrieved Moho reflection (see Fig. 5.10), at zero-offset. The station positions are depicted with black dots.*

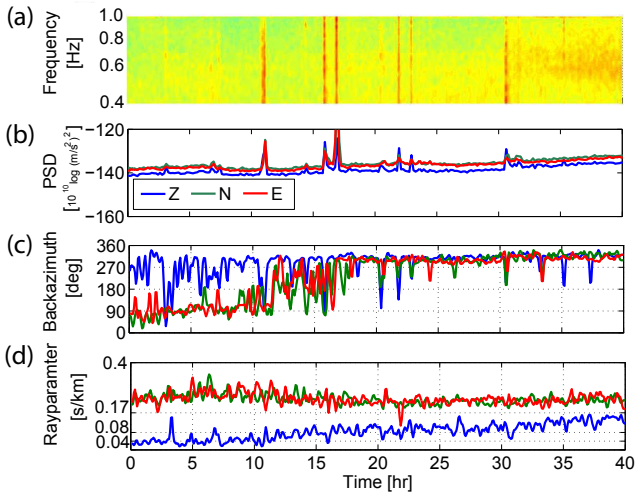


Figure 5.13 *MF-band noise-variation plots for 40 hours of data, starting 12 October 2009 at 14:00. (a) Power spectrum density (PSD) variation on the Z-component and, for all components, (b) the averaged (over frequency) PSD variation, (c) the backazimuth and (d) the rayparameter variation.*

5.6 MF band

We start the analysis of the recordings in the MF band ([0.4 - 1.0] Hz) by computing time-variation functions, as described in Section 5.5. The results are shown in Fig. 5.13. As for the DF band, we use 10 minute records at station 402 for the PSD computations (Fig. 5.13a&b). In the MF band the noise sources tend to be of a shorter duration than in the SF and DF band. Hence, for the beamforming (Fig. 5.13c&d) we limit the time windows to 5 minutes.

Only a small portion of the recorded energy is due to earthquake responses (Fig. 5.3). In Fig. 5.13(a) and (b), these can be recognized as high-energy transient events. In the background of these transient peaks, we can notice a noise distribution which is relatively quiet between 0 and 17 hours, which catches some energy related to the DF microseism between 17 and 30 hours and which increases in strength between 30 and 40 hours. The clear noise source in this later time-interval has a dominant frequency of about 0.6 Hz. Overall there is more energy on the horizontal components (Fig. 5.13b). This hints at the presence of Love waves.

Fig. 5.13(c) shows the dominant backazimuth variation. Between 0 and 17 hours, $\theta_{dom}(t)$ for the horizontal components (green and red lines) differs largely from the one for the vertical component (blue line). Hence, during this quiet time, the horizontal components pick up noise from a different source than the vertical component. From 17 hours onwards

the backazimuth estimations become identical for all components; all components detect predominantly noise from a source region WNW of the array.

Fig. 5.13(d) shows the dominant-rayparameter variation. A clear difference can be seen between the vertical component (blue line) and the horizontal components (green and red lines). The rayparameters estimated for the Z-component increase with time. For increasing time, these rayparameters can be explained by global, teleseismic and regional P-wave sources, respectively (see Fig. 5.8). It appears that a P-wave source migrates towards the array. The rayparameters on the horizontal components are significantly larger and can be explained by a mix of crustal phases, S_g ($p \approx$0.31 s/km), L_g ($p \approx$0.28 s/km) and S_n ($p \approx$0.21 s/km) (Isacks & Stephens, 1975).

The rayparameter distribution estimated for the Z-component is favorable for body-wave SI processing. The further processing is almost identical to the one described for the DF band (Section 5.5).

From Figs 5.1 and 5.5(a) we can infer that the azimuthal distribution of the sources is best suited for the retrieval of reflections below subarray 2. WNW of the Egypt array there is a good distribution of sources, both with respect to rayparameter and azimuth. Source locations on the ESE side are absent. Consequently we have only one-sided illumination and we can use equations 5.4 or 5.5.

We consider the 40 hours of noise presented on Fig. 5.3 for all stations in subarray 2 and split up the records in time windows of 5 minute duration. We leave out time windows with p_{dom} larger than 0.08 s/km as were found through beamforming (Fig. 5.13d) to omit the necessity of a decomposition into P- and S-waves. Also we leave out time windows with $p_{dom} < 0.08$ s/km, but with a notable surface-wave pollution. Consequently, from the 480 panels available, only 142 are used. Each panel is root-mean-square normalized. For each selected time window, all traces are mutually crosscorrelated. Subsequently, all crosscorrelations pertaining to the same station combination, are stacked. The resulting traces are ordered into shotgathers. For each shotgather, the imprint of $S_n(t)$ (see equation 5.3) is mitigated by applying a source deconvolution. As a deconvolution trace, a time window between -3 and 3 seconds is selected from the virtual source trace, which trace is the one obtained for $\mathbf{x}_\mathcal{A}$ and $\mathbf{x}_\mathcal{B}$ (see equation 5.5) both at the same station. Subsequently, the spurious event near t=0 is muted. Finally, the retrieved responses are regularized to a station grid of 0.5 km to simplify the further processing.

Fig. 5.14 shows five reflection responses thus obtained. Until about 7 seconds, a few clear reflections can be recognized on all shotgathers. Notably, the primary reflection from the basement of the sedimentary basin at 3.1 s. After resorting the shotgathers to common-midpoint gathers, we estimate the average velocity of the basin to be 3.2 km/s. Hence, the basement can be found at about 5 km depth. From gravity data it was found that the basement depth of the Abu Gharadig depositional center varies between 6 and 12 km (Awad, 1985). Our Egypt array was located at the northeastern edge of this basin.

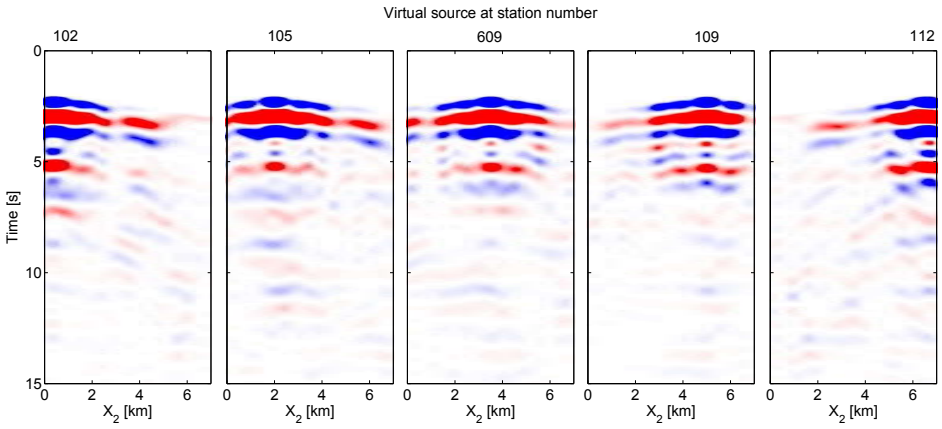


Figure 5.14 *Retrieved shotgathers for, from left to right, a virtual source at station number 102, 105, 609, 110 and 112, respectively, and receivers on all other station locations of subarray 2 (Fig. 5.1).*

5.7 Discussion and conclusions

We analyzed 40 hours of continuous data recorded by an array of three-component stations in Egypt. The purpose was to asses the applicability of body-wave SI.

We split up the noise in three distinct frequency bands (SF, DF and MF). For each band, we searched for the dominant noise sources by beamforming. The dominant noise sources turned out to be different for all considered bands.

The origins of the noise in the MF band seem to be largely unrelated to the DF microseism. This is consistent with the theory that the DF microseism is (indirectly) generated by swell, whereas higher frequencies are (indirectly) generated by local offshore winds (Kibblewhite & Ewans, 1985). In Zhang et al. (2009) the noise between 0.5 and 2.0 Hz showed a large correlation with regional offshore winds. For the Egypt array we did not compare the MF noise measurements with wind hindcasts. Still, between 17 and 40 hours (see Fig. 5.13), the rayparameters and backazimuths could be explained by regional and local winds in the Eastern Mediterranean. Between 0 and 17 hours, though, the detected rayparameters and backazimuths direct to a sources in the North Atlantic and Pacific. Hence, it turns out that, with the absence of local or regional winds, also teleseismic (offshore-wind) noise sources are detectable in the MF band.

After beamforming the Z-component of the SF-band, it turned out that it was dominated by surface waves. Since it was our aim to retrieve body waves, we did not further process this band. For the DF and MF band, we split up the total noise record in small windows. We computed, for each time window and for each component, the PSD and the dominant rayparameter. Doing so, we could unravel the dominant wavemodes. For the DF and MF

we found a dominance of P-waves on the Z-component and a mix of S-waves and surface waves on the other components.

Vinnik (1973) conjectured that P-waves would be the dominant wavemode at the Z-component, at epicentral distances of about 40 degrees from an oceanic source. At arrays far from offshore storms, surface waves induced by nearby storms would not mask the body-wave signal and hence primarily P-waves would be recorded. Our measurements in Egypt, which may be considered a shielded location for oceanic storms, supports his conjecture.

We found that considerable part of the Z-component noise panels in the DF and MF band was favorable for body-wave SI. The further processing of the noise records was very similar to the approach taken for transient records (Chapter 3). Only time windows with a favorable illumination and without surface-wave pollution, were further processed. We did not distinguish between panels dominated by noise or by earthquake responses. However, the contribution of the earthquake responses was little, since each record was normalized and only a few panels were dominated by earthquake responses.

We retrieved P-wave reflection responses and delineated reflectors in the crust, the Moho and possibly the Hales and Lehmann discontinuity. The results from the two frequency bands, MF and DF, turned out to be well complimentary. With noise from the MF band we obtained reflections between two-way traveltime about 1 and 7 seconds, while with DF noise we obtained reflections between 8 and 30 seconds and possibly even at later times. A longer noise registration would be necessary to find the reliability of possible transition-zone reflections. High-resolution reflection responses at shorter times can be obtained from noise at frequencies above 1 Hz, as was shown by Draganov et al. (2009).

The retrieved reflection responses could still be improved by better estimating the average autocorrelation of the noise ($S_n(t)$, see equation 5.3). In this study we estimated $S_n(t)$ by time-windowing stacked autocorrelations. This time window is truncated at the times we expect to see the first reflectivity. That is, at the time at which the gradual drop in energy from $t = 0$ onwards is broken by a local rise in energy. Though this might indeed indicate the time at which $S_n(t)$ is not dominating anymore, $S_n(t)$ has a much longer duration and might contain some notches at later times. To make a better estimation of $S_n(t)$, the autocorrelation should be repeated for a few stations that are detecting the same noise field, but are installed on very different locations.

Thus far it has been shown that ocean-generated body-wave noise may be used for P-wave tomography (Roux et al., 2005a; Zhang et al., 2010), for the retrieval of S-wave reflections (Zhan et al., 2010) and for the retrieval of P-wave reflections (this chapter). How about receiver functions (Langston, 1979)? In principle it is possible to use the same P-wave noise records for obtaining receiver functions. There are enough time windows with predominantly teleseismic P-waves arriving at the vertical component. Simultaneously though, the horizontal components pick up wavemodes with much higher rayparameters (Fig. 5.7d and 5.13d). The waves detected at the horizontal components are a mix of S-phases and surface waves. Hence, the challenge would be to clean out these wavemodes from the horizontal

components, such that only P-S converted waves are left. Alternatively, for some arrays one might be lucky to find time windows not contaminated by other waves than P-S conversions.

A large amount of empirical microseism studies have appeared over the years (e.g., Koper et al. (2010)). In addition, efforts are becoming increasingly successful for hindcasting microseismic sources. Based upon the theory by Longuet-Higgins (1950), Kedar et al. (2008) hindcasted pelagic microseismic Rayleigh-wave sources, using hindcasted ocean-wave data and bathymetry. The same modelling approach was used by Hillers et al. (2010) to identify deep-ocean regions with microseismic P-wave sources. Stutzmann et al. (2010) and Graham et al. (2010) included a model with reflection coefficients at the coasts to also hindcast microseismic sources near the continents. Hence, it becomes possible to assess where and when to measure to retrieve low-frequency P-wave reflection responses, now the microseismic (P-wave) source areas, and their yearly variations, are identified.

Compared to using earthquake records, the deployment time of arrays could be reduced if we use body-wave noise. With a favorable distribution of noise sources, a day to a week of noise recording would be sufficient, whereas a few months of array deployment would be needed to collect enough earthquake responses (Chapter 3).

Chapter 6

Basin imaging [1]

6.1 Introduction

After centuries of exploration, the world distribution of sedimentary basins is largely known (St John et al., 1984). Especially the search for aquifers and hydrocarbon bearing formations has contributed to this knowledge. Basins are currently not only used for extracting valuable resources, but also as a storage place of undesired gasses (Bachu, 2003). The overall architecture of a basin might be very complicated due to, for example, a rifting process that initiated its formation. For assessing the resource or storage potential of a basin, its dimensions play an important role. The spatial variation of total sediment thickness is also important for hazard assessment. It can be used for computing the possible amplification of earthquake induced ground motion (Herak, 2008). The thickness of the sediment package is also important for studies of the lower crust and mantle. A correction needs to be made for the basin before information of underlying rock can be unveiled. The vertical dimensions of a basin, however, are hard to constrain and might show large lateral discontinuities which are not easily resolved.

The lower interface, which is most commonly a contrast between sedimentary deposits and underlying crystalline rock, is a significant marker that shows up as a large signal in different geophysical measurements. Generally, crystalline rocks have a much higher density than sedimentary rocks. Therefore, the depth of the basin can be estimated from gravity measurements (Barbosa et al., 1997). Also, the basement rock contains a much larger amount of magnetic rock than the overlying sediments. Hence, the depth of the basement can be estimated from magnetic measurements (Salem et al., 2008). Both with gravity and magnetic methods the depth is quite poorly constrained as assumptions need to be made of the density or magnetic susceptibility of the basement. The basin-basement interface is also a large elastic impedance contrast, which makes it amenable to seismic detection. An

[1] This chapter will be published as a journal paper in Bulletin of the Seismological Society of America (Ruigrok et al., 2012a). With respect to the accepted journal version, minor changes have been introduced to make the text consistent with the other chapters of this thesis.

advantage of seismics is that only material properties of the sediment need to be known to find an accurate depth estimate of the basin-basement interface. However, the waves that are induced in a conventional surface-seismic campaign have too high of a frequency band to reach the lower portions of deep onshore basins. Even if they make it all the way down and up again, they have undergone multiple scattering which is difficult to use for reflection imaging. Using low-frequency sources is possible, but very costly. Therefore we look into passive seismic techniques.

In this study we process data collected with a densely-sampled seismic array in the Northeast Abu Gharadig Basin. This basin is located in the Western Desert in Egypt. It is part of a string of hydrocarbon bearing basins that cover the northeastern margin of Africa and share a similar history (Bosworth et al., 2008). These basins were formed in the Jura, during the breakup of supercontinent Pangaea. The Abu Gharadig is one of the more complex basins due to inversion of part of the extensional faults. This inversion occurred when the tectonic regime became compressional, when Africa started moving towards Eurasia. As a consequence, the basement depth varies significantly over the different basin blocks.

We restrict our data to a 40 hour period in which all stations were synchronically recording. In an earlier analysis of the same data (Section 5.3) we split up the low-frequency data into three distinct frequency bands, the SF- [0.03 0.09] Hz, the DF- [0.09 0.5] Hz and the MF-band [0.4 1.0] Hz. The analysis showed the SF band is dominated by surface wave noise coming from the SSW, while the DF- and MF- bands are dominated by body-waves noise coming from the SW and NW, respectively. The higher frequencies ($f > 1.0$ Hz) are dominated by surface-wave noise from the NE direction.

In principle, surface-wave noise can be used to obtain estimates of the basin depth. Toksöz (1964) and Asten & Henstridge (1984) estimated phase velocities directly from surface-wave noise. From the estimated dispersion curve they inverted for the basin depth. The errors turned out to be significant. Nowadays, the phase velocities can be more accurately determined by first applying seismic interferometry to the surface-wave noise (Shapiro et al., 2005). Still, the inversion of the phase velocities gives a limited resolution in depth, which makes it less suitable for our delineation purposes. Besides, we lack a sufficient recording of surface waves in the required frequency band. From the literature (Bosworth et al., 2008) it is known the basin-basement interface must be around 5 km depth. This interface is too deep to be resolved from the dispersion of surface waves with frequencies above 1 Hz and too shallow for frequencies below 0.09 Hz (e.g., Xia et al. (1999)).

The dominance of body-waves in the low-frequency noise makes the Egypt dataset excellent for comparing a few body-wave seismic techniques for basin delineation. In this study we consider three techniques: body-wave seismic interferometry (SI), (body-wave) horizontal-to-vertical ratio (H/V) and radial-component receiver function (RF). The working principle of these three methods is shown in cartoons (Fig. 6.1). SI (Schuster, 2009; Wapenaar et al., 2010a) can be seen as a filtering operation. Seismic records at two stations are crosscorrelated. When the records contain waves that traveled between both stations, these waves are

passed, while all other other waves are suppressed. For example, when a record contains reflected travel paths between a station at $\mathbf{x}_\mathcal{A}$ and $\mathbf{x}_\mathcal{B}$ (Fig. 6.1a, left) only the stationary reflection path between the two stations is passed —with the path between the actual source and one of the stations removed— while all the other arrivals are suppressed, given an adequate distribution of (noise) sources. After applying SI, effectively, a response is obtained as if there was a source at one of the stations (Fig. 6.1a, right). By extracting many of these reflection responses, at different offsets, a velocity model can be derived and the depth of the reflectors can be found.

Body-wave H/V-ratio (Nakamura, 2000) is a division of the amplitude spectra of body-wave noise recorded on the horizontal and vertical component. Through the division, source effects are largely removed. If P-and S-wave noise is used with a near-planar incidence (Fig. 6.1b, left), then H/V approximates the ratio of the S-wave and P-wave amplification spectra (Fig. 6.1b, right). This latter ratio can be inverted to derive layer properties of the top layer(s) (Herak, 2008).

RF (Langston, 1979) is also a ratio between a horizontal and vertical seismogram. However, RF is a complex spectral division. Through this deconvolution, source effects are removed from the horizontal component. If a time-window is selected around the P-phase arrival of a distant earthquake, the vertical component will primarily detect P-waves (most prominently Pp), while the horizontal component will primarily register P-S converted waves (most prominently Ps, see Fig. 6.1c, left). The deconvolution result is called the receiver function. From this resulting trace, the traveltime difference of P-and S-waves ($t_{Ps} - t_{Pp}$) can be read (Fig. 6.1c, right). When velocity information is available, this traveltime difference can be used to find the depth of the layer(s).

SI is only very recently being developed and is considered for extracting Earth structure at many different scales (e.g., Galetti & Curtis (2011)). SI may be applied to only one station, but more regularly data at different stations is combined. H/V is most popularly employed for constraining near-surface S-wave models for geotechnical purposes, but has also been applied for basin studies (Martini et al., 2011). RF is especially used for delineating structure in the lower crust and upper mantle. Both H/V and RF were developed as single station operations.

In this study we will first briefly analyze the 40 hour noise record. This noise analysis is required to determine what parts of data are to be used as input for the different passive seismic techniques. In the remainder, we will apply the different techniques (SI, H/V and RF) to the data with the aim to delineate the basin-basement interface. Through this exercise we are learning which techniques are best fit for this purpose.

6.2 Noise analysis

The location of the seismic array, which will be denoted with the Egypt array in the following, is about 230 km west of Cairo. While the area is unpopulated, there is some activity

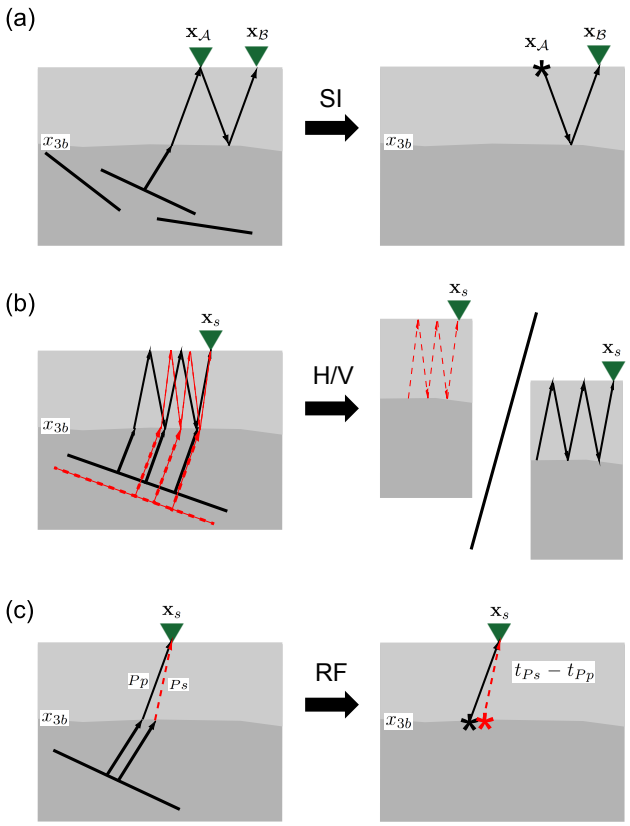


Figure 6.1 *A cartoon illustration of the three passive seismic techniques that are considered in this study: (a) body-wave seismic interferometry (SI), (b) body-wave horizontal-to-vertical ratio (H/V) and (c) receiver function (RF). For each technique, the input (left) and output (right) are shown for a one-layer-over-a-halfspace model (basin overlying a basement), with receivers (triangles) on the Earth's surface. The illumination is from below with plane P- (solid line) and or S-waves (dashed line). From the plane-wave illumination the relevant rays (lines with arrows) to the receivers have been drawn. On the right-hand figures, stars denote (effective) line sources. The subscripts $_{\mathcal{A}}$ and $_{\mathcal{B}}$ are used to distinguish two different stations. Otherwise, the subscripts $_s$ is used to denote the station is on the free surface. x_{3b} is the depth level of the basin-basement interface.*

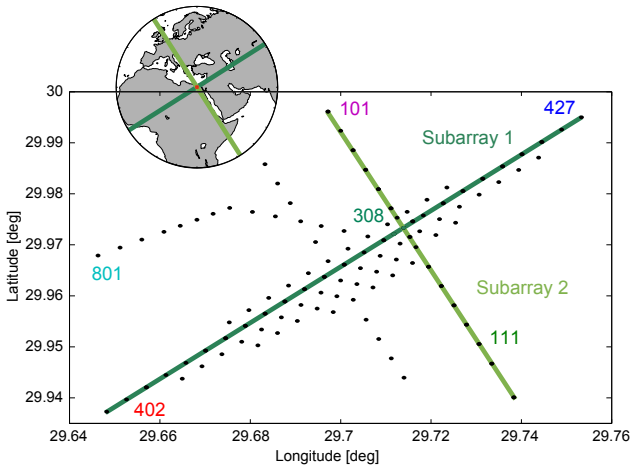


Figure 6.2 *The layout of the Egypt array and the geographic setting (inset). The station positions are indicated with dots. For a few specific stations, that will be used in the following, the station numbers are given. Two linear subarrays are denoted with straight lines, which orientation is also plotted in the inset. The color version of this figure is available only in the electronic edition.*

related to oil-and-gas production. During the day, several dirt tracks in the area are being used by traffic from local producers. The nighttime is very quiet.

Fig. 6.2 shows the geographical setting and the receiver layout. 110 broadband three-component seismometers (Trillium T40) were placed in five parallel lines and three cross lines at varying angles. Inline interstation spacing was 500 m, with a more densely sampled (350 m) area in the middle of the array. In total, about 60 hours of noise were simultaneously recorded on all 110 stations.

We restrict our data to a 40 hour period, starting October 12 2009. Fig. 6.3 depicts the power-spectrum-density (PSD) variation for these 40 hours and for all 3 components. The energy that is fairly constant over time is related to microseisms, while the transient events are caused by earthquakes. For more details, see Chapter 5. In the same chapter we classified the noise in three distinct frequency bands, encompassing different types of microseism (the SF-, DF- and MF-band, see Fig. 6.3). We found that the Z-component (vertical-component) noise in the higher frequency band (the MF-band [0.4 1.0] Hz) could be used to retrieve reflections from the upper crust. In this section we restrict ourselves to this higher frequency band. We will study the waveform content of all three components.

First, we split up the 40 hour records in windows of 5 minutes. For each time window we estimate the dominant rayparameter p_{dom} and backazimuth θ_{dom} (dominant illumination) through beamforming (Lacoss et al., 1969). A single time-window might simultaneously

pick up noise from different directions and distances. Therefore, we also estimate the second most dominant backazimuth and rayparameter combinations (subdominant illumination). Fig. 6.4 shows these estimated dominant and subdominant waveform distributions in rayparameter-backazimuth space. We leave out the E-component, since the distributions are fairly similar for the horizontal components.

The array response is not perfect over the complete (p,θ)-space under consideration. Consequently, a single plane wave maps to a main lobe at the true (p,θ)-coordinate, but also to small side lobes (aliasing). For the Z-component, the subdominant illumination maps primarily to the aliased side lobes of the dominant illumination (see the symmetry). Hence,

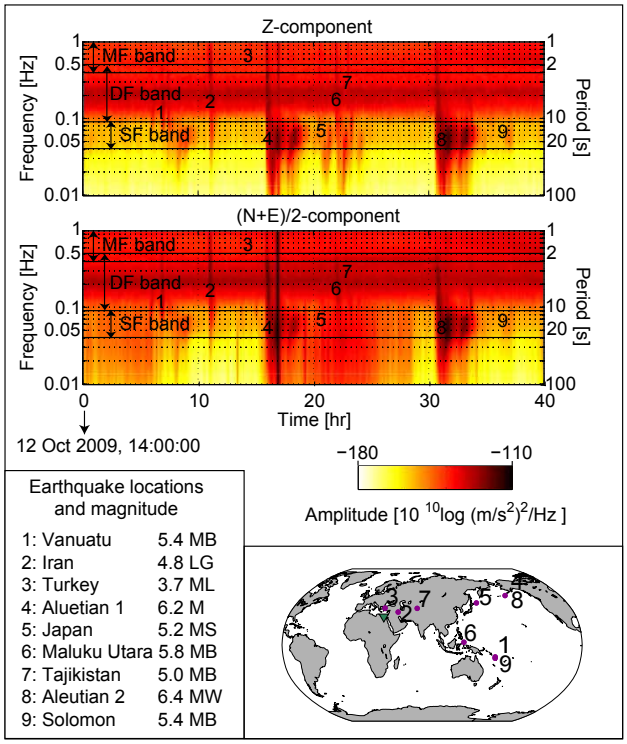


Figure 6.3 *The noise spectrograms (upper figure box) for the vertical (Z) and an average of the horizontal components ((N+E)/2), made up by a concatenation of power-spectrum densities based on 10 minute records detected at station 402. The transient events are caused by earthquakes. The identified earthquakes and their magnitudes (given in various scales) are listed in the lower-left box and are indicated on the spectrograms. Their locations are plotted on a world map (lower-right box). The data between 0.03 and 1.0 Hz are divided into three frequency bands (MF, DF and SF) marking different characteristics of the noise in the various bands.*

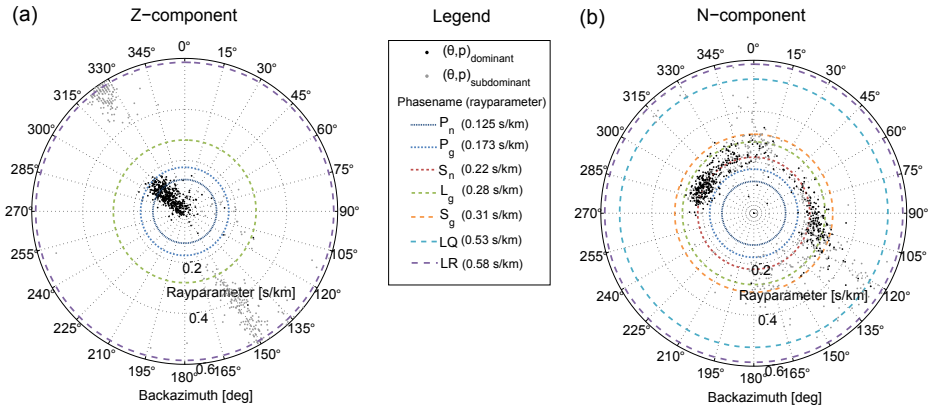


Figure 6.4 *The estimated dominant (black dots) and subdominant (grey dots) illumination for the (a) Z- and (b) N-component noise, respectively. One dot in the rayparameter-backazimuth space corresponds to the plane-wave direction and angle of incidence with the largest (or second-largest) beampower. The beampower is obtained by beamforming 5-minute time-windows, frequency limited between 0.4 and 1.0 Hz. For interpretation, rayparameters of common regional phases (see legend) have been added to the radar displays.*

the time-windows may be assumed to be dominated by one plane-wave only. The horizontal components, on the other hand, show a rich distribution of subdominant illumination which is not due to aliased side-lobes of the dominant illumination. Hence, for the horizontal components, subdominant illumination cannot be neglected.

Fig. 6.4 maps the rayparameters of a number of crustal phases to ease identification of the detected waveforms. When considering distant sources near the Earth's surface, all time-windows that map to points within the P_n and S_n ring must be dominated by teleseismic or global P-wave and S-wave phases. For a description of the phases, see, e.g., Storchak et al. (2003). LR (fundamental-mode Rayleigh wave) and LQ (fundamental-mode Love wave) have relatively low velocities and hence high rayparameters. This is due to the basin setting of the array and the relatively high frequencies of the MF-band noise.

Judging from Fig. 6.4(a) the noise on the Z-component contains primarily global and teleseismic phases, but also some regional phases. The backazimuth range is quite narrow and points towards microseismic sources in the Mediterranean and North Atlantic and possibly even the North Pacific.

The rayparameters on the horizontal components are significantly larger (Fig. 6.4b) and can be explained by a mix of lithospheric phases, S_g, L_g and S_n (Isacks & Stephens, 1975). It turns out that the horizontal components do not pick up body waves induced by primary sources in the North Atlantic and North Pacific. The backazimuth range for the horizontal components is much larger than the range of the P-waves. Moreover, this backazimuth range shows a clear correlation with the coasts near the Egypt array (compare Fig. 6.4b with the

inset in Fig. 6.2). Thus, it seems that the horizontal components pick up mostly lithospheric phases from nearby coasts (Mediterranean coast in the NW and the Red Sea coast in the ESE), which are either directly induced near the coast or converted at the ocean-continent transition.

6.3 Body-wave seismic interferometry

In this section we show results of applying SI to noise detected at subarray 2 (Fig. 6.2). Three component particle-velocity noise recordings in principle allow the reconstruction of 9 components of the Green's functions, between two station locations, $\mathbf{x}_{\mathcal{A}}$ and $\mathbf{x}_{\mathcal{B}}$, where $\mathbf{x} = (x_1, x_2, x_3)$ denotes a position vector and the subscripts $_{\mathcal{A}}$ and $_{\mathcal{B}}$ distinguish two different stations when their position vectors are not written out explicitly. Each component of the Green's function is the combination of a traction source at $\mathbf{x}_{\mathcal{A}}$ in one of the orthogonal directions and a particle velocity sensor at $\mathbf{x}_{\mathcal{B}}$ in one of the orthogonal directions (Wapenaar & Fokkema, 2006). In our case, the vertical component detects different wavefields than the horizontal components (Fig. 6.4). Consequently, crosscorrelations between these components are extremely noisy, contain little to no subsurface information and are thus omitted. Also we leave out combinations between the radial and transverse component. Hence, we only retrieve the vertical, radial and transverse particle-velocity responses due to a vertical, radial and transverse traction source, respectively. Details about interferometrically processing the Z-component noise can be found in Sections 5.4 and 5.6. Applying SI to the horizontal components involves an additional preprocessing step, which is the rotation of the noise records from North (N) and East (E) to radial (R) and transverse (T). To ease processing, we define R and T with respect to subarray 2, rather than the (varying) source. For the horizontal components, only time windows are used with dominant sources approximately inline with subarray 2. Time windows with θ_{dom} varying up till 20° from the subarray orientation are still accepted. Therefore, effectively, R- and T- are still closely related to the backazimuth of the actual (primary) source. For the Z-component noise panels a backazimuth filter is not required since the illumination is anyway restricted to backazimuths close to the orientation of subarray 2 (Fig. 6.2 and 6.4a).

Fig. 6.5 shows the retrieved responses for a virtual source at the location of station 609 and receivers at all station positions of subarray 2. To interpret the different events we started off with the regional model from the Cornell Middle East and Africa Project (Seber et al., 1997) and adjusted it to correspond to the data. This model contains P-wave velocity information down to the upper mantle. However, the different basin blocks, as have been interpreted in, e.g., Bosworth et al. (2008), have been averaged out. Consequently, the largest change is increasing an average basin depth from the regional model (3 km) to a local basin depth of 4.8 km. This is not an unreasonable adjustment considering that nearby oil-bearing sediments were found at depths below 3 km (Franssen & Hoogerduijn Strating, 2006; Hoogerduijn Strating & Postuma, 2008). For this updated model (Fig. 6.5a) we compute traveltime curves for the most prominent reflections and overlay these to the retrieved

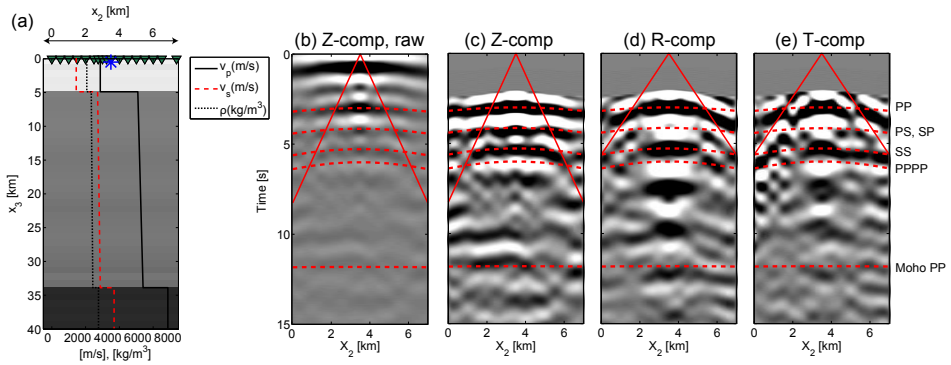


Figure 6.5 *(a) In gray shading, a P-wave velocity model of the crust below the Egypt array, augmented with a depth profile of the P-wave (solid line) and the S-wave (dashed line) velocity and the density (dotted line). The triangles on the top of the figure denote the station locations of subarray 2. The virtual source station is overlain by a star. (b) The result after applying seismic interferometry to Z-component noise, for a virtual source at station 609 and receivers at all stations of subarray 2. (c) shows the same retrieved response as (b) after muting the (spurious) direct wave. (d) and (e) are the retrieved responses using R- and T-component noise, respectively. On (c)-(e) the thick red lines boarder a fan within which physical retrievals may be expected. The dashed lines are two-way traveltime curves for a few prominent reflections, which were computed using (a).*

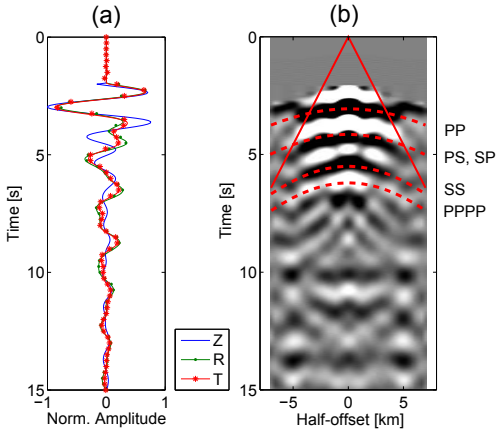


Figure 6.6 *(a) The middle traces from Fig. 6.5(c)-(e) and (b) The Z-component common-midpoint (CMP) gather for a midpoint coinciding with the middle station in subarray 2.*

responses (Fig. 6.5b-e). PP is the two-way traveltime curve of a primary P-wave reflection from the basin floor, whereas SS and PPPP denote the traveltime curve for the same interface, of an S-wave reflection and P-wave multiple, respectively. PS and SP are the P-S and S-P converted reflections on the basin-basement interface, respectively. The red solid lines in Fig. 6.5b-e denote the traveltimes after which physical retrievals may be expected, given the used illumination range (see equation 3.8). This is called the response-restriction function in the following. For the Z-component noise we used only time-windows with $|p_{dom}| < 0.08$ s/km, while for the horizontal-component noise we used time windows with dominant absolute rayparameters up till 0.35 s/km. Because a larger illumination range was used for the horizontal components, at a larger part of the $t - x$ space physical retrievals may be expected.

The effective wavelet is a flipped Ricker wavelet (white-black-white) with possibly still some additional ringing (Section 3.4). If the ringing was severe, this would lead to ghost arrivals in the retrieved responses (Fig. 6.5c-e). These ghost arrivals would show up as repetitions of a main arrival. The repetitions would have the same move-out (dt(x)/dx) as the main arrival. The general trend, though, in Fig. 6.5c-e is smaller move-outs for events at larger times. This is the traveltime behavior that is expected for (primary) reflections.

For all components PP is clearly retrieved. On the vertical component (Fig. 6.5c), this reflection has a realistic move-out over much of the considered offset range. For the horizontal retrievals (Fig. 6.5d&e), at larger offsets, the move-out behavior of the retrieved reflection deviates from the expected traveltime function. This might be due to interference with guided waves. PS and SP seem to be weak and cannot well be distinguished. The next clear event in Fig. 6.5(c)-(e) (at about 5.5 s) could be explained by either a P-wave multiple from the basin-basement interface, or an S-wave primary from the same reflector. On the horizontal components the event arrives just too late to be PPPP, but it fits well with SS when a v_p/v_s ratio is taken of 1.8, which is a common value for consolidated sediments. On the vertical component it is ambiguous whether PPPP, or SS, or a combination of the two, is retrieved. Fig. 6.6(a) shows a comparison of the retrieved responses for coinciding source and receiver position, for the 3 components. The P-wave reflection has a higher relative amplitude on the Z-component, while the S-wave reflection has a higher relative amplitude on the horizontal components.

Fig. 6.5(b)-(e) show the responses for a single source and many receiver positions. Each receiver is at a different offset from the source and therefore the reflections points in the subsurface differ. Only when the subsurface does not vary laterally, this representation of the data can be used for velocity analysis. To improve the velocity analysis we resort the Z-component retrievals in a response for which the reflection points are approximately the same for the different traces. Fig. 6.6(b) shows one resulting common-midpoint gather (Yilmaz & Doherty, 2000). It can be seen that with this representation the modeled PP and SS/PPPP better fit with the data. Note that the timing and move-out of the retrieved PP and SS/PPPP largely corresponds with the forward modeled curves (dashed lines), within the range where physical retrieval are expected (which range is bounded by the red lines). The

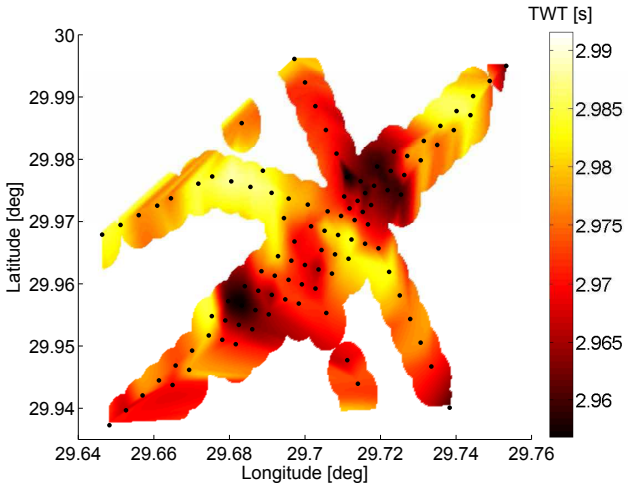


Figure 6.7 *Top-Basement interpolated two-way P-wave traveltimes (TWT) for coinciding source and receiver positions.*

velocities cannot be estimated with high precision, however, due to the limited offset-range, the limited bandwidth and small illumination artifacts.

Bosworth et al. (2008) analyzed gravity data and seismic sections for basins in NE Africa. They interpreted the Abu Gharadig basin to be around 5 km deep near the array. From the retrieved reflections we find a basin depth of 4.8 km (Fig. 6.5a). The Moho reflection is expected to arrive around a two-way traveltime of 12 s, with an almost flat move-out. In Fig. 6.5c-e some near flat events can be seen around this time. However, the amplitudes are too low for interpretation.

As a final processing step, we retrieve the Z-Z reflection responses for coinciding source and receiver position, at every station of the array, using the same data selection as was used for obtaining Fig. 6.5(c). Subsequently, we determine the timing of the retrieved P-wave basement reflections ($t(\mathbf{x}, h0)_{pp}^{basin}$). Fig. 6.7 shows a cubic interpolation of the picked arrival times. All stations used in the interpolation are shown as black dots. It turns out that the spatial time differences are minimal for the P-wave reflection. The dynamic range is 0.03 seconds, which would map to basement-top undulations of maximally 96 m using the average estimated P-wave velocity of 3.2 km/s. However, the timing differences may be as well described to lateral variations in sediment infill rather than basin-depth variations. The discontinuous nature of the lateral variations could be caused by faulting within the basin.

6.4 H/V-ratio

It is well known that a spectrum of a reflection response contains many notches, even if the source had a flat spectrum. These notches are due to the resonances of the different layers. The resonance or amplification spectrum for S- and P-waves can be computed for an arbitrary stack of layers overlying a homogeneous halfspace (Herak, 2008). Vice versa, medium properties of the layers can be inverted from a measured amplification spectrum.

6.4.1 Noise records

We assume a simple model of a one-layer sedimentary basin overlying a homogeneous halfspace, the basement. The observed P-wave and S-wave amplitude spectra can be written as

$$|\hat{v}^P(\mathbf{x}_s, f)| = |\hat{G}^P(\mathbf{x}_s, x_{3b}, f)\hat{G}^P(x_{3b}, \mathbf{p}^P_{dom}, f)\hat{N}^P_{dom}(f)|, \tag{6.1}$$

$$|\hat{v}^S(\mathbf{x}_s, f)| = |\hat{G}^S(\mathbf{x}_s, x_{3b}, f)\hat{G}^S(x_{3b}, \mathbf{p}^S_{dom}, f)\hat{N}^S_{dom}(f)|, \tag{6.2}$$

where f is the frequency, x_{3b} denotes the depth level of the basement below the array and $\mathbf{x}_s$ denotes a surface position vector. The hat above the quantities denotes that they are in the frequency domain. The right-hand side of equations 6.1 and 6.2 contain three terms. The far-right term, $\hat{N}_{dom}$, is the spectrum of the dominant noise source. The middle term is the Green's function describing the propagation of the dominant phase, parameterized with $\mathbf{p}_{dom} = (p_{dom}, \theta_{dom})$, to the basement below the array. Finally, the left term describes the propagation through the sedimentary basin. The transmission coefficients between the basement and basin have been left out, since they do not significantly affect the shape of the measured spectra. For the same reason, P-S and S-P conversions have been left out.

$|\hat{G}^{P,S}(\mathbf{x}_s, x_{3b}, f)|$ is the $P-, S-$ wave (amplification) spectrum of the sedimentary basin. In the following, we try to find this spectrum from the measurements. First, we approximate the P-wave and S-wave spectra with the vertical- and transverse-component spectra, respectively. For this approximation to hold, we would need to select data with almost vertical incidence. Secondly, we assume that not any serious resonances occur —at least not in the frequency band of interest— before the waves enter the sedimentary basin. With this assumption, $\hat{G}^{P,S}(x_{3b}, \mathbf{p}^{P,S}_{dom}, f)$ has a flat spectrum in equation 6.1, 6.2 and can be left out, yielding:

$$|\hat{v}^Z(\mathbf{x}_s, f)| \approx |\hat{G}^P(\mathbf{x}_s, x_{3b}, f)\hat{N}^P_{dom}(f)|, \tag{6.3}$$

$$|\hat{v}^T(\mathbf{x}_s, f)| \approx |\hat{G}^S(\mathbf{x}_s, x_{3b}, f)\hat{N}^S_{dom}(f)|, \tag{6.4}$$

Still, in equation 6.3 and 6.4 the resonance spectra of the basin are obscured by the noise spectra. To remove this latter influence, we would need to select time-windows where the P- and S-wave noise spectra are similar. This would be achieved when all components are picking up noise from the same source areas. Using these time-windows, we divide the measured transverse-component (amplitude) spectrum by the vertical-component spectrum

to obtain the $H/V(f)$-ratio, as is a common technique (Nakamura, 2000):

$$H/V(f) = \frac{|\hat{v}^T(\mathbf{x}_s, f)|}{|\hat{v}^Z(\mathbf{x}_s, f)|} \approx \frac{|\hat{G}^S(\mathbf{x}_s, x_{3b}, f)|}{|\hat{G}^P(\mathbf{x}_s, x_{3b}, f)|}. \tag{6.5}$$

At the low-frequency side, this ratio is colored by the first resonance frequency f_0 from the P- and S-wave amplification spectra. This resonance frequency can be expressed as (Tsai, 1970):

$$f_0^{P,S} = \frac{v_{P,S}}{4d}, \tag{6.6}$$

where d denotes the thickness of the layer and $v_{P,S}$ denotes the P-wave or S-wave velocity. Hence, from $f_0^{P,S}$ the depth of the basin can be computed when average velocities are known for the basin.

We select a 5 hour interval of noise (hour 35 to 40, see Fig. 6.3) for which θ_{dom} for all components is similar. We rotate the data using θ_{dom} (305°) to obtain a radial and transverse component. We consider the frequency band [0.06 - 0.9] Hz. Though there is contamination, the noise on the Z-component and T-component may be assumed to be dominated by P- and S-waves, respectively (see Figs. 5.7 & 5.13), at least for frequencies higher than 0.09 Hz. P-wave leakage to the T-component and S-wave leakage to the Z-component lead to a size-reduction of the peaks and troughs in $H/V(f)$. Still the overall shape remains. For the 5 hour time interval we compute the power spectrum density (PSD) for the Z- and T-component for 6 different stations at the different corners of the array (station 427, 11, 402, 801, 101 and 308, see Fig. 6.2). For the PSD computation we use 75% overlying segments with 2^{14} samples per segment. Subsequently, as a stable implementation of equation 6.5, we divide the T-component PSD by the Z-component PSD to obtain the horizontal-to-vertical spectral ratio. As a last step, we average the $H/V(f)$ over the 6 stations.

Fig. 6.8 shows both the H/V for the 6 individual stations (colored lines) and the average H/V (black line). f_0^P would lead to a notch in the $H/V(f)$-ratio. However, it is hard to identify these minima in $H/V(f)$, if present. f_0^P is always larger than f_0^S and therefore $H/V(f_0^P)$ is generally obscured by higher resonance frequencies in $|\hat{G}^S(\mathbf{x}_s, x_{3b}, f)|$. f_0^S would lead to a maximum in the $H/V(f)$-ratio. These can easily be identified in Fig. 6.8. Three clear resonance extrema can be seen, at 0.085, 0.32 and 0.83 Hz. These peaks must be related to $|\hat{G}^S(\mathbf{x}_s, x_{3b}, f)|$. The first peak is likely at a fundamental resonating frequency. Using equation 6.6 with v_s=1.85 km/s (from model 6.5a) we find it is related to a resonating layer with a thickness of 5.4 km. This layer is most likely the complete sedimentary column. The two other extrema might be caused (partly) by higher resonating frequencies from the same layer or by other distinct resonating layers within the sedimentary column. If they were fundamental resonating frequencies from other layers, the layer thicknesses would be about 1.4 and 0.56 km. A probable model could be obtained through inversion (Herak, 2008). Because of wavemode complications (see paragraph below) we leave out such inversion.

With H/V we estimate the basin depth to be 5.4 km. This is somewhat deeper than estimated

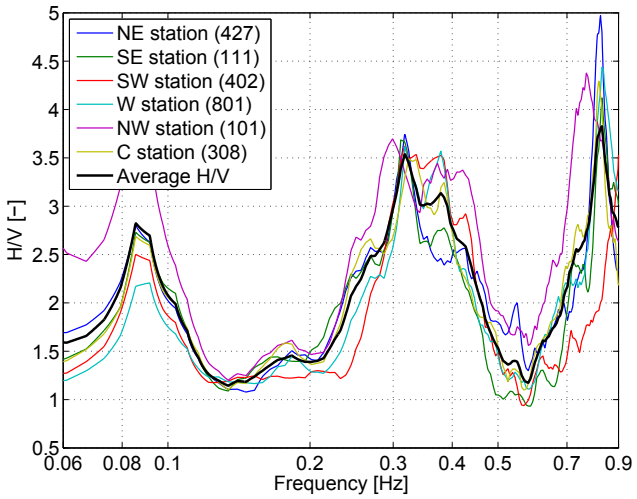


Figure 6.8 *H/V-ratio averaged over 5 hours of noise for 6 stations (thin lines), at different corners of the array. With the same colors these stations are indicated on Fig. 6.2. The color version of these figures are available only in the electronic edition. The thick line denotes the H/V-ratio averaged over the 6 stations.*

with SI (4.8 km). The resonance peak is at a frequency (0.085 Hz) which is within the band [0.03 - 0.09] Hz, which was found to be dominated by surface waves (Section 5.3). Therefore, it is surprising that H/V-ratio still gives a reasonable estimate of the basin depth. However, Lermo & Chavez-Garcia (1994) show that also the surface-wave H/V (ellipticity) has an extremum at f_0^s.

6.4.2 Earthquake records

We also measured S-phase arrivals from earthquakes, in the frequency range where f_0^s related to the basin is expected. So, we can independently estimate f_0^s, as was empirically shown in Field & Jacob (1995). Their model is quite similar to the one for noise, expressed in equations 6.1-6.5. The main difference is that the noise source spectra in equations 6.1 and 6.2 are replaced by earthquake source spectra. Further, Field & Jacob (1995) assume that the vertical component, during the S-phase arrival, is dominated by S-P conversions. In this case, the term $\hat{G}^P(x_{3b}, \mathbf{p}, f)$ in equation 6.1 would need to be replaced by $\hat{G}^S(x_{3b}, \mathbf{p}, f)$. With this change and using the same approximations as before, again equation 6.5 is obtained.

We choose an earthquake that contains broadband S-phase arrivals (Aleutian 2, no.8 in Fig. 6.3) which occurred at 96.1° from the array. We select a 1000 s time-window, which includes SKS, SKKS and SS, and compute the PSD for the Z- and T-component, using the

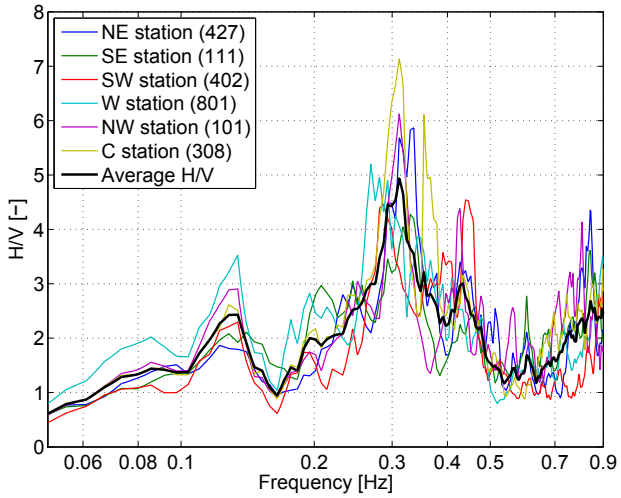


Figure 6.9 *H/V-ratio averaged over a 1000 s interval dominated by S-phases from the Aleutian 2 earthquake (Fig. 6.3, no. 8), for 6 stations (thin lines), at different corners of the array. With the same colors these stations are indicated on Fig. 6.2. The color version of these figures are available only in the electronic edition. The thick line denotes the H/V-ratio averaged over the 6 stations.*

same recipe as before. The resulting PSDs are used to compute $H/V(f)$. Fig. 6.9 shows the resulting $H/V(f)$ for the same 6 stations as in Fig. 6.8. This time, two clear resonance extrema can be seen, one at 0.13 and one at 0.31 Hz. Again, these peaks must be related to $|\hat{G}^S(\mathbf{x}_s, x_{3b}, f)|$. Using again equation 6.6 with $v_S = 1.85$ we find two resonating layers with thicknesses of 3.6 and 1.5 km, respectively.

6.4.3 Comparison

When comparing Fig. 6.8 and 6.9 we find large similarities in the middle frequency band, where both are dominated by body waves. With both methods the extremum at about 0.31 Hz is resolved. Note that the $H/V(f)$ amplitudes are different. This is also expected, since the one method (Fig. 6.8) has direct P-wave illumination, while the other method (Fig. 6.9) has primarily S-P conversions on the vertical component . At the higher end of the frequency band, the noise $H/V(f)$ (Fig. 6.8) has a clear peak, while for the earthquake $H/V(f)$ (Fig. 6.9) this extremum is poorly developed. This is not unexpected, considering that for the earthquake H/V, especially, core phases were used, for which the higher frequencies are attenuated. At the lower end of the frequency band, both methods resolve a different extremum. The extremum found with the noise is indicative of the ellipticity of the surface waves. The ellipticity, for this frequency band, is governed by the complete sedimentary package and thus a thickness estimate of the complete package is resolved (5.4 km). The

extremum found with the earthquake S-phase arrivals seem to be indicative of the resonance of a single layer within the sedimentary package. Based on this interpretation the basin thus seems to consist of two distinct layers with a thickness of 3.6 and 1.5 km, resulting in a total thickness estimate of 5.1 km.

6.5 Receiver function

With the receiver function (RF) method a clean P- or S-phase from a distant earthquake is used (Langston, 1979). We will only apply it to P-phase arrivals, as the recorded S-wave phases are severely contaminated with P-wave coda. For a P-phase response it is assumed that all recorded S-waves are due to conversions in the lithosphere below the stations. The RF can be seen as a scaled version of the R-component, deconvolved for the source-time-function and with the removal of P-wave multiples (Ammon, 1991). Consequently, on the RF, the arrival times of the converted waves with respect to the direct P-wave can be picked. When a velocity model is known, the traveltime differences between the P-wave and the subsequent P-S conversions can be used to find the depths of the interfaces.

The best RFs are achieved when the P-phase is recorded over a broad frequency band. This is the case for both the Aleutian 1 and 2 earthquake (nos. 4 and 8 in Fig. 6.3). Fig. 6.10 shows the RFs. On the left-hand side the RFs are plotted for stations in subarray 2 (see Fig. 6.2). The RFs vary from station to station. E.g., between 5 and 10 s two phases with a large move-out can be noticed. Since the subsurface may be assumed to be approximately layered for the offset-range and frequencies considered, these phases are unlikely part of the RF. More likely, these phases are caused by microseism contamination. Indeed, for both earthquakes there is still considerable microseism energy on the Z- and R-component. Consequently, also the RFs will be affected. These microseism related events turned out to have the largest move-out on subarray 2. Therefore, the RFs are averaged over this subarray to yield the final RFs, as displayed on the right-hand side in Fig. 6.10.

We will attempt to explain the final RFs with the model obtained by adjusting a starting model with the SI results (Fig. 6.5a). The model contains a basin (depth=4.8 km) and crystalline crust (depth=34 km) overlying a homogeneous halfspace (the mantle). To clearly identify the different phases, first we forward model a direct plane-wave P-wave response with a Ricker wavelet with a central frequency of 1.0 Hz (Fig. 6.11a). We use the raypa-rameter of the P-phase from the Aleutian responses (0.04 s/km). The synthetic response for this two-layer-over-a-halfspace model contains just the direct P wave (Ppp), the conversion on the basement-basin interface (Pps), the conversion on the Moho (Pss) and the conversion on both interfaces (Psp). This last arrival has a negligible amplitude with respect to the other arrivals and is therefore hardly noticeable in Fig. 6.11. The R-component in Fig. 6.11(a) is hard to interpret due to the complicated source-time-function used in the forward modeling. However, after deconvolving R- with the Z-component —thus on the RF— both interfaces show a clear imprint. In Fig. 6.11(b) we choose a central frequency close to the observed one of the Aleutian P-phase arrivals ($f_0 = 0.2$ Hz). Now the Z- and R-component

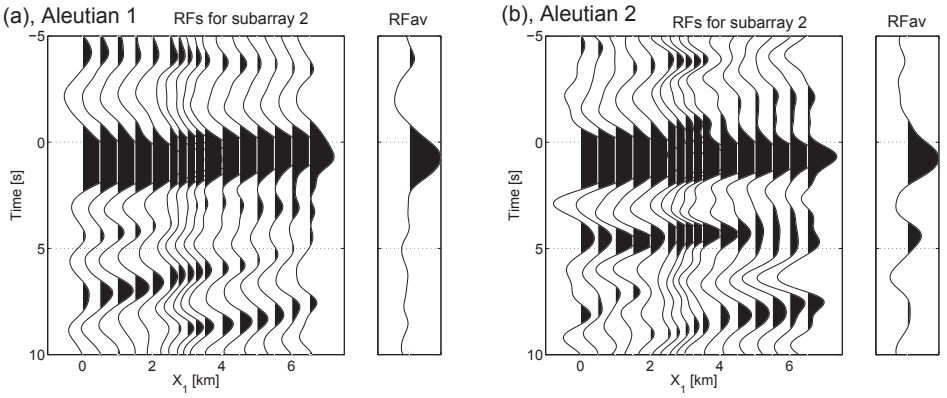


Figure 6.10 *Receiver functions (RFs) for (a) event Aleutian 1 and (b) event Aleutian 2 (see Fig. 6.3). On the left-hand sides all RFs for subarray 2 (see Fig. 6.2) are shown while on the right-hand sides the averages over all these RFs are plotted.*

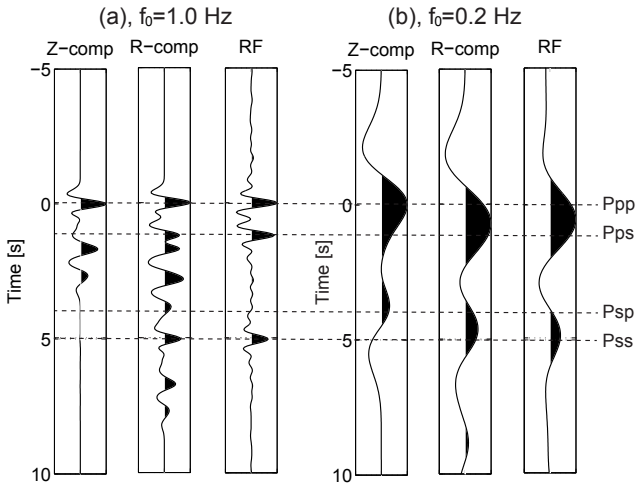


Figure 6.11 *Synthetic P-wave forward scattered responses for the model in Fig. 6.5(a) and a ray-parameter of 0.04 s/km, for a source-time function composed of Ricker wavelets with a central frequency of (a) 1.0 and (b) 0.2 Hz. To achieve the same sign of the phases as in Langston (1979) the R-component points away from the source and the Z-component points upwards.*

responses and also the RF only show the event due to the Moho conversion clearly. Pps and Ppp interfere constructively to a phase with t=0.5 s in the RF. In principle, this time shift with respect to t=0 could be used to find the depth of the basement-basin interface.

For the field data RFs (Fig. 6.10), a similar time-shifted phase near $t = 0$ can be seen as in the forward modeled RF (Fig. 6.11b). For the field data, the time shift of the peak is 0.74 and 0.77 s for Aleutian 1 and 2, respectively. These time shifts are considerably larger than the one of the forward modeled RF (0.5 s). Yet, it is complicated to use this time-shift to update the model. This time shift is caused by an interference and is not only dependent on the traveltime difference between Ppp and Pps, but also on the near-surface amplification of Pps with respect to Ppp. Furthermore, in addition to the basin-basement interface, there might be shallower interfaces that lead to conversions that also add to the interference pattern.

The main other phase in the forward modeled RF is due to the Moho conversion (Pss). This event seems to be well resolved in the average RF for Aleutian 2 (Fig. 6.10b). In the average RF for Aleutian 1 (Fig. 6.10a) the same event is not visible, possibly due to destructive interference with microseism related noise.

To map an observed traveltime difference to depth, a P- and S-wave velocity model would be required. Here we could use the one updated by body-wave SI (Section 6.3). Otherwise, e.g., a velocity model obtained by surface-wave inversion or body-wave tomography could be used.

6.6 Discussion and conclusions

We analyzed 40 hours of data recorded over the Abu Gharadig Basin in Egypt. In an earlier study we found the frequency band of [0.09 1.0] Hz to be dominated by body waves. To this band, we applied a variety of passive seismic methods with the goal to obtain the depth (variation) of the sedimentary basin. From the literature it is known that this interface is located at about 5 kilometers depth. With body-wave seismic interferometry (SI) we could extract PP and SS reflections from this interface. The Z-component responses contained a broad illumination band inline with a subarray, unlike the horizontal components. Consequently, the best-quality reflection responses were obtained for the vertical component. Using those, we could confirm the depth of the basin to be around 4.8 km. Also, we could extract spatial traveltime differences of PP reflections, but we could not uniquely relate these to basin-depth topography or spatial variations within the basin. As a second technique we estimated the resonance spectrum of the basin, using the horizontal-to-vertical spectral ratio (H/V). Using surface-wave noise, we found an extremum in the H/V (ellipticity) which is related to the complete sedimentary package. Using this extremum, we found a basin depth of 5.4 km. Using S-phase arrivals, we found two extrema in the H/V, which are probably related to the S-wave resonances of two distinct layers in the basin. Adding up their estimated thicknesses, we found a basin depth of 5.1 km. Thirdly, with a RF study we could confirm the presence of a large interface in the upper crust. However, for the frequency range that was needed to achieve good-quality RFs, the conversion on the basin-basement interface could not directly be observed. Instead, an interference pattern was seen between the P and S transmission. This interference pattern could not reliably be inverted for the basin depth.

Using a 40 hour passive record, we did succeed in finding the average depth of the basin, using body-wave SI. Also we found that the lateral variations of the basin floor are less than 100 m below the array. Thus, we could establish that the entire array is located within the same basin block.

For H/V a large number of approximations had to be made (Beq. 6.1–6.5). Moreover, the results could only be interpreted with some prior information about the basin, like the amount of resonating layers expected. Therefore, H/V seems to be more suitable for testing a certain model rather than for exploration purposes.

Body-wave SI gave good results on the Z-component, due to a balanced noise illumination inline with one of the subarrays. The retrieved responses on the horizontal components were of a lesser quality, due to missing illumination with steep angles of incidence and subdominant illumination not inline with the subarray.

Worldwide, basin depths may vary from virtually ground level to about 15 km (Laske & Masters, 1997). Body-wave H/V will be especially useful in the delineating a basin when its depth does not exceed more than 3 km. For reliably delineating larger depths, body-wave noise would be required in the SF-band. Ambient noise in the SF-band is predominantly caused by the interaction of ocean swell waves with continental shelves (Webb, 2002). This interaction does not seem to induce body waves of any markable size. Hence, for larger depths, surface wave H/V ratio would need to be used.

Body-wave SI, on the other hand, is easier to apply when the basin depth exceeds 2 km. For shallower interfaces, body-wave noise above 1 Hz would be required, which tends to be obscured by surface wave arrivals. When noise below 1 Hz is used, reflections from shallower interfaces are covered by a spurious direct wave.

The third considered method, using teleseismic receiver functions, only becomes practical when the basin depth exceeds 5 km. In this case, the direct wave and converted wave could show up as individual events in the receivers function and their traveltime difference could easily be picked. In our study, we only had high-quality seismicity from distances exceeding 90^0. This resulted in receiver functions with a rather low central frequency, which would only allow a basin depth estimation if the depth were below 8 km. In principle, regional seismicity could be used to obtain receiver functions with a larger central frequency. However, crustal multipathing would make it tedious to interpret the results. Similar to an exploration-scale application (van Manen et al., 2003) a large number of receiver functions would need to be stacked before obtaining interpretable signal from the basin-basement interface. In general it is unlikely that this large distribution of regional seismicity would be present, given a limited acquisition time.

A similar passive survey as discussed in this study could be upscaled by a factor of 20 to find a basin depth map over a large region. In this case the inline station sampling would be about 10 km. For a total survey area of 100 by 100 km it may be assumed that the low-frequency seismicity is fairly constant. Still, a denser subarray would be required for beamforming the noise and to pick out the time-windows with a favorable illumination.

The large separation of the stations in the main array would only allow the retrieval of reflections for coinciding source and receiver position from the (relatively shallow) basin-basement interface. Therefore, a velocity model for the basin would need to be available through other means.

6.7 Data and resources

Seismic data used in this study were provided by Shell Egypt NV and are proprietary. They cannot be released to the public. Events in the data were recognized by raytracing phase-arrival times from major earthquakes in the IRIS earthquake browser (www.iris.edu/ieb/). The raytracing was done with TTBOX, which is available at www.dr-knapmeyer.de/downloads/. All the maps were made with M_Map, which is available at www.eos.ubc.ca/ rich/map.html. The websites in this section were last accessed August 2011.

Chapter 7

Conclusions and outlook

7.1 Conclusions

In this thesis we have shown that reflection responses between station positions can be extracted from natural-source responses, using body-wave seismic interferometry (SI). We used these reflections to image portions of the deep Earth. More specific conclusions of the different studies were drawn in the individual chapters. Here we give a summary of the conclusions related to the overall goal of the thesis: improving the imaging of the deep Earth by the application of SI to natural source responses.

In Chapter 2 we derived SI relations for a closed system, like the solid Earth as a whole. Using synthesized earthquake responses, we showed that the complete responses could be extracted between any two stations on the globe. However, an unrealistic distributions of sources would be required to do this. Still, we showed that relevant reflections can be extracted when using realistic surface distributions of seismicity, like the Sumatra 2004 and Tohoku 2011 aftershock sequence. At many places on the Earth, however, there is only a sparse distribution of seismicity, but there are more-and-more well-sampled arrays of stations. In Appendix A we propose an SI relation that allows the retrieval of reflections with only one source.

For the applications to field data (Chapters 3 to 6) we had to address issues related to natural sources: (1) their irregular distribution and (2) their non-impulsive source-time functions. We focused on imaging only small portions of the Earth's deep subsurface. Still, we used wavefields induced by distant seismicity. This gave rise to another issue: (3) wavefields have already undergone multiple reverberations before entering the domain of interest. Finally, (4) different wave modes are simultaneously initiated and recorded, while only P- or S-wave reflections are to be extracted for seismic reflection imaging.

In principle, issues (1) to (3) could be addressed with SI by multidimensional deconvolution (Wapenaar et al., 2011b). However, the required station spacings and wavefield separations are not yet reached in the current practice (Appendix D). Therefore, we resorted still to SI by crosscorrelation (Wapenaar & Fokkema, 2006). The latter relations require a well-

sampled source distribution. For lithospheric and basin-scale imaging (Chapters 3 to 6), these distributions cannot be found. Therefore, we recast the integration over sources to an integration over rayparameters. By selecting a set of time windows from earthquake responses, we could reach quite a regular distribution in rayparameters (Chapter 3). Further balancing approaches, like binning, adding integration weights and integrand regularization (Ruigrok et al., 2009a) turned out only to degrade the result, mainly because of source-side reverberations (issue 3). We showed that the result did improve when contributions from effective sources with either positive or negative rayparameters were time-reversed prior to integration. In Chapter 4 we evaluated only a small part of the integrand. This allowed only the retrieval of zero-offset responses. The large oversampling of the integrand for the evaluated range made it possible to well address issues (2) and (3). For noise sources (Chapters 5 and 6) we reached a balanced illumination by first beamforming time windows of noise and subsequently only using noise with favorable illumination characteristics.

We found that for earthquake responses, the source-time functions (STFs) need little attention (Chapter 3). In principle, a good estimate of STFs can be made, when measuring an earthquake's response at a number of different terrains. This estimate could be used to deconvolve the STF from the response prior to the application of SI. However, for most earthquakes the moment release is a strongly decaying function of time. Consequently, the autocorrelation of the STF has a strong peak at t=0 and there are few notches at later times. The notches that do exist are different for each source and therefore stacked out successfully. Also for noise sources, we assumed that the average of the autocorrelations of the noise STFs (i.e., the effective STF) has negligible contributions at times larger than zero. With this assumption, we interpreted the amplitudes retrieved at times larger than zero to be caused by subsurface structure. For the MF band (Sections 5.6 and 6.3) it was easy to prove that the effective STF did not contain considerable notches. Retrieved reflections had a different move-out than the retrieved spurious direct wave and could therefore not be explained as notches in the effective STF. Moreover, the timing and the move-out of the reflections corresponded with known structure. For the DF band (Sections 5.5) we could make it plausible that retrieved amplitudes at later times are caused by the reflectivity of the subsurface. The small size of the used array with respect to the depth of the reflectors, however, did not allow to prove this solidly with a move-out argument. For a solid proof, we would need to use records of the same noise field, but detected over different terrain (e.g. with a different Moho depth). We did not have such records for the Egypt study.

The third issue were the triplications. Not only one stationary ray path exists between the source and the medium of interest, but many. When multiple wavefields arrive within the same time window, spurious cross terms arise after applying SI (see equation 3.10). These cross terms are different for different sources and are therefore suppressed when multiple source responses are stacked in. The cross terms may have significant amplitude in comparison with retrieved reflections. Therefore, there might still be an imprint of the artifacts after the application of SI. In Figs 3.6 and 4.4 the artifacts can be recognized as events at later times, but approximately parallel to the spurious direct wave. For multi-offset

reflection responses (Chapter 3), these artifacts were suppressed with wavenumber filtering and normal-move-out correction and stacking. For the single-offset reflection responses (Chapter 4), we could take advantage of a strong lateral variation of the actual reflectivity. Consequently, we could suppress the artifacts by removing the scaled average trace over the array, from each individual trace. A prerequisite for this method to work was that we did not include time windows with phase arrivals (triplications) with different rayparameter (Section 4.3).

In this thesis we focused on retrieving P-wave reflections, in order to obtain P-wave reflectivity images. For earthquakes records from distant seismicity (Chapters 3 and 4) it was relatively straightforward to restrict the input for SI to P-waves. For the larger earthquakes, the location and timing are known well enough to estimate the arrival of P-wave phases, which are well separated in time from arrivals of S-phases and surface waves. By only taking time windows around P-phase arrivals, we restricted the input already to primarily P-waves. In Chapter 3, the remaining S-wave amplitudes (due to P-S conversions at the receiver side) were suppressed by the application of a wavemode decomposition prior to SI. For a non-horizontally layered medium the used decomposition relations are inaccurate and therefore it is likely that still S-wave energy remained, also in the final image (Fig. 3.10). In Chapter 4 we could leave out a wavemode decomposition, since only P-phases were used with small angles of incidence. This approach probably led to a negligible amount of S-wave leakage to the final image below Tibet (Fig. 4.5). For the Himalaya transect (Fig. 4.A.3) more S-wave contamination is expected, caused by conversions on dipping structure. For noise sources, we largely suppressed surface waves by using only time-windows dominated by small rayparameters. However, separating S-waves from P-waves turned out to be not so trivial. When we used only the Z-component noise recordings and time-windows dominated by small rayparameters (Section 5.6 and 6.3), still we also retrieved S-waves. Thus, although dominated by P-waves, these time windows also turned out to contain S-wave noise. Also for the DF-band processing (Section 5.5), it cannot be excluded that S-wave energy leaked to the extracted reflection responses 5.11. Consequently, for noise records a more elaborate decomposition is required than implemented, either prior to or after applying SI.

We have shown that the application of SI to earthquake recordings is sufficiently mature to yield high-resolution images of the lithosphere (Chapters 3 and 4), without the need of active sources, nor natural sources near the lithosphere under investigation. Relations for imaging deeper structure have been worked out and modus operandi have been thought through (Chapter 2). However, the reality check is still to be encountered with a field-data application. Furthermore, we have shown that the applications of SI to microseisms can be used to yield information about a basin depth (Chapter 6). Moreover, we have shown the great promise of microseism applications for unveiling the complete lithosphere, using only a few days of noise recordings (Chapter 5).

7.2 Outlook

It is needless to say that proposed methodologies and implemented processing can still be improved.

The global-scale relations have not yet been applied to field data. As described in Section 2.5.2, e.g., a PcP phase could be retrieved between two station positions by integrating over a surface distribution of sources. Finding a surface distribution of (high magnitude) seismicity is possible. E.g., aftershock sequences of the Sumatra 2004 and Tohoku 2011 earthquakes do span significant surfaces. The processing as proposed in Section 2.5.2 could be applied to field data, with the aim of imaging the core-mantle boundary zone. An alternative implementation is discussed in Appendix A.

In this thesis, we focused on extracting P-wave reflectivity. However, using the same methodologies, S-wave reflectivity images could be obtained. E.g., for the multi-offset lithospheric-scale application (Chapter 3) one could use time windows selected around S, SS, ScS and SKS phases as an input for SI.

GloPSI (Chapter 4) could be applied for almost any station on the globe. With relatively little processing effort, the zero-offset reflection response can be extracted. Thus far, we applied the technique to a line of stations. Without any change in processing, GloPSI can be applied to 2D patches of stations. A future advancement would be to image structures deeper than the lithosphere, notably reflectivity in the mantle-transition zone. For global P-wave phases we could not take large-enough time windows for retrieving reflectivity from the transition zone, because of the subsequent arrival of the PP-phase. With S-wave phases, however, one might be able to take large-enough time windows. Especially around ScS a very long time window can be selected without any other phase arriving.

Another approach would be to apply GloPSI to microseism records instead of earthquake records. Global phases have been proven to exist in these records (Chapter 5; Vinnik, 1973; Gerstoft et al., 2008). However, more often microseism records are dominated by surface waves (e.g., Bensen et al., 2007) and trapped crustal waves (e.g., Zhan et al., 2010), induced by storms on nearby oceans. Hence, the challenge is to find the time-windows for which global phases are significant. This challenge can be attacked both from the sources' perspective (when and where do ocean storms lead to significant downwards radiation of energy) and the receivers' perspective (processing methods to recognize and to enhance global-phase microseism recordings).

In this thesis, GloPSI is worked out to image the lithosphere below an array of receivers. Alternatively, the reciprocal version could be worked out (Curtis et al., 2009). In this case, the global-phase response of one source, detected with a patch of stations, would be used. The recordings would be autocorrelated and subsequently stacked over station positions. After source-time-function deconvolution (and a correction for the moment tensor), a response would be retrieved as if there was a source and a receiver at the source position. The virtual source (after again applying source-receiver reciprocity) would radiate primarily vertically

up- and vertically downwards. A number of these retrieved responses would allow imaging the lithosphere near earthquake zones or below microseism-prone patches of the ocean.

For transition-zone imaging, in principle, we could also use internal events (Section 2.B.3 and Appendix B). As in Chapters 3 and 4, we would use limited time windows around phase arrivals as an input for SI. These time windows would be chosen large enough to include internal multiples between transition-zone reflectors (notably between the 410 and 660 discontinuities). These time windows would be chosen short enough not to include interactions with the transition zone after free-surface reflection of the main phase. Consequently, the application of SI would lead to internal events. E.g., an internal event would be constructed with the kinematics as if there were a source and a receiver on top of the 410, measuring a reflection from the 660 discontinuity. After identification, this internal event can be used to invert for the temperature in the transition zone (Helffrich, 2000). By retrieving this ghost event over a large array, a transition-zone temperature map could be obtained.

As stated before (Section 7.1), for low-frequency noise records still more attention needs to be paid to separating P- and S-waves. Also, as outlined in the previous section, the estimation of the average noise-source spectrum needs to be improved.

In this thesis, we applied SI and imaging only to approximately linear arrays of stations. Especially in complicated orogenic zones (as in Chapters 3 and 4) also reflections from interfaces located crossline to the array are retrieved. With the 2D migration algorithms used, these reflections are erroneously mapped to reflectivity below the array. In order to further improve the imaging of the lithosphere —like already accomplished in exploration geophysics— the shift to well-sampled 2D arrays and 3D migration would need to be made. This would require the development of broadband stations that can be installed with little effort.

Appendix A

CMB imaging

A.1 Introduction

In Chapter 2 we derived relations for retrieving reflections from deep reflectors. These relations can be applied when a well-sampled distribution of high-magnitude seismicity is available. This distribution rarely exists. When the velocity model is known, still only a few earthquakes could suffice to build a structural image (Schuster et al., 2004; Artman et al., 2004; Draganov et al., 2006; Nowack et al., 2006; Almagro Vidal et al., 2012). However, to find more quantitative information about the subsurface it is desirable to obtain reflections at a few different offsets. In this appendix we show that, for specific settings, it is still possible to retrieve high-quality reflections, using only one, or a few, sources. We take advantage of the availability of a well-sampled receiver array and write an interferometric relation that incorporates an integration over midpoints instead of over sources. The midpoints are defined between virtual-source and actual receiver locations. As an example, we apply the method to core-reflected phases. We show that information of the core-mantle boundary (CMB) can be obtained below an array of receivers.

A.2 SI by midpoint integration

In this appendix we only consider a 2D configuration (Fig. A.1). Assume we have one large array of receivers. E.g., a line of receivers from the USArray. We use the location of the southernmost receiver in the array ϕ_1 as the reference point. Thus, ϕ_1 is at 0°. The northernmost station is at location ϕ_n. An arbitrary station within the array is denoted with ϕ_i. We consider a source at ϕ_s that is either relatively close to the array, or a source that is at the other side of the globe. Both sources lead to reflection travel paths within the array. The precise location of the sources is not relevant. We define midpoint m as a location within the array and the offset h as the distance from m along the array, where a northwards direction is taken as positive. If $\phi_1 \leq m - h \geq \phi_n$ and $\phi_1 \leq m + h \geq \phi_n$ for a range of m, we can

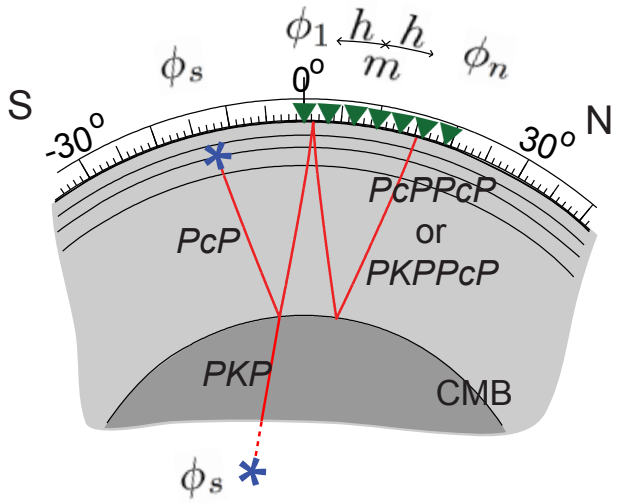


Figure A.1 *A global-scale configuration for seismic interferometry by midpoint integration (MSI). The location of sources (blue stars) and receivers (green triangles) is given in degrees with respect to the southernmost station in the array of receivers. The source leading to a PKP and $PKPPcP$ arrival at the array is at the other side of the globe (Fig. 2.13 and cover of this thesis).*

evaluate the following interferometric relation

$$\int_{\partial\mathbb{S}_1} X((m-h),\phi_s,-t) * XY((m+h),\phi_s,t)dm \propto Y((\breve{m}+h),(\breve{m}-h),t), \quad \text{(A.1)}$$

where the asterisk $*$ denotes a temporal convolution and a proportionality sign is used since we have left out all the amplitude terms. $X((m-h),\phi_s,t)$ denotes a phase observed at location $(m-h)$ (one of the receivers in the array) due to a source at ϕ_s and XY is a free-surface multiple of X. $\partial\mathbb{S}_1$ is the line segment of midpoints over which is integrated.

By evaluating the left-hand side of equation A.1 we retrieve $Y((\breve{m}+h),(\breve{m}-h),t)$, which is the response of phase Y for a source at $(\breve{m}-h)$ and a receiver at $(\breve{m}+h)$. If the retrieved phase is a primary reflection or a turning wave, it has its reflection point or turning point below the stationary midpoint $\breve{m}$. When we denote the integrand of equation A.1 with I, $\breve{m}$ is the location where $dI/dm = 0$. Hence, $\breve{m}$ can directly be estimated from the crosscorrelated data. If X in equation A.1 is substituted by phase P and XY by PP we would retrieve P within the array. We would retrieve PcP within the array by substituting X with PcP or PKP and XY with $PcPPcP$ or $PKPPcP$ (Fig. A.1).

Relation A.1 also holds for finding phases with midpoints in between two (similarly oriented) arrays of receivers. In this case, a range of m is chosen in between the arrays, for which $m-h$ coincides with locations in array 1 and $m+h$ coincides with locations in array

2.

In the following, application of equation A.1 and a subsequent stationary-phase analysis to find $\breve{m}$, we will call midpoint seismic interferometry (MSI).

A.3 Numerical illustration

We illustrate equation A.1 numerically using the configuration as depicted in Fig. A.1. We do not take exactly the same source positions as indicated on Fig. A.1, however. We consider a well-sampled array of stations from ϕ=0 to ϕ=20°. A source at ϕ=$-11°$, at a depth of 200 km, occurs at t=0. The source-time function (STF) is a delta pulse. Figs. A.2(a) and (b) are the traveltimes of the forward modeled responses at the array, time-windowed around PcP and $PcPPcP$, respectively. We aim to retrieve PcP within the array with h=7°. For this offset, the integral (equation A.1) can be evaluated between $\sim$7 and $\sim$ 13°. Note that the midpoint limits are not exactly 7 and 13° due to the (unknown) depth of the source. Computing the integrand of equation A.1 results in Fig. A.2(c). From this integrand we determine $\breve{m}$, which equals $9.84°$. Integrating the integrand would give a pulse at $t(\breve{m})$=519.62 s, and two minor pulses at later times, which are due to the edges of the integration line. The latter pulses could be suppressed by tapering the integrand. The main pulse retrieved is the response that would be found if there was a delta-pulse source at ϕ=$2.84°$ and the PcP phase was measured at ϕ=$16.84°$. Indeed, raytracing PcP for an epicentral distance of $14°$ from a source at the Earth's surface gives an arrival time of 519.62 s. Using the same source, we could repeat the upper procedure to find PcP at different offsets and midpoints. However, by using only one source we cannot retrieve PcP at more than one offset per midpoint.

To find more offset and midpoint combinations we use the response from a distant source. We put a source at ϕ=$-160°$, at the free surface. Figs. A.2(d) and (e) are the responses at the array, time-windowed around PKP_{DF}[1] and $PKP_{DF}PcP$, respectively. As an example, we aim to retrieve PcP at h=5°. Computing the integrand of equation A.1 results in Fig. A.1(f). From this integrand we determine $\breve{m}$, which equals $8.40°$. Integrating the integrand would give a main pulse at $t(\breve{m})$=515.10 s. This same pulse we find when we place a source at ϕ=$3.40°$ and measure the PcP phase at ϕ=$13.40°$. So, not only we found the response between two seismically not active points, but also we found the exact excitation time and place for this response. For actual data, which its bandlimitations and noisiness, it is expected that the timing of the pulse can be well retrieved. It will be difficult though to exactly estimate $\breve{m}$.

[1]For a description of the DF branch of PKP see, e.g., Stein & Wysession (2003).

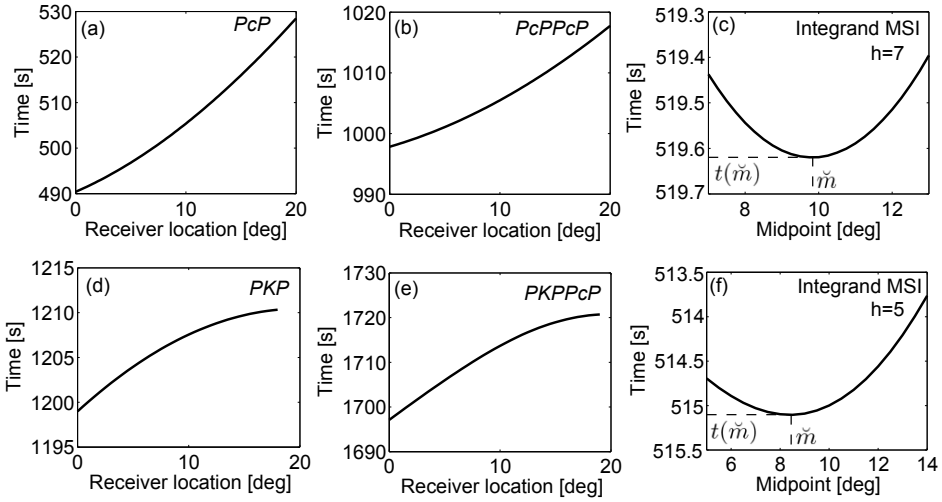


Figure A.2 *A numerical illustration of seismic interferometry by midpoint integration (MSI). The left and middle panels depict arrival times of different phases, measured at an array of receivers (Fig. A.1), induced by (a)&(b) a source near the array and (d)&(e) a source at the other side of the globe. (c)&(f) depict the correlation panels for the application of MSI to the responses on the left-hand side, for an offset of 7 and 5°, respectively. From these correlation panels, a response for midpoint location $(\breve{m})$ is retrieved by integration over midpoint*

A.4 Discussion

The correlation integral (equation A.1) can be evaluated for varying h. The possible range depends on the configuration. Consequently, for a range of midpoints, the response of phase Y would be obtained, for a different offset at each midpoint. This dataset in h and m can directly be imaged using a prestack migration. When another earthquake happens more or less inline, the exercise can be repeated and the image can be improved by stacking in the new image. Alternatively, when the data for a few earthquakes is available, the midpoints could be binned. All offsets within a bin could be normal-moveout corrected and stacked and a poststack migration could be applied to obtain an image of the CMB. At the same time, reflections from reflectors near the CMB would be retrieved. This would allow, e.g., making an image of the D''-region below the USA or Europe. Previously, such an image was only obtained for a region in between extensive seismicity an extensive receiver networks (Wang et al., 2006). The retrieval of reflections at multiple offsets, at each midpoint, also allows the estimation of a velocity model.

The numerical illustration as depicted in Figs. A.2(a)-(c) can possibly not be applied to field data. The reason is that, in general, $PcPPcP$ does not conquer the noise floor. However,

$ScSScS$ is being recorded (Astiz et al., 1996), which allows retrieval of ScS. The numerical illustration as depicted in Figs. A.2(d)-(f) could be applied to field records, since both PKP_{DF} and $PKP_{DF}PcP$ are actually recorded (Astiz et al., 1996).

Note that the rayparameters of the phases we used in the previous section are small. As a consequence, also the integrands (Fig A.2c & f) show little time variation as function of midpoint. For this reason it will not be easy to estimate $\breve{m}$ from band-limited field data. The time variation becomes larger, however, when larger h are considered. It is therefore advantageous to evaluate equation A.1 for two distantly spaced arrays, e.g., between the USArray and the VESBSN (van Eck et al., 2011).

We illustrated MSI for a global-scale setting, with the aim of retrieving reflections. MSI can also be used for retrieving multiple reflections and turning waves. Moreover, MSI can also be applied in an exploration-scale setting, for updating a clear target reflector, when there is good receiver network, but there is only a limited amount of (natural) sources.

Also for multiple reflectors, MSI could work. The time-windowing, as applied in section A.3, could be left out. However, the retrieved trace would need to be split up in different time windows and for each reflector (time window), another $\breve{m}$ would need to be picked. This could turn out to be a too laborious approach. Instead, the correlation panel could directly be used for imaging. After all, in the MSI correlation panel the stationary points are already at (almost) the right locations in space and time.

With MSI, all correlations in the integrand of the interferometric relation (i.e., the correlation panel) have the same STF imprint. For the global-scale seismic interferometric relations (GSSI) derived in Chapter 2 each correlation has an imprint from a different source. Consequently, for MSI it is relatively straightforward to apply an interpolation of the correlation panel, while for GSSI it is not. This interpolation is useful since $m-h$ and $m+h$ (equation A.1) unlikely correspond with exact station locations. Moreover, the interpolation could be used to account for an irregular receiver spacing. The flip of the coin, for MSI, is that a STF deconvolution is required, before the interferometric result can be interpreted in terms of reflectivity. For an integration over sources, the STF deconvolution may, in some cases, be left out (Chapter 3).

Appendix B

Q-estimation [1]

B.1 Introduction

In the search for new hydrocarbon reservoirs a number of sedimentary basins have so far been underexplored, mainly because of exploration challenges. One example is the basins hidden under flood basalts. The heterogeneous and attenuating nature of the basalt makes it hard to look beneath. The first exploration data for such basins could be delivered by using natural seismicity and seismic interferometry (SI). For this purpose, arrays with continuously recording receivers would need to be installed in the exploration area. With SI, seismicity due to natural sources in the subsurface can be remapped to receiver positions on the Earth's surface. The remapped responses can subsequently be used to create a (low-frequency) reflectivity image of the subsurface. In a desert setting, SI with natural sources has already been proven to be a valuable exploration asset (Draganov et al., 2007). Initially, SI was proposed as a crosscorrelation (CC) of responses. Recently, an alternative remapping procedure for passive data was proposed, where instead of CC one performs a multidimensional deconvolution (MDD) (Wapenaar et al., 2008c). In the following we will review the two approaches for the example of a sedimentary basin covered by flood basalts. For both methods, losses in the basalt lead to artifacts in the retrieved response. We will show how these artifacts can be recognized as being spurious events. Moreover, we will use the artifacts to estimate the loss-factor of the basalt.

B.2 Seismic interferometry by crosscorrelation (CC)

We consider a simplified flood-basalt setting as illustrated in Fig. B.1, which is loosely based on the model discussed in Martini et al. (2005). The acoustic model consists of 4 layers: from top to bottom, a basalt-layer succession associated with continental break-up, a pre-existing sedimentary basin (2 layers), which might contain hydrocarbons, and a

[1] This first part of this appendix has been published as an extended abstract in the workshop proceedings of the 2^{nd} *EAGE Passive Seismic Workshop*, A09 (Ruigrok et al., 2009b).

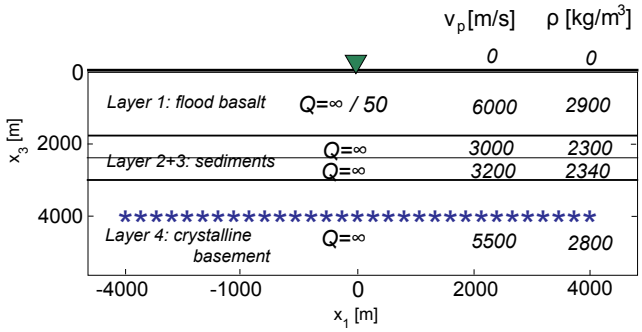
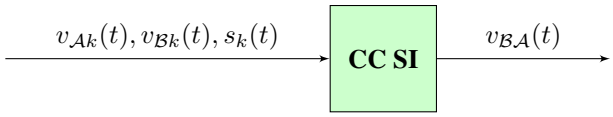


Figure B.1 *Model of a flood-basalt succession (layer 1) over a sedimentary basin (layer 2 and 3) with seismicity in the basement (layer 4). The responses initiated by the sources (blue stars) are recorded by a receiver on the free surface (green triangle).*

crystalline basement. As compared to a conventional sedimentary basin, the model has a sharp velocity decrease going from the basalt to the sediments and strong (scattering) losses in the basaltic package. The scattering losses are caused by the heterogeneous nature of the basalt, but this heterogeneity has not explicitly been built in to keep the model simple. Instead, a constant quality factor Q of 50 is used. For comparison reasons, also a model without losses is used.

As source mechanism we assume small abrupt displacements over faults in the crystalline basement. We assume an idealized seismic-source distribution, indicated with the blue stars in Fig. B.1. The sources are transients with a dominant frequency of 9 Hz. The responses due to all individual sources are recorded by a single receiver (green triangle). In Wapenaar & Fokkema (2006) exact relations are derived to retrieve a response between two receiver positions ($\mathbf{x}_\mathcal{A}$ and $\mathbf{x}_\mathcal{B}$), without having an actual source at one of the positions. These relations only hold when the medium is lossless. The application of these relations is called seismic interferometry by crosscorrelation (CC SI). It can be summarized in a flow-chart as



where $v_{\mathcal{A}k}(t)$ denotes the (particle velocity) response measured at $\mathbf{x}_\mathcal{A}$ due to the k^{th} source in the subsurface and $v_{\mathcal{B}k}(t)$ is the response due to the same source measured at $\mathbf{x}_\mathcal{B}$. By crosscorrelating $v_{\mathcal{A}k}(t)$ and $v_{\mathcal{B}k}(t)$ and stacking the crosscorrelation results for different sources k, we obtain $v_{\mathcal{B}\mathcal{A}}(t)$, which would be the response between $\mathbf{x}_\mathcal{A}$ and $\mathbf{x}_\mathcal{B}$ if the source distribution was favorable and no losses occurred. If a good dynamic retrieval of $v_{\mathcal{B}\mathcal{A}}(t)$ is required, also the source wavelet $s_k(t)$ of the displacement sources need to be well estimated.

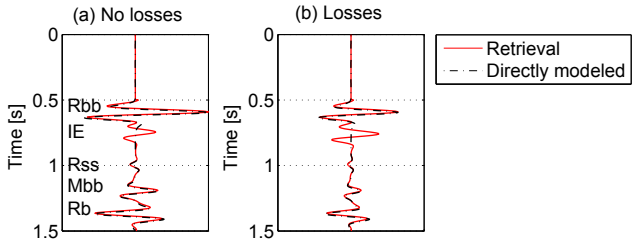


Figure B.2 *The directly modeled (black dashed lines) and retrieved responses (red lines) for (a) a model without losses and (b) a model with losses.*

In the first experiment, we assume that there is no attenuation in the medium. We choose $\mathbf{x}_{\mathcal{A}}$ and $\mathbf{x}_{\mathcal{B}}$ to correspond with the location of the receiver in Fig. B.1. Thus, the application of CC SI is now equivalent to applying equation 4.2 (which contains in fact autocorrelations instead of crosscorrelations). In Fig. B.2(a) the result of applying CC SI is shown (red trace) and compared with a directly modeled response (black dashed trace) for a collocated source and a receiver. The amplitudes before the arrival of the first reflection (the first 0.5 seconds) were muted and both traces were normalized with the maximum amplitude in the trace. On the directly modeled response, successively, the basalt-base reflection (Rbb), the sediment-sediment reflection (Rss), the first-order multiple from the basalt base (Mbb) and reflection from the basement (Rb) can be distinguished. The retrieved response is almost identical to the directly modeled, but contains additionally one spurious event, a so-called internal event (IE), which occurrence will be explained later.

The model is made more realistic by building in an effective attenuation in the basalt layer. In Fig. B.2(b) the directly modeled response (black dashed trace) and the retrieved response (red trace) for the model with losses is shown. Again, there is a good correspondence between the directly modeled and retrieved trace, but again, additionally, an IE has been retrieved. In comparison with the response in the model without losses (Fig. B.2a) the drop in relative amplitudes can be noted. Comparing Fig. B.2(a) with (b) it can be concluded that also with losses the physical events are retrieved almost perfectly, but the artifact - the internal event - becomes relatively stronger.

The spurious event has previously been noted and explained in Snieder et al. (2006), for an open configuration with sources at the free surface and in Section 2.B.3, for a closed system. This type of spurious event is called an IE because it appears as if the event was both initiated as well as recorded at a boundary within the Earth (Fig. B.3, box I). In the correlation process both IEs with unaltered phase (Fig. B.3, box II) and with opposite phase (Fig. B.3, box III) are created. Only if the requirements for CC SI are perfectly satisfied, all unaltered-phase and opposite-phase IEs cancel each other. For the retrieval in Fig. B.2(a) the cancelation is not perfect due to suboptimal illumination from the sides. For the retrieval in Fig. B.2(b) the cancelation is not perfect, both due to suboptimal illumination and due

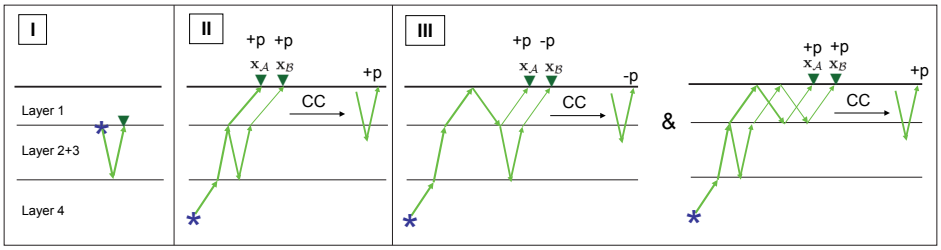


Figure B.3 *In box I, the main internal event is depicted. In box II and III creation of this internal event with unaltered phase (+p) and opposite phase (-p) is shown. The green lines depict rays and crosscorrelation is abbreviated as CC. The model parameters are given in Fig. B.1. In box II, if the source sends a positive spike then the two rays arriving at $\mathbf{x}_\mathcal{A}$ and $\mathbf{x}_\mathcal{B}$ will also be positive spikes and also the crosscorrelation of both events will be a positive spike. In box III, on the left-hand side, a ray will reach $\mathbf{x}_\mathcal{A}$ as a positive spike, whereas the other ray will reach $\mathbf{x}_\mathcal{B}$ as a negative spike and therefore the crosscorrelation will give a negative spike. On the right-hand side a correlation is shown that again leads to a positive spike.*

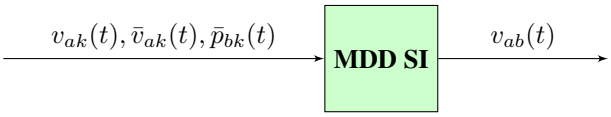
to losses. In Fig. B.3 only the first order (box II) and the two second order (box III) IE contributions are shown. Those are the most important contributions, though an infinite number of higher order contributions exists.

The IEs can be both a merit and a defect. A defect, since they might well be misinterpreted to be primary reflections. A merit, since they contain additional information. In Draganov et al. (2010) an approach is suggested to identify and use these IEs to estimate a Q model of the subsurface.

B.3 Seismic interferometry by multidimensional deconvolution (MDD)

In Wapenaar et al. (2008c) seismic interferometry by multidimensional deconvolution (MDD SI) for passive data was introduced. In this section, we evaluate this alternative interferometric approach. We assess whether, for the configuration as depict in Fig. B.1, an artifact-free response can be retrieved.

In a flow chart MDD SI can be summarized as



where $v_{ak}(t)$ denotes the particle-velocity response measured at an array of receivers due to the k^{th} source in the subsurface, $\bar{v}_{ak}(t)$ is the response at the same array of receivers, but without free-surface interaction and $\bar{p}_{ak}(t)$ is the acoustic pressure of that same response,

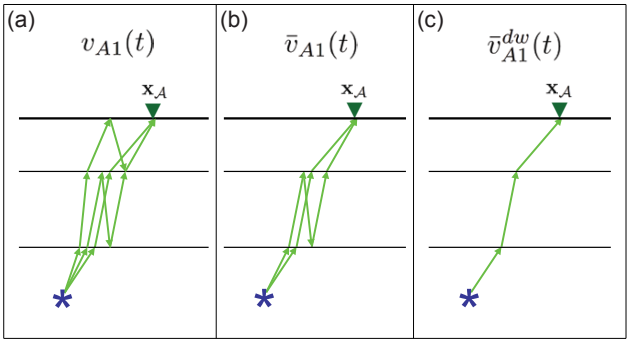


Figure B.4 *Ray visualization of the particle-velocity response at $\mathbf{x}_A$ due to a subsurface source, with index $_1$; (a) the first arrivals of the complete response, (b) the response without free-surface interaction and (c) the direct-wave response without free-surface interaction.*

for the same (or a nearby) array. For a single source and receiver $v_{ak}(t)$ and $\bar{v}_{ak}(t)$ are visualized in Fig. B.4. $v_{ab}(t)$ denotes a set of responses between all receiver positions within the array. With MDD $v_{ab}(t)$ is estimated through a matrix inversion (Appendix D). Given a favorable source distribution and given that a proper stabilization for the MDD is chosen, a good estimation is found for $v_{ab}(t)$.

For MDD SI a response needs to be detected at a regularly sampled array of receivers, whereas CC SI can be performed for a single receiver pair. On the other hand, for CC SI the source distribution needs to be regularly sampled, whereas MDD SI can correct for the effects of source irregularity. For MDD SI losses are taken into account correctly, whereas for CC SI losses lead to small amplitude deviations and the occurrence or amplification of internal events. For an extensive comparison between the two approaches, see Wapenaar et al. (2011b).

In Wapenaar et al. (2008c) MDD SI is performed for the same configuration as in Fig. B.1, though the model is different. In this reference, MDD SI is applied for the case that all the required input is available. The result is depicted in Fig. B.5(a) in red and compared with a directly modeled response in dashed black. It can be noted that the response is perfectly retrieved. A problem is that in practical situations $\bar{v}_{ak}(t)$ (Fig. B.4b) cannot easily be separated from $v_{ak}(t)$ (Fig. B.4a) and hence also $\bar{p}_{bk}(t)$ cannot easily be estimated from $v_{bk}(t)$. If the responses due to different sources are well separated in time, at least the direct-wave arrival without free surface interaction $\bar{v}^{dw}_{ak}(t)$ (Fig. B.4c) can be separated by time-windowing and a division by 2. If the responses are not well separated in time, the direct-wave contributions can still be estimated after crosscorrelation (van der Neut et al., 2010).

Fig. B.5(b) depicts the MDD SI result when using $\bar{v}^{dw}_{ak}(t)$ and $\bar{p}^{dw}_{bk}(t)$ instead of $\bar{v}_{ak}(t)$ and $\bar{p}_{bk}(t)$. Still the events are retrieved well, but additionally a spurious event is introduced.

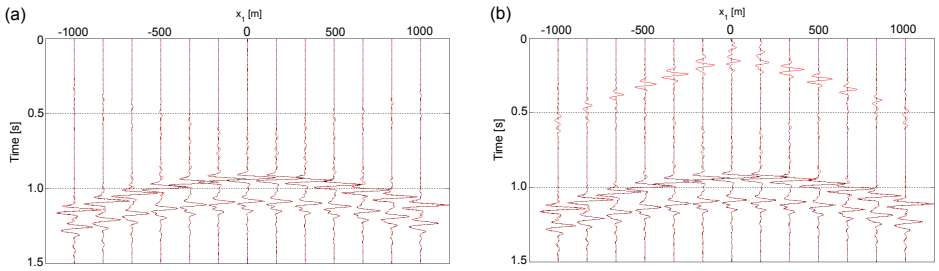


Figure B.5 *(a) A response retrieved with MDD SI for which all the requirements are met and (b) a response retrieved when $\bar{v}_{ak}(t)$ and $\bar{p}_{bk}(t)$ are approximated with $\bar{v}^{dw}_{ak}(t)$ and $\bar{p}^{dw}_{bk}(t)$, respectively. The retrieved responses (red traces) are compared with directly modeled responses (black dashes).*

This spurious event is again an internal event (IE), as we found in the previous section for CC SI. This IE has the kinematics as if there was a source and a receiver at an interface within the Earth (Fig. B.3a).

In conclusion, also MDD SI, for realistic passive seismic settings, cannot straightforwardly be applied without the occurrence of IEs.

B.4 Tracking internal events

Since also for MDD SI the occurrence of IEs cannot be circumvented in realistic settings, another solution is sought. We replace $v_{Ak}(t)$ in the input for CC SI (see the chart in Section B.2) with $v^{dw}_{Ak}(t)$; that is, from the response recorded in $\mathbf{x}_{\mathcal{A}}$ we only use the direct wave. We still use the complete response recorded in $\mathbf{x}_{\mathcal{B}}$. Fig. B.6 shows the CC SI results for retrieving a response as if there were a source and receiver at the location of the receiver in Fig. B.1. In Fig. B.6(a) the result is compared when using $v^{dw}_{Ak}(t)$ (green trace) instead of $v_{Ak}(t)$ (red trace). In Fig. B.6(b) the same comparison is made for the model with losses.

In Fig. B.6 it can be seen that the physical events are still retrieved well when $v_{Ak}(t)$ is replaced by $v^{dw}_{Ak}(t)$. The amplitude of the physical events (Rbb, Rss, Mbb and Rb) has decreased slightly, because all correlations between higher-order events are left out when only the direct wave is used for one of the responses. The amplitude of the IE, on the other hand, has increased significantly, both for the model without (Fig. B.6a) and for the model with (Fig. B.6b) losses. This can be understood by looking again at Fig. B.3. The creation of the predominantly opposite-phase IE as depicted in box III cannot occur when only $v^{dw}_{Ak}(t)$ is used. The creation of the unaltered-phase IE (box II) still occurs. The net-effect is an increase in amplitude of the IE.

As illustrated in Fig. B.6, the execution of both CC SI with full responses and CC SI with a full response and only a direct wave, can be used to distinguish an IE. The increase in

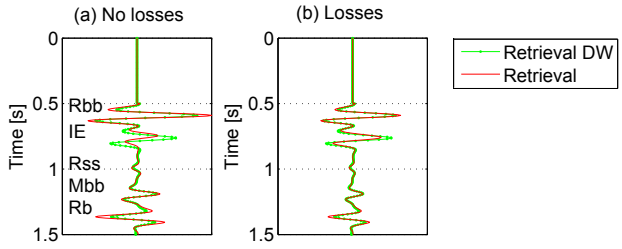


Figure B.6 *The CC SI retrieved response when using full responses (red) and when replacing one of the responses with only the direct wave (green), (a) for a model without losses and (b) a model with losses.*

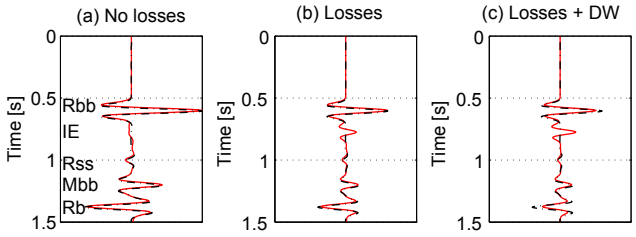


Figure B.7 *The directly modeled (black dashed lines) and retrieved plane-wave responses (red lines) for (a) a model with no losses, (b) a model with losses and (c) a model with losses and using only the direct wave at $\mathbf{x}_{\mathcal{A}}$.*

amplitude, which only occurs for the artifact, might be significant enough to recognize it, also when additional noise is added. In Fig. B.6 the IE is separated in time from the physical events. Therefore it is easy to remove it after recognition. In the general case of interfering internal and physical events, it will be a bigger challenge to recognize and remove the IEs.

B.5 Q-estimation with internal events

In this section, we will use the IE to estimate the losses in the upper basalt layer. In our earlier example we used local seismicity (see Fig. B.1). Even with quite ideal illumination and a model without losses, we got an IE (Fig. B.2a). To estimate Q with a high accuracy we replace the local seismicity in Fig. B.1 with a plane-wave arriving due to distant seismicity. As before, we apply SI for the model with and without losses. For the model with losses, we also apply the direct-wave strategy to recognize the IE (see Section B.4). The results are shown in Fig. B.7.

In Fig. B.7(a) the advantage of using only a plane-wave can be seen. For this 1D model an artefact-free reflection response is retrieved. In Fig.B.7(b) the IE reappears, which is now

only caused by losses in the upper medium, not by insufficient illumination. In Fig.B.7(c) it can be seen again that the IE exhibits a stronger amplitude than in Fig.B.7(b), while the physical events exhibit a smaller amplitude, when only the direct wave is used in $\mathbf{x}_{\mathcal{A}}$.

Note that the effective source wavelet in Fig. B.7 is zero phase, unlike the previous results (Fig. B.2 & B.6). Correlation leads to a zero-phase wavelet. Previously, the SI result was obtained by integrating over crosscorrelated traces. This integration gives another $\pi/4$ phase shift (Snieder, 2004), that can be noted in, e.g., Fig. B.2. In Fig. B.7 we only used the stationary-phase contribution and left out the integration. Hence, the zero-phase wavelet. But for the phase, also the amplitude behavior differs between Fig. B.2 and Fig. B.7. In Fig. B.2 we retrieved a line source, with 2D geometrical spreading. In Fig. B.7, using only one plane-wave response, we retrieve the reflection response due to a plane-wave source, without geometrical spreading (equation 4.1).

In Draganov et al. (2010) a method was presented to use IEs to estimate losses in the overburden. With this method the complete transmission responses are compensated with different quality factors Q before applying CC SI. When the correct overburden Q is chosen, the IE, caused by the losses in the overburden, disappears. Though this method is theoretically sound, it is hard to apply to field data. The main reason is that the method is not robust in the occurrence of noise. In general, long transmission records need to be used. By applying the Q-compensation, noise at later times is increasingly blown up. The amplified crosscorrelated noise appears also at small time lags and interferes with the IE. This makes it hard to visually interpret for which Q the IE disappears. Here we present an alternative method that is more robust in a noisy setting.

We turn back to the model as depicted in Fig. B.1. For simplicity we neglect the small contrast between layer 2 and 3 and threat the sediments as a single layer, as in Fig. B.3. A common technique to estimate Q would be to apply the spectral-ratio technique (e.g., Tonn (1991)). The amplitude of the direct wave at $\mathbf{x}_{\mathcal{A}}$ can be expressed as

$$A_{DW} = t_{32}t_{21}qs \tag{B.1}$$

and the ghost reflection as

$$A_{GH} = -t_{32}t_{21}r_{12}q^3s, \tag{B.2}$$

where t_{32} is the plane-wave, zero-offset transmission coefficient from layer three to layer two (from the crystalline basement to the sediment package), r_{12} is the plane-wave, zero offset reflection coefficient at the base of layer one (i.e., at the basalt-sediment interface), q is the amplitude loss factor due a one-way travelpath through the basalt layer and s is the amplitude of the planar wavefield before interacting with the upper layers. By a (spectral) division of equation B.2 with equation B.1,

$$R_1 = \frac{A_{GH}}{A_{DW}} = -q^2r_{12}, \tag{B.3}$$

q can be found. However, the impedance of layer 1 and 2 needs to be known.

To obviate the need to know r_{12}, we add the expressions for the amplitude of the first- and second-order IE contributions, as depicted in Fig. B.3 in box II and III, respectively:

$$A_{IE,1} = -(t_{32})^2(t_{21})^2 r_{12} r_{23} q^2 s^2, \tag{B.4}$$

$$A_{IE,2} = (t_{32})^2(t_{21})^2 r_{23} r_{12} q^6 s^2 (t_{21}t_{21} - (r_{12})^2). \tag{B.5}$$

The division of $A_{IE,2}$ by $-A_{IE,1}$ can be expressed as

$$R2 = \frac{A_{IE,2}}{-A_{IE,1}} = q^4(t_{21}t_{12} - (r_{12})^2) = q^4(1 - 2(r_{12})^2). \tag{B.6}$$

Combining equations B.3 & B.6 we have two equations and two unknowns and we can solve for both q and for r_{12}:

$$q = \sqrt[4]{R_2 + 2(R_1)^2}, \tag{B.7}$$

$$r_{12} = \frac{-R_1}{\sqrt{R_2 + 2(R_1)^2}}. \tag{B.8}$$

We use the following expression (Aki & Richards, 1980) relating q and Q: $q = exp\frac{-t\pi f_0}{Q}$, where f_0 is the peak frequency of the wave, t is the one-way traveltime through the lossy layer and Q its quality factor. Inverting for Q yields:

$$Q = \frac{-t\pi f_0}{\ln q}. \tag{B.9}$$

In the following we will solve for Q of the basalt layer in model B.1, using the plane-wave transmission response. In principle, a frequency-dependent Q could be obtained by evaluating the above equations in the frequency domain. Here, we extract the maximum amplitudes in the time domain, which is an approximation of solving Q for the peak frequency. We obtain A_{GH} and A_{DW} from the transmission panels, giving $R_1 = 0.309$. We find $A_{IE,1}$ and $A_{IE,2}$ through the following procedure. First, we restrict the duration of the transmission panels such that only the first- and second-order contributions (equation B.4 & B.5) remain. We apply correlation and extract $A_{IE} = A_{IE,1} + A_{IE,2}$. Next, we extract $A_{IE,1}$ by using only the direct wave for one of the traces before correlation (Section B.4). Finally, we find $A_{IE,2}$ by taking the difference of A_{IE} and $A_{IE,1}$. Consequently, we have all the required input to compute $R_2 = 0.340$. Subsequently, evaluation equations B.7 and B.8 yields q=0.854 and r_{12}=-0.424. Finally, we use equation B.9 to estimate Q. We find $f_0 = 9.0$ Hz by evaluating the amplitude spectrum of the first arrival. We find the one-way traveltime through the basalt $t = 0.30$ s from the retrieved basalt-base reflection (Rbb, see Fig. B.7). Thus, filling in equation B.9 yields $Q = 53.6$. This value is slightly higher than the one we used for the forward modeling, due to errors in time-windowing and picking. For this numerical example we obtained the plane-wave responses by summing over line responses (Wapenaar et al., 1992), which operation could have contributed to the error as well.

Note that equations B.1 to B.9 also hold when a plane-wave response is used with an angle of incidence ϕ larger than zero. The computation would be the same as above. The only difference is that an angle dependent $r_{12}(\phi)$ is retrieved with equation B.8 and that an angle-dependent one-way traveltime needs to be use in equation B.9 (which would still be obtained similarly as before after correlation).

B.6 Conclusions

For CC SI, moderate losses in the medium do not pose a severe problem for the retrieval of physical events, but specific artifacts, so-called internal events, are amplified —if present— due to the losses. With MDD SI, losses in the medium are treated correctly, given that the required wavefield responses can be collected. Practically, it will be especially hard to get the required response without free-surface interaction. When this response is approximated by the direct wave, still the physical events are retrieved correctly but, additionally, internal events appear. These internal events can be recognized by applying both CC SI with full responses and CC SI with a full response and only a direct wave. After recognition, the internal events can be removed from either the MDD SI or the CC SI result. Thus, in some cases, a hybrid approach can be applied in which MDD SI is used to account for losses in the medium and to correct for the effects of source irregularity and a dual CC SI is applied to recognize spurious events in the MDD result. Though they are spurious, internal events do contain subsurface information.

We derived a new method to extract subsurface information from internal events, for an approximately layered subsurface, illuminated from below by a plane-wave. The method is largely data-driven. The required input can be extracted from the transmission response. The only a-priori knowledge required is the approximate timing of ghost reflection from the base of the internal-event layer. The outputs of the method are the quality factor of the lossy layer and the reflection coefficient at the base of the lossy layer.

Appendix C

Anomaly scanning with P_{diff} [1]

C.1 Introduction

The Earth's velocity model is one-dimensional (1D) only to first order. Lateral variations exist not only in the lithosphere, but also in the transition zone and the lower mantle. These variations were discovered by inverting surface-wave velocity dispersion data (Knopoff, 1961), body-wave arrival times (Aki et al., 1977), and a combination of both (Masters et al., 1996). Recently, resolution of lithosphere models has improved due the use of microseisms as signal (e.g., Shapiro & Campillo, 2004). Although all of these inversion methods have proven valuable, they share one major disadvantage: they require large data volumes and many computing and human analysis hours before a final model is obtained. For example, the velocity model of Burdick et al. (2010) requires the inversion of $1,390,000$ travel-time residuals.

Here, we consider the use of differential times of P_{diff}, the P-wave diffraction along the core-mantle boundary (CMB). This diffracted arrival has a distinct difference when compared to other body-wave arrivals: ray paths of a core-mantle diffraction do not deviate significantly until at the receiver side (Fig. C.1). Consequently, arrival-time perturbations measured across an array of receivers can be attributed to receiver-side structure. In the following sections we show that just a few P_{diff} arrivals suffice to identify the major crust $\&$ mantle anomalies in the western US, without doing any inversion. We first describe the method, and in subsequent sections apply the method to 1D and 2D distributions of USArray stations.

[1] This appendix has been published as a journal paper in *Geophysical Research Letters*, **39**, L11301, doi:10.1029/2012GL051443 (Ruigrok et al., 2012b). Note that minor changes have been introduced to make the text consistent with the other chapters of this thesis.

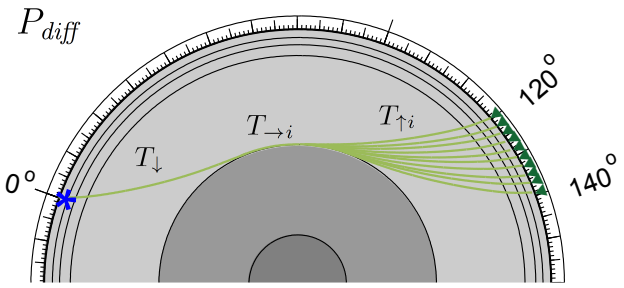


Figure C.1 *A cross-section of half the Earth showing P_{diff} arrivals from one source (blue star) and an array of receivers (green triangles). The travel-time segments at the source side, along the diffractor (i.e., core mantle boundary), and at the receiver side are denoted with $T_{\downarrow}$, $T_{\rightarrow i}$ and $T_{\uparrow i}$, respectively, where $_i$ is a receiver index.*

C.2 Crosscorrelation method

We can represent a diffraction due to a unit source at position $\mathbf{x}_S$ recorded at receiver position $\mathbf{x}_\mathcal{A}$ in the frequency domain as

$$u(\mathbf{x}_\mathcal{A}, \mathbf{x}_S, \omega) = A(\mathbf{x}_\mathcal{A}, \mathbf{x}_S, \omega) e^{-j\omega(T_{\downarrow\mathcal{A}} + T_{\rightarrow\mathcal{A}} + T_{\uparrow\mathcal{A}})} s(\omega), \tag{C.1}$$

where $A(\mathbf{x}_\mathcal{A}, \mathbf{x}_S, \omega)$ is an amplitude term that describes the amplitude loss over the travel path, $s(\omega)$ is the source spectrum, j is the imaginary unit and ω is the angular frequency. (See equation 2.1 for the used definition of the Fourier transform.) $T_{\downarrow\mathcal{A}}$, $T_{\rightarrow\mathcal{A}}$ and $T_{\uparrow\mathcal{A}}$ are travel-time segments between the source and diffractor, along the diffractor and between the diffractor and receiver, respectively (Fig. C.1). A similar expression can be written for this diffraction induced by the same source, but detected at station $\mathbf{x}_\mathcal{B}$. If we consider a source and receivers that lie on the same great circle path, as in Fig. C.1, the ray paths from source to diffractor overlap and we can use the equality $T_{\downarrow\mathcal{A}} = T_{\downarrow\mathcal{B}}$. Crosscorrelating the diffraction arrivals, using the above equality and neglecting amplitude terms, yields the relationship

$$u(\mathbf{x}_\mathcal{A}, \mathbf{x}_S, \omega)^* u(\mathbf{x}_\mathcal{B}, \mathbf{x}_S, \omega) \propto e^{-j\omega(T_{\rightarrow\mathcal{B}} - T_{\rightarrow\mathcal{A}} + T_{\uparrow\mathcal{B}} - T_{\uparrow\mathcal{A}})} |s(\omega)|^2. \tag{C.2}$$

The crosscorrelation result is a zero-phase wavelet ($|s(\omega)|^2$) with a maximum occurring at a lag time corresponding to the travel-time difference between both diffractions. Repeating the crosscorrelation between varying receiver positions $\mathbf{x}_\mathcal{B}$ and a fixed reference receiver $\mathbf{x}_\mathcal{A}$, we estimate the travel-time difference function:

$$tt_A(\mathbf{x}_\mathcal{A}, \mathbf{x}_\mathcal{B}, \theta) = T_{\rightarrow\mathcal{B}} - T_{\rightarrow\mathcal{A}} + T_{\uparrow\mathcal{B}}(\theta) - T_{\uparrow\mathcal{A}}(\theta). \tag{C.3}$$

We parameterize the effective illumination by the source using the back-azimuth and ray parameter (θ and p, respectively). If we assume the propagation velocity to be constant

along the receiver-side of the diffractor, the source dependence of tt_A is limited to θ, which determines the ray path through the medium at the receiver side. We rewrite equation C.3 in terms of p as

$$tt_A(\Delta_{\mathcal{AB}}, \theta) = p\Delta_{\mathcal{AB}} + dT_{\mathcal{AB}}(\theta), \tag{C.4}$$

where $\Delta_{\mathcal{AB}}$ is the epicentral distance between $\mathbf{x}_{\mathcal{A}}$ and $\mathbf{x}_{\mathcal{B}}$. The receiver-side travel-time difference is now expressed in one term: $dT_{\mathcal{AB}}(\theta) = T_{\uparrow\mathcal{B}}(\theta) - T_{\uparrow\mathcal{A}}(\theta)$. When $dT_{\mathcal{AB}}(\theta)$ is assumed to be known, equation C.4 can be used to estimate p (e.g., Wysession et al., 1999; Mikesell et al., 2009). In this study we take an alternative approach. We assume p to be known and use equation C.4 to estimate receiver-side anomalies. Note that p only needs to be known for the CMB-trajectory where the rays deviate (Fig. C.1). Therefore, the CMB may strongly vary along parts of the path that overlap. The signal-to-noise of tt_A can be improved by averaging over multiple inline sources, since tt_A is not a function of the source distance, nor of source depth (equation C.4).

C.3 Inline scanning

We apply the anomaly-scanner to a linear sub-array of USArray, shown in Fig. C.2. The data come from the Mw=7.4 Simeulue (Indonesia) earthquake, which occurred February 20, 2008. The event and the selected stations lie approximately along the same great circle path, so that the path from the earthquake to the CMB is constant for the entire sub-array. For each station we have the instrument-response function. We remove it from the data by implementing a deconvolution in the frequency domain. Subsequently we band-pass filter the vertical component seismograms between 0.01 and 0.12 Hz; a band in which there is little disturbance from the double-frequency microseism (Longuet-Higgins, 1950). Then we isolate P_{diff} by applying a tapered time-window around the main pulse. The length of this time-window is of the order of the dominant period. Taking a longer time-window would increase the risk of including concurrent phases and reverberations from non-radially symmetric interfaces, which would bias the estimation of the receiver-side anomaly. After isolating P_{diff} we crosscorrelate P_{diff} at the reference station with P_{diff} at all the other stations. From the crosscorrelations we estimate the differential travel-time function (equation C.4), which to first order is a linear function through the origin, with slope p. This feature has been observed for shallower applications in seismology, and termed the "virtual refraction" by Mikesell et al. (2009). We largely remove this linear term by assuming a reference ray parameter of 4.66 s/deg (Fig. C.A.1 explains how we found this value), leaving the receiver-side anomaly, $dT_{\mathcal{AB}}(\theta)$ (Fig. C.2b, black line). To eliminate topography as the source of these anomalies, we generate a static correction based on an upper-crustal velocity of 5.8 km/s. Applying the static yields the red line in Fig. C.2(b). This correction shows that topography does lead to a significant time delay, but has little influence on the overall shape of the anomaly.

Equation C.2 assumes that the wavelets of P_{diff} at the two receiver locations are identical. However, this wavelet might vary due to propagation effects and the radiation pattern

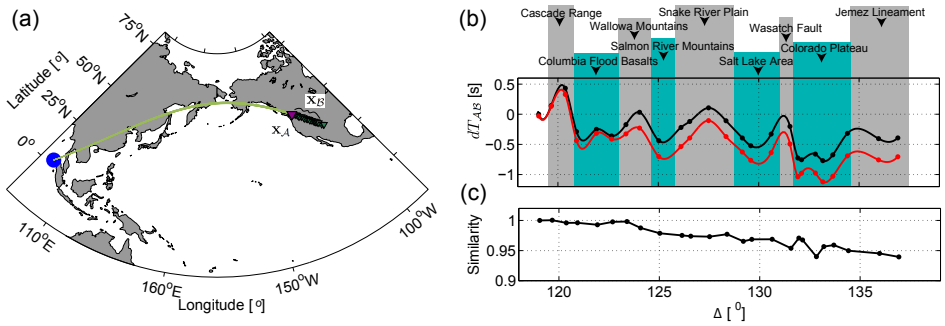


Figure C.2 *P_{diff} travel-time anomalies for an inline configuration with one earthquake (blue circle) and a line of receivers (green triangles). (a) shows the configuration. Correlation of the P_{diff} arrival at a purple reference station with its arrival on all other stations is used to find the P_{diff} travel-time anomalies as are shown in (b). Dots represent the extracted anomalies at the different stations, and the lines are created through spline interpolation of these points. In (b) the red and black lines denote the functions with and without a static correction for topography, respectively. Panel (c) depicts the waveform similarity between the P_{diff} arrival at the reference station and all the other stations.*

of the source. We check the validity of this assumption by computing the waveform similarity (the maximum amplitude of the crosscorrelation between $\mathbf{x}_{\mathcal{A}}$ and $\mathbf{x}_{\mathcal{B}}$, scaled by the maximum amplitude of the autocorrelation at $\mathbf{x}_{\mathcal{A}}$). A value of one means the effective source wavelets are identical. Figure C.2c shows that the similarity is high throughout and only decays slowly from the reference trace, which indicates that the subtle changes in the wavelet of P_{diff} are not the source of the observed anomaly. Instead, travel-time anomalies of Figure C.2b correlate with large-scale known features under the receivers. For example, positive anomalies correlate with known elevated temperatures in the crust and mantle, some of which have surface expressions in the form of volcanism. In Figure C.2b, the Cascade Range displays a positive anomaly (i.e., decreased velocity), related to active volcanism. Similar correlations can be seen for the Wallowa Mountains and Snake River Plain. Stations near the Wasatch Fault and just north of the Jemez Lineament also show a positive anomaly. Near these stations there are currently no surface expressions of volcanism, but these stations are just north of known volcanic areas. Negative P_{diff} travel-time anomalies are present below the Columbia Flood Basalts and the Colorado Plateau, where subsurface velocities are known to be relatively fast (e.g., Obrebski et al., 2011).

The CMB region below the Pacific is known to be heterogeneous (Wysession et al., 1999). In Figure C.2 we assumed a p=4.66 s/deg to remove the main linear trend in the P_{diff} arrival times. Wysession et al. (1999) found values between 4.41 and 4.90 s/deg for raypaths crossing the Pacific. Figure C.A.3 shows the anomaly-function for p values ranging from 4.4 to 4.9 s/deg, with steps of 0.1 s/deg. Realistic structural trends remain only at p values near 4.66 s/deg.

To obtain a measure of the accuracy of the inline scan, we extract the receiver-side anomaly for three more earthquakes. We use the same station array as in Fig. C.2. These earthquakes are again from the Sumatra region and are therefore still approximately inline with the array. Fig. C.A.4 shows the anomaly functions for the individual earthquakes as well as the mean anomaly function. The average standard deviation from the mean anomaly function is 0.163 s.

C.4 Testing for source-side anomalies

The linear configuration underlying equation C.4 means that travel-time anomalies can be attributed to the receiver-side. However, this configuration (Fig. C.2a) is not practical to create a 2D anomaly map. Each line of receivers would require an earthquake – or earthquakes – on the great circle path through the line of receivers, and the results for different lines could not easily be combined to create a single anomaly map. Therefore, we extend the P_{diff} travel-time anomaly scanner to 2D seismic arrays.

When the source and receivers do not lie along the same great-circle path (i.e., in one plane), the source-side ray paths do not overlap, and we need to include the source-side anomaly term:

$$dT_{\mathcal{AB}}(\tilde{\theta}) = T_{\downarrow\mathcal{B}}(\tilde{\theta}) - T_{\downarrow\mathcal{A}}(\tilde{\theta}) + T_{\uparrow\mathcal{B}}(\tilde{\theta}) - T_{\uparrow\mathcal{A}}(\tilde{\theta}), \tag{C.5}$$

where $\tilde{\theta}$ is now an average back-azimuth.

To test the significance of the source-side anomaly term, we select an approximately North-South line of 28 seismic stations from the USArray (Fig. C.3a). It crosses various tectonic regions, among others, the eastern edge of the Rocky Mountains. During the time these stations were active (Sept. 2008 to August 2010), numerous P_{diff} arrivals were recorded, especially from earthquakes in Southeast Asia. Due to the large distance traversed by P_{diff} (Δ can be $100 - 150°$), some arrivals have a poor signal-to-noise ratio. Therefore, we only consider five events with Mb>6.5, with easily identifiable P_{diff} arrivals in the seismic record. The reference station is the purple triangle in Fig. C.3(a), and we apply the same processing as in Section C.3 to estimate P_{diff} travel-time anomalies for each of the five earthquakes.

Fig. C.3(b) displays travel-time anomalies as a function of station latitude, for the five different earthquakes. Although there are differences between the five functions, the major features (high-amplitude and relatively small wavelength) are common to all. This leads to the conclusion that source-side features and variations in velocity along the CMB are secondary.

Residual linear trends are to be expected among the five events because we know that the lower mantle below the Pacific is heterogeneous (Wysession et al., 1999). Therefore, it is formally not correct to assume a constant p for each event, when removing the linear term in equation C.4. The average remaining linear trend in Fig. C.3(b) is -0.087 s/deg. The standard deviation σ of this linear trend is 0.028 s/deg (same as in Fig. C.A.1). This σ is

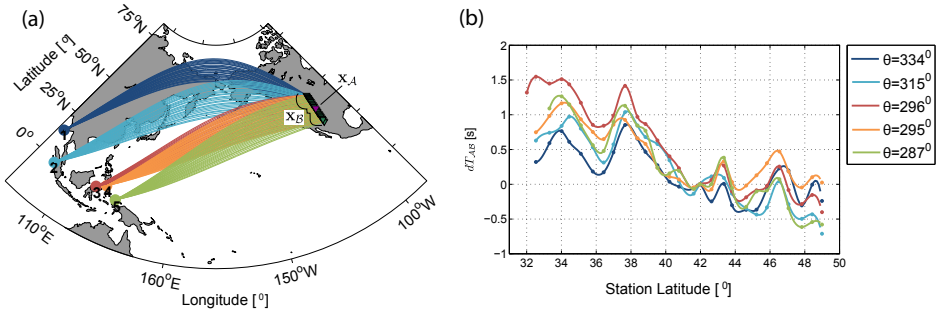


Figure C.3 *P_{diff} travel-time anomalies for multiple earthquakes (colored circles) that are not inline with a line of receivers (green triangles, i.e., line 21 from the USArray). (a) shows the configuration. Correlation of the P_{diff} arrival at a purple reference station with its arrival on all other stations is used to find the P_{diff} travel-time anomalies as are shown in (b). Dots represent the extracted anomalies at the different stations, and the lines are created through spline interpolation of these points. On the right-hand side of panel (b), the average back-azimuths for the 5 earthquakes are given.*

almost three times as high as for closely located sources (Fig. C.A.4). Still, it is only 0.6 % of the reference rayparameter (4.66 s/deg), indicating that there is – on average – little velocity variation over the different CMB paths as depicted on Fig. C.3(a).

In summary, even though there are some differences in trend and local P_{diff} travel times, generally the same travel-time anomalies are recovered in Fig. C.3(b) for each of the five events. Therefore, the influence of source-side velocity anomalies in equation C.5 turns out to be small with respect to the receiver-side anomalies. A positive velocity anomaly in the South is correlated to unstable Proterozoic terranes and a negative velocity anomaly in the North is the result of a stable Archean lithosphere. Superposed on these large features are smaller-scale travel-time perturbations common to all five earthquakes, but difficult to correlate with known features using just one line. In the following section, we neglect the source term in equation C.5 and image receiver-side anomalies in a 2D sense.

C.5 Map scanning

Since 2006 USArray seismic stations have covered a large part of the USA. Most stations are moving from the West to the East in a roll-along fashion (the transportable array), see Levander et al. (1999). Simultaneously, there is a reference network consisting of permanent stations. We use data from September of 2007 to June of 2010 to image receiver-side anomalies from the West Coast to the Great Plains. The distribution of stations used in this study is depicted in Figure C.4a. The permanent and quiescent station TA.R11A in Nevada ($\mathbf{x}_{\mathcal{A}}$ = 38.3489° N, 115.5854° W) is used as the reference station to scan for heterogeneity in the crust and mantle using the P_{diff} arrival from nine earthquakes with Mb>6.5. These

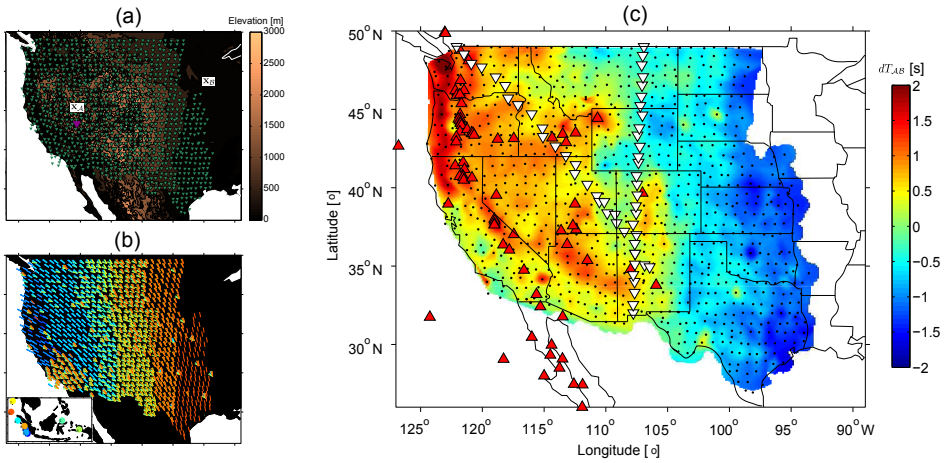


Figure C.4 *(a) The location of USArray stations used in this study (green triangles) projected onto a topographic map of part of the USA. The reference station at position $\mathbf{x}_{\mathcal{A}}$ is indicated by the purple triangle. (b) Illumination map –the colored lines denote the back-azimuth to the earthquakes and these correspond to the colors of the circles in the inset (Indonesian Archipelago). (c) P_{diff} travel-time anomaly map, combined with 1) the primarily Holocene volcanism (red triangles, source: http://www.volcano.si.edu/); 2) USArray stations used in this study (black dots); 3) the station locations used in Fig. C.2 (NE-SW subarray of white triangles) and Fig. C.3 (N-S subarray of white triangles).*

events occurred around the Indonesian Archipelago (Figure C.4b, inset) such that most of the great-circle paths cross Alaska. Hence, the contiguous USArray stations are illuminated with a back-azimuth close to NW, as shown in Figure C.4b. On the same figure, swaths of North-South stations that were simultaneously active for a given event can be recognized. We select a total of 4076 arrival times for 993 different stations. Thus, each station is illuminated on average by $\sim$4 events.

For each event in Fig. C.4(b, inset), we cross-correlate the windowed P_{diff} arrival at $\mathbf{x}_{\mathcal{A}}$ with all other available stations. We extract the differential travel-time function and remove the linear term to isolate the receiver-side travel-time anomaly $dT_{\mathcal{AB}}(\tilde{\theta})$. To remove the linear term we use a fixed ray parameter p=4.66 s/deg (equation C.4). We average the travel-time anomalies at each station over the available events to suppress non-stationary noise. A static correction is applied in the same way as the example in Section C.3. Finally, we remove the mean from the entire 2D anomaly function (1.12 s is added) and perform a bi-cubic interpolation, resulting in the anomaly map of Fig. C.4(c).

The receiver-side anomaly map is an integration over the entire ray path from the CMB to the Earth's surface. This path is more than 3000 km long. However, the largest heterogeneity is expected near the Earth's surface, where rays converge onto the stations. To first order, the anomaly map shows similar features to those from travel-time or velocity inversion mod-

els of the western USA (e.g., Schmandt & Humphreys, 2010; Burdick et al., 2010; Obrebski et al., 2011; Ritzwoller et al., 2011). Slow velocities (positive travel-time anomalies) in the west are related to magmato-tectonic activity while high velocities (negative travel-time anomalies) in the east are related to stable Archean lithosphere. The slowest anomalies correlate well with Cenozoic volcanic activity (red triangles in Fig. C.4c). Positive travel-time anomalies below South-Dakota and Texas are likely related to thick sedimentary packages, where the extra time lag through the sediments is not compensated by a thinner crust. Fig. C.A.5 compares our results with a recent inversion model by Obrebski et al. (2011).

C.6 Discussion

This new method resembles P- and S-wave residual mapping (e.g., Dziewonski & Anderson, 1983; Martynov et al., 2004); however rather than comparing the observed arrival time at $\mathbf{x}_{\mathcal{B}}$ with a synthetic arrival at $\mathbf{x}_{\mathcal{B}}$, we compare the relative arrival time between $\mathbf{x}_{\mathcal{A}}$ and $\mathbf{x}_{\mathcal{B}}$, after a correction for the differential CMB path. When looking at lateral structure, the main advantage to our method is that our results are data driven. A good estimate of the CMB velocity is required, but it can be directly obtained from the data. Residual mapping depends on an accurate source location and velocity model to derive synthetics. Errors in either of these will propagate into the mapped residuals. Fig. C.A.2 compares raypath characteristics of the P_{diff}-phase that we use to the P-phase used in residual mapping.

Data processing is limited to removing the instrument response, time-windowing around the P_{diff} arrival, low-pass filtering below microseism disturbances, and crosscorrelation to extract the differential arrival times. Removing the instrument-response is a vital step because near the low end of the frequency band we use, USArray stations can have phase differences exceeding 10 deg. These phase delays may be on the same order as the delays caused by receiver-side structure and therefore need to be corrected.

Our results illustrate the benefit of adding global-phases for tomographic inversion to improve lateral resolution of subsurface images. In tomography, travel-time perturbations are smeared along the entire ray path. Incorporating receiver-side information from the swift P_{diff} anomaly scanner may serve to establish lateral resolution with greater confidence. Furthermore, S_{diff} can be used instead of P_{diff} to swiftly scan S-wave anomalies. This methodology could also be applied to P_n or S_n to scan specifically for crustal anomalies, establishing better constraints on depth.

The main advantage of the new method lies in its speed and simplicity. The anomaly scanner is especially useful to identify features that deserve a more expensive inversion and a denser seismic array. The quality of the extracted features depends directly on the data signal-to-noise ratio and the GPS clock accuracy at each station. In the frequency band used, the noise is primarily caused by the single-frequency microseism. Since this noise is non-stationary, we suppress its influence by averaging travel-time anomaly functions from many events with similar back-azimuths. If the anomaly-scan is to be used in a quantitative way, then

also a good estimate of CMB velocities is important.

We found that no small-wavelength features are introduced in the travel-time anomaly when different CMB paths are used (Fig. C.3, C.A.1 and C.A.4). This means that small-scale CMB heterogeneity, if present, does not map into the differential travel times. The long-wavelength character of the anomaly function, however, does change when different CMB paths are considered. This wavenumber separation between receiver-side and CMB imprints creates the possibility for a simultaneous inversion. One could invert for a CMB structure for which the travel-time anomalies from different CMB trajectories, as in Fig. C.3(b), would optimally overlap. In this way, one could simultaneously estimate a CMB model while improving the absolute amplitudes of the receiver-side anomaly map.

C.7 Conclusion

We identified velocity anomalies in the crust and mantle under a linear array of receivers from differential P_{diff} arrivals from earthquakes inline with the receivers. Using just one earthquake, clear receiver-side structure is resolved. We confirmed the stability of the scan by using a set of nearby earthquakes. We extended the method to earthquakes not inline with the receivers. This extension proved valid as source-side and CMB structure resulted in only small variations in the mapped anomalies. This allowed us to apply the scan to a regional grid of receivers across the western half of contiguous USA. By averaging the results from 9 different earthquakes, we created a 2D map of the receiver-side structure. Strong correlation with known features under the western half of the USA confirmed the validity of this fast and robust technique. P_{diff} travel-time anomalies are capable of high lateral resolution under the receivers, but average in the vertical direction. Therefore, the method is complementary to surface- and body-wave tomography, where averaging takes place in the lateral sense.

C.A P_{diff} auxiliary material

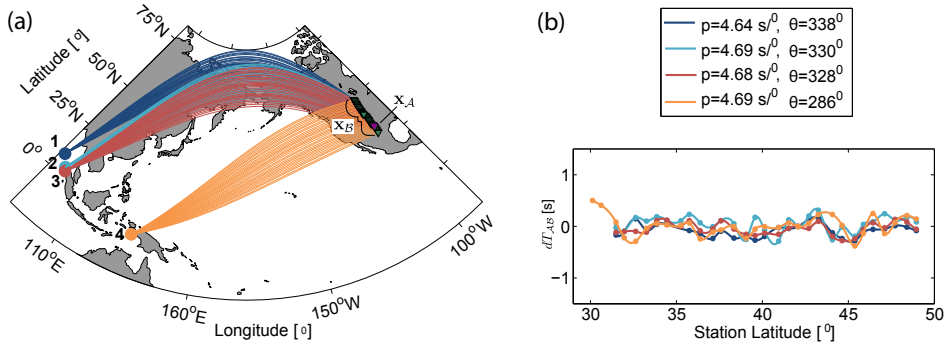


Figure C.A.1 *Procedure for estimating an average rayparameter p for P_{diff}-raypaths over the Northern Pacific. (a) Depicts the configuration. The difficulty in reliably estimating p is that the apparent velocity of P_{diff} along the receiver array is affected by long-wavelength velocity variations near the array. Therefore, we use a linear array (green triangles) through the Great Plains, where little trend is expected in the receiver-side structure. For a collection of high-magnitude events from the Indonesian Archipelago (colored circles) we estimate –per event– a best-fitting line through the picked differential traveltimes (equation 4) and remove this linear trend, resulting in the functions as displayed in (b). The slope of the linear trends are an estimate of the rayparameter. The estimated rayparameters and the average backazimuths θ are shown on the right-hand side of (b). The mean and standard deviation of p are 4.66 and 0.028 s/deg, respectively.*

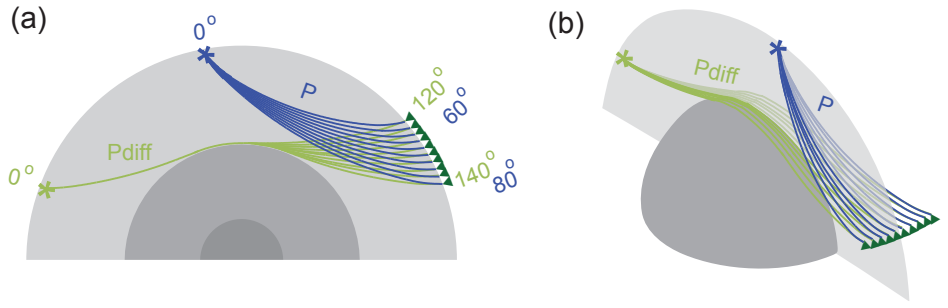


Figure C.A.2 *Comparison of rayspreading for a P phase and a P_{diff} phase detected at a large array ($\Delta = 20^0$) of stations (green triangles). (a) and (b) show the rayspreading for an 'inline' and 'crossline' array, respectively.*

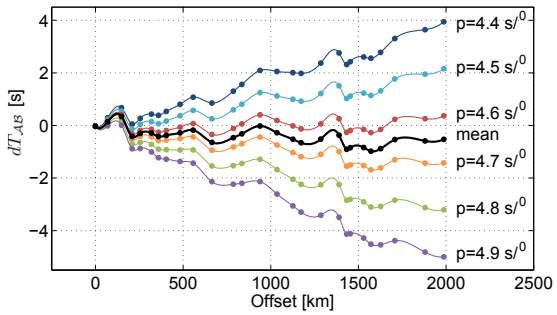


Figure C.A.3 *The sensitivity of the extracted receiver-side anomaly $dT_{\mathcal{AB}}(\theta)$ to different linear-correction slopes p. The same source-and-receiver configuration is used as in Fig. C.2. The extracted receiver-side anomaly is plotted as function of distance with respect to the reference station $\mathbf{x}_{\mathcal{A}}$ (offset).*

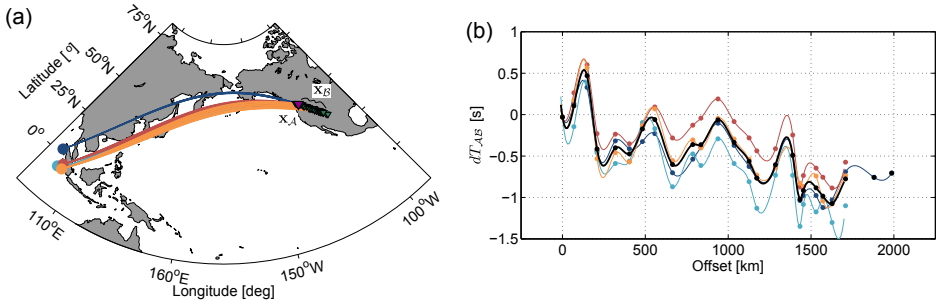


Figure C.A.4 *Travel-time anomalies found with P_{diff} arrivals from four closely located earthquakes. (a) The configuration with the distribution of sources (circles) and receivers (green triangles) and the connecting great-circle paths (curved lines). The receiver array is the same as was used for Fig. C.2. Also, the earthquake denoted with the blue circle, is the same as was used for Fig. C.2. We show (b) the extracted travel-time anomalies as function of distance with respect to station $\mathbf{x}_{\mathcal{A}}$. The dots represent the extracted travel-time anomalies at the different stations, and the lines are created by spline interpolation of the dots. The black line is the average travel-time anomaly function. The standard deviation from the mean anomaly function is 0.163 s. The standard deviation from the mean linear trend is 0.010 s/deg.*

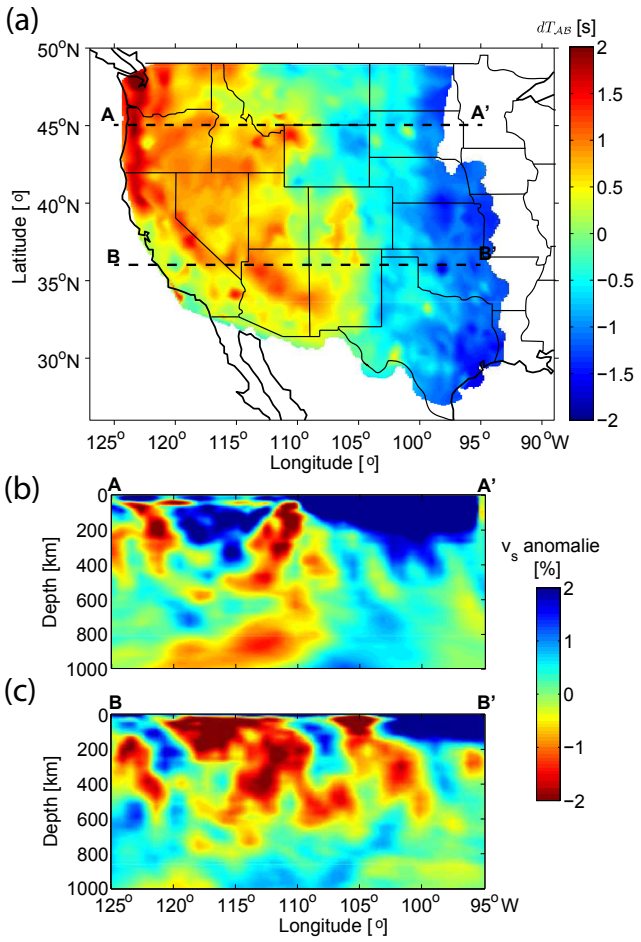


Figure C.A.5 *Comparison of (a) the P_{diff} travel-time anomaly map with (b&c) two sections from DNAS-10S. The dashed lines in (a) denote the location of two cross-sections, A-A' (b) and B-B' (c). DNAS-10S is the most recent inversion model that incorporates the Great Plains (Obrebski et al., 2011). Although this is an S-wave model, Schmandt & Humphreys (2010) showed that similar features are resolved for a P-wave model. We extract two sections from DNAS-10S to compare with our anomaly map in depth. It is apparent that the features resolved in (a) come from an integration over depth of the features in (b) and (c). For example, the feeding channel for the Yellowstone volcanism (at about -113^0 longitude in (b)) extends far in depth, leading to a very slow anomaly in (a). The fast (blue) lithosphere block west of Yellowstone, however, does not lead to a fast anomaly in (a) since it is underlain by a slow anomaly in the lower mantle (at about 800 km in (b)). For a detailed interpretation of the anomalies in the Proterozoic part of the USA, we refer to Obrebski et al. (2011) and the references therein.*

Appendix D

Multidimensional deconvolution

D.1 Introduction

In this thesis we apply primarily seismic interferometry by crosscorrelation (SI by CC). This technique consists of a correlation of responses, followed by an integration over a line (e.g., equation 3.2) or surface (e.g., equation 2.13) distribution of sources. In nature, most sources are not regularly distributed over a line or surface. The integration is thus approximated by stacking over an irregular source distribution. This approximation may introduce severe errors. Different techniques are applied to correct for this irregular sampling. These techniques can be subdivided into two groups: 1 prestack and 2 poststack methods. The prestack methods adjust the integrand of the interferometric relation. The poststack methods make corrections to a first interferometric result.

A few examples of prestack methods can be found in this thesis. In Section 3.4 we consider the addition of summation weights before stacking. Also, we test time reversing of (a part of) the integrand before stacking (TRBI, see equation 3.7). Furthermore, in Ruigrok et al. (2009a), we test binning and interpolation of the integrand. In Chapter 5 we estimate illumination characteristics of noise measurements through beamforming. Subsequently, we populate the integrand only with data with the desired illumination. Melo et al. (2010) applied a singular-value decomposition to the integrand. They enhance the stationary contributions by subsequently removing the higher eigenvalues. The same could be achieved by filtering out the higher wavenumbers before stacking.

The following methods are applied after stacking. van der Neut & Bakulin (2009) use a linear array of stations to estimate the radiation of the wavefield that is used for the retrieval of reflections. They use this radiation pattern to improve the estimated reflection response. Their approach is valid for laterally invariant media. Curtis & Halliday (2010b) propose an alternative post-stack processing that may be applied to more heterogeneous media. However, the incoming wavefield needs to be detected at a grid of receivers. They estimate parameters for directional balancing by minimizing the difference between the perturbed actual and a desired illumination. van der Neut (2012) proposes another minimization ap-

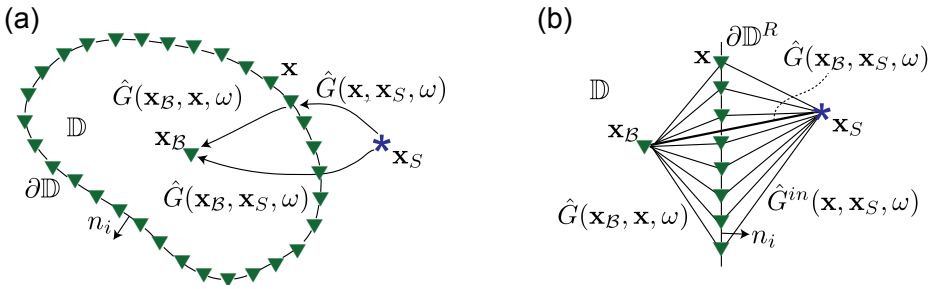


Figure D.1 *(a) Configuration for the convolution-type Green's function representation (equation D.1), in which the complete response between $\mathbf{x}_S$ and $\mathbf{x}_\mathcal{B}$ (including multiple scattering and attenuation) can be written as an integral of crossconvolutions of responses detected at the boundary of domain $\mathbb{D}$ due to $\mathbf{x}_S$ and responses detected at $\mathbf{x}_\mathcal{B}$ due to sources at $\partial\mathbb{D}$. (b) Configuration for the simplified crossconvolution integral relation (equation D.3), where $\partial\mathbb{D}^R$ is the right-hand side of the closed (integration) surface $\partial\mathbb{D}$ that is depicted in (a).*

proach, this time casted in the $\tau - p$ domain. van Groenestijn & Verschuur (2010) use SI by CC as the first estimate of the primary, rather than the full, reflection response. They subsequently update this primary reflection response with a sparse iterative inversion.

In this appendix we discuss another approach that is part of the second class of techniques: SI by multidimensional deconvolution (MDD). This technique may be thought of as the extension of the technique described in van der Neut & Bakulin (2009), to arbitrarily heterogeneous media. This technique was already briefly discussed for a body-wave application (Section B.3). In this appendix we write down the basics for a configuration that is practical for surface-wave applications. Using numerical data, we show how the obtained relation could be used for improving Rayleigh-wave retrievals. Furthermore, we shortly describe the current state of applying MDD to teleseismic body waves. For the details we refer to the published papers.

D.2 Theory for one-sided illumination

For the configuration as depicted in Fig. D.1(a) we can write the following convolution-type representation (Wapenaar et al., 2011b):

$$-\oint_{\partial\mathbb{D}} \frac{1}{j\omega\rho(\mathbf{x})}\{\partial_i\hat{G}(\mathbf{x}_\mathcal{B}, \mathbf{x}, \omega)\hat{G}(\mathbf{x}, \mathbf{x}_S, \omega) - \hat{G}(\mathbf{x}_\mathcal{B}, \mathbf{x}, \omega)\partial_i\hat{G}(\mathbf{x}, \mathbf{x}_S, \omega)\}n_i d^2\mathbf{x} = \hat{G}(\mathbf{x}_\mathcal{B}, \mathbf{x}_S, \omega), \quad \text{(D.1)}$$

where $\hat{G}(\mathbf{x}_\mathcal{B}, \mathbf{x}_S, \omega)$ is the impulse response due to a source at $\mathbf{x}_S$ and a receiver at $\mathbf{x}_\mathcal{B}$ and ω is the angular frequency. The hat above the quantities denotes that they are in the frequency

domain. Operator ∂_i denotes differentiation with respect to the spatial coordinates and n_i is the outward-pointing unit vector normal to $\partial\mathbb{D}$.

Slob et al. (2007) derived the electromagnetic equivalent of equation D.1 with source-receiver reciprocity applied to $\hat{G}(\mathbf{x}, \mathbf{x}_S, \omega)$. With this change, both $\mathbf{x}_S$ and $\mathbf{x}_\mathcal{B}$ are receiver positions and $\partial\mathbb{D}$ is populated with sources. The response between these receiver positions can then be estimated by a crossconvolution of wavefields, integrated over source positions $\mathbf{x}$. On the other hand, in the configuration we consider (Fig. D.1a), the unknown response is $\hat{G}(\mathbf{x}_\mathcal{B}, \mathbf{x}, \omega)$. This response is part of the integrand in equation D.1. A process that inverts $\hat{G}(\mathbf{x}_\mathcal{B}, \mathbf{x}, \omega)$ from equation D.1 or a similar integral relation, is called SI by MDD, or just MDD.

In equation D.1 $\hat{G}(\mathbf{x}_\mathcal{B}, \mathbf{x}, \omega)$ appears twice in the integrand, once as a monopole, and once as a dipole response. This makes equation D.1 impractical for MDD. Wapenaar et al. (2011b) split up $\hat{G}(\mathbf{x}, \mathbf{x}_S, \omega)$ in a field that is inward propagating at $\partial\mathbb{D}$ and a field that is outward propagating at $\partial\mathbb{D}$ (denoted with superscripts ^{in} and ^{out}, respectively). They show that, when using only $\hat{G}^{in}(\mathbf{x}, \mathbf{x}_S, \omega)$, equation D.1 can be simplified to

$$\oint_{\partial\mathbb{D}} \hat{G}_d(\mathbf{x}_\mathcal{B}, \mathbf{x}, \omega)\hat{G}^{in}(\mathbf{x}, \mathbf{x}_S, \omega)d^2\mathbf{x} = \hat{G}(\mathbf{x}_\mathcal{B}, \mathbf{x}_S, \omega), \tag{D.2}$$

where $\hat{G}_d(\mathbf{x}_\mathcal{B}, \mathbf{x}, \omega) = \frac{-2}{j\omega\rho(\mathbf{x})}\{n_i\partial_i\hat{G}(\mathbf{x}_\mathcal{B}, \mathbf{x}, \omega)\}$.

Equation D.2 remains valid when only the part of the integral is evaluated that contains the non-canceling stationary phases. For the configuration as depicted in Fig. D.1(b), the expression is thus

$$\int_{\partial\mathbb{D}^R} \hat{G}_d(\mathbf{x}_\mathcal{B}, \mathbf{x}, \omega)\hat{G}^{in}(\mathbf{x}, \mathbf{x}_S, \omega)d^2\mathbf{x} = \hat{G}(\mathbf{x}_\mathcal{B}, \mathbf{x}_S, \omega), \tag{D.3}$$

where $\partial\mathbb{D}^R$ is only the right-hand-side part of the former enclosing surface.

In case of a non-impulsive source we do not measure $\hat{G}^{in}(\mathbf{x}, \mathbf{x}_S, \omega)$ and $\hat{G}(\mathbf{x}_\mathcal{B}, \mathbf{x}_S, \omega)$, but these Green's functions multiplied with the source spectrum $s(\omega)$ (which corresponds to convolution with the source time function $s(t)$ in the time domain). Also for actual registrations equality D.3 remains valid, because both sides can be multiplied with $s(\omega)$ to obtain quantities that are measured in practise.

We can only isolate $\hat{G}_d(\mathbf{x}_\mathcal{B}, \mathbf{x}, \omega)$ from equation D.3 when we measure the responses at $\mathbf{x}$ and $\mathbf{x}_\mathcal{B}$ due to multiple sources $\mathbf{x}_S^{(i)}$, where i is a source index. Only from this wide illumination we can characterize the impulse responses between (all) positions on $\partial\mathbb{D}^R$ and $\mathbf{x}_\mathcal{B}$.

For N sources on the right-hand side of $\partial\mathbb{D}^R$ and M receivers on $\partial\mathbb{D}^R$ we rewrite equation D.3 in matrix-vector notation (Berkhout, 1982) as

$$\hat{\mathbf{G}}_d\hat{\mathbf{G}}^{in} = \hat{\mathbf{G}}, \tag{D.4}$$

where

$$\hat{\mathbf{G}}_d = \left[\begin{array}{ccc} \hat{G}_d(\mathbf{x}_\mathcal{B}, \mathbf{x}_1) & ... & \hat{G}_d(\mathbf{x}_\mathcal{B}, \mathbf{x}_M) \end{array} \right], \tag{D.5}$$

$$\hat{\mathbf{G}}^{in} = \begin{bmatrix} \hat{G}^{in}(\mathbf{x}_1, \mathbf{x}_S^{(1)}) & \cdots & \hat{G}^{in}(\mathbf{x}_1, \mathbf{x}_S^{(N)}) \\ \vdots & \ddots & \vdots \\ \hat{G}^{in}(\mathbf{x}_M, \mathbf{x}_S^{(1)}) & \cdots & \hat{G}^{in}(\mathbf{x}_M, \mathbf{x}_S^{(N)}) \end{bmatrix} \tag{D.6}$$

and

$$\hat{\mathbf{G}} = \left[\begin{array}{ccc} \hat{G}(\mathbf{x}_\mathcal{B}, \mathbf{x}_S^{(1)}) & ... & \hat{G}(\mathbf{x}_\mathcal{B}, \mathbf{x}_S^{(N)}) \end{array} \right]. \tag{D.7}$$

In the above three equations we left out the variable ω for compactness.

From equation D.4 $\hat{\mathbf{G}}_d$ can be isolated through matrix inversion: $\hat{\mathbf{G}}(\hat{\mathbf{G}}^{in})^{-1} = \hat{\mathbf{G}}_d$, where $(\hat{\mathbf{G}}^{in})^{-1}$ is the inverse of $\hat{\mathbf{G}}^{in}$. This inverse might not be computable. As an alternative, Minato et al. (2011) solve a similar matrix equation with singular-value decomposition. We consider a damped least-squares inversion. To find the least-squares solution, first both sides of equation D.4 are matrix-multiplied by the adjoint of $\hat{\mathbf{G}}^{in}$:

$$\hat{\mathbf{G}}_d \hat{\mathbf{G}}^{in} \{\hat{\mathbf{G}}^{in}\}^\dagger = \hat{\mathbf{G}} \{\hat{\mathbf{G}}^{in}\}^\dagger, \tag{D.8}$$

where the superscript † denotes transposition of the matrix and complex conjugation of each entry in the matrix. Next, $\hat{\mathbf{G}}_d$ is isolated through a water-level stabilized inversion:

$$\hat{\mathbf{G}} \{\hat{\mathbf{G}}^{in}\}^\dagger (\hat{\mathbf{G}}^{in} \{\hat{\mathbf{G}}^{in}\}^\dagger + \epsilon^2 \mathbf{I})^{-1} = \hat{\mathbf{G}}_d, \tag{D.9}$$

where $\mathbf{I}$ is the identity matrix, and ϵ^2 is a stabilization parameter.

van der Neut et al. (2010) show that with least-squares inversion, in fact, the original problem (equation D.3) is first remapped before it is solved. This becomes obvious when we write out the matrix equation (equation D.8) in (Riemann) summations:

$$\int_{\partial \mathbb{D}^R} \hat{G}_d(\mathbf{x}_\mathcal{B}, \mathbf{x}, \omega) \hat{\Gamma}(\mathbf{x}, \mathbf{x}_\mathcal{A}, \omega) = \hat{C}(\mathbf{x}_\mathcal{B}, \mathbf{x}_\mathcal{A}, \omega), \tag{D.10}$$

where $\mathbf{x}_\mathcal{A}$ is a position on $\partial \mathbb{D}^R$ and

$$\hat{C}(\mathbf{x}_\mathcal{B}, \mathbf{x}_\mathcal{A}, \omega) = \sum_{i=1}^{N} \hat{G}(\mathbf{x}_\mathcal{B}, \mathbf{x}_S^{(i)}, \omega) \{\hat{G}^{in}(\mathbf{x}_\mathcal{A}, \mathbf{x}_S^{(i)}, \omega)\}^* \tag{D.11}$$

and

$$\hat{\Gamma}(\mathbf{x}, \mathbf{x}_\mathcal{A}, \omega) = \sum_{i=1}^{N} \hat{G}^{in}(\mathbf{x}, \mathbf{x}_S^{(i)}, \omega) \{\hat{G}^{in}(\mathbf{x}_\mathcal{A}, \mathbf{x}_S^{(i)}, \omega)\}^*. \tag{D.12}$$

Equation D.11 can be recognized as being an implementation of SI by crosscorrelation, for sources only at the right-hand side of the configuration. In the following we will call this equation the crosscorrelation function (CF). Equation D.12 is a crosscorrelation of the

incoming wavefields at the receiver array. In the following we will call this the point-spread function (PSF). Equation D.10 thus expresses that the CF is in general not equal to the impulse response between $\mathbf{x}_\mathcal{B}$ and $\mathbf{x}$. The CF is only equal to $\hat{G}_d(\mathbf{x}_\mathcal{B}, \mathbf{x}, \omega)$ when the PSF is a band-limited spatial (and temporal, after inverse fourier transform of equation D.10) delta pulse. When the PSF is no delta pulse, the CF is a blurred —and possibly ghost-haunted— version of the Green's function. Both the blurring and the ghosts are expressed in the PSF. MDD can thus be seen as the process of removing the blurring and the ghosts from the CF.

In equation D.10 all source positions have been stacked out (see equations D.11 & D.12). Thus, with the least-squares approach (equation D.9), the responses from (unknown) sources are first remapped to known receiver positions before isolating $\hat{G}_d(\mathbf{x}_\mathcal{B}, \mathbf{x}, \omega)$. To allow this remapping, the sources need to have a wide distribution with no large illumination gaps. Though, there may be clusters of sources. This overillumination caused by the source clusters consistently affects the PSF and the CF and is therefore divided out through MDD. This is numerically illustrated in the next section.

In Wapenaar et al. (2011b) it is shown that relation D.10 can also be computed for simultaneously acting, and mutually uncorrelated, noise sources. In this case, the CF and the PSF are obtained by crosscorrelating noise observations and averaging these crosscorrelations over different time segments.

D.3 Application to surface waves

In this section we give a numerical illustration of surface-wave MDD. The numerical example has been published in Wapenaar et al. (2011a). Fig. D.2–D.4 are a copy of their example. Moreover, we explain how surface-wave MDD is applied in a more complicated setting, as published in Wapenaar et al. (2011b).

Fig. D.2 shows the configuration from Wapenaar et al. (2011a). A North-South array of stations (green triangles) from the transportable USArray records wavefields induced by sources (blue dots) on the Atlantic. The same wavefields are recorded by a collection of backbone stations, east of the North-South array. Note that this configuration is similar to Fig. D.1(b). The main difference is that there are now multiple sources and multiples receivers $\mathbf{x}_\mathcal{B}$. As before (in equations D.9–D.12) the goal is to find the response between stations at $\partial\mathbb{D}^R$ (the North-South array) and stations west of $\partial\mathbb{D}^R$ (the backbone stations). However, in the current example only the fundamental-mode Rayleigh-wave is sought after, not the entire Green's function.

Storms on the Atlantic are considered to be sources of single-frequency microseims (Section 5.2). All sources are assumed to be simultaneously acting and largely uncorrelated. For a limited frequency band (blue line in Fig. D.2a) the fundamental-mode Rayleigh waves are forward modeled, using the dispersion curve as depicted with the black line in Fig. D.2(a). The dispersion curve is computed for the upper 300 km of a 1D Earth model (PREM, Dziewonski & Anderson (1981)), using the approach as described by Wathelet et al. (2004).

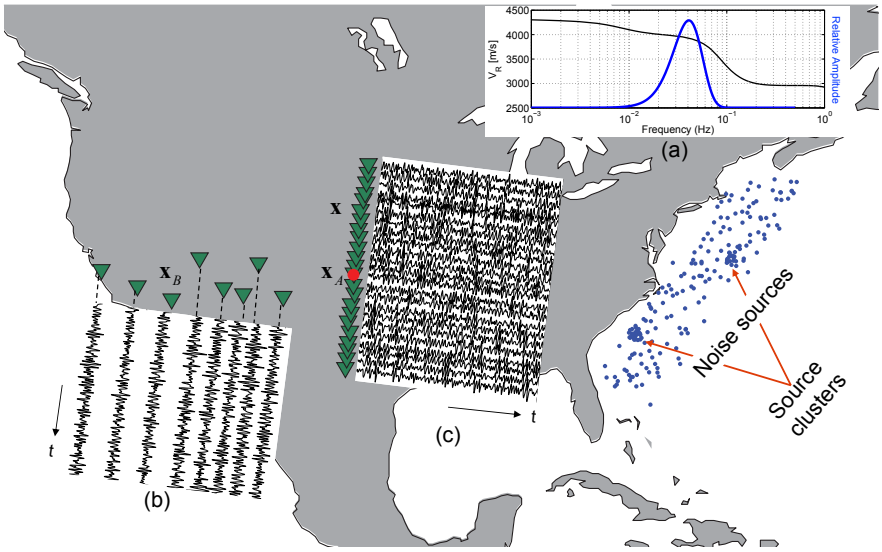


Figure D.2 *A configuration for the application of seismic interferometry by multidimensional deconvolution, to surface waves. The surface waves are induced by oceanic sources (blue dots) near the East Coast of the USA. The overlapping noise-source responses are recorded by a North-South array of stations (green triangles) and a more scattered distribution of stations at the Western half of the USA. (a) depicts the used dispersion curve for the forward modeling (black line) and source spectrum (blue line). (b) and (c) are examples of noise registrations. Redrawn from Wapenaar et al. (2011a).*

The noisy character of the sources and the overlap of their responses results in noise panels as shown in Fig. D.2(c) and (d).

The goal is to create a virtual source at $\mathbf{x}_{\mathcal{A}}$, which is indicated with a red dot in Fig. D.2. Approximately two days of noise registrations are used to compute the CF and the PSF (equations D.11 and D.12, respectively). Fig. D.3(a) shows the obtained CF (red traces) in comparison with a directly modeled response for a source at $\mathbf{x}_{\mathcal{A}}$ and receivers at $\mathbf{x}_{\mathcal{B}}$ (black traces). The match between retrieved and directly modeled responses is clearly not perfect. This mismatch is not only caused by the irregularity of the source distribution, but also by the limited duration of the noise responses. Due to the limited duration, cross terms between different sources remain in the CF. Similar source-irregularity and correlatedness artifacts color the PSF (Fig. D.3b). Consequently, the PSF is a poor approximation of a bandlimited delta pulse, which can also be seen through its frequency-wavenumber ($f - k$) spectrum (D.3c). Equation D.10 expresses that the artifacts in the PSF and CF are related. In fact, the CF may be seen as the response due to a spatially and temporally extended source as defined by the PSF (D.3b). After applying MDD (equation D.9) the panels in Fig. D.4 are obtained. It can be seen that with MDD indeed the source-irregularity and correlatedness artifacts are

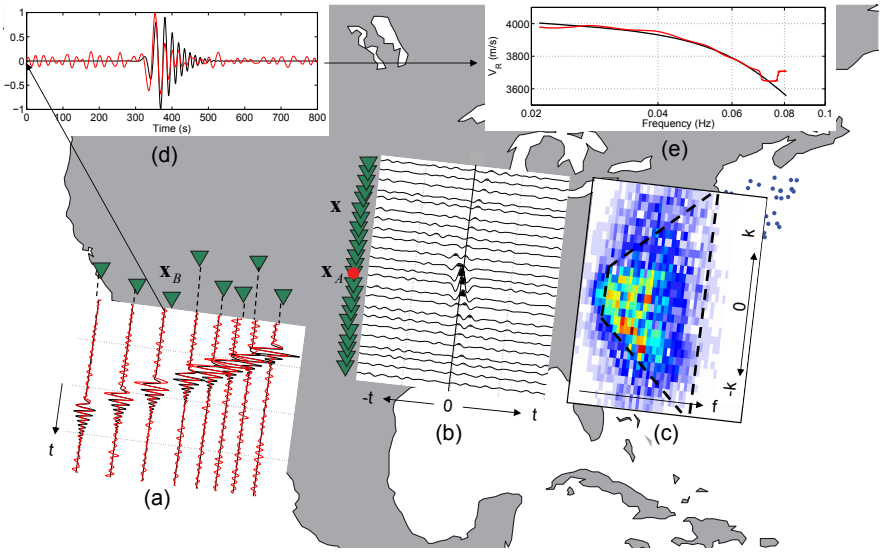


Figure D.3 *Results of the application of seismic interferometry by merely crosscorrelating registrations from microseism sources in the Atlantic. (a) is the obtained correlation function (equation D.11) for a virtual source at $\mathbf{x}_\mathcal{A}$ and receivers at $\mathbf{x}_\mathcal{B}$. (b) is the point-spread function (equation D.12) for the North-South array with $\mathbf{x}_\mathcal{A}$ at the position of the red dot. (c) is the frequency-wavenumber spectrum of (b). (d) is the zoomed version of one of the traces in (a). (e) is the dispersion curve, which is found from (d) with relation D.14. In (a), (d) and (e) the retrieved results (red lines) are compared with the directly modeled results (black lines). Redrawn from Wapenaar et al. (2011a).*

removed from the CF. This results in an excellent match with the directly modeled and the retrieved response (Fig. D.4a).

As a quality check the inverse PSF is applied to itself (by replacing $\hat{\mathbf{G}}$ with $\hat{\mathbf{G}}^{in}$ in equation D.9), using the same stabilization parameter ϵ as for the MDD. The result is depicted in Fig. D.4(b) and Fig. D.4(c) shows the $f-k$ spectrum . Fig. D.4(b) is now a much better approximation of a bandlimited delta pulse than before (Fig. D.3b). The spectrum remains limited within the bounds indicated by the dashed black lines in Fig. D.4(e). The band limitedness results from the limited frequency spectrum of the microseism sources and the limited extend of the source distribution. Within the dashed black lines the spectrum is not perfectly smooth. This is caused by limited extend and sampling of the North-South array and the need for stabilization.

The retrieved responses are (far-field) dipole responses (equation D.9), with the following phase term:

$$\Phi(\omega) = \omega|\mathbf{r}|/c(\omega) - \pi/4, \tag{D.13}$$

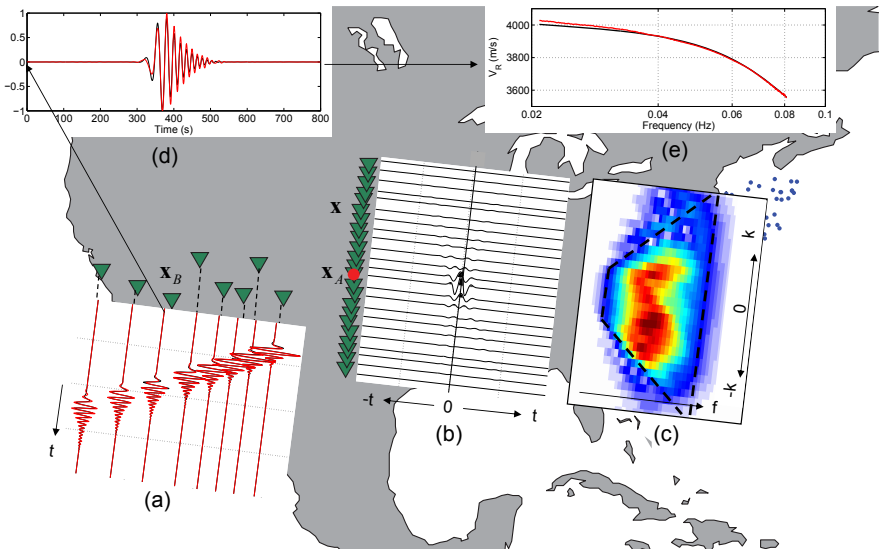


Figure D.4 *Illustration of seismic interferometry by multidimensional deconvolution (MDD). (a) is the result of applying MDD, using registrations from microseism sources in the Atlantic. It is an estimate of the response as if there were a source at $\mathbf{x}_\mathcal{A}$ and receivers at $\mathbf{x}_\mathcal{B}$. (b) is the inverse point-spread function applied to the point-spread function (Fig. D.3b) and (c) is the frequency-wavenumber spectrum of the resulting function. (d) is the zoomed version of one of the traces in (a). (e) is the dispersion curve, which is found from (d) with relation D.14. In (a), (d) and (e) the retrieved results (red lines) are compared with the directly modeled results (black lines). Redrawn from Wapenaar et al. (2011a).*

where $\mathbf{r} = \mathbf{x}_\mathcal{B} - \mathbf{x}_\mathcal{A}$ and $c(\omega)$ is the dispersion curve. Hence, from the retrieved seismogram the dispersion curve can be found with

$$c(\omega) = \frac{\omega|\mathbf{r}|}{\Phi(\omega) + \pi/4}. \tag{D.14}$$

Fig. D.3(d) depicts one of the retrieved responses using merely crosscorrelations. We time-window this response around the Rayleigh-wave arrival and isolate its phase spectrum $\Phi(\omega)$. Subsequently we use relation D.14 to compute the dispersion curve. Fig. D.3(e) shows a comparison of the obtained dispersion curve (red line) and the one used for the forward modeling (black line). The same exercise is repeated for one of the responses obtained with MDD (Fig. D.4d), yielding the dispersion curve as depicted in Fig. D.4(e). It can be seen that the dispersion curve obtained with MDD is more accurate than the one obtained using merely crosscorrelations. Only at the lower end of the frequency spectrum small mismatches remain. This mismatch would be removed if a wider illumination of sources was used.

In Wapenaar et al. (2011b) another numerical example is shown. This time not only direct waves are considered, but also scattered waves due to a scatterer in $\mathbb{D}$ (Fig. D.1). Note that $\mathbb{D}$ may be arbitrarily heterogeneous and that the scattered waves therefore do not pose a theoretical problem for MDD. However, there is the practical challenge of obtaining the required wavefields. At $\partial\mathbb{D}^R$ (Fig. D.1b) both incoming waves (due to sources on the right-hand side) and outgoing waves (due to the scattering from the scatterer on the left-hand side) are recorded. These scattering contributions cannot be removed directly from the recording for the case of simultaneously acting noise sources. Therefore, first the PSF and CF are computed using the full wavefields. When the scatterer is not too close to the $\partial\mathbb{D}^R$, most contributions of G^{out} can well be separated from contributions from G^{in}, through time windowing. In Wapenaar et al. (2011b) this time windowing is applied to the PSF and the CF. It is shown that with the resulting functions the correct Green's function is estimated with MDD. This retrieved Green's function includes arrivals from $\mathbf{x}$, via the scatterer, to $\mathbf{x}_{\mathcal{B}}$.

In Wapenaar et al. (2011b) also an alternative implementation is shown. Equations D.11 and D.12 remain valid when the crosscorrelations with the incoming fields $\hat{G}^{in}(\mathbf{x}_{\mathcal{A}}, \mathbf{x}_S^{(i)}, \omega)$ are replaced by crosscorrelations with the full fields $\hat{G}(\mathbf{x}_{\mathcal{A}}, \mathbf{x}_S^{(i)}, \omega)$. The advantage of using the latter relations is that less time-windowing is required. The CF does not need to be time-windowed at all. From the PSF only causal cross terms between G^{in} and G^{out} are to be removed. Less time-windowing introduces less errors and retains more data to compute the MDD with. Wapenaar et al. (2011b) show that the latter approach indeed gives a cleaner result.

D.4 Application to teleseismic body waves

MDD was numerically tested for lithospheric-scale imaging, using distant seismicity (Ruigrok et al., 2010b). MDD could only improve the results of applying merely cross-correlation (as in Chapter 3) when a large illumination range was available and a large array was used (> 50 km). The large illumination range is achieved by considering not only teleseismic, but also global and regional phases (Fig. 1.2). However, there are little to no arrays on the Earth that are inline with a well-sampled distribution of seismicity from all these distances. Moreover, the high rayparameter of regional phases requires a dense station sampling[1]. Large broadband arrays with this dense receiver spacing are not current practise.

Another challenge for lithospheric applications is the separation of the PSF and the CF. For body-wave applications with a single seismic array on the free surface (van der Neut et al., 2010) the required PSF and CF are approximated by crosscorrelating full wavefields and time-windowing the result. We took advantage of the fact that the main contributions of the PSF are at $t = 0$ at $\mathbf{x}_{\mathcal{A}}$ (see, for example, Fig. D.3b). Hence, an estimate of the PSF was

[1]The station spacing in the array should satisfy Nyquist sampling criterion, $dx_{rcv} < \frac{v_{min}}{2f_{max}} = \frac{1}{2f_{max}p_{max}}$. Thus for f_{max}=1.5 Hz and p_{max}=0.12 s/km (Fig. 5.8), we find $dx_{rcv} < 2.8$ km.

obtained in the $\tau - p$ domain, by selecting a band including all rayparameters around $\tau = 0$. Still, reflections from shallow reflectors contaminated the selected PSF, while sidelobes of autocorrelations of long source-time functions polluted the CF.

The above challenges are to be addressed before MDD may improve lithospheric-scale imaging using (distant) seismicity.

Bibliography

Abe, S., Kurashimo, E., Sato, H., Hirata, N., Iwasaki, T., & Kawanaka, T., 2007. Interferometric seismic imaging of crustal structure using scattered teleseismic waves, *Geophysical Research Letters*, **34**, L19305, doi:10.1029/2007GL030633.

Aki, K., 1965. A note on the use of microseisms in determining the shallow structures of the Earth's crust, *Geophysics*, **30**, 665–666.

Aki, K. & Richards, P. G., 1980. *Quantitative seismology: theory and practice*, Freeman.

Aki, K., Cristoffersson, A., & Husebye, E., 1977. Determination of the three-dimensional seismic structure of the lithosphere, *Journal of Geophysical Research*, **82**, 277–296.

Almagro Vidal, C., van der Neut, J., Draganov, D., Wapenaar, K., & Verdel, A., 2012. Passiver interferometric imaging for limited illumination using slowness diagnosis and directionally constrained Gaussian Beam Migration, SEG, Extended abstracts.

Ammon, C., 1991. The isolation of receiver effects from teleseismic P waveforms, *Bulletin of the Seismological Society of America*, **81**, 2504–2510.

Artman, B., Draganov, D., Wapenaar, K., & Biondi, B., 2004. Direct migration of passive seismic data, EAGE, Extended abstracts, P075.

Asten, M. & Henstridge, J., 1984. Array estimators and the use of microseisms for reconnaissance of sedimentary basins, *Geophysics*, **49**, 1828–1837.

Astiz, L., Earle, P., & Shearer, P., 1996. Global stacking of broadband seismograms, *Seismological Research Letters*, **67**, 8–18.

Awad, G., 1985. A geophysical study on the Abu Gharadig basin, Egypt, *Geophysics*, **50**.

Bachu, S., 2003. Screening and ranking of sedimentary basins for sequestration of CO_2 in geological media in response to climate change, *Enviromental Geology*, **44**, 277–289.

Bakulin, A. & Calvert, R., 2004. Virtual Source: new method for imaging and 4D below complex overburden, SEG, Extended abstracts, 2477–2480.

Bakulin, A. & Calvert, R., 2006. The virtual source method: theory and case study, *Geophysics*, **71**(4), SI139–SI150.

Bakulin, A., Mateeva, A., Calvert, R., Jorgensen, P., & Lopez, J., 2007. Virtual shear source makes shear waves with air guns, *Geophysics*, **72**(2), A7–A11.

Barbosa, V., Silva, J., & Medeiros, W., 1997. Gravity inversion of basement relief using approximate equality constraints on depths, *Geophysics*, **62**, 1745–1757.

Bensen, G., Ritzwoller, M., Barmin, M., Levshin, A., Lin, F., Moschetti, M., Shapiro, N., & Yang, Y., 2007. Processing seismic ambient noise data to obtain reliable broad-band surface wave dispersion measurements, *Geophysical Journal International*, **169**, 1239–1260.

Berkhout, A., 1982. *Seismic migration: imaging of acoustic energy by wave field extrapolation*, Elsevier.

Berkhout, A. & Verschuur, D., 1997. Estimation of multiple scattering by iterative inversion, Part I: Theoretical considerations, *Geophysics*, **62**, 1586–1595.

Bijwaard, H. & Spakman, W., 2000. Non-linear P-wave tomography by iterated linearized inversion, *Geophysical Journal International*, **141**, 71–82.

Bleistein, N., 1999. Hagedoorn told us how to do Kirchhoff migration and inversion, *The Leading Edge*, **18**, 918–927.

Bonnefoy-Claudet, S., Cotton, F., & Bard, P.-Y., 2006. The nature of noise wave field and its application for site effects studies; a literature review, *Earth-Science Reviews*, **79**, 205–227.

Bormann, P., 1998. Conversion and comparability of data presentations on seismic background noise, *Journal of Seismology*, **2**, 37–45.

Bostock, M., 2004. Green's functions, source signatures, and the normalization of teleseismic wave fields, *Journal of Geophysical Research*, **109**, B03303, doi:10.1029/2003JB002783.

Bostock, M. & Rondenay, S., 1999. Migration of scattered teleseismic body waves, *Geophysical Journal International*, **137**, 732–746.

Bosworth, W., El Hawat, A., Helgeson, D., & Burke, K., 2008. Cyrenaican "shock absorber" and associated inversion strain shadow in the collision zone of northeast Africa, *Geology*, **36**, 695–698.

Bromirski, P., 2001. Vibrations from the 'perfect storm', *Geochem. Geophys. Geosyst.*, **2**, 1030, doi:10.1029/2000GC000119.

Burdick, S., van der Hilst, R., Vernon, F., Martynov, V., Cox, T., Eakins, J., Karasu, G., Tylell, J., Astiz, L., & Pavlis, G., 2010. Model update 2010: upper mantle heterogeneity beneath North America from travel time tomography with gobal and USArray Transportable Array data, *Seismological Review Letters*, **81**, 689–693.

Buske, S., Lüth, S., Meyer, H., Patzig, R., Reichert, C., Shapiro, S., Wigger, P., & Yoon, M., 2002. Broad depth range seismic imaging of the subducted Nazca Slab, North Chile, *Tectonophysics*, **350**, 273–282.

Campillo, M. & Paul, A., 2003. Long-range correlations in the diffuse seismic coda, *Science*, **299**, 547–549.

Cessaro, R., 1994. Sources of primary and secondary microseisms, *Bulletin of the Seismological Society of America*, **84**(1), 142–148.

Chaput, J. & Bostock, M., 2007. Seismic interferometry using non-volcanic tremor in Cascadia, *Geophysical Research Letters*, **34**, L07304, doi:10.1029/2007GL028987.

Chen, W.-P., Martin, M., Tseng, T.-L., Nowack, R., Hung, S.-H., & Huang, B.-S., 2010. Shear-wave birefringence and current configuration of converging lithosphere under Tibet, *Earth and Planetary Science Letters*, **295**, 297–304.

Chulick, G. & Mooney, W., 2002. Seismic structure of the crust and uppermost mantle of North America and adjacent oceanic basins: a synthesis, *Bulletin of the Seismological Society of America*, **92**, 2478–2492.

Claerbout, J., 1968. Synthesis of a layered medium from its acoustic transmission response, *Geophysics*, **33**, 264–269.

Cloetingh, S., Thybo, H., & Faccenna, C., 2009. TOPO-EUROPE: Studying continental topography and deep-Earth processes in 4D, *Tectonophysics*, **474**, 4–32.

Curtis, A. & Halliday, D., 2010a. Source-receiver wave field interferometry, *Physical Review E*, **81**, 04660, doi:10.1103/PhysRevE.81.046601.

Curtis, A. & Halliday, D., 2010b. Directional balancing for seismic and general wavefield interferometry, *Geophysics*, **75**(1), SA1–SA14.

Curtis, A., Nicolson, H., Halliday, D., Trampert, J., & Baptie, B., 2009. Virtual seismometers in the subsurface of the earth from seismic interferometry, *Nature Geoscience*, **2**, 700–704.

Curtis, A., Behr, Y., Townend, J., Bannister, S., Entwistle, E., & Galetti, E., 2011. Breaking causality in observational science (including in earthquake observation and analysis), *AGU Fall Meeting Abstracts*, S31F–02.

Dahlen, F. & Tromp, J., 1998. *Theoretical Global Seismology*, Princeton University Press, Princeton, New Jersey.

de Hoop, A., 1988. Time-domain reciprocity theorems for acoustic wave fields in fluids with relaxation, *Journal of the Acoustic Society of America*, **84**, 1877–1882.

Derode, A., Larose, E., Campillo, M., & Fink, M., 2003a. How to estimate the Green's function of a heterogeneous medium between two passive sensors? Application to acoustic waves, *Applied Physics Letters*, **83**, 3054–3056.

Derode, A., Larose, E., Tanter, M., de Rosny, J., Tourin, A., Campillo, M., & Fink, M., 2003b. Recovering the Green's function from field-field correlations in an open scattering medium, *Journal of the Acoustic Society of America*, **113**, 2973–2976.

Deuss, A., Woodhouse, J., Paulssen, H., & Trampert, J., 2000. The observation of inner core shear waves, *Geophysical Journal International*, **142**, 67–73.

Díaz, J., Villaseñor, A., Morales, J., Pazos, A., Córdoba, D., Pulgar, J., García-Lobón, L., Harnafi, M., Carbonell, R., Gallart, J., & Group, T. S. W., 2010. Background noise characteristics at the IberArray broadband seismic network, *Bulletin of the Seismological Society of America*, **100**, 618–628.

Dix, C., 1955. Seismic velocities from surface measurements, *Geophysics*, **20**, 68–86.

Dong, S., Sheng, J., & Schuster, G., 2006. Theory and practice of refraction interferometry, SEG, Extended abstracts, 3021–3025.

Dong, S., Li, T., Gao, R., Hou, H., Li, Q., Li, Y., Zhang, S., Keller, G., & Liu, M., 2011. A multidisciplinary Earth science program in China, *EOS*, **92**, 313–314.

Draganov, D., 2007. *Seismic and electromagnetic interferometry*, Delft University of Technology, PhD thesis.

Draganov, D., Wapenaar, K., Artman, B., & Biondi, B., 2004a. Migration methods for passive seismic data, SEG, Extended abstracts, ST 1.5.

Draganov, D., Wapenaar, K., & Thorbecke, J., 2004b. Passive seismic imaging in the presence of white noise sources, *The Leading Edge*, **23**, 889–892.

Draganov, D., Wapenaar, K., & Thorbecke, J., 2006. Seismic interferometry: Reconstructing the earth's reflection response, *Geophysics*, **71**(4), SI61–SI70.

Draganov, D., Wapenaar, K., Mulder, W., Singer, J., & Verdel, A., 2007. Retrieval of reflections from seismic background-noise measurements, *Geophysical Research Letters*, **34**, L04305, doi:10.1029/2006GL028735.

Draganov, D., Campman, X., Thorbecke, J., Verdel, A., & Wapenaar, K., 2009. Reflection images from ambient seismic noise, *Geophysics*, **74**(5), A63–A67.

Draganov, D., Ghose, R., Ruigrok, E., Thorbecke, J., & Wapenaar, K., 2010. Seismic interferometry, intrinsic losses and Q-estimation, *Geophysical Prospecting*, **58**, 361–373.

Dueker, K. & Zurek, B., 2001. Thick-structured proterozoic lithosphere of the Rocky Mountain region, *GSA Today*, **11**, 4–9.

Dziewonski, A. & Anderson, D., 1983. Travel times and station corrections for P waves at teleseismic distances, *J. Geophys. Res*, **88**(B4), 3295–3314.

Dziewonski, M. & Anderson, D. L., 1981. Preliminary reference earth model, *Physics of The Earth and Planetary Interiors*, **25**, 297–356.

Fan, C., Pavlis, G., Weglein, A., & Nita, B., 2006. Removing free-surface multiples from teleseismic transmission and constructed reflection responses using reciprocity and the inverse scattering series, *Geophysics*, **71**(4), SI71–SI78.

Field, E. & Jacob, K., 1995. A comparison and test of various site-response estimation techniques, including three that are not reference-site dependent, *Bulletin of the Seismological Society of America*, **85**, 1127–1143.

Fokkema, J. & van den Berg, P., 1993. *Seismic Applications of Acoustic Reciprocity*, Elsevier, Amsterdam, the Netherlands.

Franssen, R. & Hoogerduijn Strating, E., 2006. Discovering and developing a deep Jurassic play in the mature Western Desert - Abu Gharadig Basin, Egypt, *SPE Europec/EAGE Annual Conference and Exhibition*, SPE 100125.

Galetti, E. & Curtis, A., 2011. Generalized receiver functions and seismic interferometry, *Tectonophysics*, **in press**, doi: 10.1016/j.tecto.2011.12.004.

Gerstoft, P., Sabra, K., Roux, P., Kuperman, W., & Fehler, M., 2006. Green's functions extraction and surface-wave tomography from microseisms in Southern California, *Geophysics*, **71**(4), SI23–SI31.

Gerstoft, P., Shearer, P. M., Harmon, N., & Zhang, J., 2008. Global P, PP and PKP wave microseisms observed from distant storms, *Geophysical Research Letters*, **35**, L23306, doi:10.1029/2008GL036111.

Graham, N., Clayton, R., Kedar, S., Webb, F., & Jones, C., 2010. Modeling microseism generation off Southern California with a numerical wave model: coastal wave reflection and open ocean interactions, *AGU Fall Meeting Abstracts*, S13B2017G.

Grandi, S. & Oates, S., 2009. Microseismic event location by cross-correlation migration of surface array data for permanent reservoir monitoring, EAGE, Extended abstracts, X012.

Griffin, J., Nowack, R., Chen, W.-P., & Tseng, T.-L., 2011. Velocity structure of the Tibetan lithosphere: constraints from P-wave travel times of regional earhtquakes, *Bulletin of the Seismological Society of America*, **101**, 1938–1947.

Gutenberg, B., 1958. Microseisms, *Advances in Geophysics*, **5**, 53–92.

Halliday, D., Curtis, A., Robertsson, J., & van Manen, D., 2007. Interferometric surface-wave isolation and removal, *Geophysics*, **72**(5), A69–A73.

Hansen, S. & Dueker, K., 2009. P- and S-wave receiver function images of crustal imbrication beneath the Cheyenne Belt in southeast Wyoming, *Bulletin of the Seismological Society of America*, **99**, 1953–1961.

Helffrich, G., 2000. Topography of the transition zone seismic discontinuities, *Reviews of Geophysics*, **38**, 141–158.

Herak, M., 2008. ModelHVSR - A Matlab tool to model horizontal-to-vertical spectral ratio of ambient noise, *Computer Geosciences*, **34**, 1514–1526.

Hillers, G., Graham, N., Landes, M., Hubans, F., Campillo, M., Shapiro, N., Paul, A., Kedar, S., & Clayton, R., 2010. Global oceanic microseism sources as seen by seismic arrays and predicted by wave action models, *AGU Fall Meeting Abstracts*, S31B05H.

Hoogerduijn Strating, E. & Postuma, W., 2008. Reservoir compartimentalisation in the JG field Western Desert Egypt, *SPE Europec/EAGE Annual Conference and Exhibition*, SPE 113865.

Hung, S.-H., Chen, W.-P., & Chiao, L.-Y., 2011. A data-adaptive, multiscale approach of finite-frequency, traveltime tomography with special reference to *P* and *S* wave data from central Tibet, *Journal of Geophysical Research*, **116**, B06307, doi:10.1029/2010JB008190.

Hunziker, J., 2012. *Marine controlled-source electromagnetic interferometry*, Delft University of Technology, PhD thesis.

Isacks, B. & Stephens, C., 1975. Conversion of Sn to Lg at a continental margin, *Bulletin of the Seismological Society of America*, **65**, 235–244.

Karlstrom, K. & Humphreys, E., 1998. Persistent influence of Proterozoic accretionary boundaries in the tectonic evolution of southwestern North America: Interaction of cratonic grain and mantle modification events, *Rocky Mountain Geology*, **33**, 161–179.

Kedar, S., Longuet-Higgins, M., Webb, F., Graham, N., Clayton, R., & Jones, C., 2008. The origin of deep ocean microseisms in the North Atlantic Ocean, *Proc. R. Soc. London*, **464**, 777–793.

Kennett, B., 1991. The removal of free surface interactions from three-component seismograms, *Geophysical Journal International*, **104**, 153–163.

Kennett, B., Engdahl, E., & Buland, R., 1995. Constraints on seismic velocities in the Earth from travel times, *Geophysical Journal International*, **122**, 108–124.

Kibblewhite, A. & Ewans, K., 1985. Wave-wave interactions, microseisms, and infrasonic ambient noise in the ocean, *Journal of the Acoustic Society of America*, **78**, 981–994.

Kind, R. & Li, X., 2007. Deep Earth structure - transition zone and mantle discontinuities, in Earthquake Seismology: Treatise on Geophysics (V. 4), pp. 591–618, ed. Kanamari, H., Elsevier.

Knapmeyer, M., 2004. TTBox: A Matlab toolbox for the computation of 1D teleseismic travel times, *Seismological Research Letters*, **75**, 726–733.

Knopoff, L., 1961. Green's function for eigenvalue problems and the inversion of Love wave dispersion data, *Geophysical Journal International*, **4**, 161–173.

Koper, K., Seats, K., & Benz, H., 2010. On the composition of the Earth's short-period seismic noise field, *Bulletin of the Seismological Society of America*, **100**, 606–617.

Kroonenberg, S., 2011. *Waarom de hel naar zwavel stinkt (Why hell stinks of sulphur)*, Atlas.

Kumar, M. & Bostock, M., 2006. Transmission to reflection transformation of teleseismic wavefields, *Journal of Geophysical Research*, **111**, B08306, doi:10.1029/2005JB004104.

Lacoss, R. T., Kelly, E. J., & Toksöz, M. N., 1969. Estimation of seismic noise structure using arrays, *Geophysics*, **34**, 21–38.

Landes, M., Hubans, F., Shapiro, N., Paul, A., & Campillo, M., 2010. Origin of deep ocean microseisms by using teleseismic body waves, *Journal of Geophysical Research*, **115**, B05302.

Langston, C., 1977. Corvallis, Oregon, crustal and upper mantle receiver structure from teleseismic P and S waves, *Bulletin of the Seismological Society of America*, **67**, 713–724.

Langston, C., 1979. Structure under Mount Rainier, Washington, inferred from teleseismic body waves, *Journal of Geophysical Research*, **84**, 4749–4762.

Larose, E., Margerin, L., Derode, A., van Tiggelen, B., Campillo, M., Shapiro, N., Paul, A., Stehly, L., & Tanter, M., 2006. Correlation of random wavefields: theory and application, *Geophysics*, **71**(4), SI11–SI21.

Laske, G. & Masters, G., 1997. A global digital map of sediment thickness, *EOS Trans. AGU*, **78**, F483.

Lermo, J. & Chavez-Garcia, F., 1994. Are microtremors useful in site response evaluation?, *Bulletin of the Seismological Society of America*, **84**, 1350–1364.

Levander, A., 2003. USArray design implications for wavefield imaging in the lithosphere and upper mantle, *The Leading Edge*, **22**, 250–255.

Levander, A., Humphreys, E., Ekstrom, G., Meltzer, A., & Shearer, P., 1999. Proposed project would give unprecedented look under north america, *EOS*, **80**, 245–251.

Lines, L. R., Slawinski, R., & Bording, R., 1999. A recipe for stability of finite-difference wave-equation computations, *Geophysics*, **64**, 967–969.

Longuet-Higgins, M., 1950. A theory of the origin of microseisms, *Philisophical Transactions of the Royal Society of London*, **Series A 243**.

Martini, F., Hobbs, R., Bean, C., & Single, R., 2005. A complex 3D volume for sub-basalt imaging, *First Break*, **23**, 41–51.

Martini, F., Lokmer, I., Jonsdottir, K., Bean, C., Hauser, F., Mollhoff, M., de Barros, L., Doherty, J., Ryan, C., & Mongan, J., 2011. A passive low frequency seismic experiment in the Albertine Graben, Uganda: Basin structure control?, EAGE, Extended abstracts, PAS19.

Martynov, V., Vernon, F., Kilb, D., & Roecker, S., 2004. Directional variations in traveltime residuals of teleseismic P waves in the crust and mantle beneath Northern Tien Shan, *Bulletin of the Seismological Society of America*, **94**(2), 650–664.

Masters, G., Johnson, S., Laske, G., & Bolton, H., 1996. A shear-velocity model of the mantle, *Phil. Trans.: Math. Phys. Eng. Sci.*, **354**, 1385–1411.

Mehta, K., Bakulin, A., Sheiman, J., Calvert, R., & Snieder, R., 2007. Improving the virtual source method by wavefield seperation, *Geophysics*, **72**(4), V79–V86.

Melo, G., Malcom, A., Mikesell, D., & van Wijk, K., 2010. Using SVD for improved interferometric Greens function recovery, SEG, Extended abstracts, 3986–3990.

Mikesell, D., van Wijk, K., Calvert, A., & Haney, M., 2009. The virtual refraction: usefull spurious energy in seismic interferometry, *Geophysics*, **74**(3), A13–A17.

Minato, S., Matsuoka, T., Tsuiji, T., Draganov, D., Hunziker, J., & Wapenaar, K., 2011. Seismic interferometry using multidimensional deconvolution and crosscorrelation for crosswell seismic reflection data without borehole sources, *Geophysics*, **76**(1), SA19–SA34.

Mykkeltveit, S., Ringdahl, F., Kværna, T., & Alewine, R. W., 1990. Application of regional arrays in seismic verification research, *Bulletin of the Seismological Society of America*, **80**(6), 1777–1800.

Nábělek, J., György, H., Vergne, J., Sapkota, S., Kafle, B., Jiang, M., Su, H., Chen, J., Huang, B.-S., & the Hi-CLIMB Team, 2009. Underplating in the Himalya-Tibet collision zone revealed by the Hi-CLIMB experiment, *Science*, **325**, 1371–1374.

Nakamura, Y., 2000. Clear identification of fundamental idea of Nakamura's technique and its applications, Proceedings of the 12th World Conference on Earthquake Engineering, Aukland, New Zealand, Paper No. 2656.

Neidell, N. & Taner, M., 1971. Semblance and other coherency measures for multichannel data, *Geophysics*, **36**, 482–497.

Nowack, R., Dasgupta, S., Schuster, G., & Sheng, J.-M., 2006. Correlation migration using Gaussian beams of scattered teleseismic body waves, *Bulletin of the Seismological Society of America*, **96**, 1–10.

Nowack, R., Chen, W.-P., & Tseng, T.-L., 2010. Application of Gaussian-beam migration to multiscale imaging of the lithosphere beneath the Hi-CLIMB array in Tibet, *Bulletin of the Seismological Society of America*, **100**, 1743–1754.

Obrebski, M., Allen, R., Pollitz, F., & Hung, S.-H., 2011. Lithosphere-asthenosphere interaction beneath the western United States from the joint inversion of body-wave traveltimes and surface-wave phase velocities, *Geophysical Journal International*, **185**, 1003–1021.

Okada, H., 2003. *The Microtremor Survey Method*, chap. Fundamental properties of microtremors, Soc. of Expl. Geophys.

Okada, Y., Kasahara, K., Hori, S., Obara, K., Sekiguchi, S., Fujiwara, H., & Yamamoto, A., 2004. Recent progress of seismic obseravation networks in Japan —Hi-net, F-net, K-NET and KiK-net—, *Earth Planets Space*, **56**, xv–xxviii.

Pao, Y. H. & Varatharajulu, V., 1976. Huygens' principle, radiation conditions, and integral formulations for the scattering of elastic waves, *Journal of the Acoustic Society of America*, **59**, 1361–1371.

Peterson, J., 1993. *Observations and modeling of seismic background noise*, USGS Open-File Report 93-322.

Poletto, F. & Farina, B., 2010. Synthesis of a seismic virtual reflector, *Geophysical Prospecting*, **58**, 375–387.

Poletto, F. & Wapenaar, K., 2009. Virtual reflector representation theorem (acoustic medium), *JASA Express Letters*, **125**, EL111–EL116.

Randey, M., Tandukar, R., Avouac, J., Vergne, J., & Heritiér, T., 1999. Seismotectonics of the Nepal Himalaya from a local seismic network, *Journal of Asian Earth Sciences*, **17**, 703–712.

Rickett, J. & Claerbout, J., 1999. Acoustic daylight imaging via spectral factorization: Helioseismology and reservoir monitoring, *The Leading Edge*, **18**, 957–960.

Ritzwoller, M., Lin, F.-C., & Shen, W., 2011. Ambient noise tomography with a large seismic array, *Comptes Rendus Geoscience*, **343**, 558–570.

Rost, S. & Thomas, C., 2002. Array seismology: methods and applications, *Reviews of Geophysics*, **40**, 1008, doi:10.1029/2000RG000100.

Roux, P. & Fink, M., 1997. Experimental evidence in acoustics of the violation of time reversal invariance induced by vorticity, *Europhysics Letters*, **32**, 25–29.

Roux, P., Sabra, K., Gerstoft, P., Kuperman, W., & Fehler, M., 2005a. P-waves from cross-correlation of seismic noise, *Geophysical Research Letters*, **32**, L19303–1–L19303–4.

Roux, P., Sabra, K., Kuperman, W., & Roux, A., 2005b. Ambient noise cross correlation in free space: Theoretical approach, *Journal of the Acoustic Society of America*, **117**, 79–84.

Ruigrok, E. & Wapenaar, K., 2012. Global-phase seismic interferometry unveils P-wave reflectivity below the Himalayas and Tibet, *Geophysical Research Letters*, **39**, L11303, doi:10.1029/2012GL051672.

Ruigrok, E., Draganov, D., Thorbecke, J., van der Neut, J., & Wapenaar, K., 2008a. Sampling and illumination aspects of seismic interferometry in horizontally layered media, EAGE, Extended abstracts, P277.

Ruigrok, E., Draganov, D., & Wapenaar, K., 2008b. Global-scale seismic interferometry: theory and numerical examples, *Geophysical Prospecting*, **56**, 395–417.

Ruigrok, E., Campman, X., & Wapenaar, K., 2009a. Lithospheric-scale seismic interferometry: a comparison of approaches to deal with an irregular source distribution and source-side reverberations, DGG, Extended abstracts, 125–129.

Ruigrok, E., Wapenaar, K., van der Neut, J., & Draganov, D., 2009b. A review of cross-correlation and multidimensional deconvolution seismic interferometry for passive data, EAGE, Extended abstracts, A09.

Ruigrok, E., Campman, X., Draganov, D., & Wapenaar, K., 2010a. High-resolution lithospheric imaging with seismic interferometry, *Geophysical Journal International*, **183**, 339–357.

Ruigrok, E., van der Neut, J., Djikpesse, H., Chen, C.-W., & Wapenaar, K., 2010b. A feasibility study for the application of seismic interferometry by multidimensional deconvolultion for lithospheric-scale imaging, in Geophysical Research Abstracts, vol. 12, EGU2010-9370.

Ruigrok, E., Campman, X., & Wapenaar, K., 2011. Extraction of P-wave reflections from microseisms, *Comptes Rendus Geoscience*, **343**, 512–525.

Ruigrok, E., Campman, X., & Wapenaar, K., 2012a. Basin delineation with a 40-hour passive seismic record, *Bulletin of the Seismological Society of America*, **102**(1), doi:10.1785/0120110242.

Ruigrok, E., Mikesell, T., & van Wijk, K., 2012b. Scanning for velocity anomalies in the crust and mantle with diffractions from the core-mantle boundary, *Geophysical Research Letters*, **39**, L11301, doi:10.1029/2012GL051443.

Ryu, J., 1982. Decomposition (decom) approach applied to wave field analysis with seismic reflection records, *Geophysics*, **47**, 869–883.

Salem, A., Williams, S., Fairhead, D., Smith, R., & Ravat, D., 2008. Interpretation of magnetic data using tilt-angle derivatives, *Geophysics*, **73**(1), L1–L10.

Schmandt, B. & Humphreys, E., 2010. Complex subduction and small-scale convection revealed by body-wave tomography of the western United States, *Earth and Planetary Science Letters*, **297**, 435–445.

Schuster, G., 2001. Theory of daylight/interferometric imaging: tutorial, EAGE, Extended abstracts, A-32.

Schuster, G., 2009. *Seismic Interferometry*, Cambridge University Press, Cambridge, UK.

Schuster, G. & Zhou, M., 2006. A theoretical overview of model-based and correlation-based redatuming methods, *Geophysics*, **71**(4), SI103–SI110.

Schuster, G., Yu, J., Sheng, J., & Rickett, J., 2004. Interferometric/daylight seismic imaging, *Geophysical Journal International*, **157**, 838–852.

Seber, D., Vallve, M., Sandvol, E., & Steer, D., 1997. Middle East tectonics: Application of geographic information systems, *GSA Today*, **7**, 1–5.

Shapiro, N. & Campillo, M., 2004. Emergence of broadband Rayleigh waves from correlations of the ambient seismic noise, *Geophysical Research Letters*, **31**, doi:10.1029/2004GL019491.

Shapiro, N., Campillo, M., Stehly, L., & Ritzwoller, M., 2005. High-resolution surface wave tomography from ambient seismic noise, *Science*, **307**, 1615–1618.

Shiraishi, K., Onishi, K., Ito, S., Aizawa, T., & Matsuoka, T., 2006. Seismic interferometry with underground moving source, EAGE, Extended abstracts, A043.

Slob, E., Draganov, D., & Wapenaar, K., 2006. GPR without a source, Proceedings of the eleventh international conference on ground penetrating radar (Ohio State University, Columbus, OH, 2006).

Slob, E., Draganov, D., & Wapenaar, K., 2007. Interferometric electromagnetic Green's functions representations using propagation invariants, *Geophysical Journal International*, **169**, 60–80.

Snieder, R., 2004. Extracting the Green's function from the correlation of coda waves: a derivation based on stationary phase, *Physical Review E*, **69**, 046610–1–046610–8.

Snieder, R., 2007. Extracting the Green's function of attenuating acoustic media from uncorrelated waves, *Journal of the Acoustic Society of America*, **121**(5), 2637–2643.

Snieder, R. & Safak, E., 2006. Extracting the building response using seismic interferometry: Theory and application to the Millikan Library in Pasadena, California, *Bulletin of the Seismological Society of America*, **2006**, 503–523.

Snieder, R., Wapenaar, K., & Larner, K., 2006. Spurious multiples in seismic interferometry of primaries, *Geophysics*, **71**(4), SI111–SI124.

Snieder, R., Wapenaar, K., & Wegler, U., 2007. Unified Green's function retrieval by cross-correlation; connection with energy principles, *Physical Review E*, **75**, 036103–1–036103–14.

Snieder, R., Miyazawa, M., Slob, E., Vasconcelos, I., & Wapenaar, K., 2009. A comparison of strategies for seismic interferometry, *Surveys in Geophysics*, **30**, 503–523.

Snieder, R., Slob, E., & Wapenaar, K., 2010. Lagrangian Green's function extraction, with application to potential fields, diffusion, and acoustic waves, *New Journal of Physics*, **12**, 063013–1–063013–24.

Spetzler, J. & Snieder, R., 2004. Tutorial: The Fresnel volume and transmitted waves, *Geophysics*, **69**, 653–663.

St John, B., Bally, A., & Klemme, H., 1984. *Sedimentary provinces of the world — hydrocarbon productive and non-productive*, AAPG Special Publications.

Stein, S. & Wysession, M., 2003. *An Introduction to Seismology, Earthquakes, and Earth Structure*, Blackwell.

Storchak, D. A., Schweitzer, J., & Bormann, P., 2003. The IASPEI standard seismic phase list, *Seismological Research Letters*, **74**, 761–772.

Stutzmann, E., Schimmel, M., Ardhuin, F., & Mangeney, A., 2010. Observing and modeling seismic noise variations, *AGU Fall Meeting Abstracts*, S13B2016S.

Tanimoto, T. & Atru-Lambin, J., 2007. Interaction of solid-Earth, Atmosphere, and Ionosphere, in Earthquake Seismology: Treatise on Geophysics (V. 4), pp. 421–444, ed. Kanamari, H., Elsevier.

Tatanova, M., Bakulin, A., Mehta, K., Korneev, V., & Kashtan, B., 2008. Reconstructing head waves with virtual source method, SEG, Extended abstracts 27, 183–187.

Toksöz, M. N., 1964. Microseisms and an attempted application to exploration, *Geophysics*, **29**, 154–177.

Toksöz, M. N. & Lacoss, R. T., 1968. Microseism: Mode structure and sources, *Science*, **159**, 872–873.

Tonegawa, T., Nishida, K., Watanabe, T., & Shiomi, K., 2009. Seismic interferometry of teleseismic S-wave coda for retrieval of body waves: an application to the Philippine Sea slab underneath the Japanese Islands, *Geophysical Journal International*, **178**, 1574–1586.

Tonn, R., 1991. The determination of the seismic quality factor Q from VSP data: a comparison of different computational methods, *Geophysical Prospecting*, **39**, 1–27.

Trampert, J., Cara, M., & Frogneux, M., 1993. SH propagator matrix and Qs estimates from borehole- and surface-recorded earthquake data, *Geophysical Journal International*, **112**, 290–299.

Tsai, N., 1970. A note on the steady-state response of an elastic half-space, *Bulletin of the Seismological Society of America*, **60**, 795–808.

Tseng, T.-L., Chen, W.-P., & Nowack, R., 2009. Northward thining of Tibetan crust revealed by virtual seismic profiles, *Geophysical Research Letters*, **36**, L24304, doi:10.1029/2009GL040457.

van der Hilst, R., Widiyantoro, S., & Engdahl, E., 1997. Evidence for deep mantle circulation from global tomography, *Nature*, **386**, 578–584.

van der Neut, J., 2012. Downhole interferometric illumination diagnosis and balancing, *Geophysical Prospecting*, **submitted**.

van der Neut, J. & Bakulin, A., 2009. Estimating and correcting the amplitude radiation pattern of a virtual source, *Geophysics*, **74**(2), SI27–SI36.

van der Neut, J., Ruigrok, E., Draganov, D., & Wapenaar, K., 2010. Retrieving the earth's reflection response by multi-dimensional deconvolution of ambient seismic noise, EAGE, Extended abstracts, P406.

van Eck, T., Giardini, D., Sleeman, R., & Dost, B., 2011. Integrating the European Observational Seismology Infrastructure: NERIES developments, in Earthquake Data in Engineering Seismology, eds Akkar, S. & G P.

van Groenestijn, G. & Verschuur, D., 2010. Estimation of primaries by sparse inversion from passive seismic data, *Geophysics*, **75**(4), SA61–SA69.

van Manen, D., Robertsson, J., Curtis, A., Ferber, R., & Paulssen, H., 2003. Shear wave statics using receiver functions, *Geophysical Journal International*, **153**, F1–F5.

van Wijk, K., Mikesell, D., Schulte-Pelkum, V., & Stachnik, J., 2011. Estimating the Rayleigh-wave impulse response between seismic stations with the cross terms of the Green tensor, *Geophysical Research Letters*, **38**, doi:10.1029/2011GL047442.

Vasconcelos, I. & Snieder, R., 2008. Interferometry by deconvolution, Part I: Theory for acoustic waves and numerical examples, *Geophysics*, **73**(3), SI15–SI28.

Verschuur, D., 2006. *Seismic multiple removal techniques: past, present and future*, EAGE, Houten, the Netherlands.

Verschuur, D. & Berkhout, A., 1997. Estimation of multiple scattering by iterative inversion, Part II: Practical aspects and examples, *Geophysics*, **62**, 1596–1611.

Vinnik, L., 1973. Sources of microseismic P-waves, *Pure and Applied Geophysics*, **103**(1), 282–289.

Virieux, J., 1986. P-SV wave propagation in heterogeneous media: Velocity-stress finite-difference method, *Geophysics*, **51**, 889–901.

Wang, P., de Hoop, M., van der Hilst, R., Ma, P., & Tenorio, L., 2006. Imaging of structure at and near the core mantle boundary using a generalized radon transform: 1. Construction of image gathers, *Journal of Geophysical Research*, **111**, B12304, doi:10.1029/2005JB004241.

Wapenaar, K., 2003. Synthesis of an inhomogeneous medium from its acoustic transmission response, *Geophysics*, **68**, 1756–1759.

Wapenaar, K., 2004. Retrieving the elastodynamic Green's function of an arbitrary inhomogeneous medium by cross-correlation, *Physical Review Letters*, **93**, 254301–1–254301–4.

Wapenaar, K., 2006. Nonreciprocal Green's function retrieval by cross correlation, *Journal of the Acoustic Society of America*, **120**, EL7–EL13.

Wapenaar, K. & Fokkema, J., 2006. Green's functions representations for seismic interferometry, *Geophysics*, **71**(4), SI33–SI46.

Wapenaar, K. & Snieder, R., 2007. Chaos tamed, *Nature*, **447**, 643.

Wapenaar, K., Verschuur, D., & Hermann, P., 1992. Amplitude preprocessing of single and multicomponent seismic data, *Geophysics*, **57**, 1178–1188.

Wapenaar, K., Thorbecke, J., Draganov, D., & Fokkema, J., 2002. Theory of acoustic daylight imaging revisited, SEG, Extended abstracts, ST 1.5.

Wapenaar, K., Draganov, D., van der Neut, J., & Thorbecke, J., 2004. Seismic interferometry: a comparison of approaches, SEG, Extended abstracts, ST 1.5.

Wapenaar, K., Slob, E., & Snieder, R., 2006. Unified Green's function retrieval by cross correlation, *Physical Review Letters*, **97**, 234301, 10.1103/PhysRevLett.97.234301.

Wapenaar, K., Draganov, D., & Robertsson, J., 2008a. *Seismic Interferometry: history and present status*, SEG.

Wapenaar, K., Slob, E., & Snieder, R., 2008b. Seismic and electromagnetic controlled-source interferometry in dissipative media, *Geophysical Prospecting*, **56**, 419–434.

Wapenaar, K., van der Neut, J., & Ruigrok, E., 2008c. Passive seismic interferometry by multidimensional deconvolution, *Geophysics*, **75**(6), A51–A56.

Wapenaar, K., Draganov, D., Snieder, R., Campman, X., & Verdel, A., 2010a. Tutorial on seismic interferometry: Part 1-Basic principles and applications, *Geophysics*, **75**(5), 75A195–75A209.

Wapenaar, K., Slob, E., Snieder, R., & Curtis, A., 2010b. Tutorial on seismic interferometry: Part 2-Underlying theory and new advances, *Geophysics*, **75**(5), 75A211–75A227.

Wapenaar, K., Ruigrok, E., van der Neut, J., & Draganov, D., 2011a. Improved surface-wave retrieval from ambient seismic noise by multi-dimensional deconvolution, *Geophysical Research Letters*, **38**, L01313, doi:10.1029/2010GL045523.

Wapenaar, K., van der Neut, J., Ruigrok, E., Draganov, D., Hunziker, J., Slob, E., Thorbecke, J., & Snieder, R., 2011b. Seismic interferometry by crosscorrelation and by multi-dimensional deconvolution: a systematic comparison, *Geophysical Journal International*, **185**, 1335–1364.

Wathelet, M., Jongmans, D., & Ohrnberger, M., 2004. Surface-wave inversion using a direct search algorithm and its application to ambient vibration measurements, *Near Surface Geophysics*, **2**, 211–221.

Weaver, R., 2008. Ward identities and the retrieval of Green's functions in the correlations of a diffuse wave field, *Wave Motion*, **45**, 596–604.

Weaver, R. & Lobkis, O., 2001. Ultrasonics without a source: thermal fluctuation correlations at MHz frequencies, *Physical Review Letters*, **87**, 134301–1–134301–4.

Webb, S., 2002. Seismic noise on land and on the sea floor, *International Geophysics*, **81**, 305–318.

Wilson, D. & Aster, R., 2005. Seismic imaging of the crust and upper mantle using regularized joint receiver functions, frequency-wave number filtering, and multimode Kirchhoff migration, *Journal of Geophysical Research*, **110**, B05305, doi:10.1029/2004JB003430.

Wilson, D., Leon, J., Aster, R., Ni, J., Schlue, J., Grand, S., Semken, S., Baldridge, S., & Gao, W., 2002. Broadband seismic background noise at temporary seismic stations observed on a regional scale in the southwestern united states, *Bulletin of the Seismological Society of America*, **92**(8), 3335–3341.

Wysession, M., Langenhorst, A., Fouch, M., Al-Eqabi, K. F. G., Shore, P., & Clarke, T., 1999. Lateral variations in compressional/shear velocities at the base of the mantle, *Science*, **284**, 120–125.

Xia, J., Miller, R., & Park, C., 1999. Estimation of near-surface shear-wave velocity by inversion of Rayleigh waves, *Geophysics*, **64**, 691–700.

Xiao, X., Luo, Y., Fu, Q., Jervis, M., Dasgupta, S., & Kelamis, P., 2009. Locate microseismicity by seismic interferometry, EAGE, Extended abstracts, A22.

Xu, Q., Zhao, J., Pei, S., & Liu, H., 2011. The lithosphere-astenosphere boundary revealed by S-receiver functions from the Hi-CLIMB experiment, *Geophysical Journal International*, **187**, 414–420.

Yao, H., van der Hilst, R., & de Hoop, M., 2006. Surface-wave array tomography in SE Tibet from ambient seismic noise and two-station analysis: I - phase velocity maps, *Geophysical Journal International*, **166**, 732–744.

Yilmaz, O. & Doherty, S., 2000. *Seismic data analysis: processing, inversion and interpretation of seismic data*, SEG.

Yin, A. & Harrison, T., 2000. Geologic evolution of the Himalayan-Tibetan orogen, *Ann. Rev. Earth Planet. Sci.*, **28**, 211–280.

Zhan, Z., Ni, S., Helmberger, D., & Clayton, R., 2010. Retrieval of moho-reflected shear wave arrivals from ambient seismic noise, *Geophysical Journal International*, **182**, 408–420.

Zhang, J., Gerstoft, P., & Shearer, P., 2009. High-frequency P-wave seismic noise driven by ocean winds, *Geophysical Research Letters*, **36**, L09302.

Zhang, J., Gerstoft, P., & Shearer, P., 2010. Resolving P-wave travel-time anomalies using seismic array observations of oceanic storms, *Earth and Planetary Science Letters*, **292**, 419–427.

Summary

Body-wave seismic interferometry applied to earthquake- and storm-induced wavefields

Seismology is the study of the vibration of the Earth. Seismologists pay much attention to the main source of Earth vibration: earthquakes. But also other seismic sources, like mining blasts, ocean storms and windmills, are studied. All these sources induce seismic waves, which can eventually be recorded as ground vibrations. These seismic records contain not only information about the sources, but also about the part of the Earth through which the waves have propagated. This thesis focuses on a main subclass of seismology: seismic imaging. With seismic imaging, seismic records are studied with the aim to unravel the structure and composition of the Earth.

Seismic imaging finds its main use in extracting information about the solid Earth that is within our reach. With the current state of the art, we can only mine minerals from the upper 0.2 percent. Imaging the deep (*i.e.*, unreachable) Earth finds its main use in hazard assessment. Through imaging the deep Earth, we can better understand the dynamics of our planet, manifested in, amongst others, earthquakes and volcanism. By forecasting how the Earth will reshape, we can sensibly adapt. Seismic characterization of the subsurface also improves our ability to assess the direct impact of earthquakes.

A large part of the current deep-Earth images are obtained through tomographic inversion. These images are successful for identifying large-scale structural anomalies, like (remnants of) subducting slabs. However, they lack the resolution to accurately image discontinuities in space. Sharp discontinuities, like the interface between sedimentary and crystalline rock, lead to conversions and reflections of seismic waves. It is those reflections that are most suitable for imaging the discontinuities. The technique developed to do this is called seismic reflection imaging (SRI). Though SRI is considered to be an advanced technique for imaging the subsurface, the dense and wide source (and receiver) distribution requirement thus far limited the use for deep-Earth imaging.

Deep-Earth imaging is done primarily with natural sources. Their limited and irregular distribution and their unpredictable occurrence time is inconvenient for SRI. In this thesis we work on a methodology to alleviate the stringent requirement on the source distribution. This methodology is called seismic interferometry (SI). SI is a remapping operation. With SI, the responses from many sources are combined to create the response as if there were

a source at a receiver position. The response from this "virtual" source could contain both surface waves and body waves. We apply SI such that especially (reflected) body waves are retrieved, because it are these waves that are used for SRI. When we apply SI to a regularly-spaced array of receivers, we could turn uncontrolled natural sources into a well-organized succession of virtual sources, which is amenable for SRI.

The aim of this work is to improve the imaging of the interior of the Earth by the application of body-wave SI to naturally induced seismic data. A prior study focussed on the exploration-scale (*i.e.*, the part of the Earth that is being mined). In this thesis, we focus on low-frequency waves (< 2 Hz), which contain especially information about the deep Earth. In Part I we consider applications to earthquake recordings. In Part II we evaluate the retrieval of reflections using microseisms.

Part I starts by looking into the global-scale configuration. For this configuration, two seismic stations (or two arrays of stations) may be located anywhere on the globe and reflectors may be located anywhere in depth. We derive and numerically test relations to retrieve the complete response between two stations, using worldwide seismicity. The SI relations are valid for a closed entity for seismic waves, like the Earth is by approximation. The relations do not account for inelastic losses, by which eventually all seismic energy is transformed to heat. Though normally of negligible influence, the SI relations do account for the rotation of the Earth. In practice, the distribution of the larger earthquakes is not wide enough to retrieve complete responses between any two points on the Earth. However, still relevant primary reflections can be retrieved with a limited dense distribution of seismicity, like from the Tohoku (2011) aftershock sequence.

Part I proceeds by zooming in to the lithospheric-scale configuration. The lithosphere is the part of the solid Earth where most (seismic) activity takes place. It makes up the crust and the upper part of the mantle. It is this part of the Earth that, broken into plates and fueled by convection in the mantle, undergoes birth (at midoceanic ridges), collisions (resulting in stunning topography) and death (subduction back into the mantle). Inspecting the Earth in depth unveils a part of the history of the lithosphere and gives an indication of the processes still ongoing. Information about the structure of the lithosphere is hidden in the coda of wavefields that arrive due to distant seismicity. We test a few different SI approaches to extract this information. We use synthetic data with similar characteristics as field data recorded during the Laramie broad-band experiment (2000-2001). This was an array of seismic stations in Wyoming, USA, to study an suture zone. We evaluate the requirements for obtaining multi-offset reflection responses. These multi-offset reflections are important for obtaining a velocity model. We estimate this model for the subsurface below the Laramie array and we use it to map the extracted reflections to a reflectivity image of the lithosphere.

In the remainder of part I, we focus again on the lithospheric scale. This time, we assume that a velocity model is already available through other means. Consequently, only single-offset reflection responses are required to make an image. We use global phases to obtain zero-offset reflection responses. We show the robustness of the method with data from the

Hi-CLIMB experiment (2002-2005). This was a large and well-sampled seismic array, passing the Himalayas and a significant part of the Tibetan Plateau. The successive application of SRI leads to an image of the Indian-Eurasian Plate collision.

The rediscovery of body waves in low-frequency noise ($<$1 Hz) opened up the research for Part II of this thesis. The noise are in fact microseisms: Earth vibrations that are indirectly caused by ocean gravity waves. High amplitude ocean waves are caused when storms, leading to persistent wind fields, cross an ocean. We retrieve reflection responses from body-wave noise using SI approaches similar to the ones used for earthquake recordings. The main difference between applications to noise and (large) earthquake responses is that the origin of large earthquakes is known, whereas the origin of noise is generally not known. Therefore, the main challenge for noise applications is to unravel the noise illumination. For this purpose, we use a well-sampled areal array in Egypt to study the noise illumination in different frequency bands. We only select the noise records with a favorable body-wave content and process them into separate reflection responses, of both the lithosphere and the upper crust. We further evaluate what basin-scale information can be extracted from the retrieved reflections. The wavelengths of the reflections extracted from low-frequency noise are too long to image a sedimentary basin in detail. However, the sharp boundary between the sediments and the underlying crystalline rocks can be delineated. For the same dataset from Egypt, we compare the information that is extracted with SI with the information that is obtained when using two other passive seismic techniques, namely horizontal-to-vertical spectral ratio and receiver function.

In the appendices we discuss a few spin-off developments from the main research. In Appendix A we work out an alternative SI relation that integrates over midpoints between receiver positions, instead of over sources. Using this relation, reflections can already be retrieved using only a single source. However, a well-sampled array of receivers needs to be available and an additional evaluation needs to be performed. In Appendix B we develop a technique to estimate loss factors from plane-wave transmission responses. The losses are estimated from amplitude ratios, obtained before and after applying autocorrelation. In Appendix C we present a method that was inspired by SI. Crosscorrelations of diffractions from the core-mantle boundary are used to swiftly scan anomalies in the crust and mantle. Finally, in Appendix D we discuss an alternative implementation of SI: SI by multidimensional deconvolution. With this technique the outcome of SI may be improved. However, well-sampled arrays of receivers are required and additional processing needs to be implemented.

In this thesis, we show that the application of SI to earthquake recordings is sufficiently mature to yield high-resolution images of the lithosphere. Relations for imaging deeper structures are worked out and modus operandi are thought through. However, the reality check is still to be encountered with field-data applications. Furthermore, we show that the applications of SI to microseisms can be used to yield information about a basin depth. Moreover, we show the great promise of microseism applications for unveiling a lithosphere in depth, using only a few days of noise recordings. The more repetitive charac-

ter of microseism sources with respect to earthquakes, in fact makes them more amenable for monitoring applications, if their yearly variations and radiation characteristics are well understood.

Samenvatting

Bulkgolf seismische interferometrie toegepast op door aardbevingen en stormen opgewekte golfvelden

Seismologie is de studie van de trillingen van de aarde. Seismologen besteden veel aandacht aan de belangrijkste bron van het heftig heen en weer schudden van het aardoppervlak: aardbevingen. Maar ook andere seismische bronnen, zoals mijnbouwgerelateerde explosies, stormen over de oceaan en windmolens, worden bestudeerd. Al deze bronnen wekken seismische golven op, welke uiteindelijk geregistreerd kunnen worden als trillingen van het aardoppervlak. Deze seismische metingen bevatten niet alleen informatie over de bronnen, maar ook over het stuk aarde waardoor de golven zijn gereisd. Deze thesis focust zich op een belangrijk onderdeel van de seismologie: seismische beeldvorming. Hierbij worden seismische metingen bestudeerd met als doel om de structuur en de compositie van de Aarde in beeld te brengen.

Seismische beeldvorming wordt het meest toegepast om dat deel van de vaste Aarde in beeld te brengen waar we bij kunnen. Met de huidige stand van de techniek kunnen we alleen mineralen ontginnen van de bovenste 0.2 procent. Het in kaart brengen van de diepe (ofwel de voor ons onbereikbare) aarde heeft vooral tot nut om te beoordelen welke gevaren het leven op Aarde met zich meebrengt. Door de diepe Aarde in beeld te brengen kunnen we beter de veranderlijke aard van onze planeet begrijpen, wat zich o.a. manifesteert in aardbevingen en vulkanisme. Door een goede schatting te maken van hoe de Aarde zal transformeren, kunnen we onze eigen stappen daarop afstemmen. Door seismische karakterisatie van de ondergrond kunnen we ook beter voorspellen wat de directe impact van aardbevingen zal zijn.

Een groot deel van ons huidige inzicht in de diepe Aarde is verkregen met tomografie. Op de verkregen beelden kunnen grote anomalieën, zoals een oceanische plaat dat subduceert onder een continentale plaat, goed geïdentificeerd worden. De tomografische afbeeldingen hebben echter niet de resolutie om discontinuïteiten scherp in beeld te brengen. Plotselinge overgangen, zoals die van sedimentair naar kristallijn gesteente, leiden tot conversies en reflecties van seismische golven. Het zijn de reflecties die het best gebruikt kunnen worden om deze contrasten in beeld te brengen. De techniek ontwikkeld om juist dit te doen, is genaamd seismische reflectie imaging (SRI). Hoewel SRI gezien wordt als een geavanceerde methode om de ondergrond in beeld te brengen, wordt het tot dusverre weinig gebruikt voor

karteringen van de diepe Aarde, vanwege de noodzaak van een goed gesamplede en weidse opstelling van bronnen en ontvangers.

De diepe ondergrond wordt vooral met behulp van natuurlijke seismische bronnen in beeld gebracht. Deze bronnen zijn lastig te gebruiken voor SRI, vanwege hun gelimiteerde en irreguliere distributie, evenals de onvoorspelbaarheid van de tijden waarop de verschuivingen plaats vinden. In deze thesis werken we aan een methodologie, waarmee het ongecontroleerde karakter van natuurlijke bronnen een minder groot probleem wordt. Deze methodologie heet seismische interferometrie (SI). SI is een herkarteringsoperatie. Met SI worden de responsies van vele bronnen gecombineerd tot een nieuwe responsie, waarbij er een zogenaamde virtuele bron wordt gecreëerd op een van de ontvangerposities. De responsie op deze virtuele bron kan zowel oppervlaktegolven als bulkgolven bevatten. Wij passen SI dusdanig toe, zodat voornamelijk (gereflecteerde) bulkgolven worden verkregen, want het zijn deze golven die gebruikt worden voor SRI. Als we SI toepassen op metingen van een regulier gesamplede opstelling van ontvangers, kunnen we ongecontroleerde natuurlijke bronnen omvormen tot een netjes georganiseerde rij van virtuele bronnen, welke responsies gebruikt kunnen worden voor SRI.

Het doel van deze thesis is het verbeteren van de beeldvorming van het inwendige van de Aarde door toepassing van SI op seismische metingen verkregen m.b.v. natuurlijke bronnen. Een eerdere studie richtte zich op de exploratieschaal (dat is dat deel van de ondergrond waaruit mineralen ontgonnen worden). In deze thesis focussen we ons op laagfrequente golven (< 2 Hz), welke voornamelijk informatie bevatten over de diepe aarde. In Deel I beschouwen we toepassingen op aardbevingenresponsies. In Deel II beschouwen we het extraheren van reflecties uit microseisms.

Deel I gaat van start met een beschouwing van de mondiale schaal. Op deze schaal kunnen twee seismische sensoren, of hele opstellingen van sensoren, overal ter wereld staan en worden contrasten op elke mogelijke diepte in rekening gebracht. We leiden relaties af om de complete responsie te extraheren tussen twee ontvangers, gebruikmakende van wereldwijde seismiciteit. Ook testen we deze relaties m.b.v. synthetische data. Bij de afleiding is ervanuit gegaan dat de aarde een gesloten bol is voor seismische energie. Er is geen rekening gehouden met de verliezen die optreden waardoor de seismische energie naar verloop van tijd omgezet wordt in warmte. De afgeleide relaties houden rekening met het feit dat de aarde draait, hoewel dit slechts een beperkt effect heeft op golfvoortplanting. In de praktijk is de verdeling van de grote aardbevingen niet wijds genoeg om de complete responsie te extraheren met SI. Wel kan een dichte distributie van aardbevingen, zoals de naschoksequentie van de Tohoku beving (2011), voldoen om relevante primaire reflecties te extraheren.

Deel I gaat verder door in te zoomen op de lithosfeer. De lithosfeer is het deel van de aarde waar de meeste (seismische) actie is. Het bestaat uit de korst en de bovenste mantel. Het is dit deel van de Aarde dat, gebroken in verschillende platen en gedreven door convectie in de mantel, geboorte ondergaat (bij midoceanische ruggen), botsing (resulterend in verbazingwekkende topografie) en afsterving (subductie terug de mantel in). Met seis-

mische beeldvorming kunnen we de geschiedenis van de lithosfeer ontrafelen en achterhalen welke processen nog steeds aan de gang zijn. Informatie over de structuur van de lithosfeer ligt verborgen in de complexe reverberaties van golven die teweeggebracht zijn door verre bevingen. We testen een paar verschillende implementaties van SI om deze reflectie-informatie te extraheren. We gebruiken synthetische data met overeenkomstige karakteristieken als data opgenomen tijdens het Laramie experiment (2000-2001). Dit was een opstelling van seismische ontvangers in Wyoming, VS, om de restanten van een oude orogenese te bestuderen. We evalueren de vereisten om multi-offset reflecties te kunnen extraheren. Deze multi-offset reflecties zijn van belang om een snelheidsmodel te schatten. We schatten dit snelheidsmodel voor de ondergrond onder Laramie en we gebruiken dit snelheidsmodel om de geëxtraheerde reflecties te vertalen naar locaties van contrasten in de ondergrond. Zodoende verkrijgen we een zogenaamd reflectiviteitsbeeld.

Het laatste stuk van deel 1 gaat wederom over de lithosfeer. Deze keer nemen we aan dat er al een snelheidsmodel van de ondergrond beschikbaar is. In dit geval voldoen singleoffset reflecties om de structuur van de ondergrond in beeld te brengen. We gebruiken transmissieresponsies ten gevolge van aardbevingen aan de ander kant van de aarde om zero-offset reflecties van de lithosfeer te verkrijgen. We laten zien dat de methode goed werkt op echte data, door toepassing op de dataset van het Hi-CLIMB experiment (2002-2005). Dit was een lange en goed gesamplede lijn van seismische sensoren dwars door de Himalaya en een groot deel van het Tibetaanse Plateau. Het vervolgens toepassen van SRI leidt tot een afbeelding van de botsing tussen de Indiase en Euraziatische plaat.

De herontdekking van bulkgolven in laagfrequente ruis ($<$1 Hz) initieerde het onderzoek in Deel II van de thesis. Deze ruis zijn in feite microseisms: aardtrillingen die indirect veroorzaakt worden door oceanische gravitatiegolven. Hoge amplitude oceaangolven worden weer veroorzaakt wanneer stormen, die leiden tot standvastige windvelden, over een oceaan trekken. We extraheren reflecties uit de bulkgolfruis, gebruikmakende van soortgelijke SI implementaties als gebruikt voor aardbevingen. Het belangrijkste onderscheid tussen toepassingen op ruis en de metingen van (grote) aardbevingen is dat de locatie van aardbevingen vaak al bekend is, terwijl dit voor ruisbronnen niet het geval is. De belangrijkste uitdaging voor ruistoepassingen is daarom het achterhalen van de belichtingsrichtingen. Om deze belichting te achterhalen, voor verschillende frequentiebanden, gebruiken we een 2D netwerk van ontvangers in Egypte. We gebruiken alleen de ruismetingen met veel bulkgolven uit de gewenste richtingen en verwerken ze tot reflectieresponsies, zowel voor de hele lithosfeer als voor het bovenste stukje van de aardkorst. We evalueren verder welke informatie van een sedimentair bekken verkregen kan worden uit de geëxtraheerde reflecties. De golflengtes van de geëxtraheerde reflecties zijn te lang om een sedimentair bekken in detail in beeld te brengen. Maar het scherpe contrast tussen het bekken en het onderliggende kristallijn gesteente kan gevonden worden. Voor dezelfde dataset uit Egypte vergelijken we de informatie die verkregen wordt met bulkgolf SI met twee andere seismische technieken, te weten de horizontale-tot-verticale spectrale ratio en de ontvangerfunctie.

In de appendices tonen we een paar ontwikkelingen die nauw gerelateerd aan het

hoofdthema. In Appendix A werken we een alternatieve SI relatie uit waarbij geïntegreerd wordt over midpoint in plaats van over bronpositie. Met deze alternatieve relatie kunnen al reflecties geëxtraheerd worden met slechts een enkele bron. Wel moet er een goed gesamplede opstelling van ontvangers voorhanden zijn en moet er een extra evaluatiestap worden uitgevoerd. In Appendix B werken we een methode uit om anelastische verliezen te schatten in aardlagen, gebruikmakende van vlakke golf transmissieresponsies. De verliezen worden geschat op basis van amplitudeverhoudingen, welke verkregen worden voor en na autocorrelatie. In Appendix C tonen we een methode die geïnspireerd werd door SI. Crosscorrelaties van diffracties van de kernmantelgrens worden gebruikt om anomalieën in de korst en mantel op te sporen. Tot slot bespreken we in appenix D een alternatieve implementatie van SI: SI door middel van multidimensionale deconvolutie. Met deze techniek kan het resultaat van SI verbeterd worden. Dit kan alleen wanneer een goed gesampled netwerk van ontvangers beschikbaar is. Bovendien moeten er extra verwerkingsstappen worden uitgevoerd.

In deze thesis tonen we dat de ontwikkeling van SI voor aardbevingsresponsies rijp genoeg is om hoge resolutie afbeeldingen te verkrijgen van de lithosfeer. Relaties voor het uiteindelijk in beeld brengen van diepere structuren worden uitgewerkt en manieren van aanpak worden uitgedacht. Of de uitgedachte methode realistisch genoeg is, moet nog ondervonden worden met echte data. We tonen dat de toepassing van SI op microseisms gebruikt kan worden om de diepte van een sedimentair bekken te bepalen. Ook tonen we de mogelijkheden om met microseisms een lithosfeer plaatselijk in beeld te brengen, gebruikmakende van slechts een paar dagen data. Het meer herhalende karakter van microseismische bronnen t.o.v. aardbevingen maakt ze in feite meer geschikt voor monitoringstoepassingen, indien de jaarlijkse variaties van deze microseismische bronnen evenals de stralingskarakteristieken goed begrepen worden.

The making of

My PhD has been an exciting journey to which many people contributed. Below I will describe some excerpts of this journey and the people involved.

I started as a researcher at the Delft University of Technology, right after finishing my MSc. This was halfway November 2006. I was on an interesting ISES (the Netherlands Research Centre for Intergrated Solid Earth Science) project, which was also on seismic interferometry (SI). However, NWO (the Netherlands Organisation for Scientific Research) had just started a new PhD program, the so-called Toptalent grant. As a fresh graduate you could write your own proposal and compete with peers to get it funded. Kees Wapenaar, Evert Slob and Deyan Draganov motivated me to do so and supported me through the process. A few months later I had my own project which led to this thesis. I am much indebted to the Dutch tax payer for funding this project.

Before my new PhD project started (autumn 2007) I grabbed the opportunity to do an internship with Schlumberger Doll Research in Cambridge, Massachusetts, USA. Under supervision of Hugues Djikpesse, I worked on improving the location of small-magnitude seismicity near reservoirs. Using probability density functions, we worked out advantageous combinations of data attributes. Also, we developed approaches that take advantage of 3D sensor configurations, as were becoming possible with multilateral wells being instrumented. I learned much about inverse theory from Hugues and also from Michael Prange. Benoit Couet created a welcoming group to work in.

Back in Delft, my PhD started with an analysis of different codes for testing ideas to synthetic data and field data. I liked working with Matlab, but by the time there were not yet many seismic codes available in Matlab. This gave me an interesting time devoted to coding. Over the years, I could also take advantage of many splendid codes freely available. For this, I'd like to thank the Delphi, CREWES and CWP consortium and the developers of JWEED, mmap and ttbox.

At the same time, I condensed my MSc thesis and extended the theory to elastodynamic and rotating media. The result got published and made it to Chapter 2 of this thesis. Besides the coauthors, Kees and Deyan, I'd like to thank Xander Campman, Evert Slob, Jeannot Trampert and Arie Verdel for insightful comments, Jan Thorbecke for support in implementing the finite difference modeling, Andrey Bakulin and Roel Snieder for a careful review and Roel also for inspiration to extend the theory for rotating media.

Before embarking on the further details of global-scale SI (Chapter 2) I decided to pick up

an idea which I thought out together with Xander while visiting the group of Rob van der Hilst at MIT (Massachusetts Institute of Technology, May 2006). The idea itself was easy, to use SI to pick out lithospheric-scale reflections from teleseismic transmission responses. Yet, it took quite some time to work out all the details and to apply it to field data. In the end it did work and the results were published and made it to Chapter 3. This work had never been possible without the people involved with the Laramie experiment and IRIS (Incorporated Research Institutions for Seismology).

Meanwhile Kees had come up with an alternative implementation of SI: SI by multidimensional deconvolution. Joost and I had the honor to test his new algorithms for subsurface distributions of natural sources. A tiny part of this work has been used in Appendix B. I tested whether the same methodology could be used for lithospheric-scale imaging. The outcomes of this are shortly wrapped up at the end of Appendix D. Later, Kees initiated the application of the same methodology to surface waves. I took on the task to design realistic surface-wave settings. In a collaborative effort of Delft interferometry, we tested different configurations and interferometric approaches. A part of the results has been wrapped up in Appendix D.

In the spring of 2008 we organized a DOGS (Delft Organization of Geophysics Students) trip to the Middle East. We got well introduced into the real world of oil production, while seeing beautiful sites of the Arabian peninsula. This legendary trip was supported by Saudi Aramco, Fugron Jason, the Petroleum Institute, BP, ADCO, ADMA and Schlumberger.

In the autumn of 2008 I flew back to Saudi Aramco to test SI relations on their immense passive seismic dataset. The seismic group at EXPEC ARC turned out to be a great place to interact with experts from around the world. We gained a number of insights with the data tests, but the stay turned out to be too short to draw definite conclusions. This is still to be continued. I'd like to thank Panos Kelamis, Yi Luo, Michael Jervis, Kent Broadhead, Cvetan Sinadinovski, Ferhan Ahmed, Xiang Xiao and Shoudong Huo for great discussions, fieldtrips and support.

After the success in 2008 DOGS could not stay home in 2009. This time we toured through Norway. We got a very surreal picture with experiencing nothing but sunshine. Thanks goes to Statoil-Hydro (as it was called still by the time), PGS, CGG Veritas, Schlumberger, BP and Shell for their hospitality and memorable presentations.

Deyan came up with a method to estimate loss factors with SI. His method was inspired by the analysis of internal events, which can be found in the appendix of chapter 2. Deyan, Karel Heller, Ranajit Ghose and me further worked out and tested the method. I thought out an alternative method, which made it to Appendix B.

On a personal level 2010 has been an exciting year. I had just moved out of the 'hard-to-say-goodbye' student house 'De Prins' in Delft to a splendid apartment in Schiedam. Anin soon joined me. But before that to happen, there was first a huge wedding party in Bandung, Indonesia, organized by my in-laws. Much gratitude goes to Edie, Diana, Anya, Aga, and the extended family for a warm welcome to their family. Also, I am grateful to my

Dutch family for making it to Indonesia and their openness to embrace a different culture. I am very pleased with many friends joining, with the wedding and the Jawa Barat trip. A sublime surprise was the party organized by Nihed, Jürg and other colleagues, just before the wedding. It became clear that their sincerity and kindness over the years had made me too good of trust.

The summer of 2010 was the initiation of the second part of the thesis. Shell Egypt had available a high-quality passive dataset. Xander had the bright idea to use it for testing interferometric approaches and I was the lucky guy that could dive into this. The quality of the dataset allowed a thorough analysis of the recorded microseisms and, surprisingly, body waves reflections could actually be extracted from them. I am grateful to Shell Egypt NV for the allowance to publish the fascinating outcomes and to Shell International Exploration and Production B.V. for paying my salary for a few months and providing a pleasant place to work. The analysis done during the stay at Shell was published and made it to Chapter 5. Deyan, two anonymous reviewers and Michel Campillo helped to improve the drafts for this chapter. Especially, I'd like to thank Xander for his guiding, enthusiasm and his contributions.

I presented the above results at the AGU Fall Meeting of 2010 and at the 3rd Passive Seismic Workshop in Athens, 2011. I got much positive feedback. This motivated me to further evaluate what information could be extracted from the body-wave microseisms, with respect to more conventional techniques. This study got published and made it to Chapter 6. Besides my coauthors, I'd like to thank Mei Zhang, Arie Verdel, Mohammed Ali and Francesca Martini for valuable discussion. Johan Robertsson and an anonymous reviewer helped improving the manuscript.

A disadvantage of the lithosphere-imaging approach as discussed as in Chapter 3 was that the array of stations had to be inline with an earthquake belt. Many arrays are not. For this reason, I worked out an alternative that is more generally applicable. I could test this method on an exciting dataset, thanks to the people involved with the Hi-CLIMB experiment and IRIS. The work got published and made it to Chapter 4. Shu-Huei Hung made a large contribution to the appendix of this chapter. Robert Nowack and an anonymous reviewer helped improving Chapter 4.

Inspired by a visit of BSU (Boise State University) student Dylan Mikesell to our labs in 2009, I visited the Physical Acoustics Lab in Idaho, USA, in the summer of 2011. I got a very warm welcome by Dylan and Kasper and Mila van Wijk. The adventure of that year was with no doubt going down the Hell's Canyon on a multiday rafting trip. Andy Lamb showed me beautiful sights of Idaho. Besides all this outdoor adventure, we actually got some work done. The most tangible result is the swift anomaly scanner, which made it to Appendix C. The interesting results could only be achieved by IRIS providing us data from the impressive USArray network of stations. Kees, Vera Schulte-Pelkum, Josh Stachnik, Raúl Valenzuela and one anonymous reviewer gave excellent suggestions. Another outcome of the BSU visit is a Slinky seismometer sensing the Earth now from Delft. I would like to

thank Kasper and Ted Channel for involving me with the Slinky project.

I am grateful to Deyan for involving me with the Malargüe project: a new and extensive seismic array in the south of the Mendoza Province, Argentina, just east of the Andes. I must admit that my involvement has been a distraction for writing this thesis, however I would not have liked to miss it. The design phase enabled me to use recently gained insights for creating something tangible. The instrument training at PASSCAL in Socorro, New Mexico, was fantastic, with Noel, Pnina and Mouse as our enthusiastic trainers. Last winter (austral summer) we actually built this array, together with a great bunch of people: Greg, Martin, Nidia, Ana-Rosa, Amalia and Nico.

A main motivator has been the possibility to travel. As an Earth scientist it is simply vital to sample different places of the Earth. I would like to thank my promotor and the funding agencies for facilitating this freedom.

In the above list my promotor Kees is often not explicitly mentioned, but he played an important role with all the chapters. His derivations are the starting point for most of this thesis. Moreover, with his exceptional knowledge and patience, he provided the first quality check for the different chapters. After processing his comments, most of the review processes have gone relatively smooth. It has been great to work under a person whose work and actions always make a lot of sense.

I would like to thank all the committee members for their interest in this thesis. I am very happy that this fine selection of intellectuals agreed to joining the committee and took on all the work that is connected with it.

Jan Thorbecke I would like to thank for providing his thesis layout files. This saved me a lot of work. Long-time neighbor Nihed sacrificed good deeds for other people to check the introduction. Deyan was refrained from finding new rare pieces for his collection because of proofreading appendix B. Jürg sacrificed a good beer in the sun to help me out with the propositions and the current section. Joost delayed a neat derivation, to check the summary.

My colleagues at the Geoscience and Engineering department contributed to the creative and joyful atmosphere in which this thesis could mature. Over the years there has been great selection of intellects, with interestingly varying cultural backgrounds. Undoubtedly I would do some wrong by attempting to mention them all. Julius and Joana I would like to thank interesting excursions to infrasound and volcanology, respectively.

My friends outside of work gave me the vital distractions to keep somewhat mentally sane and physically fit. I look forward to many more shared adventures.

I have the privilege to regard my family also as good friends. I am much indebted to my parents, Jaap and Ada, for giving me all the freedom to explore and all the support when necessary.

Anin gave me the main connection with the non-geophysical world. The dinners have been great and astonishingly they are still getting better all the time. Her humanness and adaptability are amazing and will be an inspiration for a long time to come.

Curriculum Vitae

PERSONAL

Name:	Elmer Niels Ruigrok
Born:	14th of January 1981, Eindhoven
Nationality:	Dutch

EDUCATION

2007 - 2012:	Ph.D. in Applied Geophysics and Petrophysics, Delft University of Technology, Delft, NL
Summer 2011:	Study visit to Physics Acoustics Lab, Boise State University, Boise, ID, US
Summer 2010:	Research internship at Shell International Exploration & Production B.V., Rijswijk, NL
Autumn 2008:	Work visit to Saudi Aramco EXPEC Advanced Research Centre, Dhahran, SA
Summer 2007:	Research internship at Schlumberger Doll Research, Cambridge, MA, US
1999 - 2006:	M.Sc. in Applied Geophysics, B.Sc. in Applied Earth Sciences, both at the Delft University of Technology, Delft, NL
Spring 2006:	Study visit to MIT Earth Resources Laboratory, Cambridge, MA, US
Summer 2004:	Research internship at Schlumberger Cambridge Research, Cambridge, UK
2003 - 2003:	Erasmus exchange, Montanuniversitt Leoben, Leoben, AT
1993 - 1999:	A-level secondary education (VWO) at Sint Willibrord Gymnasium, Deurne, NL

JOURNAL PUBLICATIONS

Ruigrok, E., X. Campman and K. Wapenaar, 2012, Basin delineation with a 40-hour passive seismic record, Bulletin of the Seismological Society of America, 102, doi:10.1785/0120110242.

Ruigrok, E. and K. Wapenaar, 2012, Global-phase seismic interferometry unveils P-wave reflectivity below the Himalayas and Tibet, Geophysical Research Letters, Geophysical Research Letters, 39, L11303, doi:10.1029/2012GL051672.

Ruigrok, E., T.D. Mikesell and K. van Wijk, 2012, Scanning for velocity anomalies in the crust and mantle with diffractions from the core-mantle boundary, Geophysical Research Letters, 38, L11301, doi:10.1029/2012GL051443.

Ruigrok, E., X. Campman and K. Wapenaar, 2011, Extraction of P-wave reflections from microseisms, C. R. Geoscience, 343, 512-525.

Wapenaar, K., J. van der Neut, E. Ruigrok, D. Draganov, J. Hunziker, E. Slob, J. Thorbecke & R. Snieder, 2011, Seismic interferometry by crosscorrelation and by multi-dimensional deconvolution: a systematic comparison, Geophysical Journal International, 185, 1335-1364.

Wapenaar, K., E. Ruigrok, J. van der Neut and D. Draganov, 2011, Improved surface-wave retrieval from ambient seismic noise by multi-dimensional deconvolution, Geophysical Research Letters, 38, L01313, doi:10.1029/2010GL045523.

Ruigrok, E., X. Campman, D. Draganov and K. Wapenaar, 2010, High-resolution lithospheric imaging with seismic interferometry, Geophysical Journal International, 183, 339-357.

Draganov, D., R. Ghose, E. Ruigrok, J. Thorbecke and K. Wapenaar, 2010, Seismic interferometry, intrinsic losses and Q-estimation, Geophysical prospecting, 58, 361-373.

Wapenaar, K, J. van der Neut and E. Ruigrok, 2008, Passive seismic interferometry by multidimensional deconvolution, Geophysics, 73, A51-A56.

Ruigrok, E, D. Draganov and K. Wapenaar, 2008, Global-scale seismic interferometry: theory and numerical examples, Geophysical Prospecting, 56, 395-417.

The above article was reprinted in Wapenaar, K., D. Draganov, and J. Robertsson, (2008), Seismic interferometry: history and present status, Society of Exploration Geophysicists Reprint Series, 26, ISBN 978-1-56080-150-4.

CONFERENCES AND WORKSHOP

2012

Ruigrok, E. and K. Wapenaar, 2012, global-phase seismic interferometry unveils P-wave reflectivity below the Himalayas and Tibet, Abstract ES2:010, European Seismological Commission 33rd General Assembly, August 19-24, Moscow, Russia.

Ruigrok, E., D. Mikesell and K. van Wijk, 2012, Scanning for velocity anomalies in the crust and mantle with diffractions from the core-mantle boundary, Science highlights at the 2012 IRIS Workshop, June 13-15, Boise, Idaho.

Fricke, J., E. Ruigrok, L. Evers, D. Simons and K. Wapenaar, 2012, Results of infrasound interferometry in the Netherlands, Geophysical Research Abstracts, 14, EGU2012-6155-3.

van Dalen, K., E. Ruigrok and K. Wapenaar, 2012, Surface-wave retrieval from ambient-noise observations using crosscorrelation and multidimensional deconvolution, Acoustics 2012, Nantes, France.

2011

Ruigrok, E. and K. Wapenaar, 2011, Interferometric imaging with global phases, Abstract S31E-2275 presented at the 2011 Fall Meeting, AGU, San Francisco, Calif., 5-9 Dec.

Fricke, J., E. Ruigrok, L. Evers, D. Simons and K. Wapenaar, 2011, The first results of infrasound interferometry in the Netherlands, Infrasound Technology Workshop, Dead Sea, Jordan, 30 Oct-4 Nov.

López Pumarega, M., E. Ruigrok, J. Ruzzante and D. Draganov, 2011, ICES, International research project for monitoring subsurface and active volcano zone at Malarge area, Interdisciplinary science @ the Auger Observatory: from cosmic rays to the environment, Cambridge UK, 15b.

Fricke, J., E. Ruigrok, L. Evers, D. Simons and K. Wapenaar, 2011, A large aperture infrasound array for interferometric studies, Geophysical Research Abstracts, 13, EGU2011-4471.

Ruigrok, E., X. Campman and K. Wapenaar, 2011, A deep seismic profile from noise records, Athens 2011, 3rd Passive Seismic Workshop (pp. PAS16-1-PAS-7), Houten, The Netherlands: EAGE.

2010

Ruigrok, E., X. Campman, and K. Wapenaar, 2010, Crust and upper-mantle imaging with noise, Abstract S33A-2066 presented at 2010 Fall Meeting, AGU, San Francisco, Calif., 13-17 Dec.

Wapenaar, K, J, van der Neut, E. Ruigrok, D. Draganov, J. Hunziker, E. Slob, J. Thorbecke

and R. Snieder, 2010, Seismic interferometry by crosscorrelation and by multi-dimensional deconvolution: a systematic comparison, Abstract S23C-05 presented at 2010 Fall Meeting, AGU, San Francisco, Calif., 13-17 Dec.

Wapenaar, K., E. Ruigrok, J. van der Neut, D. Draganov, J. Hunziker, E. Slob, J. Thorbecke and R. Snieder, 2010, Green's function representation for seismic interferometry by deconvolution. 80th SEG Conference (pp. 3972-3978), Tulsa, OK, USA: SEG.

Neut, J. van der, E. Ruigrok, D. Draganov and K. Wapenaar, 2010, Retrieving the earth's reflection response by multi-dimensional deconvolution of ambient seismic noise: a post-processing tool for passive interferometry, Barcelona 2010 (P406), Houten, The Netherlands: EAGE.

Wapenaar, K., J. van der Neut, E. Ruigrok, D. Draganov, J. Hunziker, E. Slob, J. Thorbecke and R. Snieder, 2010, Seismic interferometry by crosscorrelation and multidimensional deconvolution: a systematic comparison, Geophysical Research Abstracts, 12, EGU2010-5758.

Ruigrok, E., J. van der Neut, H. Djikpesse, C.-W. Chen, and K. Wapenaar, 2010, A feasibility study for the application of seismic interferometry by multidimensional deconvolution for lithospheric-scale imaging, Geophysical Research Abstracts, 12, EGU2010-9370.

Neut, J. van der, E. Ruigrok, D. Draganov, J. Thorbecke, J. Hunziker and K. Wapenaar, 2010, Surface wave retrieval from ambient noise using Multi-dimensional deconvolution, Saint Petersburg 2010, Russia International conference and exhibition on Geoscience (P240). Houten, The Netherlands: EAGE.

Ruigrok, E., J. van der Neut and K. Wapenaar, CPA, 2010, A feasibility study for the application of seismic interferometry by multidimensional deconvolution for lithospheric-scale imaging, 10th Nederlands Aardwetenschappelijk Congres (pp. 167). The Netherlands: NAC.

2009

Ruigrok, E., D. Draganov, K. Wapenaar and X. Campman, 2009, Estimation of lithospheric-scale velocity models using bodywave seismic interferometry, 79th SEG Conference, pp. 4217-4218, Houston, USA: SEG.

Thorbecke, J., E. Ruigrok, D. Draganov, J. van der Neut, J. Hunziker and K. Wapenaar, 2009, Seismic Interferometry by cross-correlation and by multi-dimensional deconvolution using ambient seismic noise, 79th SEG Conference, pp. 4219-4222, Houston, USA: SEG.

Draganov, D., E. Ruigrok, J.W. Thorbecke, J. Hunziker, J.R. van der Neut and K. Wapenaar, 2009. Seismic interferometry by cross-correlation and by multi-dimensional deconvolution using ambient seismic noise. Neustadt Workshop on Noise and Diffusive Wavefield, pp. 109-113, Neustadt an der Weinstrasse, Germany: DGG.

Ruigrok, E., X. Campman, K. Wapenaar, 2009, Lithospheric-scale seismic interferometry:

a comparison of approaches to deal with an irregular source distribution and source-side reverberations, Neustadt Workshop on Noise and Diffusive Wavefields, pp. 125-129, Neustadt an der Weinstrasse, Germany: DGG.

Ruigrok, E., K. Wapenaar, J. van der Neut and D. Draganov, 2009, A review of crosscorrelation and multidimensional deconvolution seismic interferometry for passive data, Limassol, Cyprus 2009, Workshop on Passive Seismic (A09). Houten, The Netherlands: EAGE.

Neut, J. van der, K. Wapenaar and E. Ruigrok, 2009, Seismic interferometry by multi-dimensional deconvolution for passive transient sources, Tunis 2009, 4th North African/Mediterranean Petroleum and Geosciences Conference & Exhibition Tunis (S11). Houten, The Netherlands: EAGE.

2008

Wapenaar, K., J. van der Neut, E. Ruigrok, D. Draganov, J. Hunziker, E. Slob, J. Thorbecke and R. Snieder, 2008, Seismic interferometry by multidimensional deconvolution as a means to compensate for anisotropic illumination, Eos Trans. AGU, 89(53), Fall Meet. Suppl., Abstract S23D-01.

Ruigrok, E., X. Campman and K. Wapenaar, 2008, Data requirements for the retrieval of regional-scale reflection responses by cross correlation, Eos Trans. AGU, 89(53), Fall Meet. Suppl., Abstract S31A-1900.

Wapenaar, K., J. van der Neut, E. Ruigrok, D. Draganov, E. Slob, J. Thorbecke and R. Snieder, 2008, Seismic interferometry by cross-correlation or deconvolution? 78th annual SEG meeting, Las Vegas, 2731-2736.

Ruigrok, E., D. Draganov, J. Thorbecke, J. van der Neut and K. Wapenaar, 2008, Sampling and illumination aspects of seismic interferometry in horizontally layered media. 70th EAGE Meeting, Rome 2008, Leveraging Technology (pp. P227-1-P227-5). Houten, The Netherlands: EAGE.

Draganov, D., R. Ghose, E. Ruigrok, J. thorbecke and K. Wapenaar, 2008, Effect of intrinsic losses on seismic interferometry, 70th EAGE Meeting, Rome 2008 Leveraging Technology (pp. G024-1-G024-5). Houten, The Netherlands: EAGE.

Ruigrok, E., X. Campman, D. Draganov and K. Wapenaar, 2008, Application of seismic interferometry to teleseismic array data, 9th Nederlands Aardwetenschappelijk Congres, Abstract 140, The Netherlands: NAC.

2007

Ruigrok, E., D. Draganov, J. van der Neut, and K. Wapenaar, 2007, Global-, Teleseismic and Regional-Scale Green's Function Retrieval: on the Sampling of the Surface Integral, Eos Trans. AGU, 88(52), Fall Meet. Suppl., Abstract S53B-1259.

Ruigrok, E., X. Campman, D. Draganov, K. Wapenaar and S. Rondenay, 2007, Application

of seismic interferometry to teleseismic array data, Geophysical Research Abstracts, 9, EGU2007-A-10593.

2006

Wapenaar, K., D. Draganov, E. Ruigrok, W. Mulder, J. Singer and A. Verdel, 2006, Seismic Interferometry Applied to Passive Data, Workshop 'Passive Seismic: Exploration and Monitoring Applications', EAGE, Dubai.

Ruigrok, E., D. Draganov, K. Wapenaar, and J. Thorbecke, 2006, Global-scale seismic interferometry: Numerical validation of the acoustic correlation integral, 76th Annual International Meeting, SEG, Expanded Abstracts, SM 1.7.

Ruigrok, E., D. Draganov and K. Wapenaar, 2006, Global-scale seismic interferometry, Workshop 'What Can EP Learn from Seismology and Vice Versa', 68th EAGE Conference & Exhibition, Vienna.

Draganov, D., E. Ruigrok, K. Wapenaar and J. Thorbecke, 2006, Seismic Interferometry - Reconstruction of the Earth's Reflection Response, 8th Nederlands Aardwetenschappelijk Congres, The Netherlands: NAC.